

AD-A186 635

DTIC FILE COPY

Bulletin 50  
(Part 4 of 4 Parts)

# THE SHOCK AND VIBRATION BULLETIN

Part 4  
Dynamic Properties of Materials  
Applications of Materials, Shock and Blast,  
Fragments

SEPTEMBER 1980

A Publication of  
THE SHOCK AND VIBRATION  
INFORMATION CENTER  
Naval Research Laboratory, Washington, D.C.

DTIC  
ELECTE  
NOV 19 1987  
S  
C  
D

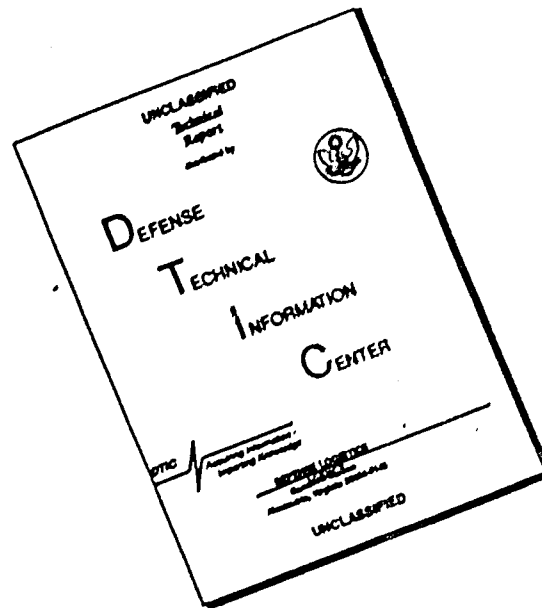


Office of  
The Under Secretary of Defense  
for Research and Engineering

Approved for public release; distribution unlimited

87 10 28 002

# DISCLAIMER NOTICE



THIS DOCUMENT IS BEST QUALITY AVAILABLE. THE COPY FURNISHED TO DTIC CONTAINED A SIGNIFICANT NUMBER OF PAGES WHICH DO NOT REPRODUCE LEGIBLY.

## **SYMPOSIUM MANAGEMENT**

### **THE SHOCK AND VIBRATION INFORMATION CENTER**

Henry C. Pusey, Director

Rudolph H. Volin

J. Gordan Showalter

Carol Healey

Elizabeth A. McLaughlin

#### **Bulletin Production**

Publications Branch, Technical Information Division,  
Naval Research Laboratory

Bulletin 50  
(Part 4 of 4 Parts)

# THE SHOCK AND VIBRATION BULLETIN

SEPTEMBER 1980

A Publication of  
THE SHOCK AND VIBRATION  
INFORMATION CENTER  
Naval Research Laboratory, Washington, D.C.

The 50th Symposium on Shock and Vibration was held at the Antlers Plaza Hotel, Colorado Springs, CO on October 16-18, 1979. The U.S. Air Force Academy, Colorado Springs, CO, was host on behalf of the Air Force.



Office of  
The Under Secretary of Defense  
for Research and Engineering

Accession For	
NTIS GRA&I	<input checked="" type="checkbox"/>
DTIC TAB	<input type="checkbox"/>
Unannounced	<input type="checkbox"/>
Justification	
By	
Distribution	
Availability Codes	
Dist	Avail and/or Special
A-1	



## PAPERS APPEARING IN PART 4

### DYNAMIC PROPERTIES OF MATERIALS

MATERIAL DAMPING AS A MEANS OF QUANTIFYING FATIGUE DAMAGE IN COMPOSITES	1
P. J. Torvik, Air Force Institute of Technology, Wright-Patterson AFB, OH and C. J. Bourne, Air Force Flight Test Center, Edwards AFB, CA	
SONIC FATIGUE TESTING OF THE NASA L-1011 COMPOSITE AILERON	13
J. Soovere, Lockheed-California Company, Burbank, CA	
MODELING A TEMPERATURE SENSITIVE CONFINED CUSHIONING SYSTEM	25
V. P. Kobler, U.S. Army Missile Command, Huntsville, AL, R. M. Wyskida and J. D. Johannes, The University of Alabama in Huntsville, Huntsville, AL	

### APPLICATIONS OF MATERIALS

PRELIMINARY HARDNESS EVALUATION PROCEDURE FOR IDENTIFYING SHOCK ISOLATION REQUIREMENTS	35
R. J. Bradshaw, Jr., U.S. Army Engineer Division, Huntsville, Huntsville, AL and P. N. Sonnenburg, U. S. Army Construction Engineering Research Laboratory, Champaign, IL	
AN APPLICATION OF TUNED MASS DAMPERS TO THE SUPPRESSION OF SEVERE VIBRATION IN THE ROOF OF AN AIRCRAFT ENGINE TEST CELL	59
J. L. Goldberg, N. H. Clark and B. H. Meldrum, CSIRO Division of Applied Physics, Sydney, Australia	
COMPARISON OF ANALYTICAL AND EXPERIMENTAL RESULTS FOR A SEMI-ACTIVE VIBRATION ISOLATOR	69
E. J. Krasnicki, Lord Kinematics, Erie, PA	
AN EXPERIMENTAL INVESTIGATION OF NOISE ATTENUATING TECHNIQUES FOR SPACE-SHUTTLE MANIFESTERS	77
L. Mirandy, General Electric Company, Philadelphia, PA, F. On and J. Scott, NASA Goddard Space Flight Center, Greenbelt, Md	
DYNAMIC INTEGRITY METHODS INCLUDING DAMPING FOR ELECTRONIC PACKAGES IN RANDOM VIBRATION	91
J. M. Medaglia, General Electric Company, Philadelphia, PA	
AN OVERVIEW OF SHOCK ANALYSIS AND TESTING IN THE FEDERAL REPUBLIC OF GERMANY	105
K. -E. Meier-Dornberg, Institut fur Mechanik, Technische Hochschule Darmstadt, Federal Republic of Germany	
CONSERVATISM IN SHOCK ANALYSIS AND TESTING	117
T. L. Paez, The University of New Mexico, Albuquerque, NM	
MEASUREMENT OF DYNAMIC STRUCTURAL CHARACTERISTICS OF MASSIVE BUILDINGS BY HIGH-LEVEL MULTIPULSE TECHNIQUES	137
D. G. Yates and F. B. Safford, Aghabian Associates, El Segundo, CA	
CONSIDERATION OF AN OPTIMAL PROCEDURE FOR TESTING THE OPERABILITY OF EQUIPMENT UNDER SEISMIC DISTURBANCES	149
C. W. Jr Silva, Carnegie-Mellon University, Pittsburgh, PA, F. Locoff and K. M. Vashi, Westinghouse Nuclear Energy Systems, Pittsburgh, PA	
DYNAMIC LOADING OF METAL RIVETED JOINTS	159
R. L. Sierakowski, C. A. Rom, J. Hoover, University of Florida, Gainesville, FL and W. S. Strickland, USAF Armament Lab, AFATL/DLYV Eglin AFB, FL	

GENERALIZED GRAPHICAL SOLUTION FOR ESTIMATING RECOILLESS RIFLE BREECH BLAST OVERPRESSURES AND IMPULSES .....	175
P. S. Westine, G. J. Friesenhahn and J. P. Riegel, III, Southwest Research Institute, San Antonio, TX	
PREDICTING THE MOTION OF FLYER PLATES DRIVEN BY LIGHT-INITIATED EXPLOSIVE FOR IMPULSE LOADING EXPERIMENTS .....	191
R. A. Benham, Sandia Laboratories, Albuquerque, NM	

#### FRAGMENTS

SCALING OF INITIATION OF EXPLOSIVES BY FRAGMENT IMPACT ; .....	139
W. E. Baker, M. G. Whitney and V. B. Parr, Southwest Research Institute, San Antonio, TX	
EQUATIONS FOR DETERMINING FRAGMENT PENETRATION AND PERFORATION AGAINST METALS ; .....	213
I. M. Gyllenspetz, National Defense Research Institute (FOA), Stockholm, Sweden	
BREACHING OF STRUCTURAL STEEL PLATES USING EXPLOSIVE DISKS .....	223
D. L. Shirey, Sandia Laboratories, Albuquerque, NM	

#### PAPERS APPEARING IN PART 1

##### WELCOME

##### WELCOME

Brigadier General William A. Orth, United State Air Force Academy

##### WELCOME

Colonel Ralph L. Kuster, Air Force Flight Dynamics Laboratory

##### KEYNOTE ADDRESS

##### U.S. ARMY KEYNOTE ADDRESS

Lieutenant General Robert J. Baer, U.S. Army Material Development and Readiness Command

##### U.S. NAVY KEYNOTE ADDRESS

Dr. T. T. G. Horwath, Naval Material Command

##### U.S. AIR FORCE KEYNOTE ADDRESS

Brigadier General Brien D. Ward, Air Force Systems Command

##### INVITED PAPERS

##### MEASUREMENT IN PERSPECTIVE

Professor Robert M. Mains, Washington University

##### DYNAMIC ANALYSIS AND DESIGN-CHALLENGE FOR THE FUTURE

Mr. Robert Hager, Boeing Company

##### MATERIALS IN DYNAMICS

Mr. Richard Shea and Mr. John Mccall, U.S. Army Materials and Mechanics Research Agency

##### DYNAMIC TESTING -- HOW FAR WE'VE COME -- HOW MUCH FURTHER TO GO

Dr. Allen J. Curtia, Hughes Aircraft Company

#### PAPERS APPEARING IN PART 2

##### MEASUREMENT TECHNIQUES AND DATA ANALYSIS

##### A PRECISION INERTIAL ANGULAR VIBRATION MEASURING SYSTEM

H. D. Morris and R. B. Peters, Systron-Donner Corporation, Concord, CA and  
P. H. Merritt, Air Force Weapons Laboratory, Kirtland AFB, NM

ANGULAR ACCELERATION MEASUREMENT ERRORS INDUCED BY LINEAR ACCELEROMETER  
CROSS-AXIS COUPLING

A. S. Hu, New Mexico State University, Las Cruces, NM

A METHOD FOR EXPERIMENTALLY DETERMINING ROTATIONAL MOBILITIES OF STRUCTURES

S. S. Sattinger, Westinghouse-Bettis Atomic Power Laboratory, Pittsburgh, PA

TRANSIENT EFFECTS IN ACOUSTIC SOUND REDUCTION MEASUREMENTS

A. J. Kalinowski, Naval Underwater Systems Center, New London, CT

SHOCK MEASUREMENT DURING BALLISTIC IMPACT INTO ARMORED VEHICLES

W. S. Walton, U.S. Army Aberdeen Proving Ground, Aberdeen Proving Ground, MD

AUTOMATIC DATA CHANNEL CALIBRATION AND NOISE IDENTIFICATION

E. E. Nesbit, Lawrence Livermore Laboratory, Livermore, CA

STATISTICAL ESTIMATION OF SIMULATED YIELD AND OVERPRESSURE

P. F. Mlakar and R. E. Walker, U.S. Army Engineer, Waterways Experiment Station, Vicksburg, MS

DYNAMIC MEASUREMENTS

AN ASSESSMENT OF THE COMMON CARRIER SHIPPING ENVIRONMENT

F. E. Ostrem, GARD, Inc., Niles, IL

SHOCK AND VIBRATION ENVIRONMENT IN A LIVESTOCK TRAILER

M. T. Turczyn, U.S. Department of Agriculture, Beltsville, MD, D. G. Stevens and T. H. Camp,  
U.S. Department of Agriculture, College Station, TX

SHOCK INDUCED IN MISSILES DURING TRUCK TRANSPORT

D. B. Neeker and J. A. Sears, Pacific Missile Test Center, Point Mugu, CA

DYNAMIC CHARACTERISTICS OF AN INDUCED-DRAFT FAN AND ITS FOUNDATION

S. P. Ying and E. E. Dennison, Gilbert/Commonwealth, Jackson, MI

VIBRATION AND ACOUSTICS

A METHOD TO DETERMINE REALISTIC RANDOM VIBRATION TEST LEVELS TAKING INTO ACCOUNT  
MECHANICAL IMPEDANCE DATA - PART 1: BASIC IDEAS AND THEORY

O. Sylwan, IFM Akustikbyran AB, Stockholm, Sweden

A METHOD TO DETERMINE REALISTIC RANDOM VIBRATION TEST LEVELS TAKING INTO ACCOUNT  
MECHANICAL IMPEDANCE DATA - PART 2: VERIFICATION TESTS

T. Hell, SAAB-SCANIA AB, Linköping, Sweden

VIBRATION ANALYSIS OF A HELICOPTER PLUS AN EXTERNALLY-ATTACHED STRUCTURE

D. J. Ewins, Imperial College of Science and Technology, London, England, J. M. M. Silva,  
University of Lisbon, Portugal and G. Maleci, Nuovo Pignone, Florence, Italy

IMPROVING VIBRATION TECHNIQUES FOR DETECTING WORKMANSHIP DEFECTS IN ELECTRONIC  
EQUIPMENT

J. W. Burt and M. A. Condouris, U.S. Army Electronics Command, Fort Monmouth, NJ

SINGLE-POINT RANDOM AND MULTI-SHAKER SINE SPACECRAFT MODAL TESTING

M. Ferrante, C. V. Stahle and D. G. Breakman, General Electric Company, Space Division,  
King of Prussia, PA

BIAS ERRORS IN A RANDOM VIBRATION EXTREMAL CONTROL STRATEGY

D. O. Smallwood and D. L. Gregory, Sandia Laboratories, Albuquerque, NM

A NEW METHOD OF IMPROVING SPECTRA SHAPING IN REVERBERANT CHAMBERS

J. N. Scott, NASA Goddard Space Flight Center, Greenbelt, MD and R. L. Burkhardt, Northrop Services,  
Inc., NASA, Goddard Space Flight Center, Greenbelt, MD

THE VIBRATION TEST UNIT A UNIQUE RAIL VEHICLE VIBRATION TEST FACILITY  
R. O. Coupland and A. J. Nintzel, Wyle Laboratories, Colorado Springs, CO

THE APPLICATION OF COMPUTERS TO DYNAMIC RAIL VEHICLE TESTING  
B. Clark, Wyle Laboratories, Colorado Springs, CO

LOW FREQUENCY STRUCTURAL DYNAMICS OF THE SPACE SHUTTLE SOLID ROCKET BOOSTER MOTOR  
DURING STATIC TESTS  
M. A. Behring and D. R. Mason, Thiokol Corporation/Wasatch Division, Brigham City, UT

VIBRATION ENVIRONMENT OF THE SPACE SHUTTLE SOLID ROCKET BOOSTER MOTOR DURING  
STATIC TESTS  
D. R. Mason and M. A. Behring, Thiokol Corporation/Wasatch Division, Brigham City, UT

ELIMINATION OF A DISCRETE FREQUENCY ACOUSTICAL PHENOMENON ASSOCIATED WITH THE  
SPACE SHUTTLE MAIN ENGINE OXIDIZER VALVE-DUCT SYSTEM  
L. A. Schutzenhofer, J. H. Jones, R. E. Jewell and R. S. Ryan, NASA, George C. Marshall Space Flight Center,  
Marshall Space Flight Center, AL

#### PAPERS APPEARING IN PART 3

##### DYNAMIC ANALYSIS

THE RELATIVE COMPLEXITIES OF PLATE AND SHELL VIBRATIONS  
A. W. Leissa, Ohio State University, Columbus, OH

IN-FLUID CYLINDRICAL BEAM VIBRATION WITH MULTI-DEGREE OF FREEDOM ABSORBERS  
B. E. Sandman and J. S. Griffin, Naval Underwater Systems Center, Newport, RI

DYNAMIC STABILITY OF FIBROUS COMPOSITE CYLINDERS UNDER PULSE LOADING  
R. J. Stuart and S. Dharmarajan, San Diego State University, San Diego, CA

TRANSFER-MATRIX ANALYSIS OF DYNAMIC RESPONSE OF COMPOSITE-MATERIAL STRUCTURAL  
ELEMENTS WITH MATERIAL DAMPING  
M. M. Wallace and C. W. Bert, The University of Oklahoma, Norman, OK

CONTRIBUTIONS TO THE DYNAMIC ANALYSIS OF MAGLEV VEHICLES ON ELEVATED GUIDEWAYS  
K. Popp, Technical University Munich, West Germany

DYNAMICS OF LONG VERTICAL CABLES  
F. H. Wolff, Westinghouse R&D Center, Pittsburgh, PA

RESPONSE AND FAILURE OF UNDERGROUND REINFORCED CONCRETE PLATES SUBJECTED TO BLAST  
C. A. Ross and C. C. Schauble, University of Florida Graduate Engineering Center, Eglin AFB, FL and P. T. Nash,  
USAF Armament Laboratory, Eglin AFB, FL

WHIPPING ANALYSIS TECHNIQUES FOR SHIPS AND SUBMARINES  
K. A. Bannister, Naval Surface Weapons Center, White Oak, Silver Spring, MD

LIMITATIONS ON RANDOM INPUT FORCES IN RANDOMDEC COMPUTATION FOR MODAL  
IDENTIFICATION  
S. R. Ibrahim, Old Dominion University, Norfolk, VA

STRUCTURAL-DYNAMIC CHARACTERIZATION OF AN EXPERIMENTAL 1200-KILOVOLT ELECTRICAL  
TRANSMISSION-LINE SYSTEM  
Leon Kempner, Jr., Bonneville Power Administration, Portland, OR and Stephen Smith and Richard C. Stroud,  
Synergistic Technology Incorporated, Cupertino, CA

#### DESIGN TECHNIQUES

##### **ANALYSIS AND DESIGN OF THE SHUTTLE REMOTE MANIPULATOR SYSTEM MECHANICAL ARM FOR LAUNCH DYNAMIC ENVIRONMENT**

D. M. Gossain, E. Quittner and S. S. Sachdev, Spar Aerospace Limited, Toronto, Canada

##### **STRUCTURAL DYNAMIC CHARACTERISTICS OF THE SPACE SHUTTLE REACTION CONTROL THRUSTERS**

G. L. Schachne and J. H. Schmidt, The Marquardt Company, Van Nuys, CA

##### **MODIFICATION OF FLIGHT VEHICLE VIBRATION MODES TO ACCOUNT FOR DESIGN CHANGES**

C. W. Coale and M. R. White, Lockheed Missiles and Space Company, Sunnyvale, CA

##### **EVALUATION OF AIRBORNE LASER BEAM JITTER USING STRUCTURAL DYNAMICS COMPUTER CODES AND CONTROL SYSTEM SIMULATIONS**

C. L. Buddle and P. H. Merritt, Air Force Weapons Laboratory, Kirtland AFB, NM and  
C. D. Johnson, Anamet Laboratories, Inc., San Carlos, CA

##### **FATIGUE LIFE PREDICTION FOR MULTILEVEL STEP-STRESS APPLICATIONS**

R. G. Lambert, General Electric Company, Utica, NY

##### **LATERAL INSTABILITY DURING SPIN TESTS OF A PENDULOUSLY SUPPORTED DISC**

F. H. Wolff, A. J. Molnar, G. O. Sankey and J. H. Bitzer, Westinghouse R&D Center, Pittsburgh, PA

#### **TITLES AND AUTHORS OF PAPERS PRESENTED IN THE SHORT DISCUSSION TOPICS SESSION**

NOTE: These papers were only presented at the Symposium. They are not published in the Bulletin and are only listed here as a convenience.

##### **DAMAGE EQUIVALENCE BETWEEN DISCRETELY APPLIED AND COMPLEX HARMONICS**

J. J. Richardson, USAMICOM, Huntsville, AL

##### **ON A UNIFIED THEORY OF VIBRATION CONTROL AND ISOLATION**

P. W. Whaley, Air Force Institute of Technology, Wright-Patterson AFB, OH

##### **THE VIBRATION OF WELDED PLATES**

S. M. Dickinson and M. M. Kaldas, The University of Western Ontario, London, Ontario, Canada

##### **SENSIBLE DISPLAY OF PSD INFORMATION**

W. D. Everett, Pacific Missile Test Center, Point Mugu, CA

##### **RAIL SHIPMENT SHOCK SIMULATION ON A PEACEFUL NUCLEAR EXPLOSION INSTRUMENT VAN**

R. O. Brooks, Sandia Laboratories, Albuquerque, NM

##### **FREE FALL TESTING OF ARRESTMENT DEVICES FOR MAN CONVEYANCES IN MINE SHAFTS**

F. A. Peening, Colorado School of Mines, Golden, CO, and E. H. Skinner, Spokane Mining Research Center, Spokane, WA

##### **REVERSAL IN TIME DOMAIN EQUALS COMPLEX CONJUGATE IN FREQUENCY DOMAIN**

A. J. Curtis, Hughes Aircraft Co., Culver City, CA

##### **ELIMINATION OF INTERFERING ACOUSTIC STANDING WAVES IN A SONIC FATIGUE FACILITY**

H. N. Bolton, McDonnell Douglas Corporation, Long Beach, CA

##### **TEST VEHICLE CONFIGURATION EFFECTS ON VIBRO-ACOUSTIC TESTING**

C. J. Beck, Jr., Boeing Aerospace Company, Seattle, WA

**RANDOM VIBRATION CONCEPTS CLARIFIED**

W. Tustin, Tustin Institute of Technology, Inc., Santa Barbara, CA

**TRANSMISSION-LINE WIND-LOADING RESEARCH**

R. C. Stroud, Synergistic Technology Inc., Cupertino, CA

**A METHOD FOR MEASURING END LOAD IN A HOLLOW ROD USING STRAIN GAGE ORIENTATION  
TO CONCEAL UNWANTED STRAIN OUTPUTS**

J. Favour, Boeing Aerospace Company, Seattle, WA

**CRITICAL ASPECTS OF FIXTURE DESIGN AND FABRICATION FOR 781C**

D. V. Kimball, Kimball Industries, Inc., Monrovia, CA

## Dynamic Properties of Materials

### MATERIAL DAMPING AS A MEANS OF QUANTIFYING FATIGUE DAMAGE IN COMPOSITES

Petar J. Torvik and Cynthia Bourne<sup>\*</sup>  
Department of Aeronautics and Astronautics  
Air Force Institute of Technology  
Wright-Patterson Air Force Base, Ohio

The possibility of using damping measurements as a nondestructive means of quantifying damage accumulation during the fatigue life of composites was considered. Damping measurements were made during the course of fatigue studies on a graphite epoxy composite using both the logarithmic decrement and the bandwidth techniques. Measurable increases in damping were observed during the service life, but no dramatic change was encountered immediately prior to failure. Since the changes were moderate, and gradual, these experiments suggest that damping can be used as an index of cumulative mechanical damage in composites, but that the results should be used with caution and regarded as more qualitative than quantitative.

#### INTRODUCTION

Composite materials are ideal for structural applications where high strength-to-weight ratios are required. Aircraft and spacecraft are typical weight-sensitive structures in which composite materials are cost-effective. Advanced fiber-reinforced composite materials using the new ultrahigh strength and stiffness fibers such as boron and graphite in a matrix of epoxy or metal have two major advantages: improved strength and stiffness. Such composites can be tailored to efficiently meet design requirements of strength, stiffness, and other parameters and should lead to new and more efficient aircraft and spacecraft designs. The strength of composites is governed by their flaw-initiated characteristics. Thus, the mechanics of fracture including crack propagation, extension, and delamination are of extreme importance in the design analysis of composite structures. Salkind [1] has proposed that composites may fail by matrix cracking, fiber failure, and delamination, either separately or in combination. He also suggests that a fatigue failure criterion could be the number of cycles to a given change in stiffness rather than the number of cycles to fracture since the loss of stiffness can result in structural failure long before complete fracture occurs. However, small changes in stiffness are not readily observed. Thus stiffness changes are difficult to use as a means of quantifying damage.

<sup>\*</sup> Lt, USAF, Presently Aerospace Engineer, Air Force Flight Test Center, Edwards AFB CA

It is conjectured that the internal damping of fiber-reinforced composites is more sensitive than stiffness to the failure mechanisms previously mentioned. Accordingly, damping measurements may be useful in the early detection of structural damage. A number of investigators have considered the damping of composites, using various techniques. Much of this experimental work on the damping and stiffness properties of composite materials has been concerned with measuring the dependence on frequency, and temperature [2] and the effect of changing humidity [3]. However, some investigators have explored the relationship between damage and damping. Schulcs and Tsai [4] used logarithmic decrement and bandwidth techniques to test aluminum and glass fiber-reinforced plastics in flexural vibration. They found that the amount of fatigue cracking correlated reasonably well with the amount of increase in damping. Others [5] have studied the change in the damping of free vibrations and found crack damage present as changes in damping occurred.

For the commercial utilization of composites, it is necessary to assure material integrity through reliable methods. Several non-destructive techniques for quantifying damage (NDT) are currently being investigated. Of these, holography and ultrasonics show the most promise. Because damping can be expected to be sensitive to microstructural damage, damping measurements made at low levels of vibratory stress may provide another method for nondestructive evaluation of damage, both during the materials manufacturing process, and in service.

The feasibility of using the change in material damping to quantify structural damage in the course of a destructive bending fatigue test on composite beams was considered in this work. Observed changes in damping were compared with NDT results in order to provide a comparison between these two means of evaluating damage.

The experiments conducted were developed to determine the nature of the damping changes which occur during the service life of a composite member. Three questions are of particular interest. First, what is the magnitude of the change in damping, i.e., is damping a useful index of damage, or are the changes too small to be readily observable in the presence of other loss mechanisms. Second, at what point in the life history of the structure do the damping changes occur, i.e., are there sudden increases in damping which serve as effective warnings of incipient failure, or are all changes gradual. Finally, we may ask if changes in damping appear to correlate with any other measures of damage.

#### EXPERIMENTAL PROCEDURES

Twelve specimens with the geometry shown in Fig. 1 were supplied by the Air Force Flight Dynamics Laboratory. They were machined from a single 16-ply, Thorne 300/5208, graphite-epoxy panel fabricated by Monsanto Research Corporation. The multiple layers are arranged symmetrically about the middle surface at orientations of 0, 45, -45, 90, 90, -45, 45, and 0 degrees to the longitudinal axis, starting with the outer ply and progressing to the middle surface. This layup can be expressed as  $((0/-45/90)_2)_2$ . Rectangular fiberglass and doublers, 0.118 inch thick, with one edge beveled at 30 degrees were adhesively bonded to the specimens. A circular hole was drilled in the center of each specimen. Nominally, the specimens were one inch wide, 0.085 inch thick, eight inches long, with a center hole diameter of 0.20 inch. A specimen design with circular hole was chosen, recognizing that most fatigue failures in aircraft structures initiate at fasteners. This is particularly critical in the case of composites, because of the interruption of fiber continuity and the interlaminar shear stresses at edges. An aluminum beam of the same planform and stiffness as the specimens and one defective specimen were used to develop the testing procedures. The effective length of each specimen was considered to be from the end of the tapered doubler to the accelerometer attachment position at the center of the "free" end doubler, or 5.12 inches.

Specimens were mounted as cantilever beams with tip mass and tested at resonance by driving the base so as to maintain constant tip amplitude. An M-8 electrodynamic vibration exciter, model C10E, was used for all tests. As shown in Fig. 2, it was driven by an M-8

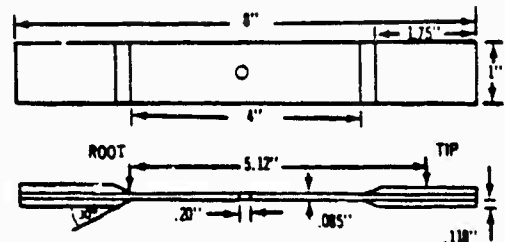


Fig. 1 - Specimen Geometry

automatic vibration exciter control, model N695/676, via an M-8 power amplifier. The moving element of the exciter was fitted with an aluminum fixture that served as the mount for each specimen and as a counter balance to specimen and accelerometer inertia. Figure 3 illustrates this arrangement. An Endevco piezoelectric accelerometer, model 2233C, was glued onto the specimen free end and provided feedback to the control unit through two Endevco preamplifiers, models 2614B and 2621. The control unit integrated the acceleration twice and drove the shaker with the sinusoidal signal required to maintain the specimens at constant resonant tip amplitude. The driving (base) amplitude was monitored at the control unit, and small adjustments made to the driving frequency to maintain resonance (minimum input). The output of the tip accelerometer and preamplifiers were also monitored with an oscilloscope. A second accelerometer of the same type was mounted on the aluminum block at the clamped end of the specimens. Its output was fed into an M-8 vibration meter, model NS24, from which base displacement was monitored.

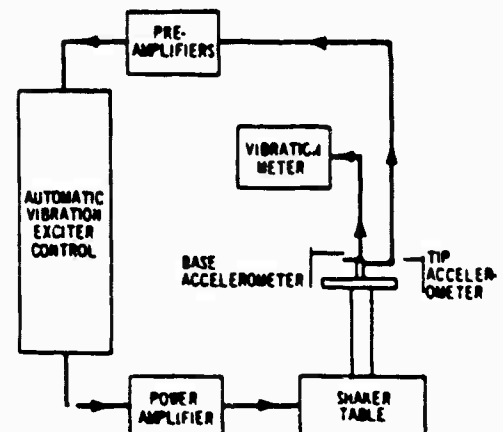


Fig. 2 - Schematic of Vibration Test System





Fig. 3 - Beam Mounted on Vibration Exciter Head

A CMC universal counter-timer, model 726C, was used to monitor driving frequency continuously. The frequency and the elapsed time were used to determine the number of cycles applied to each specimen. Eight specimens were cycled to failure, and three more were terminated before failure because of test difficulties. Failure for this experiment was defined as extensive visual fiber delamination accompanied by a significant change in resonant frequency. Stress levels were chosen so that failure would occur between  $10^5$  and  $10^6$  cycles. No discernible twisting of the specimens was encountered.

#### Measurements of Damping

Two methods were used to measure the damping during the course of the fatigue tests. As it was necessary to monitor both base and tip amplitude in order to maintain resonance, it was convenient to determine the bandwidth of the resonant response periodically. Amplitude ratios were determined at several frequencies near to resonance, and the half-power frequencies determined.

The system loss factor is defined by the ratio of the energy dissipated, per radian, to the peak strain energy. This may be shown to be equivalent to

$$\eta_s = \frac{\Delta v}{v_R} \quad (1)$$

where  $\Delta v$  is the bandwidth at half-power and  $v_R$  is the resonant frequency and associated with a stress amplitude corresponding to  $R/2$ . The resonant response curve was obtained by oscilloscope measurements of tip acceleration under constant input. Bandwidth damping measurements were only made after  $10^5$  cycles so that the additional cycles required for the damping

measurements would not contribute significantly to failure.

Each fatigue test was also interrupted several times so that damping measurements could be made by the vibration decay technique. The shaker core inertia was found to be adequate to fix the specimen base. The output of the tip accelerometers and preamplifiers was fed to a Honeywell Model 1508 visicorder, using galvanometer M-40-350A, and logarithmic decrements determined by measuring the amplitude of two maxima separated by  $n$  cycles. A system loss factor was computed from

$$\eta_s = \frac{1}{2n} \ln \left( \frac{x_0}{x_n} \right) \quad (2)$$

The damping measurements using this method were all taken at a root stress level of  $\sigma_R = 16450$  psi.

#### ANALYSIS OF BEAM STRESS AND DISPLACEMENT

The composite specimens were modeled as beams and, as such, a few simplifying assumptions have been made:

1) Beam deformations are described by the elementary theory of flexure, so that plane sections normal to beam axis remain plane and normal to the deformed axis.

2) Each ply is assumed to satisfy the linear, elastic constitutive relationship.

3) Plies are assumed to have uniform thickness.

4) End doublers and accelerometer may be considered as a point mass.

The well-known differential equation of the deflection curve of a beam whose vibrations occur in its plane of symmetry is

$$EI \frac{\partial^4 y}{\partial x^4} + sA \frac{\partial^2 y}{\partial t^2} = 0 \quad (3)$$

in which

$y(x)$  = deflection of the neutral axis,

$EI$  = stiffness,

$sA$  = beam mass per unit length.

Beam stresses at the outer fiber may then be obtained from

$$\sigma = Mc/I \quad (4)$$

where

$$M = -EI \frac{\partial^2 y}{\partial x^2} \quad (5)$$

$M$  is the bending moment at any section and  $C$  is

the beam half-thickness. The beam deflection, in any pure mode of frequency  $p$  is given by

$$y(x) = X(x) \cos pt \quad (6)$$

where

$$\frac{d^4 X}{dx^4} = k^4 X \quad (7)$$

$$k^4 = p^2 / e^4 \quad (8)$$

$$a^3 = \frac{EI}{\rho A} \quad (9)$$

the eigenvalues,  $kl$ , must satisfy a transcendental equation

$$\frac{\cos kl \cosh kl + 1}{\sin kl \cosh kl - \cos kl \sinh kl} = kl \left( \frac{m}{\rho A l} \right) \quad (10)$$

which results from requiring satisfaction of the end conditions of a cantilever beam with tip mass  $m$ .

When a tip mass is added to the "free" end of the cantilever beam, the end conditions are:

$$(X)_{x=0} = 0 \quad (11)$$

$$\left( \frac{dX}{dx} \right)_{x=0} = 0 \quad (12)$$

$$\left( \frac{d^3 X}{dx^3} \right)_{x=l} = 0 \quad (13)$$

$$\left( \frac{d^2 X}{dx^2} \right)_{x=l} = \frac{m}{EI} X(l) (-p^2) \quad (14)$$

The rotatory inertia of the tip mass has been neglected. For each  $kl$ , a natural frequency is then obtained from Equations 8 and 9.

An approximate solution, obtained through the use of Rayleigh's quotient was found useful for the original design of the experiment, and for obtaining approximate frequencies which can then be improved by iteration using Equation 10. This approximate frequency (first mode only) is given by

$$p^2 = \frac{210 EI}{16.50 Al^3 + 70 ml} \quad (15)$$

The necessary material constants for the material used in this investigation were determined and are listed in Table 1. Equation 10 was solved for  $kl$  by an iterative process. The fundamental frequency was determined to be  $p = 174.96 \text{ rad/sec}$  or  $v_R = 27.85 \text{ cps}$ . The approximate relationship gave  $v_R = 28.39 \text{ cps}$ .

Since the experimental procedure employed in this investigation used the measurement of tip displacement as a means of controlling beam stress, it was necessary to develop a relation-

ship between tip displacements and stresses at the root end of the hole. Since the ratio of root to tip displacement is determined solely by the mode shape, it is convenient to express the root stress in terms of tip acceleration as

$$\sigma_R = \left( \frac{cE}{p^2} \frac{X''(0)}{X(l)} \right) a_T \quad (16)$$

Substitution of the mode shape yields

$$\sigma_R = \frac{cE}{p^2} k^4 a_T$$

$$\left[ \frac{\sin kl + \sinh kl}{\sin kl (\cosh kl) - (\cos kl) (\sinh kl)} \right] \quad (17)$$

For the beams used in this investigation, a value of  $kl = .84142$  was found for the first mode. The relationship between root stress and tip displacement ( $\delta_T$ ) was found to be

$$\sigma_R = 55,713 \delta_T \text{ psi/inch} \quad (18)$$

The nominal stress at a distance  $b$  from the root of a beam of width  $D$  and half thickness  $C$  is

$$\sigma_n = \frac{6M(b)}{DC^2} \quad (19)$$

where

$M(b)$  = bending moment at  $b$

Inclusion of a hole of radius  $r$  at that point leads to a stress at the hole edge which is greater, in the ratio

$$\frac{\sigma_{max}}{\sigma_n} = \frac{f}{1 - 2r/D} \quad (20)$$

The factor  $f$  is [7]:

$$f = \left[ 1.79 + \frac{.25}{1 + \frac{2r}{C}} + \frac{.81}{1 + \left( \frac{2r}{C} \right)^2} - \frac{.26}{\left( 1 + \left( \frac{2r}{C} \right)^2 \right)} \right] \times \left[ 1 - 1.04 \left( \frac{2r}{D} \right) + 1.22 \left( \frac{2r}{D} \right)^2 \right] \quad (21)$$

The overall effect of the hole (reduced section plus stress concentration) was to increase the stress above the nominal stress at that station by a factor of 2.07.

Using the mode shape to evaluate the moment at  $b$  led to a relationship between stress at the edge of the hole and tip displacement of

$$\sigma_{sx} = 52,384 \delta_T \text{ psi/in}$$

This value is seen to be slightly less than the stress at the root of the beam; however, failure may be expected to initiate at the hole edge because of interlaminar edge stresses and

TABLE I.

Specimen Material Constants	
Young's Modulus, $E^*$	$1.138 \times 10^7$ psi
Area Moment of Inertia, $I$	$5.1177 \times 10^{-5}$ in <sup>4</sup>
Stiffness, $EI$	$5.8233 \times 10^2$ lb-in
Beam thickness, $2C$	0.085 in
Beam width, $D$	1.00 in
Effective beam length from root to tip mass, $l$	5.12 in
Beam Mass, $\rho A l$	$7.734 \times 10^{-3}$ slugs
Tip Mass, $m_T$ , includes accelerometer, fiberglass doublers, beam tip beyond center of accelerometer	$4.446 \times 10^{-3}$ slugs
Mass Ratio, $\frac{m_T}{\rho A l}$	5.749

\* Young's Modulus was computed by the method given in Ref. (6).

TABLE II

Fatigue Test Results			
Specimen	Maximum Stress at Hole, $\sigma_{max}$ , psi	Root Stress, $\sigma_R$ , psi	Cycles to Failure
AB 74	47850	50700	$1.07 \times 10^4$ *
AB 77	51530	54600	$6.83 \times 10^3$
AB 81	63500	67410	$9.63 \times 10^3$
AB 82	70120	74660	$3.96 \times 10^3$
AB 90	74110	78560	$3.01 \times 10^3$
AB 93	64430	68530	$2.39 \times 10^3$
AB 94	58150	61840	$6.93 \times 10^3$
AB 95	75960	80780	$1.42 \times 10^3$
AB 96**	53430	56830	
AB 98**	53960	57380	
AB 99	51860	55160	$2.80 \times 10^3$

\* Failure not observed; test terminated.

\*\* Test terminated due to mechanical failure.

imperfections generated by the process of creating the hole.

## RESULTS AND DISCUSSION

### Bending Fatigue

Results of the bending fatigue tests are presented in Table II. The stress,  $\sigma_{max}$ , is the stress computed to exist at the edge of the hole. The fatigue data in terms of maximum root stress have been plotted in the form of an S-N curve in Figure 4. The line drawn through the experimental points represents the best fit by visual means. Tests on specimens AB 96 and AB 98 were terminated due to mechanical failure of test equipment.

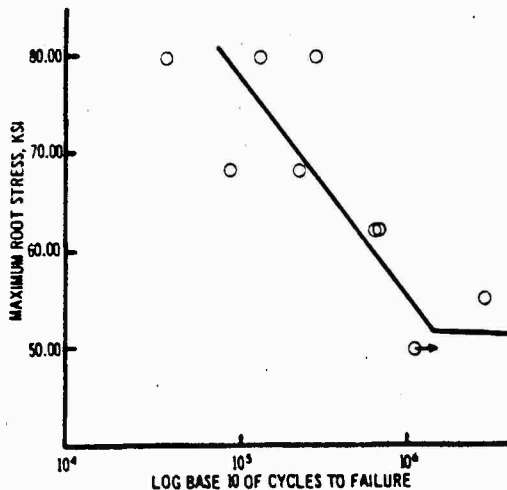


Fig. 4 - Number of Cycles to Failure of Various Levels of Constant Root Stress

Single, continuous longitudinal cracks were observed to initiate at the hole and progress to the root of each specimen. The width of the damage zone was equal to the diameter of the hole. Figures 5 and 6 illustrate damage in three of the beams which was typical of the damage in each of the specimens. Although not presented here, x-rays taken at  $\pm 15$  degrees from the perpendicular showed that the damage was not limited to the outer layer.

### Damping

Material damping data were taken at selected cycle increments and calculated from logarithmic decrement and bandwidth. As the number of cycles on each beam increased, the damping increased as expected due to the



Fig. 5 - X-rays of Typical Failure

permanent microstructural damage occurring in the specimens. The damping results show the same general pattern of increase for each specimen regardless of root stress level and total number of cycles applied. Figure 7 typically illustrates how the damping, as determined from the vibration decay experiment, changed as the number of cycles increased. Each damping value plotted was measured at the same level of root stress,  $\sigma_r = 16450$  psi. Loss factors obtained by vibration decay and bandwidth measurements for all beams are tabulated in Table III. The values in parentheses next to bandwidth in these

change in damping for each specimen over its life is presented. It should be noted that comparisons between individual members of this family of curves should not be made from this plot, as each set of data results from different levels of applied stress, but the increase in damping is clearly seen. No sharp increase immediately prior was observed.

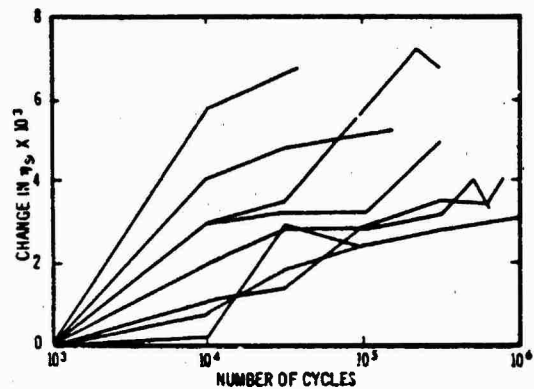


Fig. 8 - Change in Damping During Fatigue, All Stress Levels

Fig. 6 - Ultrasonic C-scans of Typical Failure

tables are the root stresses at which the bandwidth measurements were made ( $R/\sqrt{2}$ ).

The increase in damping during the fatigue life can be readily seen in the tabulated data and in the summary plot, Figure 8, where the

An experiment was performed in order to estimate the amount of air damping present. An aluminum paddle was attached to the free

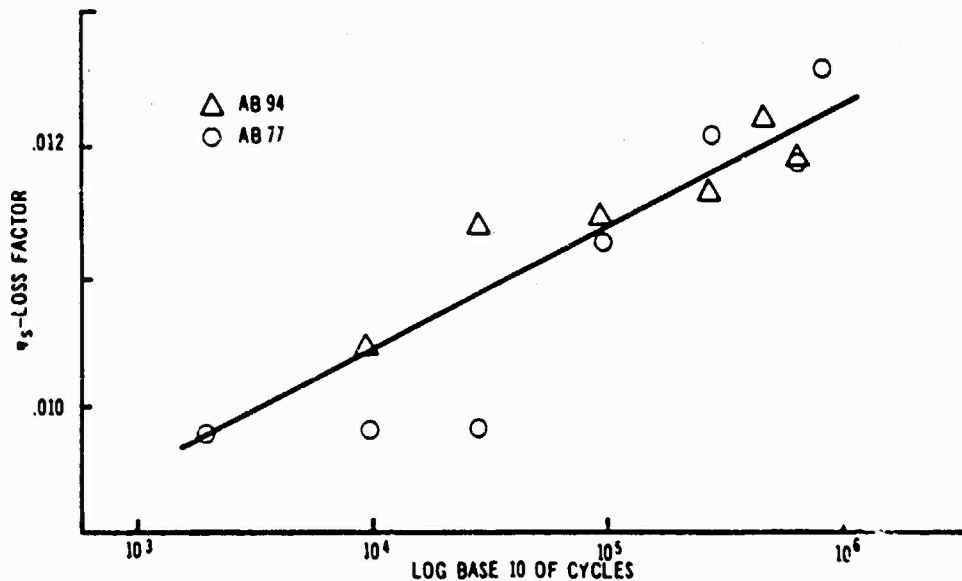


Fig. 7 - System Damping at  $\sigma_a = 16,450$  psi During Fatigue Test at Constant Amplitude,  $\sigma_R = 61,710$  psi

TABLE III

Damping Measurements During Fatigue Test  
Graphite - Epoxy Composites

Identification	Measured System Loss Factor, $\eta_s$		
	Number of Cycles	By Log Decrement at 17 ksi	By Bandwidth at Indicated Stress
Specimen AB 74 $\sigma_R = 50,700$ psi Rel Hum = 55%, T = 74°F	0	.0070	
	$10^5$		.0109 @ 32 ksi
	$10^6$	.0099	.0199 @ 32 ksi
Specimen AB 77 $\sigma_R = 54,600$ psi R.H. = 52%, T = 74°F	0	.0085	
	$10^5$	.0099	
	$3 \times 10^5$	.0099	
	$10^6$	.0113	.01354 @ 42 ksi
	$3 \times 10^6$	.0120	.0143 @ 42 ksi
	$6.83 \times 10^6$	.0119	.0121 @ 42 ksi
Specimen AB 81 $\sigma_R = 67,410$ psi R.H. = 52%, T = 74°F	$8.73 \times 10^6$	.0125	
	0	.0084	
	$10^5$	.0085	
	$3 \times 10^5$	.0113	
	$9.63 \times 10^5$	.0108	.0132 @ 47 ksi
Specimen AB 82 $\sigma_R = 74,660$ psi R.H. = 54%, T = 67°F	0	.0034	
	$10^5$	.0112	
	$3.96 \times 10^5$	.0121	.0094 @ 53 ksi
Specimen AB 90 $\sigma_R = 78,560$ psi R.H. = 50%, T = 63°F	0	.0076	
	$10^5$	.0108	
	$3 \times 10^5$	.0111	
	$2.52 \times 10^5$	.0147	
	$3.01 \times 10^5$	.0142	.0164 @ 53 ksi
Specimen AB 91 $\sigma_R = 68,530$ psi R.H. = 45%, T = 82°F	0	.0070	
	$10^5$	.0102	
	$3 \times 10^5$	.0103	
	$10^6$	.0102	
	$2.93 \times 10^6$	.0120	.0113 @ 47 ksi
Specimen AB 94 $\sigma_R = 61,840$ psi R.H. = 47%, T = 70°F	0	.0086	
	$10^5$	.0105	
	$3 \times 10^5$	.0114	
	$10^6$	.0114	
	$3 \times 10^6$	.0116	.0106 @ 41 ksi
	$5.01 \times 10^6$	.0124	.0146 @ 41 ksi
	$6.93 \times 10^6$	.0119	.0169 @ 41 ksi
Specimen AB 95 $\sigma_R = 80,780$ psi R.H. = 43%, T = 76°F	0	.0089	
	$10^5$	.0130	
	$3 \times 10^5$	.0138	
	$1.42 \times 10^6$	.0142	.0136 @ 55 ksi
Specimen AB 96 $\sigma_R = 56,830$ psi R.H. = 44%, T = 75°F	0	.0088	
	$10^5$	.0118	
	$3 \times 10^5$	.0117	
Specimen AB 98 $\sigma_R = 57,380$ psi R.H. = 41%, T = 74°F	0	.0089	
	$10^5$	.0103	
	$3 \times 10^5$	.0105	
	$10^6$	.0105	

Specimen AB 99	0	.094	
$\sigma_R = 51,860$ psi	$10^4$	.0102	
R.H. = 40%, T = 81°F	$3 \times 10^4$	.0112	
	$10^5$	.0118	.0123 @ 35 ksi
	$3 \times 10^5$	.0116	.0138 @ 35 ksi
	$10^6$	.0119	.0104 @ 35 ksi
	$3 \times 10^6$	.0114	.0104 @ 35 ksi
	$2.8 \times 10^6$	.0116	.0104 @ 35 ksi

end of one of the specimens, centered on the beam and flush with the tip so as to increase the total surface area by a factor of two. Free vibration measurements were taken of the beam by itself and then of the beam with the paddle. The results indicated that air damping was present but was only on the order of five percent of the total damping. Therefore, the damping results obtained were assumed to be primarily material damping.

In general, the bandwidth and logarithmic decrement damping values were considered to be in fair agreement. Bandwidth measurements generally led to higher damping, but bandwidth measurements were taken at higher stress levels than those at which logarithmic decrements were computed.

Damping, as determined by the vibration decay method, was found to increase as stress level of the fatigue test was increased. Figure 9 exhibits typical results of the damping increase with increase in root stress. Similar results occurred for each cycle increment at which damping was measured.

#### Frequency

For each specimen, the resonant frequency dropped to a significantly lower resonant frequency within  $3 \times 10^3$  cycles, and then decreased slowly throughout the remainder of the fatigue life. Typically, the final resonant frequency was no more than three cps less than the initial value as shown in Figure 10 and Table IV. This decrease is due, as is the damping increase, to the permanent damage experienced by the specimens. Since frequency is a measure of stiffness, this reduction indicates a permanent change in the stiffness of the material.

#### CONCLUSIONS

The results of this preliminary study show that measurable changes in damping occur during the fatigue life of composite specimens. Since large amounts of damage were evident in the ultrasonic and x-ray studies of the specimens, it is concluded that this increase in damping was due to cumulative damage occurring during the fatigue life. While the damping changes observed in graphite-epoxy specimens were observable, they were not large. In this study, the major damage was confined to about

10% of the specimen volume. Consequently, observable changes in damping should not be expected if an even smaller portion of the specimen suffers fatigue damage.

Damping changes were found to take place throughout the life of the specimen, rather than as a sudden increase which would signal an imminent failure. On the other hand, the stiffness changes which were also observed were found to take place early in the specimen life.

Some increase in damping with the level of repeated loading was observed, suggesting that a larger specimen volume undergoes damage at higher stress, as is to be expected. This is taken to be further evidence that the damping changes seen were due to cumulative mechanical damage.

#### REFERENCES

1. M. J. Salkind, "Fatigue of Composites," Composite Materials: Testing and Design (Second Conference), ASTM STP497, American Society for Testing and Materials, pp. 143-169, 1972.
2. R. F. Gibson and R. Plunkett, "A Forced Vibration Technique for Measurement of Material Damping," *Experimental Mechanics*, Aug. 1977.
3. G. Maymon, R. P. Briley and L. W. Rehfield, "Influence of Moisture Absorption and Elevated Temperature on the Dynamic Behavior of Resin Matrix Composites: Preliminary Results," *Advanced Composite Materials Environmental Effects*, ASTM STP 658, J. R. Vinson, Ed., American Society for Testing and Materials, pp. 221-233, 1978.
4. A. B. Schultz and S. W. Tsai, "Dynamic Moduli and Damping Ratios in Fiber Reinforced Composites," *Journal of Composite Materials*, Vol. 2, No. 3, pp. 368-379, July 1968.
5. J. Nevadunsky, "Fatigue Damage Behavior in Composite Materials," ADA001944, United Aircraft Corporation, Sept. 1974.
6. R. M. Jones, *Mechanics of Composite Materials*, Scripte Book Co., Washington DC, 1975.
7. R. J. Roark and W. C. Young, *Formulas for Stress and Strain* (Fifth Edition), McGraw Hill Book Company, New York, 1975.

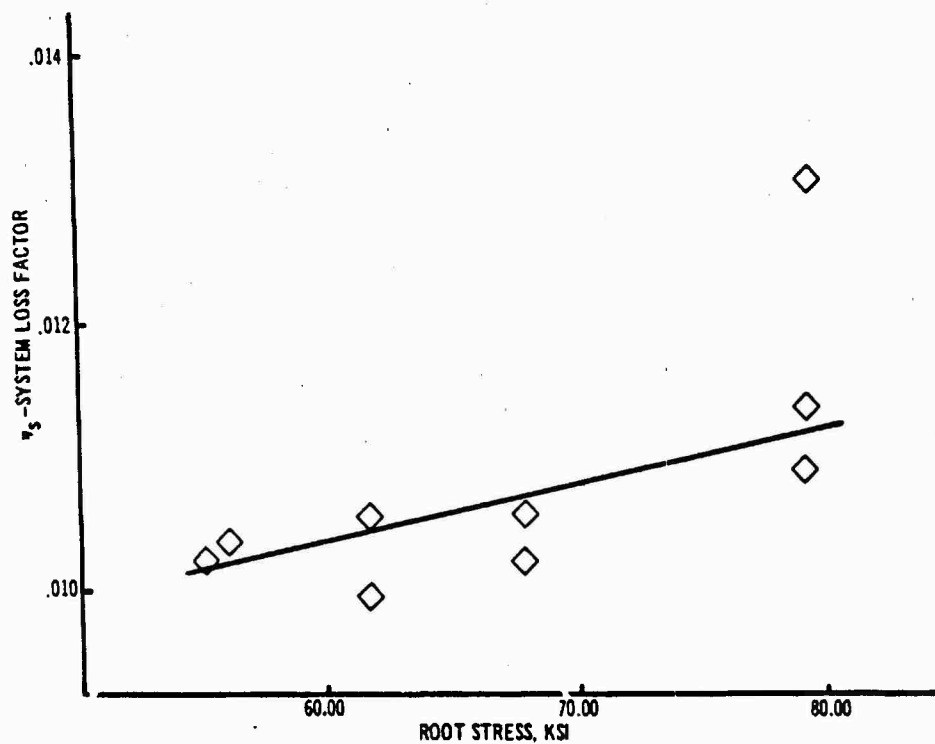


Fig. 9 - System Damping at  $\sigma_a = 16,450$  psi at  $10^6$  Cycles at Various Levels of Constant Root Stress

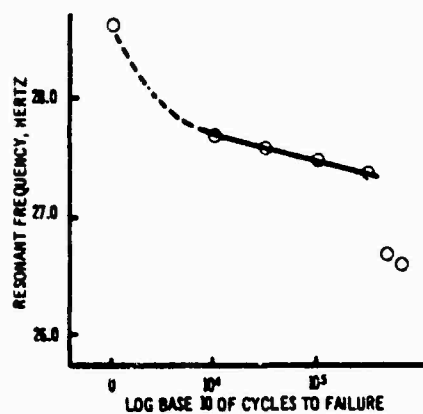


Fig. 10 - Stiffness Change During Fatigue Test at 61,840 psi



TABLE IV  
Stiffness Change of Graphite Epoxy Composite  
During Fatigue Test, as Measured by Changes in  
Natural Frequency

Specimen	Natural Frequency, CPS				
	0 Cycles	10 <sup>4</sup> Cycles	10 <sup>5</sup> Cycles	10 <sup>6</sup> Cycles	At Failure
AB 74	26.1		25.6	25.6	*
AB 77	27.5	26.8	26.6		25.9
AB 81	28.2	27.3			26.6
AB 82	27.9	26.7			25.6
AB 90	26.6	25.9	25.6		24.9
AB 93	27.0	26.2	25.8		24.7
AB 94	28.6	27.7	27.6		26.6
AB 95	27.8	26.8	25.6		25.0
AB 96	28.3	27.4			**
AB 98	26.9	26.1	26.0		**
AB 99	28.5	27.9	27.7	26.8	26.8

\* Test terminated; no failure observed.

\*\* Test terminated due to mechanical failure.

#### DISCUSSION

Mr. Selive (David Taylor Naval Ship Research & Development Center): Did you run tests without a stress concentration and did you observe a similar change in damage?

Miss Bourne: No.

Mr. Selive: Did you detect propagation limited strictly to fibers that had been cut in the hole drilling operation?

Miss Bourne: The results indicated that they started at the hole end and then progressed to the root. The fibers at the hole were the only ones that were damaged. We also had a problem in mounting the accelerometers because we couldn't mount them on blocks or drill holes in the test specimen. We finally decided to glue the accelerometers on and it worked well.

Mr. Jones (Air Force Materials Laboratory): What did you mean by air damping of five percent? Is it five percent of the nominal figures you measured or is it five percent damping?

Miss Bourne: No, it is five percent of the figures we mentioned here.

## SONIC FATIGUE TESTING OF THE NASA L-1011 COMPOSITE AILERON\*

J. Soovere  
Lockheed-California Company  
Burbank, California

The sonic fatigue test program to verify the design of the composite inboard aileron for the L-1011 airplane jet noise environment is described. The composite aileron is fabricated from composite minisandwich covers which are attached to graphite/epoxy front spar and ribs, and to an aluminum rear spar with fasteners. Coupon testing, with large electromagnetic shakers, is used to develop random S/N (stress vs. number of cycles) data for specific components in the design. Coupon failure modes are presented and discussed. The center section of the composite aileron is mounted by its hinge fittings to a test frame and sonic fatigue tested in an acoustic progressive wave tunnel. The testing involves modal studies to establish mode shapes, modal frequencies and damping, and a panel response nonlinearity test culminating in the accelerated sonic fatigue proof test.

### INTRODUCTION

The need for more weight- and cost-efficient airplane structures has stimulated the development and use of advanced composite materials. Before these materials can be applied to commercial transport airplanes, the potential weight and cost-saving must first be demonstrated through the design, fabrication and testing of actual flight hardware. The inboard aileron for the Lockheed L-1011 transport airplane has been selected as the candidate advanced composite secondary airplane structure for such a program [1].

The composite aileron, due to its close proximity to the large fan jet engine exhaust (Fig. 1), will be subjected to a high-level jet noise environment. High-cycle, random fatigue failures commonly referred to as sonic fatigue can occur in secondary airplane structures when subjected to high-level jet noise [2]. Consequently, the large-fan, jet-noise environment represents one of the design conditions for the composite aileron. This paper describes the on-going sonic fatigue test program for the NASA L-1011 composite aileron. The purpose of this program is to verify that the sonic fatigue capability of the composite aileron is consistent with the design life requirements for the L-1011 airplane.

### DESIGN REQUIREMENTS

The L-1011 aileron is required to be free from sonic fatigue failure for a design life of 50,000 flight hours representing 36,000 takeoffs and landings. The highest noise levels are encountered on the lower surface of the inboard aileron

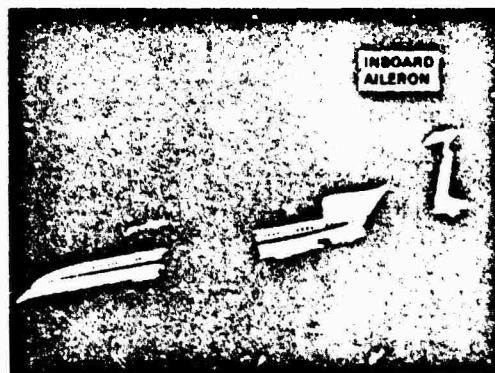


Fig. 1 - L-1011 transport airplane showing inboard aileron location relative to the wing engine

during takeoff which, therefore, represent the design noise environment for the aileron. The aileron design noise spectrum given in Fig. 2, is derived from the computer analysis of scale model jet noise test data supplemented by limited full-scale engine noise data.

The takeoff noise level is maximum at maximum engine takeoff power when the airplane is stationary, but falls off rapidly with speed as the airplane accelerates to takeoff. For design purposes, the takeoff time is compressed to an equivalent damage time [3] at the maximum takeoff noise level. The required design life for the inboard aileron is equivalent

\*This work was performed by the Lockheed-California Company as part of a joint program with the AVCO Aerostructures Division supported by NASA, Langley Research Center under Contract NAS1-15069.

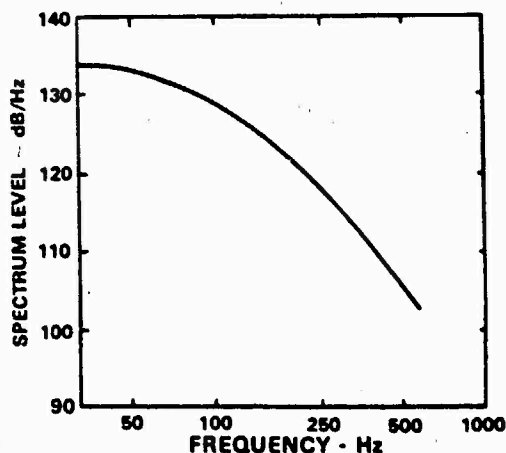


Fig. 2 - Inboard aileron design noise spectrum

to 360 hours at the maximum takeoff noise level which represents approximately  $10^8$  average stress reversals or cycles for the aileron structure.

#### COMPOSITE AILERON STRUCTURE

The production of cost-efficient composite structures requires that the components which are expensive to manufacture and assemble, such as the composite ribs, be kept to a minimum, requiring the use of large rib spacing in conjunction with very stiff covers. The required stiffness is obtained by the use of a minisandwich construction for the covers, consisting of two 3-ply 0.0546 cm (0.0215 in.) thick T300/S208 graphite/epoxy tape face sheets, separated by a 0.0953 cm (0.0375 in.) thick ADX 819 syntactic (syn) epoxy core containing glass micro-balloons. The full depth ribs are fabricated from the T300/S208 graphite/epoxy fabric, while the front spar is fabricated from T300/S208 graphite/epoxy tape. Both covers have doublers at the rib and spar locations and are attached to the ribs and spars with removable fasteners. The composite aileron is shown in Fig. 3 with the lower cover removed. The original aluminum hinge fittings, fairings and fairing support structures ahead of the front spar, the aluminum rear spar and the full depth honeycomb/glass fiber trailing edge wedge are all retained. The fiber orientation, the thickness of the covers, ribs and spars and the rib spacing were designed by loading conditions other than sonic fatigue.

#### COUPON TESTING

Limited coupon testing has been initiated to develop sonic fatigue allowables, in the form of random S/N data, for the covers and the ribs, and to identify the failure modes.

##### Coupon Configurations

The allowables for the covers were obtained with the single-cantilever SC series coupons and the double-cantilever

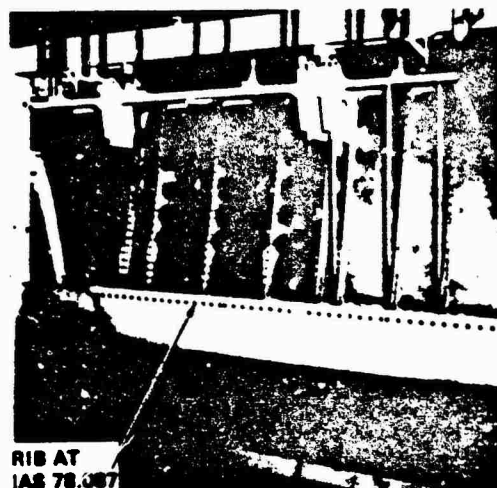






Fig. 3 - NASA L-1011 composite inboard aileron with lower covers removed

SR and SS series coupons and for the ribs with the single-cantilever RR series coupons as summarized in Table 1. The double-cantilever SR series coupons (Fig. 4) and the similar SS series coupons represent the rib/cover and the spar/cover junctions, respectively. The single-cantilever rectangular SC series coupons, representing the covers at the panel centers, were mounted between two steel blocks [4], each with a root radius to minimize stress concentration effects. The single-cantilever RR series coupons (Fig. 5) were used to develop allowables for the graphite/epoxy fabric ribs at the bend radius/fastener locations. All the coupons carried tip weights which increased the coupon root strain and provided a means of reducing coupon size while maintaining the required inertia load per fastener. The tip weights were also used to activate the inductive tip transducers (Figs. 4 and 5) which monitored the coupon response after strain gage failure.

##### Tip Transducer Calibration

The initial calibration of the tip transducer was conducted with the first SC series coupon using a specially mounted lightweight tip accelerometer which eliminated accelerometer cable failures and permitted calibration on the basis of tip displacement in addition to coupon root strain. Linear calibration was obtained between the tip transducer root mean square (rms) output, the rms root strain and the rms tip acceleration (Fig. 6), with correlation coefficients above 0.99 predicted by the regression analysis of the data. Band-limited (50 Hz.) constant spectrum base acceleration, centered at the coupon resonant frequency, was used to excite the coupon at various rms acceleration levels. The tip transducer, strain gage, and accelerometer outputs were measured by a true rms meter with a 30-second averaging time.

TABLE 1  
Summary of Coupon Configurations

Coupon Series	Coupon Type	Structure Simulated	Fiber Orientation	Coupon Configuration
SC	Single Cantilever	Covers at Panel Center	(45°, 0°, 135°, Syn) <sub>s</sub> * Graphite/Epoxy Tape	
SR	Double Cantilever	Covers at Rib/Cover Junction	(45°, 0°, 135°, Syn) <sub>s</sub> * Graphite/Epoxy Tape	
SS	Double Cantilever	Covers at Spar/Cover Junction	(45°, 90°, 135°, Syn) <sub>s</sub> * Graphite/Epoxy Tape	
RR	Single Cantilever	Ribs at Rib/Cover Junction	(45°, 0°, 135°, 0°, 45°) Graphite/Epoxy Cloth	

\*Symmetrically Laminated

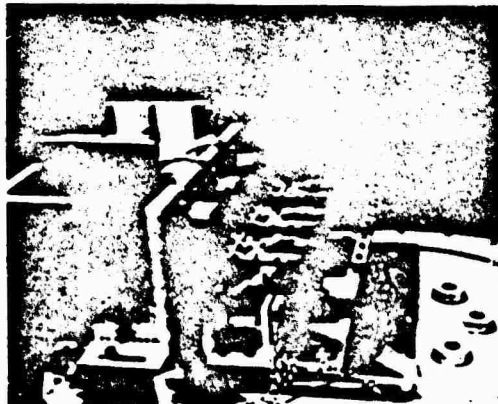


Fig. 4 - SR series coupons mounted on a large electromagnetic shaker



Fig. 5 - RR series coupon mounted on a large electromagnetic shaker

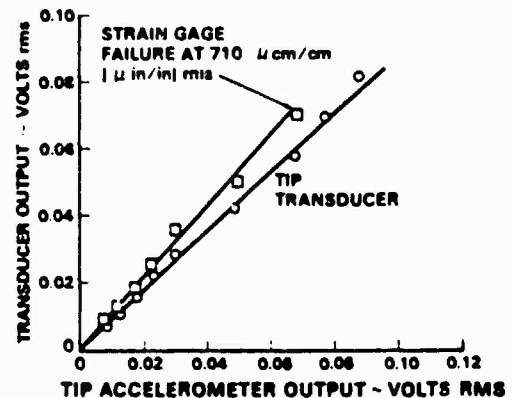


Fig. 6 - Tip transducer calibration curves for coupon SC1

#### Test Procedure

The general test procedure involved initial low-level sine sweeps to locate the resonant frequencies followed by tip transducer calibration tests, as previously described, up to the required rms strain level or until strain gage failure, whichever came first. In the case of premature strain gage failure, the required test strain level was established with the tip transducer using the extrapolated calibration curve. Thereafter, the base rms acceleration was noted and used to set the test level for the subsequent fatigue runs. The base acceleration and strain relationship is nonlinear and cannot be used as the basis for accurate projection of test strain level in the event of premature strain gage failure. Low-level sine sweeps were periodically conducted during both the calibration and the subsequent fatigue tests to detect any shift in the coupon resonant frequency. Failure is defined as a 5-percent drop in the resonant frequency. To minimize the possibility of sudden coupon failure, continuous monitoring of the coupon

response was maintained throughout the test with a real time spectrum analyzer.

#### Coupon Response

A strain survey was conducted during the calibration tests with the first coupon in each series, except coupon SC1, to establish the strain distribution at the critical location on the coupons (Fig. 7), and provide the basis for selecting strain gage locations for the subsequent coupons. The strain distribution in coupon SS1 is typical for a fastener-attached skin/stiffener joint, with the peak strain occurring in the skin just beyond the fastener center line on the rib bend radius side [5]. The peak strain in the rib coupon RR1 occurred in the middle of the inner bend radius. In the subsequent coupon tests, only two strain gages per coupon were used, together with the tip transducers to measure the coupon response.

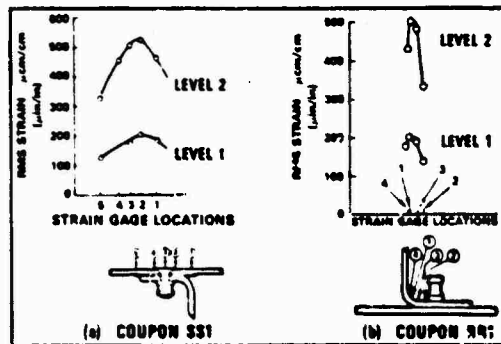


Fig. 7 - Measured strain distributions

The base acceleration spectrum and the corresponding coupon frequency response spectra, as measured during the fatigue test by the tip probe and the strain gage at the peak strain location, are illustrated in Fig. 8. The changes in the coupon frequency response curve as measured periodically during the fatigue test by the low level sine sweep are illustrated in Fig. 9. The change is characterized by a drop in both the resonant frequency and the frequency response amplitude accompanied by an increase in the damping as illustrated nondimensionally, in Fig. 10. In contrast, the rms strain level remained relatively unchanged. The increase in damping is probably due to friction at the crack face. The data in Fig. 10 indicate that a change in the panel damping may be a more sensitive barometer for detecting panel damage than a change in frequency. The variation in the coupon resonant frequency with average number of cycles during the fatigue test is illustrated in Fig. 11. Some frequency shift occurred during calibration prior to reaching the test level. Cycle counting was initiated after the initial frequency shift. Subsequently, a straight line was drawn through the data to intercept the initial frequency line, to define the 'equivalent damage' cycle count origin (Fig. 11).

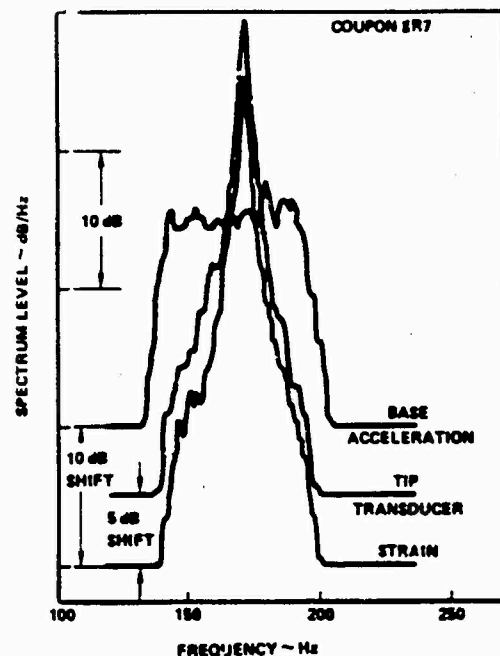


Fig. 8 - Typical superimposed base acceleration, strain, and tip transducer output spectra

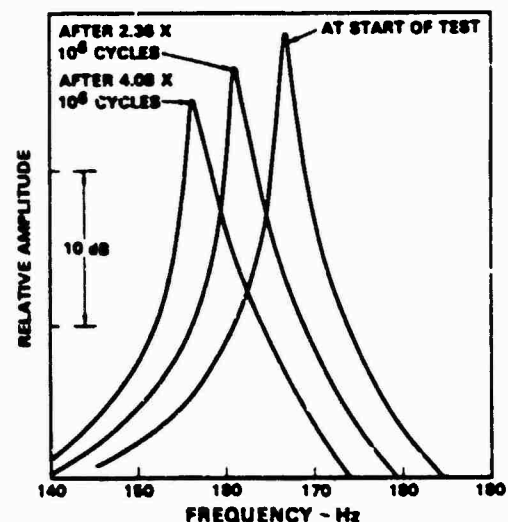


Fig. 9 - Variation of coupon SR7 response to low-level excitation during fatigue test

#### Failure Modes

The basic failure mode observed in the SC series of coupons consisted of delaminations principally between the face sheets and the core, at the root of the cantilever, as detected

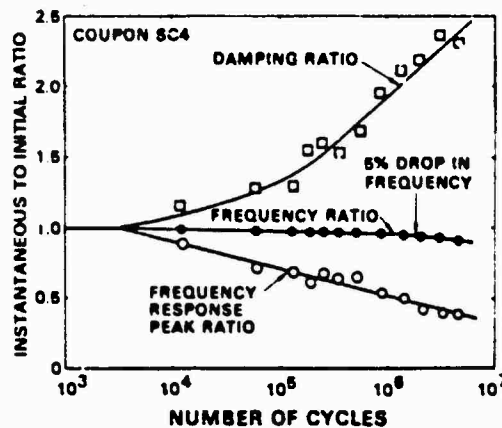


Fig. 10 - Variation of frequency, damping, and frequency response peak ratios with number of cycles

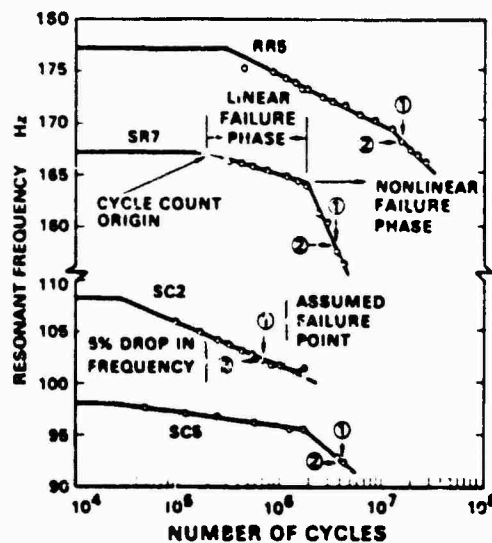


Fig. 11 - Change in coupon resonant frequency with number of cycles during fatigue test

by the C-scan ultrasonic nondestructive test (Fig. 12). Some syntactic resin cracking was also observed under the microscope in the same area. Two separate failure phases are indicated by the nature of the frequency variation with number of cycles in Fig. 11. The linear failure phase appears to be associated with the inward propagation of the delaminations/syntactic resin cracks along the maximum bending moment line, after initiation at the coupon edges. This phase is characterized by the nearly linear, single-degree-of-freedom response to low-level harmonic excitation but with progressively lower response peaks and increasing damping (Fig. 9). A nonlinear failure phase appears to be associated with the propagation of the delamination/resin cracks after the edge cracks have joined. This phase, represented by the frequency number of cycles curve after the discontinuity in the slope (Fig. 11), is

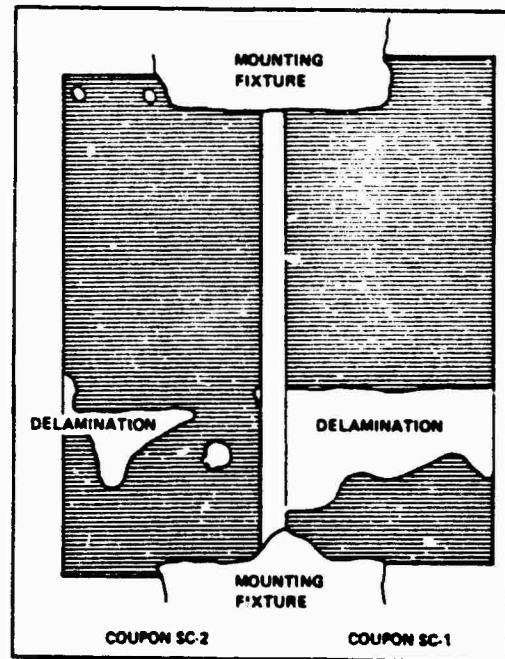


Fig. 12 - Failure areas detected by C-scan

characterized by a pronounced softening spring-type, single-degree-of-freedom response to low-level harmonic excitation (Fig. 9).

The failure modes in the double-cantilever SS and SR series coupons included interlaminar failures between the lower face sheet and the doubler, especially on the rib bend radius side (Fig. 13) and between the face sheet and the syntactic core, as well as transply (Fig. 14) and interply cracking in the face sheets. The transply cracks were visible in the surface of the upper face sheet, running parallel to the surface fibers, emanating from the countersunk fastener holes and the immediate vicinity. These coupons also exhibited the previously described two failure phases in the variation of the natural frequency with average number of cycles (Fig. 11).

The RR series coupons also exhibited similar changes in frequency with number of cycles (Fig. 11), but subsequent inspection of the fatigue tested coupons did not reveal any failures in the vicinity of the bend radius or the fasteners. The mechanism responsible for the 5-percent drop in resonant frequency in this coupon series is currently unknown.

#### Sonic Fatigue Allowables

The results of the coupon tests completed to date are summarized in the form of random S/N data in Fig. 15. These data indicate that the composite minisandwich covers approach a constant fatigue limit beyond approximately  $10^7$  cycles, similar to the coupon test data in Ref. (6). The data also indicates the magnitude of the effect of the countersunk fasteners on the fatigue allowables.



Fig. 13 - Delamination and cracks in coupon SS1



Fig. 14 - Cracks in the graphite/epoxy and the syntactic core of coupon SR9

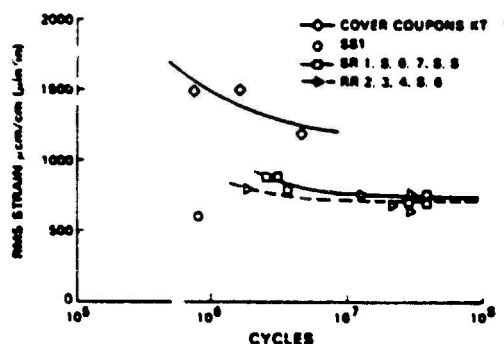


Fig. 15 - Summary of random fatigue data for composite aileron

During the coupon testing, design changes were initiated for the doublers to eliminate some fabrication problems and to provide more depth for the countersunk fasteners. Consequently, the testing of the remaining SS series coupons, which are most sensitive to the doubler design, was cancelled.

#### Additional Coupon Testing

As the doubler design change may affect the fatigue characteristics, additional coupon fatigue testing has been planned for this year involving both SR and SS series of coupons with the modified doubler. The tests will be conducted both at room and elevated temperatures (82°C (180°F)). Some of the coupons have been fabricated with built-in delamination type flaws at the critical fastener line. Other coupons will be impact damaged at the fastener line with a steel ball prior to testing.

#### AILERON SONIC FATIGUE TEST

The purpose of this test is to demonstrate that the sonic fatigue capability of the composite aileron is consistent with the design life of the aileron. The test program involves the following items:

- Installation of aileron assembly in the test frame
- Modal studies on the aileron assembly
- Spectrum shaping and calibration of the acoustic progressive wave tunnel (PWT)
- Strain survey and nonlinear response tests of the aileron assembly in the PWT
- Accelerated 10 hour sonic fatigue proof test in the PWT

#### Aileron Assembly and Mounting

The aileron assembly was required to fit into the 2-m (6-ft) square test aperture in the PWT. Since the aileron assembly is best attached (cantilevered) to the test frame through its hinge and actuator fittings, simulating the mounting on the airplane, only the aileron assembly between and including the hinge fitting ribs (Fig. 3) could be used. Fittings attached to the actuator lug positions were designed to permit aileron rotation for inspection. The remaining area within the test frame was closed out by thick plywood (Fig. 16). The plywood and the aileron lower surface were designed to be flush with the PWT inner wall containing the 2-m (6-ft) square test aperture when mounted in the PWT.

#### Modal Studies

The test frame in the modal studies was mounted horizontally on two steel A-frames such that the lower surface of the aileron assembly was uppermost and horizontal (Fig. 17). Excitation was applied to the aileron surface by means of a loudspeaker at normal (Fig. 17) and grazing incidences and also, by means of a nylon tipped impedance head hammer. Chladni nodal patterns were generated for a quick modal visualization (Figs. 16 and 17) with discrete frequency acoustic excitation. The resonant frequencies and modal damping were measured with a noncontacting displacement probe

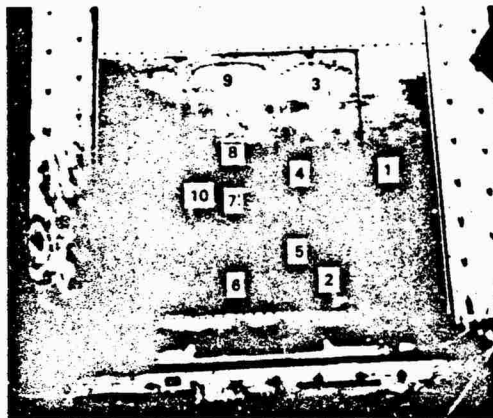


Fig. 16 - Aileron assembly in test frame showing surface strain gage locations



Fig. 17 - Typical experimental setup for modal studies with normal incidence acoustic excitation

(Fig. 17) while the mode shapes were measured with a roving ultra-lightweight accelerometer in conjunction with the displacement probe. The modal damping was measured from the frequency response curves obtained with discrete frequency excitation and hammer impact using the half-power-point (3 dB) method.

The mode shapes, the resonant frequencies and the viscous damping coefficients ( $\delta$ ) given as a fraction of the critical damping, are summarized in Figs. 18b through 18d. The force and panel center displacement spectra from the hammer impact are illustrated in Figs. 19a through 19c. The impact was applied and the response measured at location No. 1 shown in Fig. 18a. Generally, eight hammer impacts were sufficient for averaging purposes to eliminate spurious noise. Comparison of Figs. 19b and 19c indicates that smoothing was necessary to identify actual modes. Unsmoothed spectra were thereafter used to obtain the damping with the half-power-point method. For this damping to be free of bias error, the analysis bandwidth must not exceed a quarter of the response 3 dB bandwidth for the unsmoothed spectra [7 and 8]. Smoothing increases the bias error. The above requirements account for the very small analysis bandwidth used in the spectral analysis of the panel response in this program.

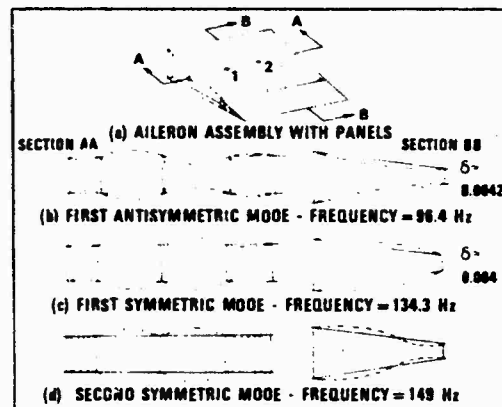


Fig. 18 - Schematic representation of measured mode shapes

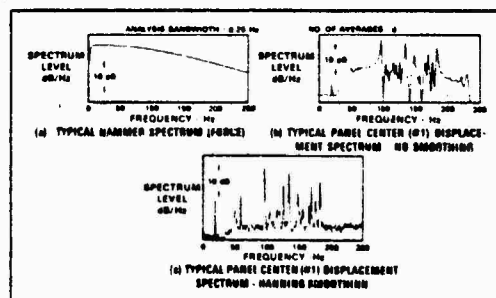


Fig. 19 - Typical panel response to hammer impact

The displacement spectra at location No. 1 (Fig. 18a), resulting from the broadband random acoustic excitation at grazing incidence, which is representative of the in-service aileron loading, is illustrated in Fig. 20. A comparison of Figs. 19b and 20 indicates that the impedance-head hammer tends to excite the antisymmetric modes more than the symmetric modes and consequently may not always indicate the dominant mode of response. Thus, the use of acoustic excitation in modal studies is still very useful.

Generally, the measured panel resonant frequencies agreed very well with the predicted frequencies. Calculations predicted that the dominant strain response should occur in the first symmetric mode at 134.6 Hz, with some contributions from the second symmetric mode at 152.3 Hz. The test results (Fig. 20), however, indicate that the second symmetric mode at 149 Hz dominates the first symmetric mode at 134.3 Hz. The theory assumed a nodal line exactly halfway along the panel length whereas the measured nodal line was displaced more towards the rear spar thereby increasing the coupling with the excitation. The location of the nodal line was sensitive to the location of the acoustic excitation due, possibly, to the variable stiffness characteristics with length, of the tapering ribs. The general broadness of the response peak at 149 Hz may be due to the presence of more than one mode. The grazing incidence random noise tests also confirmed the results of the calculations, namely, that the antisymmetric modes would not be strongly excited (Fig. 20).



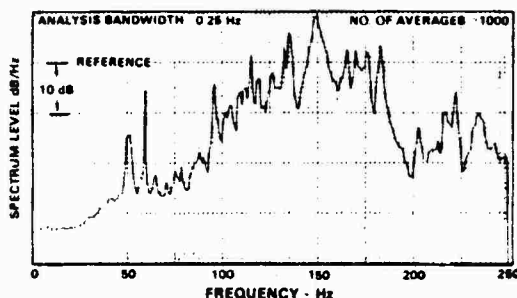


Fig. 20 - Typical panel center (No. 1) displacement spectrum due to random broadband grazing incidence acoustic excitation

The measured viscous damping coefficient ( $\delta$ ) of 0.004 in the fundamental mode is much lower than anticipated and previously observed in stiffened composite panels [6 and 9] and box type airplane structures [10 and 11].

#### Spectrum Shaping in the PWT

The 2-m (6-ft) square test aperture in the PWT was blocked off with a flush-mounted concrete plug for the calibration and spectrum shaping tests. Three flush-mounted microphones covering the area to be occupied by the composite aileron were calibrated with two upstream reference microphones. The upstream reference microphones were expected to be least influenced by the acoustic field radiated by the aileron panels. Power was supplied by a NORAIR Mk VII noise generator. Spectrum shaping was accomplished by means of a bank of adjustable level one-third octave filters.

The degree of spectrum shaping obtained at the center of the aileron test area, as measured by a real time one-third octave spectrum analyzer, is illustrated in Fig. 21 for a range of overall sound pressure levels (OASPL). The corresponding L-1011 aileron design noise spectrum and the accelerated test spectrum are included for comparison. The spectrum shape was generally maintained throughout the length of the PWT.

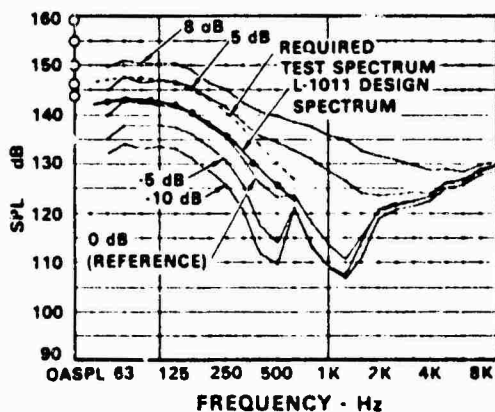


Fig. 21 - 1/3-Octave band analysis of shaped acoustic PWT noise at center of aileron test area

#### Strain Survey and Nonlinearity Test

The test frame with the aileron assembly was mounted in the 2-m (6-ft) square test aperture in the PWT (Fig. 22) in place of the concrete plug. A non-contacting displacement probe was positioned opposite the center of a panel in the aileron upper cover, outside the PWT (Fig. 22), for correlation with strain gages in case of premature strain gage failure. The modal studies indicated that both covers participated nearly equally in the modal responses, and therefore, changes to the structural response may be detected by monitoring the response of either cover. Twenty-four strain gages were installed on the composite aileron. Twelve strain gages were mounted externally, 10 on the lower aileron cover (Fig. 16) and 2 on the front spar. The remaining 12 strain gages were mounted internally with one placed on the rear spar and 11 distributed between the two ribs at and to the right of IAS 78.087 (Fig. 3), placed primarily in the bend radius and adjacent to the lightening holes. The strain gages were calibrated by the shunt resistance method. Three microphones, the two reference microphones and the one composite the center of the aileron, were used to measure the noise environment in the PWT. A lightweight accelerometer was also placed on the displacement probe to monitor vibration levels transmitted through the probe supports.



Fig. 22 - Aileron assembly mounted in the acoustic progressive wave tunnel

The preliminary aileron strain survey was conducted with the broadband air no  $\approx$  some 30 dB below the test spectrum level. This test verified the results obtained in the modal studies with the grazing incidence loudspeaker excitation with regard to the modal damping, frequencies and the modes being excited. The highest strain level was recorded at strain gage No. 5, closely followed by strain gage No. 4 (Fig. 16), both on IAS 78.087. The narrow-band power spectrum of the strain from strain gage No. 5, illustrated in Fig. 23 was obtained with the zoom algorithm in Hewlett-Packard 551C Fourier analyzer. This analyzer also has the modal analysis capability.

The low-level strain survey was followed by the displacement probe calibration test involving incremental increases in

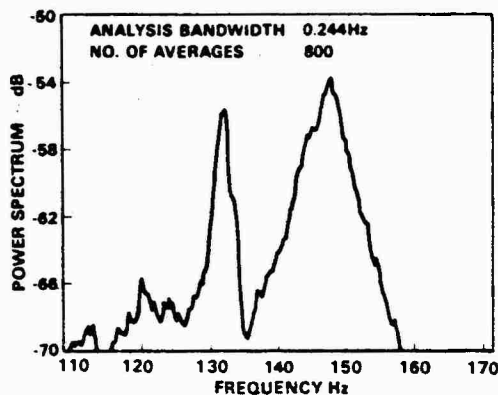


Fig. 23 - Narrow-band analysis of strain gage No. 5 output - low-level air noise excitation

the spectrum level up to the test spectrum level. All the test data were recorded on 14-channel magnetic tape. In addition, three strain gages, No. 5, 6 and 8 (Fig. 16), selected from the results of the low level response tests, together with the reference microphones, the displacement probe and the accelerometer, were monitored throughout the test by means of a scope and a real-time, one-third octave analyzer. The rms levels were measured by a calibrated true rms meter with 30 seconds averaging time. A linear relationship was obtained between the rms strain from the three strain gages and the rms tip probe output, verifying this method of monitoring the panel response. The variations of the rms strains and the rms displacement probe output with the noise level in the 125 Hz, one-third octave band, are illustrated in Fig. 24. The narrow-band power spectrum of the strain, measured at the proof test noise level with strain gage No. 5, is illustrated in Fig. 25.

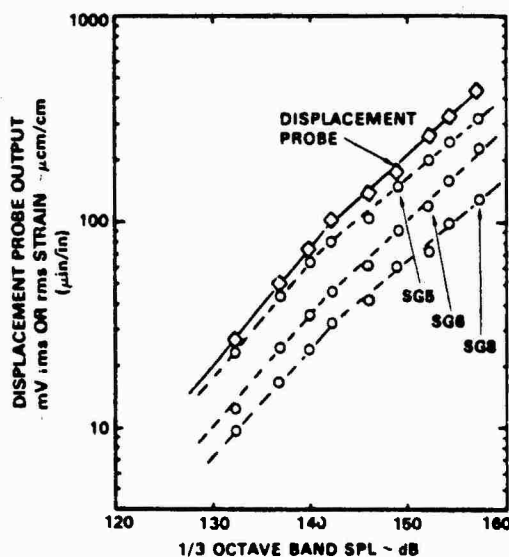


Fig. 24 - Displacement probe output and strain as a function of 1/3-octave band SPL centered at 125 Hz

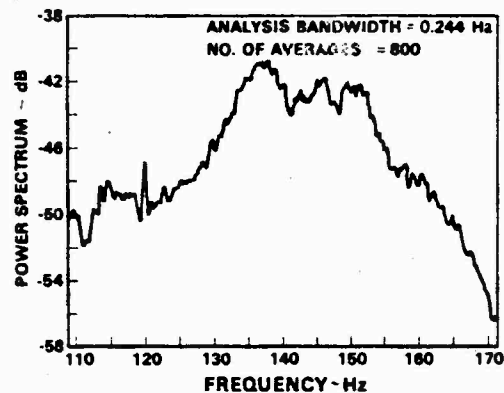


Fig. 25 - Narrow-band analysis of strain gage No. 5 output - during proof test

The knee in the strain and displacement probe output curves with noise level (Fig. 24) indicates the presence of large-amplitude nonlinear response. The nonlinear response is characterized by an upward shift in frequency and a broadening in the response peaks, as can be observed by comparing the narrow-band analysis of strain response both at the proof test noise level (Fig. 25) and at the low noise level (Fig. 23). Calibration of the displacement probe with a small accelerometer placed on the panel indicates an rms displacement of 0.122 cm (0.048 in.) at the test noise level, which is close to the panel thickness of 0.21 cm (0.0825 in.). The random nature of the noise results in many peaks which exceed the rms level by factors of 2 or more. This nonlinear response produces membrane strains which limit the vibration strain amplitude.

#### Accelerated Proof Test

The spectrum level for the proof test was increased by 4.5 dB above the L-1011 design spectrum to reflect the reduction in test time from 360 hours to 10 hours and the effects of moisture on the fatigue life.

The effect of moisture reduced most static allowables by a factor equivalent to 2 dB. As the fatigue limit in composites is generally a constant percentage of the ultimate strength for a given configuration, this 2-dB factor was also assumed for the random fatigue allowable for the composite aileron. This factor will be verified in future coupon testing previously described. The remaining 2.5 dB are comprised of a 1-dB factor to cover scatter in the random S/N data and a 1.5-dB factor derived from the S/N data (Fig. 15) to account for the increment in strain between a 10 hour and a 360 hour test time, modified by the strain relationship with noise level in Fig. 24.

The proof testing was initiated as soon as the proof test noise level was reached. During the proof test, the panel was visually inspected at intervals of 1.1, 1.4, 2.5, and 5 hours. The lower surface of the aileron assembly is shown in Fig. 26, rotated out for inspection after completion of the proof test.

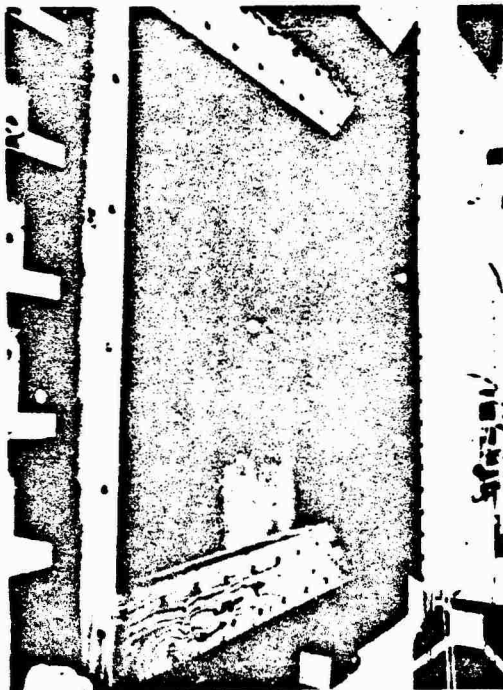


Fig. 26 - The aileron assembly rotated out for inspection after completion of proof test

During these inspection intervals the aileron was also excited by low-level air noise and the response analyzed with the narrow-band spectral analyzer to detect frequency shift. No substantial frequency shift was obtained.

The maximum rms strain level of  $310 \mu \text{m/cm}$  ( $\mu \text{in./in.}$ ) was measured by strain gage No. 5 at the fastener line IAS 78.087. This strain level represents a margin of 7.5 dB for the aileron design based on the random fatigue allowables in Fig. 15.

#### CONCLUSIONS

The composite aileron has been shown by proof testing to have a margin of 7.5 dB relative to the random sonic fatigue allowables obtained from the coupon tests. This relatively large margin, in spite of the lower-than-expected damping, was largely due to the presence of large amplitude nonlinear panel response, producing membrane strains which limit the panel response amplitude. Weight efficient composite structures which are designed by sonic fatigue requirements must, therefore, be designed to operate in the nonlinear panel response region. This requirement is made possible by the higher random strain fatigue allowables obtained with graphite epoxy composites in comparison with aluminum alloy structures where nonlinear panel response is associated with a short sonic fatigue life.

Graphite/epoxy composite control surfaces with full depth ribs which are connected to the covers with fasteners exhibit much lower damping, with viscous damping coefficients around 0.004, than previously observed on similar metal structures. The assumption of a single mode response in the sonic fatigue analysis of large aspect ratio composite panels or indeed metal panels is not generally valid. Higher order axial modes must be included to obtain the location of maximum rms strain from acoustic excitation parallel to the longest panel side. The energy sharing between the ribs and both covers observed in similar metal control surface structures [12] is also observed in composite control surface structures.

#### ACKNOWLEDGEMENTS

The author gratefully acknowledges the encouragement given by C.F. Griffin, the Engineering Manager for the L-1011 Composite Aileron Program at Lockheed-California Company, and the test and data analysis support provided by J.L. Hayward, M. Rapko and C.J. Looper.

#### REFERENCES

1. Griffin, C.F., "Design Development of An Advanced Composite Aileron," paper 79-1807 presented at the AIAA Aircraft Systems Technology Meeting, New York City, 20-22 August 1979.
2. Rieben, T.R., "Sonic Fatigue Testing and Development of Aircraft Panels," WADC-TR-57-512, November 1957, pp. 283.
3. Rudder, F.F. and Plumblee, H.E., "Sonic Fatigue Design Guide for Military Aircraft," AFFDL-TR-74-112, 1975.
4. Bartel, H.W. and Schneider, C.W., "High Cycle Random Fatigue Testing," AFFDL-TR-76-50, May 1976.
5. Bayerdorfer, G., "Acoustic Fatigue Tests for the Production of Design Charts," paper presented at the Conference on Current Developments in Sonic Fatigue, Institute of Sound and Vibration Research, Southampton, England, 6-9 July 1970.
6. Jacobson, M.J., "Advanced Composite Joints: Design and Acoustic Fatigue Characteristics," AFFDL-TR-71-120, April 1972.
7. White, R.G., "Measurement of Structural Frequency Response by Transient Excitation," JRAcS Vol. 73, December 1969.
8. Soovere, J., "Turbulence Excited Frequency Domain Damping Measurement and Truncation Effects," paper presented at the NASA Symposium on Flutter Testing Techniques, Flight Research Center, Edwards, CA, October 9-10, 1975.

9. Soovere, J., "Dynamic Properties of Graphite Fiber Honeycomb Panels," paper 73-326 presented at the AIAA Dynamics Specialist Conference, Williamsburg, VA, March 19-20, 1975.
10. Rudder, F.F., "Acoustic Fatigue Resistance of Internal Airframe Structure," AFFDL-TR-71-107, July 1971.
11. Clarkson, B.L., "Estimates of the Response of Box Type Structures to Acoustic Loading," AGARD-CP-113, May 1973.
12. Clarkson, B.L., "Stresses in Skin Panels Subjected to Random Acoustic Loading," AFML-TR-67-199, June 1967.

#### DISCUSSION

Mr. Volin (Shock and Vibration Information Center): You showed the measurement of the shift in damping as a method of detecting the failure. How did you measure the damping and did you measure the damping while the coupon tests were going on?

Mr. Soovere: No. We used low level sinusoidal excitation and we basically used the 3 db point damping method and that proved generally as accurate. The reason we did that is if we are going to test for a shift in damping in the field we would probably use a hammer type of excitation or a low level type of excitation so this system has to work for low level excitation.

MODELING A TEMPERATURE SENSITIVE  
CONFINED CUSHIONING SYSTEM

Virginia P. Kobler  
U. S. Army Missile Command  
Huntsville, Alabama 35809

Richard M. Wyskida  
Industrial and Systems Engineering Department  
The University of Alabama in Huntsville  
Huntsville, Alabama 35807

and

James O. Johannes  
Computer Science Department  
The University of Alabama in Huntsville  
Huntsville, Alabama 35807

This paper reports on the modeling of the impact response for the Minicel cushioning material in the confined state. This objective was satisfied through the development of an experimental drop test design, conducting an extensive drop test program, and then modeling the resultant test data. A general mathematical model for a confined cushioning system and a general mathematical model for the exterior container which surrounds the confined corner void configured cushions are presented.

INTRODUCTION

Extensive experimentation has been conducted by various researchers on cushioning materials in the "unconfined" state, that is, the cushioning material is not confined by the sides of a rigid structure. However, investigating the dynamic properties of "unconfined" cushioning materials, and applying the results to "confined" applications, disregards the effects of confinement upon the dynamic behavior of the cushion. Confinement is defined as a cushioning system which is located within an external structure or container with lateral movement possible.

It appears that Mazzei [1], Blake [2], and Gammell and Gretz [3] were early investigators into the effects of confinement upon the dynamic properties of cushioning materials. Mazzei's early work concentrated upon the dynamic cushioning properties of confined rubberized hair. Later results indicate a cursory evaluation of confined polyurethane foam. However, Mazzei's confined cushioning material research was conducted at a temperature of 294.4°K. Blake tested a variety of materials contained in corrugated fiberboard boxes at

294.4°K. Gammell and Gretz compared the effects of corner and edge drops to flat drops at 294.4°K. Grabowski [4] utilized polystyrene and flat drops with minimal testing at temperature extremes. Stern [5] has shown the effects of various containers on rubberized hair and polyurethane.

The apparent dearth of experimental results on confined cushioning materials at the temperature extremes prompted an experimental investigation to determine the effects, if any, on cushioning material confinement. The cushioning material selected was Minicel, which possessed a density of 32.04 kg/m<sup>3</sup>. A 50.8 mm thickness of this cushioning material was configured as corner void pads about a 482.6 mm plywood cube enclosed in a standard military cleated shipping container as shown in Fig. 1. The four standard drop heights of 304.8, 457.2, 609.6 and 762.0 mm were performed at temperatures of 219, 244, 266, 294, 316, and 344 K. A complete description of the experimental aspects are contained in [6]. Standard modeling procedures were utilized in obtaining a general model which incorporates the principal parameters [7].

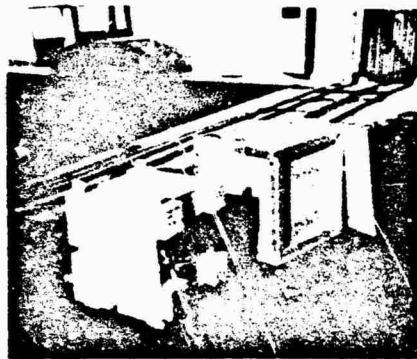


Fig. 1 - Plywood cube to be protected with cushion attached and container

The developed general model [8] portraying the peak accelerations of the confined cushioning system utilizing 32.04 kg/m<sup>3</sup> Minicel material is

$$G = C_0 + \sum_{k=0}^1 h^{k/2} \sum_{k=0}^1 \frac{1}{T^{(k+1/2)}} \cdot \sum_{j=1}^1 \theta^j \sum_{i=0}^1 C_{ijk} (1 - \cos \sigma_s)^i + \sum_{n=1}^3 \theta^n \sum_{m=0}^1 C_{mn} (1 - \cos \sigma_s)^m$$

Utilizing standard curve fitting procedures, the interior box Minicel model becomes:

$$G = -14.475784 + 3.285697 \frac{\theta h^{1/2}}{T^{3/2}} - 0.004766 \frac{\theta^2 h^{1/2}}{T^{3/2}} - 0.000016 \frac{\theta^3 (1 - \cos \sigma_s)^2}{T^{1/2}} + 69.329995 \frac{\theta}{T^{3/2}} + 153.363819 \frac{\theta (1 - \cos \sigma_s)^2}{T^{3/2}} + 0.003063 \frac{\theta^3 (1 - \cos \sigma_s)}{T^{3/2}} - 0.003311 \theta^2 (1 - \cos \sigma_s) - 0.000001 \theta^3$$

$$\text{where } \theta = \frac{F + 460}{1.8}$$

The interior box general model is predicated upon viscoelastic theory and incorporates the effect of drop height, static stress, thickness, and temperature of the cushion upon the peak acceleration of a confined cushioning system.

In addition, a general model was developed portraying the peak acceleration of the total box. The total box general model prediction of peak acceleration is a function of weight, temperature, and drop height. From this total box general model it is possible to identify the combination of terms which best describes the situation to be modeled. The resulting total box model becomes:

$$G = -6.35487467 + 0.00004649 \theta^2 h^{1/2} W - 0.00000001 \theta^3 h^{1/2} W$$

#### RESEARCH FINDINGS

It is desirable to view the two general models as an integrated pair, in which the interior box general model is a subset of the total box general model. Then, it is possible to isolate the shock absorption capabilities of the cushioning material by taking the difference between the total box model results and the interior box model results for selected values of static stress.

Since the two models were developed with different (but related) parameters, to achieve compatibility it is necessary to utilize the basic equation:

$$\sigma_s = \frac{W}{A}$$

where

$\sigma_s$  = an interior box static stress value

$W$  = weight of the total box

$A$  = footprint of the total box.

The footprint of the total box is the surface area of that portion which makes contact with the rigid surface. Each experimental total box possessed a surface area of 1112.90 mm<sup>2</sup>. Since the weight range of the experimental boxes was from 24.95 to 27.89 kg, substitution of these values in the previous equation gives the range of static stress values for comparison purposes.

Utilizing 533.4 mm drop height data as an example (Tables 1 through 6), it is observed that the interior box has not reached the optimum loading point at any temperature level. The optimum point would be an inflection point on the curve plotted from the interior box column. In fact, the interior box peak accelerations are decreasing slightly with increases in total box weight. Furthermore, in each case the cushion still possesses sufficient ability to absorb the increase in peak acceleration which occurs as a function of increased weight. As expected, the total box peak accelerations continue to increase as a function of increased total box weight.

TABLE 1  
Integrated Confined Model Data for  
219 K and a 533.4 mm Drop Height

Box Weight (kg)	Acceleration (G)		
	Total Box	Interior Box	Cushion
24.95	135.59	41.38	94.20
25.17	136.88	41.33	95.55
25.40	138.17	41.27	96.90
25.63	139.46	41.21	98.25
25.85	140.75	41.15	99.60
26.08	142.04	41.09	100.94
26.31	143.33	41.03	102.29
26.54	144.62	40.97	103.64
26.76	145.91	40.91	105.00
26.99	147.20	40.85	106.35
27.22	148.49	40.79	107.70
27.44	149.78	40.73	109.05
27.67	151.07	40.67	110.40
27.90	152.37	40.61	111.75

TABLE 4  
Integrated Confined Model Data for  
294 K and a 533.4 mm Drop Height

Box Weight (kg)	Acceleration (G)		
	Total Box	Interior Box	Cushion
24.95	161.55	39.65	121.89
25.17	163.07	39.59	123.48
25.40	164.60	39.54	125.06
25.63	166.13	39.48	126.65
25.85	167.65	39.42	128.23
26.08	169.18	39.36	129.82
26.31	170.71	39.30	131.41
26.54	172.23	39.23	132.99
26.76	173.76	39.17	134.58
26.99	175.29	39.11	136.17
27.22	176.81	39.05	137.76
27.44	178.34	38.99	139.35
27.67	179.86	38.92	140.94
27.90	181.39	38.86	142.52

TABLE 2  
Integrated Confined Model Data for  
244 K and a 533.4 mm Drop Height

Box Weight (kg)	Acceleration (G)		
	Total Box	Interior Box	Cushion
24.95	149.64	42.27	107.37
25.17	151.06	42.20	108.85
25.40	152.47	42.14	110.33
25.63	153.89	42.08	111.81
25.85	155.31	42.02	113.29
26.08	156.73	41.96	114.77
26.31	158.15	41.89	116.25
26.54	159.57	41.83	117.73
26.76	160.98	41.77	119.21
26.99	162.40	40.70	120.70
27.22	163.82	41.64	122.18
27.44	165.24	41.57	123.66
27.67	166.66	41.51	125.15
27.90	168.07	41.44	126.63

TABLE 5  
Integrated Confined Model Data for  
316 K and a 533.4 mm Drop Height

Box Weight (kg)	Acceleration (G)		
	Total Box	Interior Box	Cushion
24.95	157.81	36.47	121.33
25.17	159.30	36.42	122.88
25.40	160.80	36.37	124.42
25.63	162.29	36.32	125.97
25.85	163.78	36.26	127.51
26.08	165.27	36.21	129.06
26.31	166.77	36.16	130.60
26.54	168.26	36.10	132.15
26.76	169.75	36.05	133.70
26.99	171.24	36.00	135.24
27.22	172.74	35.94	136.79
27.44	174.23	35.88	138.34
27.67	175.72	35.83	139.89
27.90	177.21	35.77	141.43

TABLE 3  
Integrated Confined Model Data for  
266 K and a 533.4 mm Drop Height

Box Weight (kg)	Acceleration (G)		
	Total Box	Interior Box	Cushion
24.95	157.99	41.85	116.13
25.17	159.48	41.79	117.69
25.40	160.98	41.73	119.24
25.63	162.47	41.67	120.80
25.85	163.96	41.60	122.36
26.08	165.46	41.54	123.92
26.31	166.95	41.47	125.47
26.54	168.45	41.41	127.03
26.76	169.94	41.35	128.59
26.99	171.44	41.28	130.15
27.22	172.93	41.21	131.71
27.44	174.42	41.15	133.27
27.67	175.92	41.08	134.83
27.90	177.41	41.02	136.39

TABLE 6  
Integrated Confined Model Data for  
344 K and a 533.4 mm Drop Height

Box Weight (kg)	Acceleration (G)		
	Total Box	Interior Box	Cushion
24.95	143.45	30.63	112.82
25.17	144.81	30.59	114.22
25.40	146.18	30.55	115.62
25.63	147.54	30.51	117.02
25.85	148.90	30.48	118.42
26.08	150.26	30.44	119.82
26.31	151.62	30.40	121.22
26.54	152.99	30.36	122.62
26.76	154.35	30.32	124.02
26.99	155.71	30.28	125.42
27.22	157.07	30.24	126.83
27.44	158.43	30.20	128.23
27.67	159.79	30.16	129.63
27.90	161.16	30.12	131.03

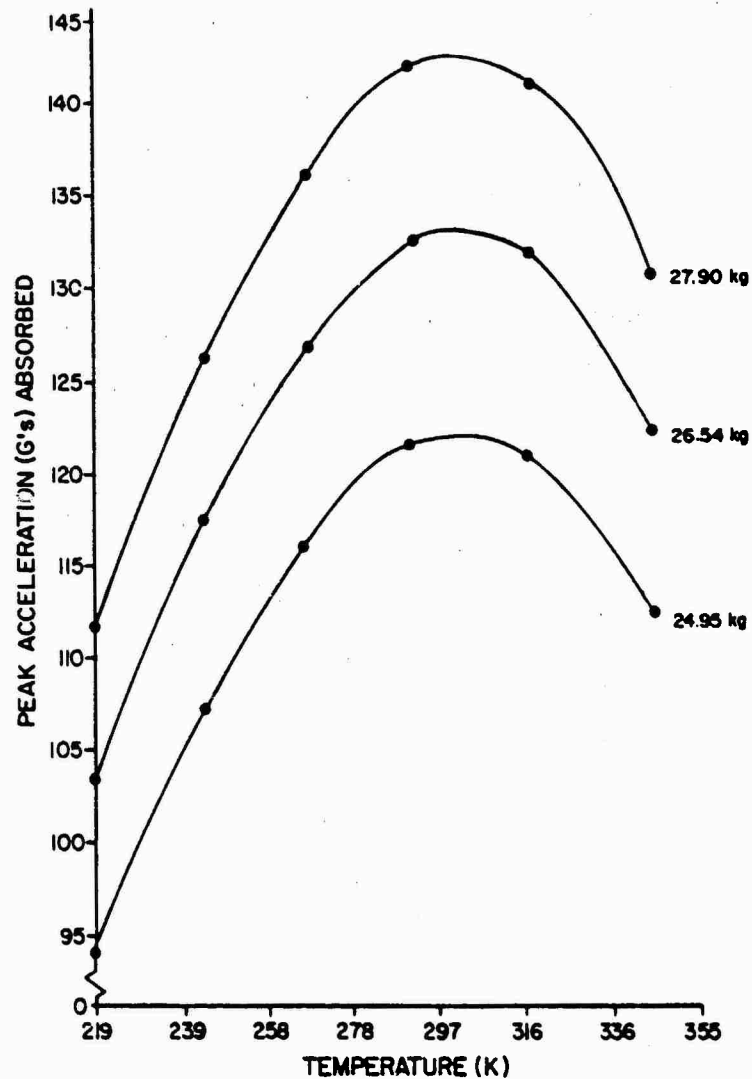


Fig. 2 - Cushion absorption as a function of temperature and total box weight for a 533.4 mm drop height

Perhaps the most significant finding of this research effort is the column entitled "Cushion" in Tables 1 through 6. Heretofore, the actual peak acceleration absorbed by a cushion as a function of weight and temperature has never been calculated. Consequently, Fig. 2 illustrates the effect of temperature upon the interior box cushion as a function of total box weight. It should be noted that the Minicel cushion performs well at the lowest temperature, 219 K. This low temperature phenomenon is not common to all cushioning materials, but indicates some unique characteristics for the

Minicel material. Further observation indicates that the Minicel material performs better, from a cushioning standpoint, at approximately 294 K.

This phenomenon may be due to the closed cell construction of the foam itself. Minicel is composed of tiny closed cells in which air is entrapped. Compressing the closed cell is comparable to compressing a balloon. Two factors in the construction of the cell which contribute to the cushioning ability of the foam material are the entrapped air and the



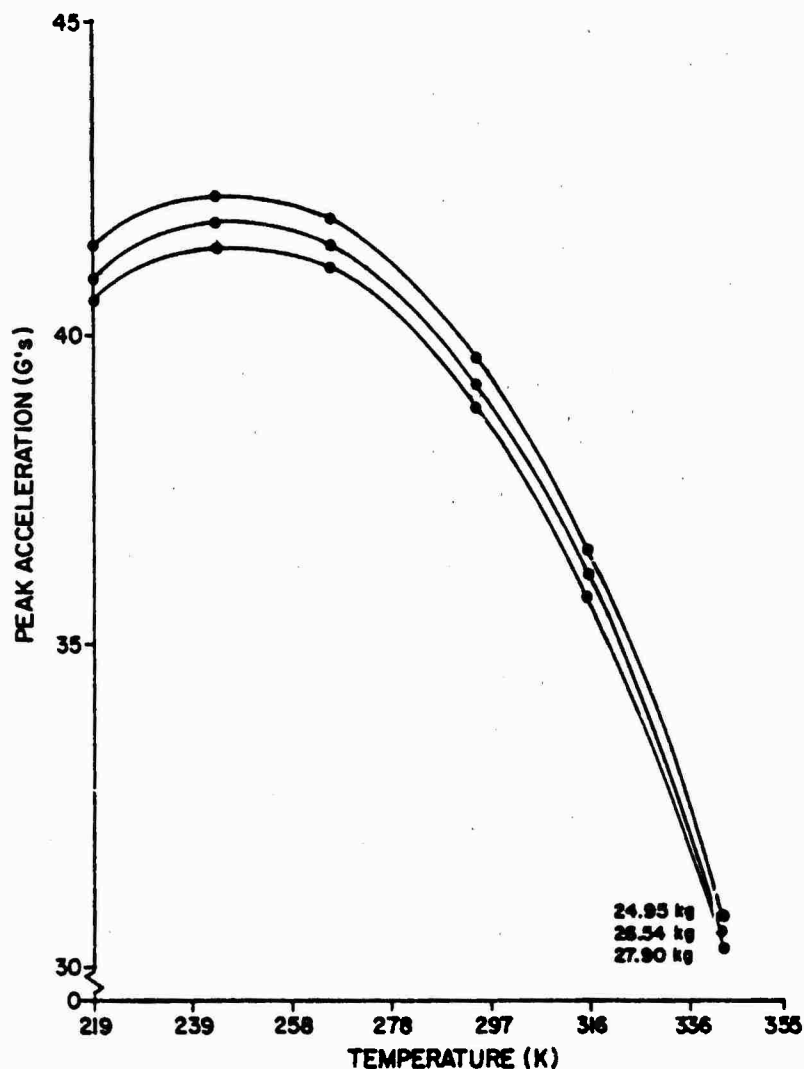


Fig. 3 - Interior box peak accelerations as a function of temperature and total box weight for a 533.4 mm drop height

walls of the cell. As the foam material is cooled, the air contracts and causes the cell to be compressed even though the cell walls are somewhat rigid from the cold temperature. At the higher temperatures, the walls of the cell become softer and are able to be compressed with less force than at lower temperatures. At the very low temperatures the contraction of air is a factor and at higher temperatures the flexibility of the cellular walls is a cushioning factor [9].

Fig. 3 illustrates the effect of temperature upon the interior box peak accelerations.

It is evident that the total box weight has a much smaller effect than temperature. Furthermore, the interior box experiences the greatest peak acceleration near 244 K, and the smallest peak accelerations at the high temperature extreme, 344 K.

Fig. 4 depicts the total box peak accelerations as a function of temperature. In this situation, the outside container is seen to be affected by the different temperature levels, which means the wooden construction serves as a better shock absorber at the cold and hot extremes than at ambient temperature. The wood

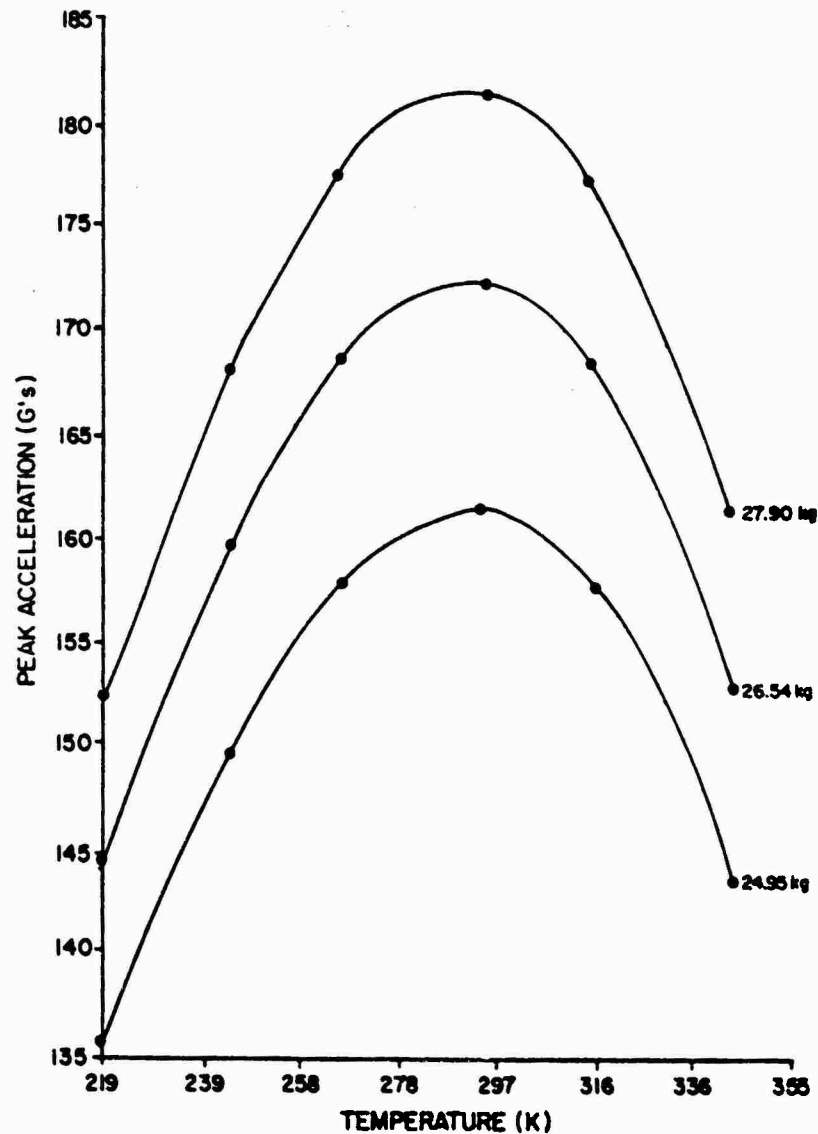


Fig. 4 - Total box peak accelerations as a function of temperature and total box weight at a 533.4 mm drop height

is considered to be a closed cell composite [9]. As a closed cell material it undergoes changes as the temperature varies.

One additional effect of temperature is observed when the data for a particular item weight from Tables 1 through 6 is selected. A summary of these data is provided in Table 7 for a 24.95 kg item. The development of an additional column in Table 7 which gives the

percent to total box G's absorbed by the cushion reveals that the Minicel cushion performs best at the highest temperature, 344 K. It is noted that at the low temperature, 219 K, the cushion absorbs 69% of the total box G's available increasing slowly until a level of 79% is achieved at 344 K. Hence, the cushion absorbs considerably more of the available shock at the higher temperature than at the lower temperatures. Similar results in cushion absorption occur for varying item weights.

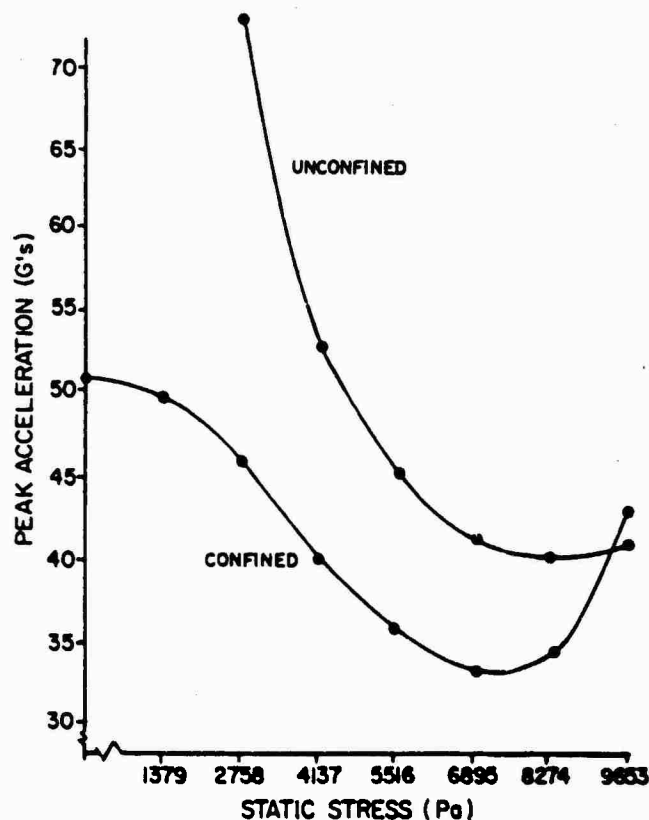


Fig. 5 - Comparison of confined and unconfined peak accelerations at 219 K with a 762.0 mm drop height

TABLE 7  
Cushion Absorption Percentage as a Function of Temperature for a Selected Item Weight and a 533.4 mm Drop Height

Temperature (K)	Acceleration (G)			Percent of G's Absorbed
	Total Box	Interior Box	Absorbed by Cushion	
219	136	41	94	69
244	150	42	107	71
266	158	42	116	73
294	162	40	122	75
316	158	36	121	77
344	143	31	113	79

that the magnitude of conservatism which was experienced was unknown. Consequently, knowledgeable cushioning system designers continue to utilize the best source currently available (i.e., unconfined data).

The results of this research permit a comparison between confined and unconfined test results. McDaniel [10] developed a general Minicel cushioning model based upon unconfined data. Both this research and McDaniel's utilized Minicel cushioning material, with each including the 50.8 mm thickness. Since both models have generalized the temperature and drop height parameters, it is possible to compare the unconfined interior box general model results with McDaniel's unconfined general model results.

#### CONFINED VERSUS UNCONFINED COMPARISONS

It is generally accepted that designing cushioning systems from unconfined (flat pad) drop tests will result in conservative (too much cushion) designs. The problem has been

Typical results are shown in Figures 5 through 7, where it is noted that the unconfined model predicts peak accelerations above the confined model when one considers the optimum cushioning point as the confined model minimum.

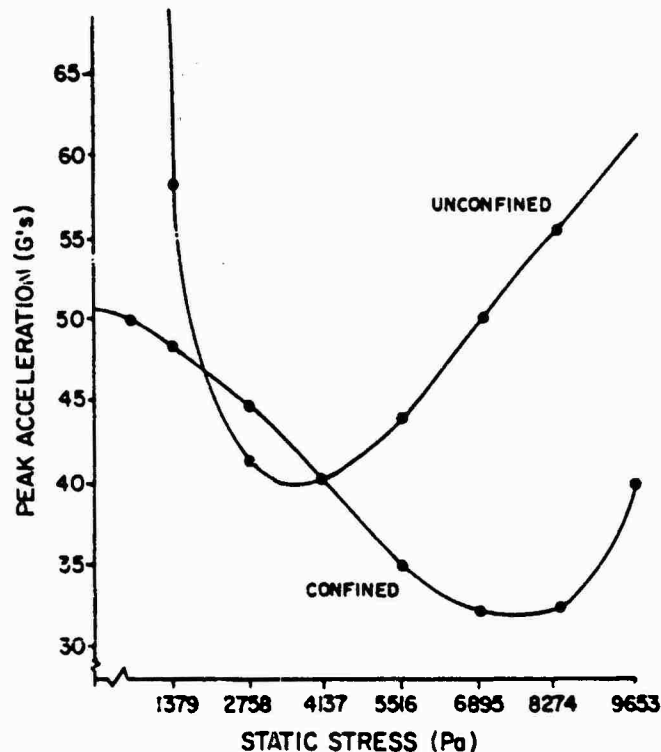


Fig. 6 - Comparison of confined and unconfined peak accelerations at 294 K with a 762.0 mm drop height

This confirms the original hypothesis that unconfined drop tests result in conservative designs. It is further noted in Figures 5 through 7 that the optimum cushioning point (lowest peak acceleration) does not occur at the same static stress level for the unconfined and confined cases. In fact, when the optimum cushioning point for the confined case is to the left of the unconfined optimum cushioning point (Fig. 5), the two curves intersect to the right of both optimum points. When the confined optimum cushioning point is to the right of the unconfined optimum point, the two curves intersect prior to the confined optimum point (Fig. 7).

Table 8 summarizes the optimum cushioning point at the six standard temperatures for the unconfined and confined cases for a 762.0 mm drop height. For five of the six temperatures, the peak acceleration minimum for the confined case is at a larger static stress value than for the unconfined case. Only at 219 K is the peak acceleration minimum at a lower static stress value for the confined case. Furthermore, irrespective of the temperature or static stress value, the peak acceleration minimums for the confined case are always lower than those for the unconfined case. Hence, once again the conservative nature of the unconfined approach is identified.

TABLE 8  
Summary of Unconfined Versus Confined Peak Acceleration Minimums for a 762.0 mm Drop Height

Temperature (K)	Unconfined		Confined	
	Static Stress	G's	Static Stress	G's
219	1.238	40	1.038	33
244	0.938	43	0.988	33
266	0.688	42	1.088	32
294	0.538	40	1.088	31
316	0.388	39	1.038	31
344	0.338	44	0.938	30

One additional point concerning the confined and unconfined general models warrants mentioning. The general models available permit the cushion designer to acquire cushion design information at any desired intermediate drop height value between 304.8 and 762.0 mm. Similar selections may be exercised for the range of temperature between 219 and 344 K.

#### CONCLUSIONS

The results of this research indicate that irrespective of the temperature value between 219 and 344 K, and a static stress value between 1379 and 9653 Pa, the peak acceleration minimums

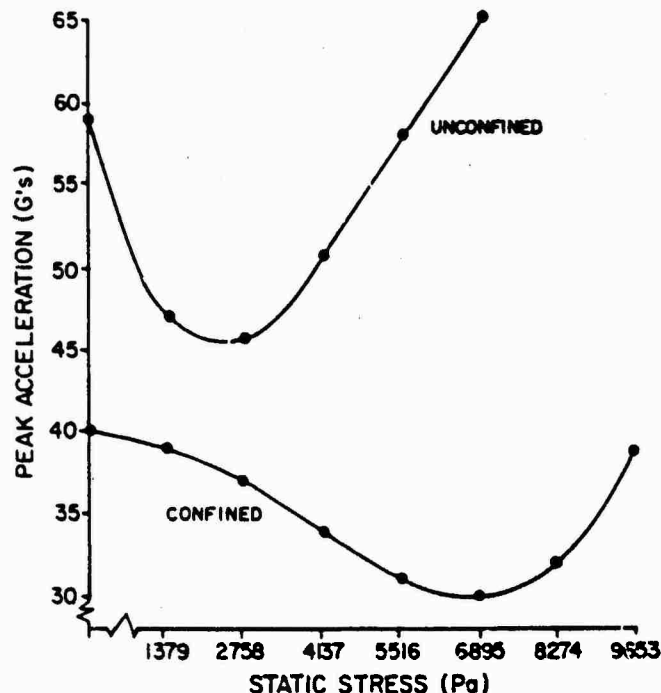


Fig. 7 - Comparison of confined and unconfined peak accelerations at 344 K with a 762.0 mm drop height

for the confined case are always lower than for the unconfined case. The conservative nature of the unconfined approach becomes very apparent. The results presented provide a measure of this conservatism for the Minicel material configured as a corner void cushion.

#### REFERENCES

1. Mazzei, H. J., "A Comparison Study: Confined vs. Unconfined Test Data," Report FRL-TR-45, Picatinny Arsenal, Dover, New Jersey, September 1961.
2. Blake, H. C. III, "Some Package Drop Tests Utilizing the Package Cushion Design Method," Michigan State University, School of Packaging, Project I, Technical Report No. 8, February 1965.
3. Gammell, L. W. and J. L. Gretz, "Effect of Drop Test Orientation on Impact Accelerations," Physical Test Laboratory, Texfoam Division, B. F. Goodrich Sponge Products Division, Shelton, Connecticut, 1955.
4. Grabowski, T. J., *Shock and Vibration Bulletin*, No. 30, 3, February 1962.
5. Stern, R. K., "Recent American Developments in Package Cushioning," *Proceedings of Symposium on Package Cushioning Dynamics*, Royal Radar Establishment, Malvern, England, April 1960.
6. Kobler, V. P., R. M. Wyskida, and J. O. Johannes, "An Experimental Design for Total Container Impact Response Modeling at Extreme Temperatures," *Shock and Vibration Bulletin*, No. 49, 1, September 1979.
7. Wyskida, R. M. and J. D. Johannes, "Methodology for Container Cushioning Model Development and Validation," MICOM Report No. TRT-CR-79-24, August 1979.
8. Kobler, V. P., "A Methodology for Modeling Confined Temperature Sensitive Cushioning Systems," unpublished Ph.D. Dissertation, The University of Alabama in Huntsville, May 1979.
9. Otis, D. R., "Thermal Damping in Gas-filled Composite Material During Impact Loading," *American Society of Mechanical Engineers, Transactions, Series E, Journal of Applied Mechanics*, 37, March 1970.
10. McDaniel, D. M., "Modeling the Impact Response of Bulk Cushioning Materials," U. S. Army Missile Command, Redstone Arsenal, Alabama, Report No. RD-75-16, 1975.

## Applications of Materials

### PRELIMINARY HARDNESS EVALUATION PROCEDURE FOR IDENTIFYING SHOCK ISOLATION REQUIREMENTS

Richard J. Bradshaw, Jr.  
US Army Engineer Division, Huntsville  
Huntsville, AL

and

Paul N. Sonnenburo  
US Army Construction Engineering Research Laboratory  
Champaign, IL

The Ballistic Missile Defense System SAFEGUARD experience indicates that there is a need to develop a procedure based on past test experience that can be used during the early design phase to identify shock isolation requirements. The procedure would provide designers a more concrete basis for making decisions concerning isolation requirements prior to receiving the results of the hardness verification program. This paper presents such a procedure. It is based on the shock test results for the equipment installed in the SAFEGUARD Ballistic Missile Defense System. These shock tests cover over 300 commercial items of equipment found in mechanical and electrical systems. The test data has been used to verify the hardness of over 30,000 items of equipment. In addition, the data base may be the largest and most extensive in existence for go/no-go shock testing of commercial equipment hardness to nuclear shock environments. The procedure is written to and for designers of future land-based hardened facilities (nuclear or non-nuclear) that use commercial equipment for which no fragility data exists.

#### INTRODUCTION

During the pre-design and design phases of hardened land-based military facilities, decisions must be made as to which equipment can be bolted to the floor (hardmounted) and which equipment must be shock isolated. Since equipment fragility to the expected shock environment is rarely known until after procurement and shock testing, these decisions are very difficult to make. The result is a tendency to take the safe but more expensive and conservative approach of providing more isolation than is required. Also, due to a lack of experimental data or guidance from past programs, planners and designers do not know how much shock testing is really required nor do they have any indication of the areas of potential weakness. Lack of this information results in designs that may magnify the problem and in testing programs that are more costly than necessary. Design uncertainty in the minds of designers will also result in higher preliminary cost estimates. Therefore, there is a definite need to develop a procedure for use during pre-design and design phases to provide guidance for identifying shock isolation requirements.

This paper presents a procedure for identifying shock isolation requirements based on test data from the SAFEGUARD Ballistic Missile Defense program. The procedure can also be used to identify potential areas of weakness and shock testing requirements. Presently, it is being incorporated into a chapter in TMS-855-1, Fundamentals of Protective Design (Non-Nuclear). The following paragraphs explain the approach used to develop the procedure, the justification for the approach, and the procedure. In addition, two examples are included to demonstrate correct usage of the procedure. All the required shock spectra are provided in the appendix.

#### PROCEDURE DEVELOPMENT

The initial idea for the procedure was to:

- a. Use the data base from the SAFEGUARD program to develop in-structure shock response spectra that generic equipment groups can survive without failure or malfunction.

b. Compare actual or estimated in-structure response spectra for a particular facility to the spectra developed in Step a. to determine if shock isolation is required. SAFEGUARD test data was published in 58 test reports (References 1-58) that contained thousands of test shock spectra representing over 300 tested items of equipment. Because this test data was so extensive, it had to be condensed. Two steps were taken to reduce this data to a size and form that would be used by designers. First, the tested equipment was assigned to the generic groups below.

#### GENERIC GROUPS

GROUP NO.	GROUP
1	Air-Conditioning Units
2	Air-Handling Units
3	Air-Conditioning and Chemical and Biological Filters
4	Fans
5	Dampers, Diffusers and Extractors
6	Piping Components
7	Pumps
8	Heat Exchangers
9	Heating and Cooling Coils
10	Air Compressors, Storage Tanks, Instrument Air Dryers
11	Water Chillers
12	Water Purification Units
13	Heat Sensing Devices
14	Indicators
15	Instrument Panels
16	Control Panels
17	Monitoring and Control Devices
18	Motor Generators
19	Diesel Engine Generators
20	Gas Turbine Generators
21	Generator Accessories
22	Circuit Breakers
23	Relays

GROUP NO.	GROUP
24	Electric Motor Control Center
25	Metal-Clad Switchgear
26	Dry Transformers
27	Electrical Panelboards
28	Station Battery Sets
29	Unit Substations
30	Light Fixtures
31	Computers
32	Communications Equipment

These groupings were the same used during the testing program to develop test packages of similar and related items. The next step was to reduce the thousands of test spectra to the undamped horizontal and vertical in-structure shock response spectra that each group can resist without failure or malfunction. The approach taken to reduce the test spectra to one horizontal and one vertical spectrum for each group is as follows:

(1) Identify for each tested item in the group the highest horizontal and the highest vertical test level passed without failure or malfunction.

(2) Draw an envelope of the test spectra that does not exceed the lowest points as shown in Fig. 1.

(3) Overlay all horizontal envelopes and draw another envelope of the low side of the overlay as shown in Fig. 2. This final envelope is the horizontal envelope that all the equipment in that group will pass without failure or malfunction. Repeat for the vertical spectra.

(4) Repeat Steps 1, 2, and 3 for each generic group.

These steps were modified for relays, motor control centers, and metal-clad switchgear since these devices are extremely sensitive to shock. SAFEGUARD testing experience with commercial equipment of this type shows that they pass without failure or malfunction at very low levels of shock. Therefore, in order to give designers more flexibility when working with these categories of equipment two different levels or environments of horizontal and vertical spectra were developed. The higher environment represents the level of shock at which these items survive without structural damage. At this higher level the relays in these types of

equipment malfunction by contact chattering and dropping out requiring manual reset. The lower environment is developed in accordance with Steps 1, 2, and 3 above.

These steps were further modified for groups having equipment with widely spaced levels of resistance. These groups were broken into two or more subgroups where the environments for equipment in the subgroups were closer. For example, the group Pumps was broken into two subgroups: a. Sump Pumps and b. Peripheral Turbine, Centrifugal and Positive Displacement Pumps. Each subgroup has its own horizontal and vertical environment that it passes without malfunction or failure.

Table 1 is the result of applying the data condensing approach just described. In the table each group is listed with its corresponding limitations and its derived environment, which consists of one horizontal spectrum and one vertical spectrum. In some cases, subgroups are listed and treated as individual units with their own limitations and environments. For each group or subgroup environment, numbers appear in the "Horizontal Spectrum" and "Vertical Spectrum" columns. These numbers reference the horizontal and vertical spectra which are illustrated in the appendix. In the table Group No. 24, Electric Motor Control Center, has two environments which are not based upon subgroups but are defined according to two separate types of limitations.

TABLE 1  
Equipment Shock Resistance

GROUPS/SUBGROUPS	LIMITATIONS	ENVIRONMENT (APPENDIX)	
		HORIZONTAL SPECTRUM	VERTICAL SPECTRUM
1. Air-Conditioning Units	1. Small 5-ton compressor and air handling unit	1	1
2. Air-Handling Units	2. None	4	4
3. Air-Conditioning and CB Filters	3. None	4	2
4. Fans	4. Centrifugal and axial flow	5	2
5. Dampers, Diffusers, and Extractors	5. None	6	7
6. Piping Components	6. Valves (manual, control, pneumatic actuated), sediment strainers, flex hoses, fluid filters, moisture traps, expansion joints, automatic air vents, flow orifices, attenuators, etc.	19	3
7. Pumps	7.		
a. Sump Pumps	a. None	8	10
b. Peripheral Turbine, Centrifugal and Positive Displacement	b. None	4	9
8. Heat Exchangers	8. None	19	11
9. Heating and Cooling Coils	9. None	12	2



TABLE 1  
Equipment Shock Resistance  
(Continued)

GROUPS/SUBGROUPS	LIMITATIONS	ENVIRONMENT (APPENDIX)	
		HORIZONTAL SPECTRUM	VERTICAL SPECTRUM
10. Air Compressors, Storage Tanks, Instrument Air Dryers	10. None	13	14
11. Water Chillers	11. None	16	15
12. Water Purification Units	12. None	17	18
13. Heat Sensing Devices	13. None	19	20
14. Indicators	14. Pressure, flow, temperature, level	4	21
15. Instrument Panels	15. None	19	22
16. Control Panels	16.		
a. Generator Surge Pak	a. None	25	23
b. All Others	b. None	25	24
17. Monitoring and Control Devices	17. Current trips, regulator filters, switches, probes, transmitters, transducers, power supplies, controllers, thermostats, etc.	26	27
18. Motor Generators	18. None	28	29
19. Diesel Engine Generators	19. Diesel engine generator, pumps, governors, control linkage, pneumatic actuators	30	30
20. Gas Turbine Generators	20. None	31	4
21. Generator Accessories	21. Neutral resistor, neutral breaker, static exciter regulator	32	32
22. Circuit Breakers	22.		
a. Molded Case Circuit Breakers	a. None	34	34
b. All Other Types	b. None	33	33
23. Relays	23.		
a. Hardmounted to rigid surface	a. None	35	38
b. Cabinet Mounted	b. Structural limit	37	37
c. Cabinet Mounted	c. Relay chatter limit	36	36
24. Electric Motor Control Center	24. a. Structural limit b. Relay chatter limit	39 41	39 40

TABLE 1  
Equipment Shock Resistance  
(Continued)

GROUPS/SUBGROUPS	LIMITATIONS	ENVIRONMENT (APPENDIX)	
		HORIZONTAL SPECTRUM	VERTICAL SPECTRUM
25. Metal Clad Switchgear	25. Environments are those the switchgear passed structurally. At these environments the switchgear changed state and indicator flags dropped down giving false information.	42	42
26. Dry Transformers	26. None	44	43
27. Electrical Panelboard: a. Panelboards with Air Circuit Breakers b. Panelboards without Air Circuit Breakers	27. Circuit breakers, relays, meters, RFI filters, motor starters, air circuit breakers	45 45	47 46
28. Station Battery Sets a. Batteries b. AC Switchboard and DC Power Supply	28. a. None b. None	48 49	48 49
29. Unit Substations	29. Transformers, voltage regulators, circuit breakers, motor controls, motor starter	30	37
30. Light Fixtures a. OCE Type F10-B Modified b. OCE Type F-4 Modified	30. a. None b. None	50 52	51 2
31. Computers	31. None	53	54
32. Communications Equipment	32. None	55	56

#### JUSTIFICATION

There are four reasons why the approach taken to develop the procedure is justified. First, the shock tests of the 300 mechanical and electrical items of equipment upon which the procedure is based were used to verify the hardness of over 30,000 items of equipment located in the SAFEGUARD complex. A quasi-probabilistic comparison method (Reference 59) was used to accomplish this verification since testing of all 30,000 items would have been formidable.

Second, the quasi-probabilistic comparison method developed for the SAFEGUARD Hardness Verification Program was sensitive to actual recorded test spectrum points that fell

below the untested equipment's actual in-structure shock response environment. The approach used here is to construct a shock spectra that envelopes the low points of the test spectra. Therefore, if the comparison method were used with in-structure shock environments equal to or less than those in the appendix the method would show a high probability of survival.

Third, SAFEGUARD experience shows that equipment failures tend to repeat for a particular generic group so that test engineers were able to predict the types of failures and malfunctions a particular type of equipment would

experience. While this is not a foolproof conclusion, it is consistent enough to justify using the approach presented here to gain insight into shock isolation and shock testing requirements early in the design phase.

Fourth, though equipment designs change and individual pieces of equipment may develop sensitivities not previously anticipated, it is unlikely that grouped mechanical or electrical equipment will deviate much from the results of the SAFEGUARD test program in the future.

#### PROCEDURE

Step 1 - Equipment Classification. Designers must first classify the equipment as follows:

- a. Mission critical equipment that must function during and after each shock (Criticality A).
- b. Mission critical equipment that does not have to function during each shock but must function following each shock (Criticality B).
- c. Equipment not critical to the mission that does not have to function during or following an attack (Criticality C).

Criticality A and B equipment must be protected against shock. Items with Criticality C will be hardmounted and securely attached to the building structure to prevent hazards to personnel or mission critical equipment. All equipment controls and system monitoring devices, remote and local, must be either Criticality A or B. If they are Criticality B they must return to their original state following shock without requiring operators to reset, restart or readjust. This prevents confusion following each shock because of false alarms or equipment shutdown requiring operators to restart machinery and readjust each system.

Step 2 - In-Structure Shock Environment. Compute and plot the horizontal and vertical undamped in-structure shock response spectra.

Step 3 - Equipment Selection. Locate the item of equipment being considered from Table 1 and find the shock environments it will survive.

Step 4 - Shock Environment Comparison. Compare the horizontal and vertical spectra obtained from Step 3 with the horizontal and vertical in-structure response spectra from Step 2 at the location where the equipment is installed.

Step 5 - Hardmount or Shock Isolate?

- a. All equipment except relays, electric motor control centers, and metal-clad switchgear. If the design shock environment

(Step 2) falls below the environment in Table 1, the equipment can be hardmounted. If it exceeds the environment in Table 1 the designer has two options: shock isolate the equipment or shock test and retrofit if required until it survives the in-structure shock environment.

- b. Relays and electric motor control centers. More than one environment are listed for these items in Table 1. One represents the environment the equipment can be expected to survive structurally. At this level there will be considerable relay chatter that may result in electrical malfunctions. If the higher level is used the designer must design electrical circuitry for Criticality A equipment to prevent the loss or disruption of critical functions during shock motions. If the higher level is used for Criticality B equipment the designer must design electrical circuitry to prevent loss of the critical function following shock motions. The lower environment must be used if circuitry cannot be designed to prevent disruption due to relay chatter. Once the proper environment is selected from Table 1 proceed as instructed in Step 5a.

- c. Metal-clad switchgear. These devices are very sensitive to any level of shock. Environments in Table 1 are levels these devices have survived structurally. At these levels considerable contact chatter and change of state took place. Therefore, these devices must be protected by one of the following: circuitry designed to prevent disruption of Criticality A functions and to prevent loss of function requiring resetting or restarting for Criticality B functions; or shock isolate; or perform shock tests and retrofit until the switchgear survives the environment; or use another piece of already hardened equipment that provides the same service.

Using this procedure the designer can identify the amount of shock isolation and shock testing for a particular in-structure shock environment. The cost tradeoffs can be made between the cost of equipment protection (shock isolation and shock testing) and the cost of reducing in-structure shock.

#### EXAMPLES

The following example illustrates the use of the procedure.

Example 1:

Given: A Criticality A Chiller mounted in a location having the vertical and horizontal shock response spectra shown in Fig. 3.

Decide whether to isolate or hardmount the chiller.

Step 1: Given Criticality A Chiller.

Step 2: Given in Fig. 3.

Step 3: Water chillers should be able to survive environments 16 and 15 as shown in Item 11, Table 1.

Step 4: The in-structure shock response spectra are compared to environments 16 and 15 in Figs. 4 and 5.

Step 5: Since the in-structure shock response spectra do not exceed the allowable environments (15 and 16) from Table 1, the chiller can be hardmounted.

#### Example 2:

Given: Same as in the preceding example except that the in-structure vertical and horizontal shock response spectra are given in Fig. 6.

Decide whether to isolate or hardmount.

Step 1: Given Criticality A Chiller.

Step 2: Given in Fig. 6.

Step 3: Same as Step 3 in above example.

Step 4: The in-structure shock response spectra are compared to environments 16 and 15 in Figs. 7 and 8.

Step 5: Since the vertical in-structure shock response spectra exceed environment 15 the chiller should be isolated or shock tested and retrofitted.

#### CONCLUSIONS

In closing we draw the following conclusions:

a. The procedure will improve the capability of designers and planners to objectively determine shock isolation requirements with a higher degree of confidence early in the pre-design and design phases.

b. This improved capability will reduce uncertainty and therefore result in more accurate cost estimates of large projects.

c. Using this procedure designers will be able to identify potential problem areas and correct them early in the design, thereby saving costly retrofit actions.

d. While the procedure should result in a high implicit probability of survival it does not explicitly predict the probability of survival. Therefore, it does not eliminate the need for a hardness verification program.

e. The procedure can be used to develop a hardness verification program since it identifies potential weak links and strong points.

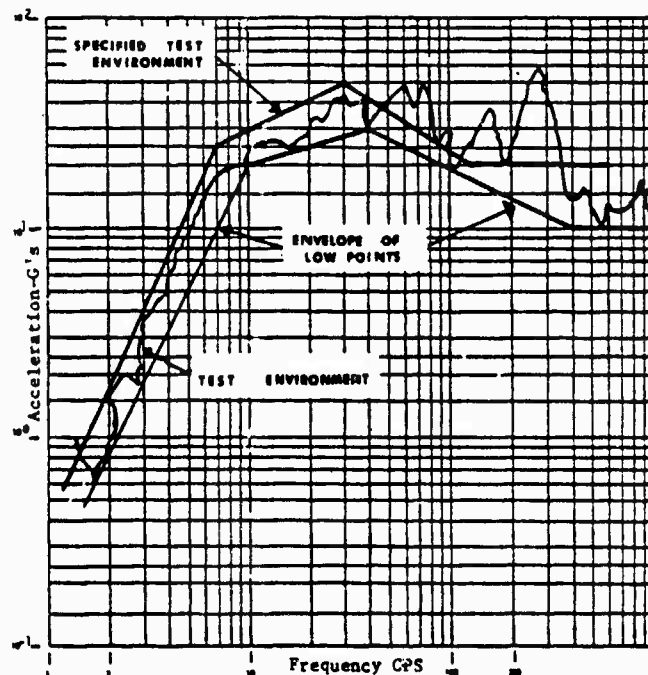


Fig. 1 - Example of envelope of test spectrum low points

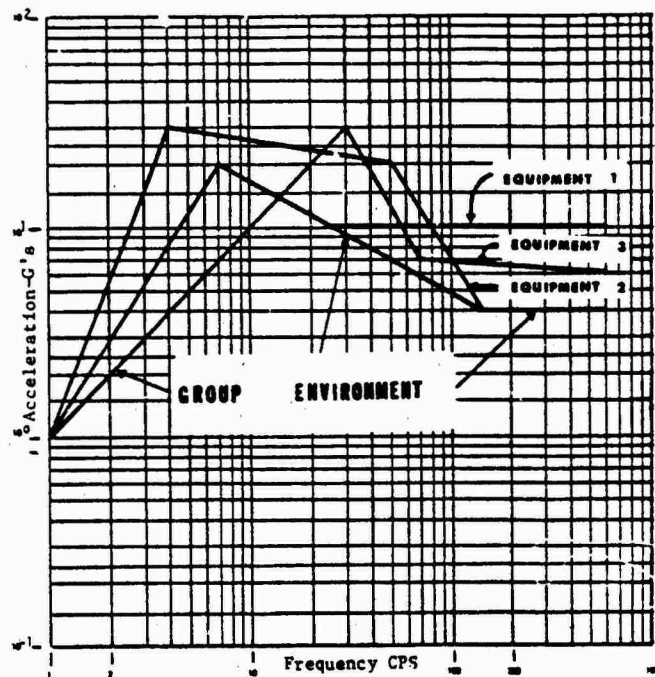


Fig. 2 - Example of method used to obtain group environment

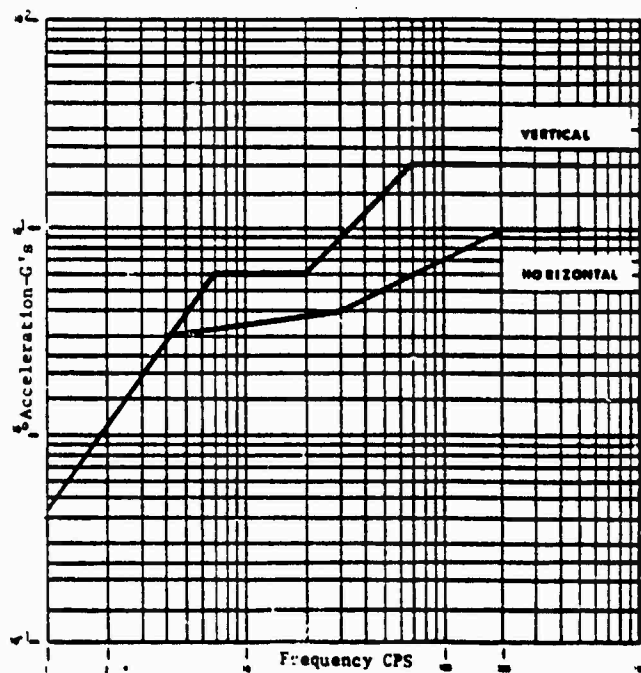


Fig. 3 - Example 1 - Given in-structure vertical and horizontal response spectra

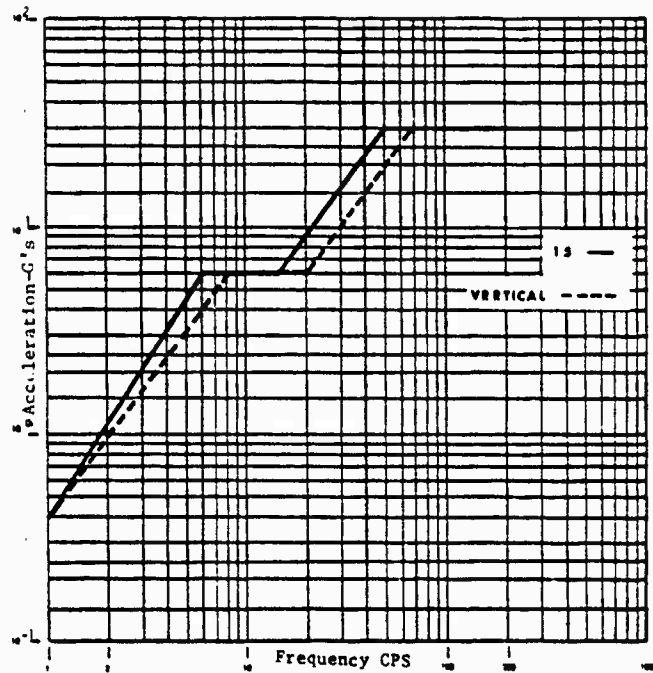


Fig. 4 - Example 1 - Comparison of spectrum 15 in appendix with given vertical spectra in Fig. 3

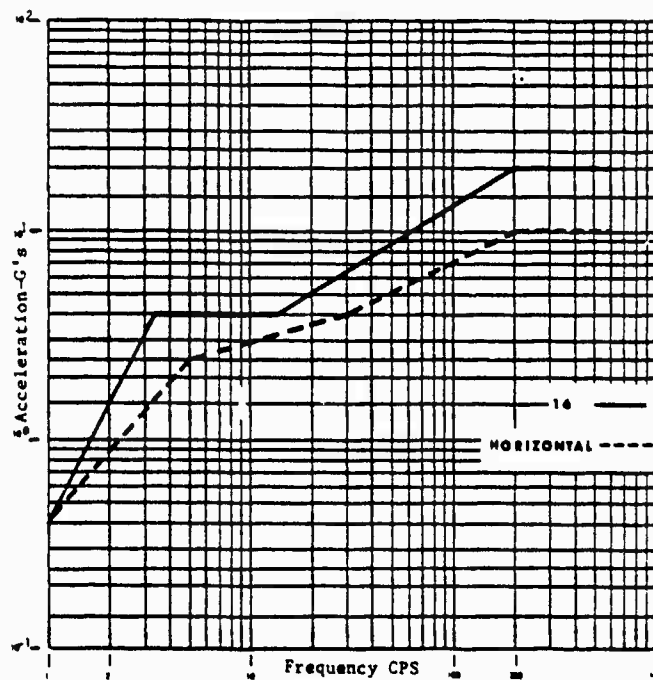


Fig. 5 - Example 1 - Comparison of spectrum 15 in appendix with given horizontal spectra in Fig. 3

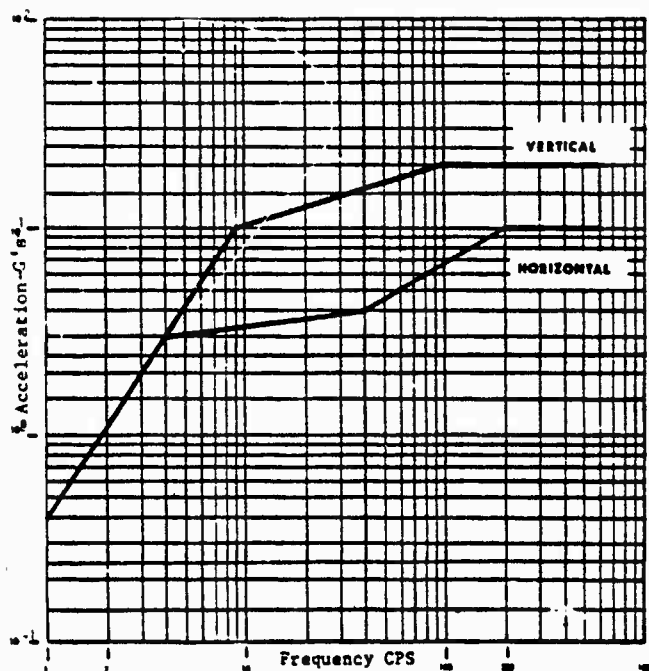


Fig. 6 - Example 2 - Given in-structure vertical and horizontal response spectra

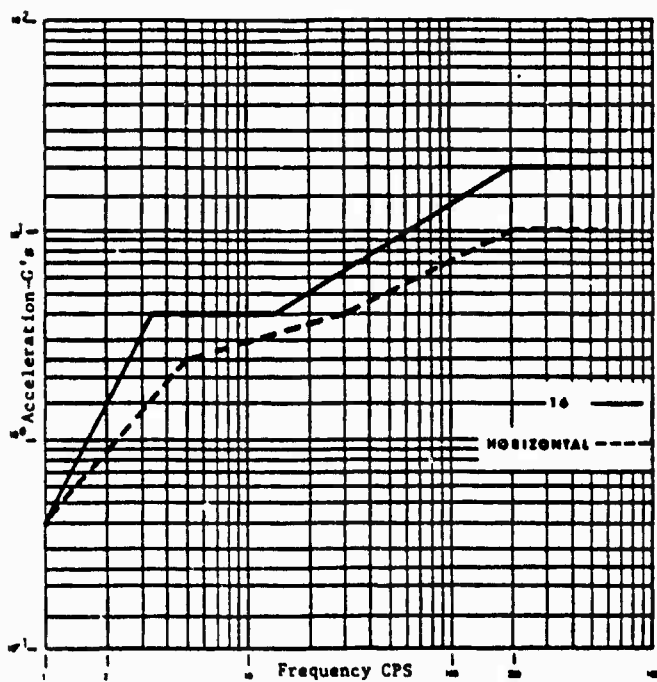


Fig. 7 - Example 2 - Comparison of spectrum 16 in appendix with given horizontal spectra in Fig. 6

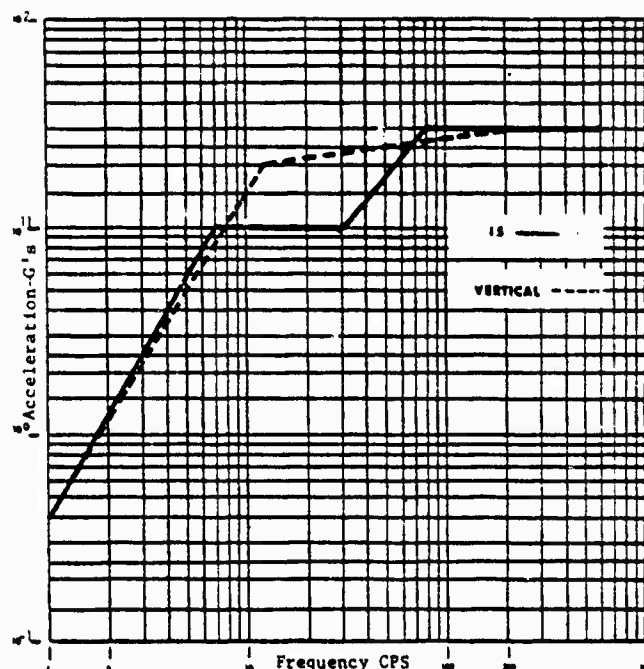


Fig. 8 - Example 2 - Comparison of spectrum 15 in appendix with given vertical spectra in Fig. 6

#### REFERENCES

The following list of references consists of reports published by the US Army Engineer Division, Huntsville.

1. "Shock Test Program, Air Handling Unit (H06AU), For SAFEGUARD TSE Systems and Equipment," HNDSP-74-325-ED-R, 31 December 1974.
2. "Shock Test Program, Three Piping Segments (P02PC), For SAFEGUARD TSE Systems and Equipment," HNDSP-74-326-ED-R, 31 December 1974.
3. "Shock Test Program, Piping Segment (P39PC), For SAFEGUARD TSE System and Equipment," HNDSP-74-327-ED-R, 31 December 1974.
4. "Shock and Equipment, Piping Segment (P30PC), For SAFEGUARD TSE Systems and Equipment," HNDSP-74-328-ED-R, 31 December 1974.
5. "Shock Test Program, Gas Turbo-Generator Assembly (E01GT), For SAFEGUARD TSE Systems and Equipment," HNDSP-74-329-ED-R, 31 December 1974.
6. "Shock Test Program, Unit Substation Switch - Transformer - Voltage Regulator - Circuit Breaker (E0455), For SAFEGUARD TSE Systems and Equipment," HNDSP-74-330-ED-R, 31 December 1974.
7. "Shock Test Program, Unit Substation Voltage Regulator - Circuit Breaker (E0555)-8, For SAFEGUARD TSE Systems and Equipment," HNDSP-74-332-ED-R, 31 December 1974.
8. "Shock Test Program, Unit Substation Motor Control Center (E1255), For SAFEGUARD TSE Systems and Equipment," HNDSP-74-333-ED-R, 31 December 1974.
9. "Shock Test Program, Unit Substation Transformer (E1655), For SAFEGUARD TSE Systems and Equipment," HNDSP-74-334-ED-R, 31 December 1974.
10. "Shock Test Program, Unit Substation Circuit Breakers (E2755), For SAFEGUARD TSE Systems and Equipment," HNDSP-74-335-ED-R, 31 December 1974.
11. "Shock Test Program, Unit Substation Circuit Breakers (E2955), For SAFEGUARD TSE Systems and Equipment," HNDSP-74-336-ED-R, 31 December 1974.
12. "Shock Test Program, Motor Generator Set (E03G4), For SAFEGUARD TSE System and Equipment," HNDSP-74-337-ED-R, 31 December 1974.
13. "Shock Test Program, Motor Generator Set (E12G4), For SAFEGUARD TSE Systems and Equipment," HNDSP-74-338-ED-R, 31 December 1974.



14. "Shock Test Program, Air Conditioner Test, For SAFEGUARD TSE Systems and Equipment," HNDSP-71-58-ED-R, 15 May 1972.
15. "Shock Test Program, Station Battery System, For SAFEGUARD TSE Systems and Equipment," HNDSP-72-69-ED-R, 18 August 1972.
16. "Shock Test Program, Electrical Panelboards Test, For SAFEGUARD TSE Systems and Equipment," HNDSP-72-64-ED-R, 30 September 1972.
17. "Shock Test Program, Water Purification Units, For SAFEGUARD TSE Systems and Equipment," HNDSP-72-70-ED-R, 1 April 1973.
18. "Shock Test Program, Electrical Panelboards Test, For SAFEGUARD TSE Systems and Equipment," HNDSP-72-64-ED-R, 30 September 1972.
19. "Shock Test Program, Water Chiller, For SAFEGUARD TSE Systems and Equipment," HNDSP-73-95-ED-R, 1 April 1973.
20. "Shock Test Program, Heat Exchanger, For SAFEGUARD TSE Systems and Equipment," HNDSP-73-85-ED-R, 30 April 1973.
21. "Shock Test Program, Air Conditioning and CBR Filters, For SAFEGUARD TSE Systems and Equipment," HNDSP-73-86-ED-R, 30 April 1973.
22. "Shock Test Program, Centrifugal Fans and Axial Fans, For SAFEGUARD TSE Systems and Equipment," HNDSP-73-87-ED-R, 30 April 1973.
23. "Shock Test Program, Waste Disposal Pumps, For SAFEGUARD TSE Systems and Equipment," HNDSP-73-86-ED-R, 30 April 1973.
24. "Shock Test Program, Heating and Cooling Coils, For SAFEGUARD TSE Systems and Equipment," HNDSP-73-89-ED-R, 1 May 1973.
25. "Shock Test Program, Compressor - Instrument Air Driver, For SAFEGUARD TSE Systems and Equipment," HNDSP-73-304-ED-R, 15 November 1973.
26. "Shock Test Program, Fluorescent Light Fixtures, For SAFEGUARD TSE Systems and Equipment," Volume 1, Book 2, HNDSP-72-77-ED-R, 1 July 1974.
27. "Shock Test Program, Fluorescent Light Fixtures, For SAFEGUARD TSE Systems and Equipment," HNDSP-72-77-ED-R, 31 December 1973.
28. "Shock Test Program, Peripheral Turbine Pumps, For SAFEGUARD TSE Systems and Equipment," HNDSP-73-97-ED-R, 31 December 1973.
29. "Shock Test Program, Dry Transformers, For SAFEGUARD TSE Systems and Equipment," HNDSP-73-300 ED-R, 31 December 1973.
30. "Shock Test Program, Monitoring and Control Components, For SAFEGUARD TSE Systems and Equipment," HNDSP-73-302-ED-R, 31 December 1973.
31. "Shock Test Program, Metal-Clad Switchgear, For SAFEGUARD TSE Systems and Equipment," Volume 1, Book 1 - Basic Report and SHK75 Test Data, HNDSP-74-305-ED-R, 31 December 1973.
32. "Shock Test Program, Metal-Clad Switchgear, For SAFEGUARD TSE Systems and Equipment," Volume 1, Book 2 - 5 HK350 Test Data, HNDSP-73-305-ED-R, 31 December 1973.
33. "Shock Test Program, Piping Segments, For SAFEGUARD TSE Systems and Equipment," HNDSP-74-306-ED-R, 31 March 1974.
34. "Shock Test Program, Monitor and Control - Duct Mounted Equipment, For SAFEGUARD TSE System and Equipment," HNDSP-74-307-ED-R, 1 April 1974.
35. "Shock Test Program, 60-Ton Chiller Components, For SAFEGUARD TSE Systems and Equipment," HNDSP-74-308-ED-R, 1 May 1974.
36. "Shock Test Program, Air Compressor Control Panel and Drive Motor, For SAFEGUARD TSE Systems and Equipment," HNDSP-74-309-ED-R, 1 May 1974.
37. "Shock Test Program, Switchgear Cabinet - Transfer Function Tests, For SAFEGUARD TSE Systems and Equipment," HNDSP-73-91-ED-R, 15 April 1973.
38. "Shock Test Program, Generator Control Panel, For SAFEGUARD TSE Systems and Equipment," HNDSP-74-310-ED-R, 1 June 1974.
39. "Shock Test Program, Generator Neutral Breaker, For SAFEGUARD TSE Systems and Equipment," HNDSP-74-312-ED-R, 15 July 1974.
40. "Shock Test Program, Electric Motor Control Centers (E52MC) (E87MC) For SAFEGUARD TSE Systems and Equipment," HNDSP-74-315-ED-R, 1 July 1974.
41. "Shock Test Program, Instrument Air Dryer, For SAFEGUARD TSE Systems and Equipment," HNDSP-74-316-ED-R, 30 September 1974.
42. "Shock Test Program, Monitoring and Control Components, For SAFEGUARD TSE Systems and Equipment," 31 December 1974.
43. "Shock Test Program, Thermal Water Valve, For SAFEGUARD TSE Systems and Equipment," HNDSP-74-321-ED-R, 1 October 1974.
44. "Shock Test Program, Temperature Switch (IS8TS), For SAFEGUARD TSE Systems and Equipment," HNDSP-74-322-ED-R, 20 September 1974.

45. "Shock Test Program, Generator Static Exciter/Regulator, For SAFEGUARD TSE Systems and Equipment," HNDSP-74-323-ED-R, 1 September 1974.

46. "Shock Test Program, Diesel Engine Components and M&C Components, For SAFEGUARD TSE Systems and Equipment," Volume 1, Test Report, HNDSP-74-324-ED-R, 31 December 1974.

47. "Shock Test Program, Compressor Control Oil Shutdown Switch, For SAFEGUARD TSE Systems and Equipment," HNDSP-74-34D-EO-R, 15 November 1974.

48. "Shock Test Program, Pressure Control Valve (P83VE), For SAFEGUARD TSE Systems and Equipment," HNDSP-74-342-ED-R, 20 November 1974.

49. "Shock Test Program, Heat Sensing Device Assembly, For SAFEGUARD TSE Systems and Equipment," HNDSP-74-345-ED-R, 27 November 1974.

50. "Shock Test Program, Relay - Fragility Test, For SAFEGUARD TSE Systems and Equipment," HNDSP-71-57-EO-R, 15 May 1972.

51. "Shock Test Program, Fragility Tests of Twenty-Two Electrical Components, For SAFEGUARD TSE Systems and Equipment," Volumes 1 and 2, HNDSP-75-349-ED-R, 1 July 1975.

52. "Hardness Program - Non-EMP, Test Report, For SAFEGUARD TSE Ground Facilities Shock Test Program, Fragility Testing Electric Motor Control Centers (ITCs E06MC, E52MC, E87MC, and E89MC)," Volume 1 and 2, HNDSP-73-159-ED-R, 30 March 1973.

53. "Hardness Program - Non-EMP, Heat Exchanger Dynamic Response Analysis, For SAFEGUARD TSE Ground Facilities," HNDSP-73-158-ED-R, 1 March 1973.

54. "Hardness Program - Non-EMP, Pump Piping Appurtenance, Shock Response Analysis, For SAFEGUARD TSE Ground Facilities," HNDSP-73-160-ED-R, 31 March 1973.

55. "Shock Test Program, Dynamic Analysis Diesel Engine Generator, For SAFEGUARD TSE Systems and Equipment," HNDTR-73-12-ED-R, 31 December 1973.

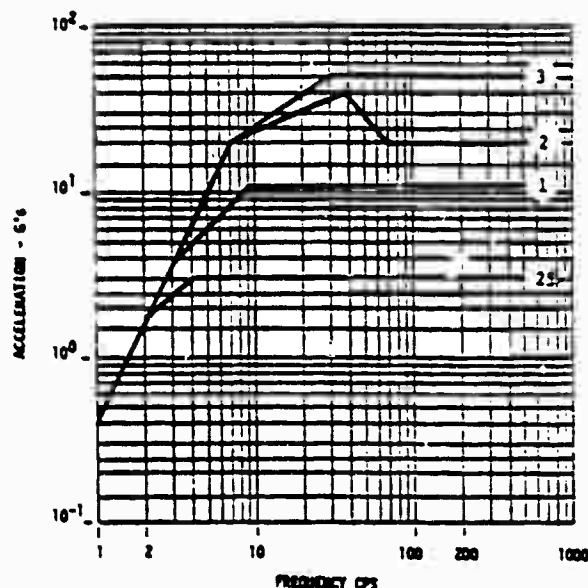
56. "Shock Test Program, Dynamic Analysis - Air Compressor (PD1CR), For SAFEGUARD TSE Systems and Equipment," HNDTR-75-22-EO-SR, 1 May 1975.

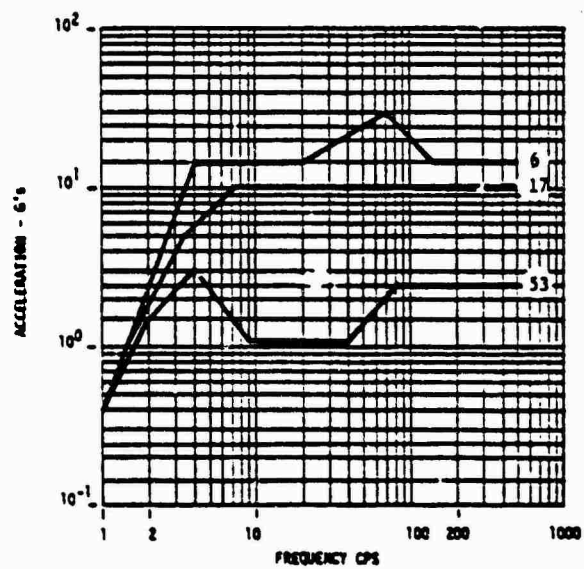
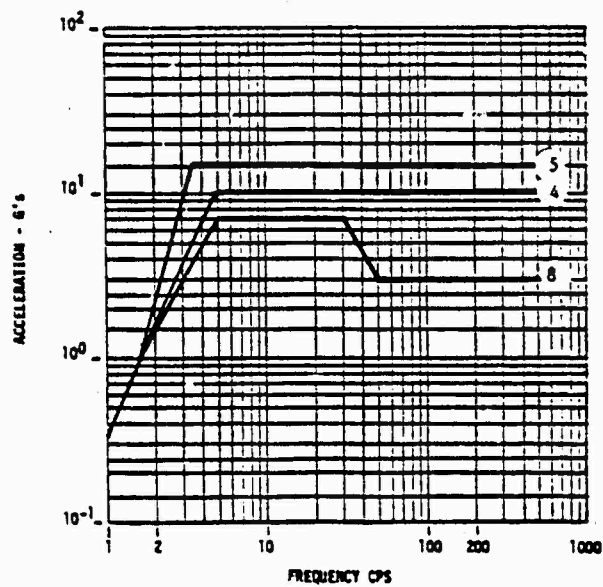
57. "Shock Test Program, Dynamic Analysis of a 660-Ton Chiller, For SAFEGUARD TSE Systems and Equipment," HNDTR-77-30-ED-SR, 30 April 1977.

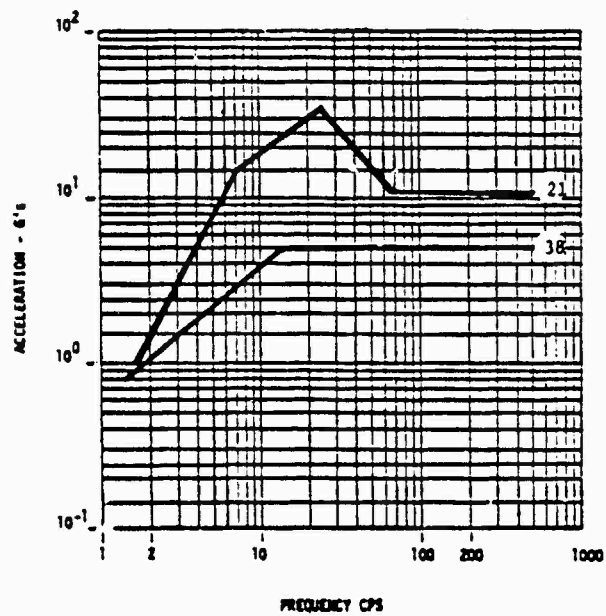
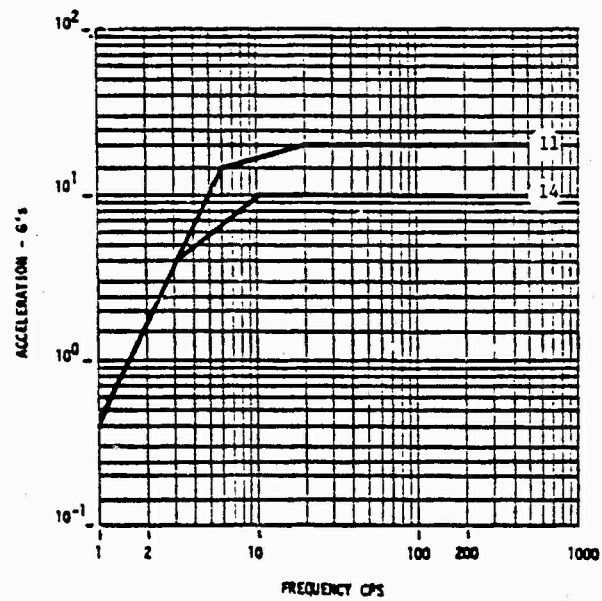
58. "Shock Test Program, Dynamic Analysis - Motor Generator Set - ITC-E12GM, For SAFEGUARD TSE Systems and Equipment," HNDSP-74-344-EO-R, 31 December 1974.

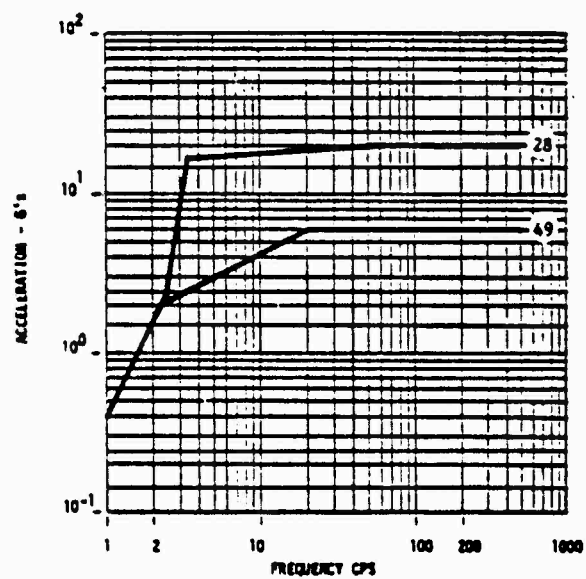
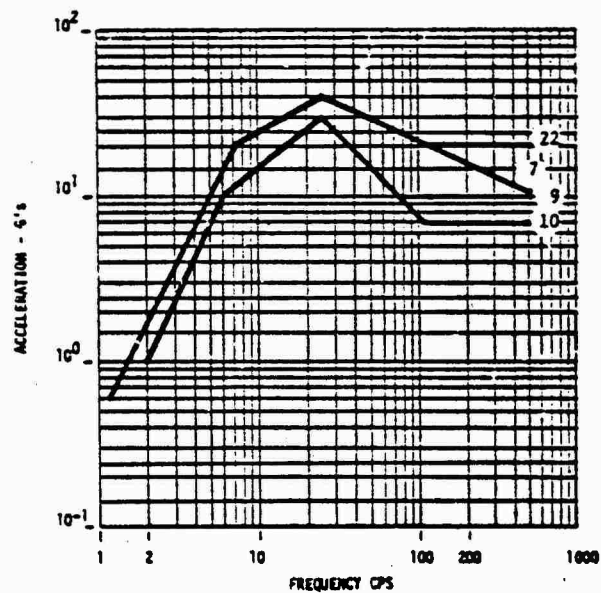
59. "Hardness Program-Non-EMP - Subsystem Hardness Assurance Analysis, For SAFEGUARD TSE Ground Facilities," Volumes 1 and 2, HNDSP-73-159-ED-R, 30 June 1975.

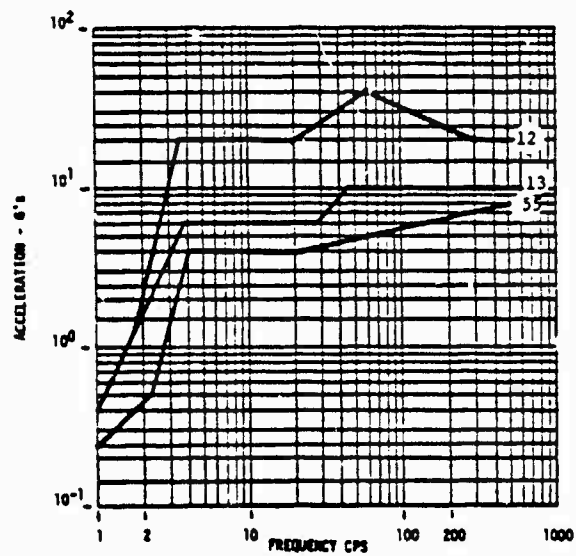
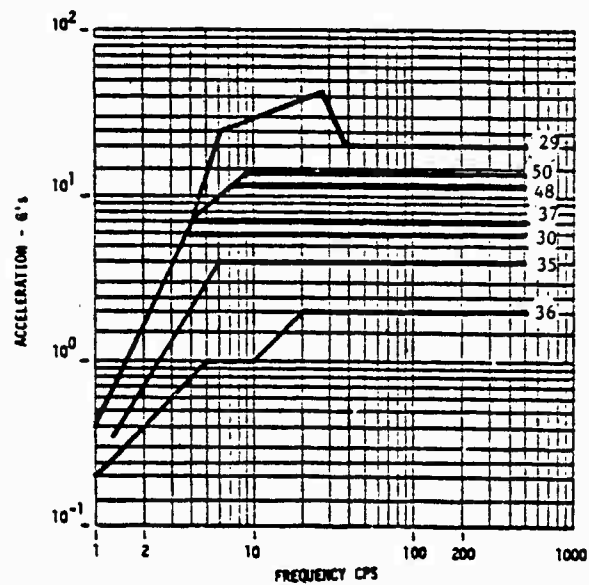
#### APPENDIX

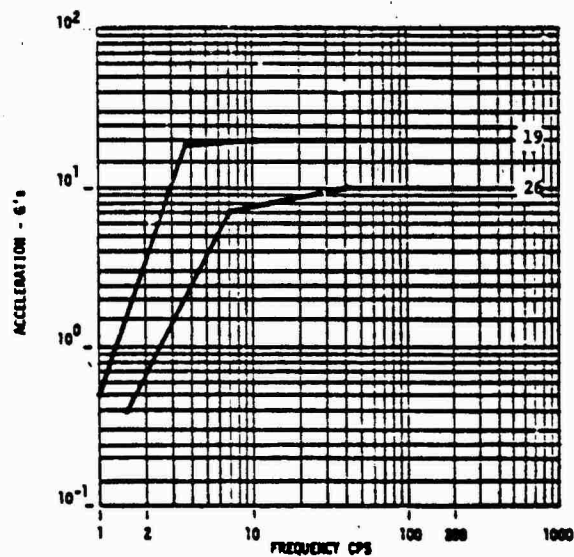
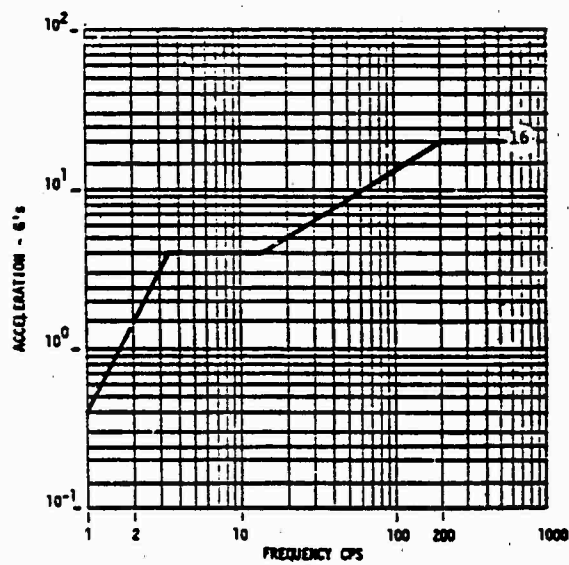


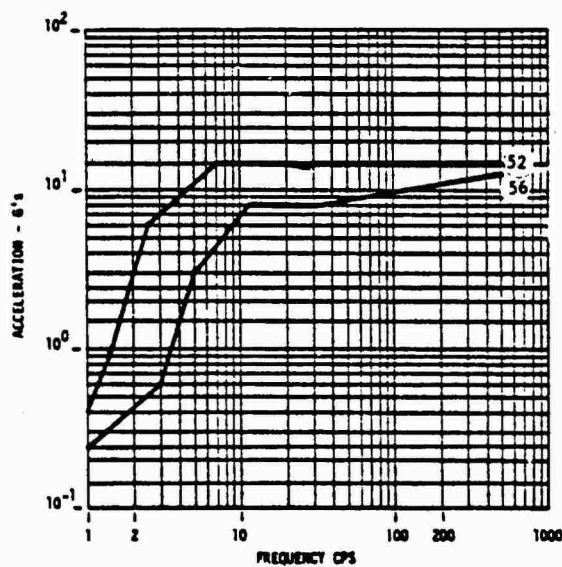
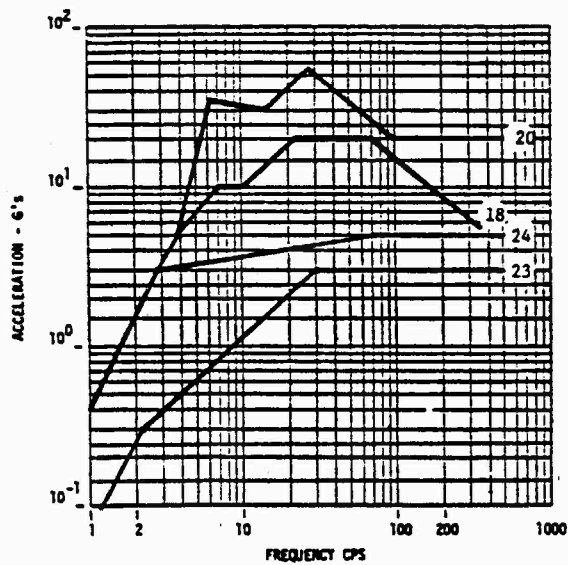




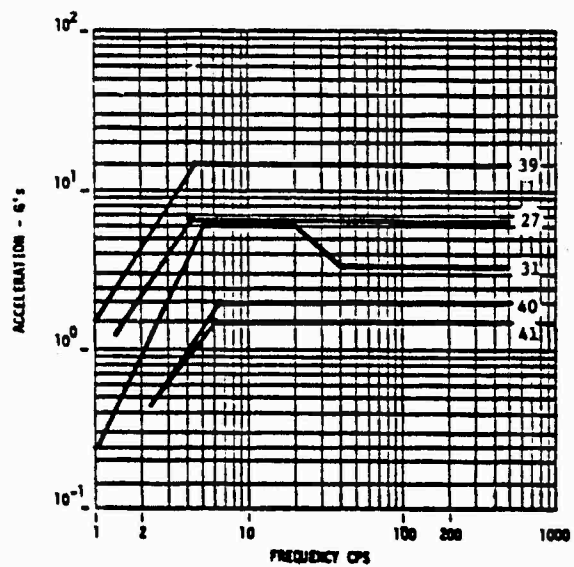
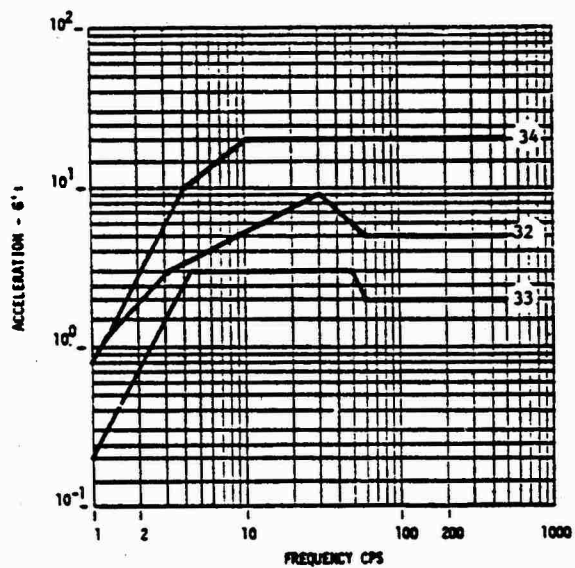


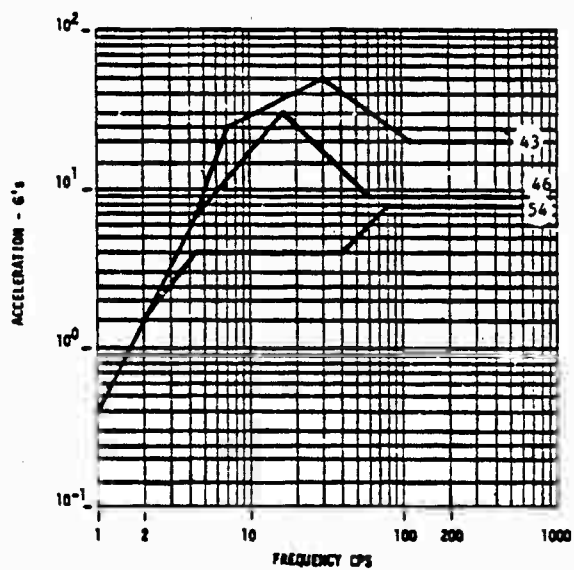
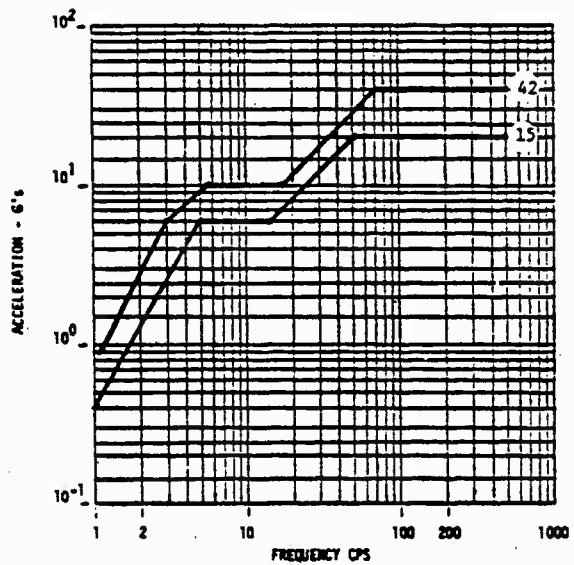


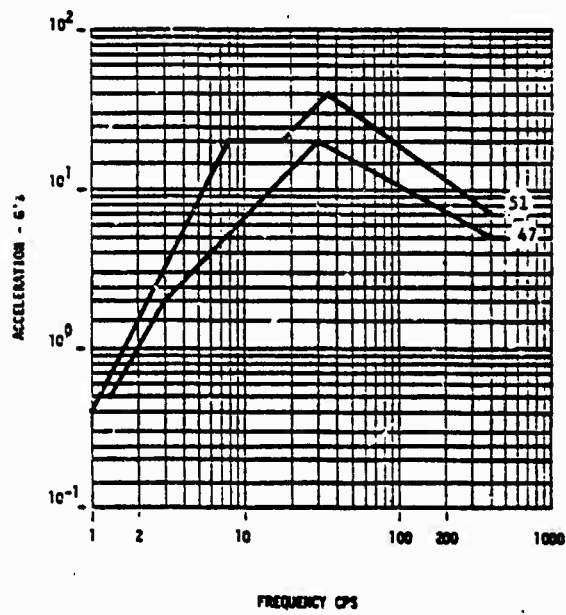
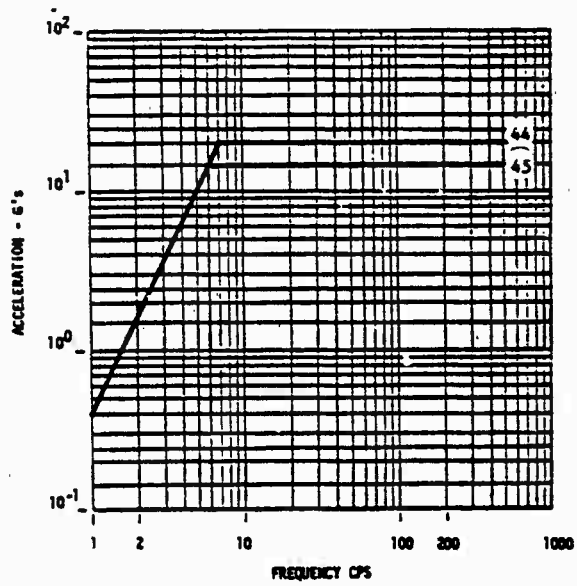












#### DISCUSSION

Voice (Army Mechanics and Materials Center):  
Did your thirty-two generic items come before  
or after you looked at their spectra?

Mr. Bradshaw: Before.

Voice: Is it possible to categorize the item  
on the basis of their shape and size?

Mr. Bradshaw: Yes. I had the benefit of the  
Safeguard program and that automatically cate-  
gorized them.

AN APPLICATION OF TUNED MASS DAMPERS TO THE SUPPRESSION OF SEVERE  
VIBRATION IN THE ROOF OF AN AIRCRAFT ENGINE TEST CELL

J.L. Goldberg, N.H. Clark and B.H. Meldrum  
CSIRO Division of Applied Physics  
Sydney, Australia 2070

Tuned mass dampers have been applied to suppress severe vibration in the concrete roof panels of a building used for testing constant speed turbo-propeller aircraft engines.

A basis for design of the dampers is described in this paper. The size and number of absorber masses and the characteristics of the spring required to effectively suppress the particular mode of the panel are determined from calculations of the modal energy using experimentally measured data.

The procedure is illustrated by examining the response of the slab situated above the propeller and subjected to the strongest excitation.

The untreated slab, of mass estimated to be in excess of 10 tonnes between wall supports, vibrates with a peak velocity amplitude of 24 mm/sec in a (3,1) mode. When treated with two absorbers of total mass 470 kg, the velocity amplitude is reduced to a safe value of 4 mm/sec in the worst region of the slab. The relevance of this reduction in satisfying vibration safety criteria is discussed.

## 1. INTRODUCTION

Both reinforced and prestressed concrete materials exhibit very low damping as shown, for example, by James *et al.* [1], and the existence of resonances in concrete structures is quite common. Two methods of increasing the structural damping have been used in civil engineering practice.

The first is an adaptation of the sandwich damping technique used in light metal aircraft structures. Grootenhius [2] has applied this technique to concrete apparently with some success, for example, in the damping of the concrete bridge deck of the suspended railway sections on the Barbican re-development site in the U.K.

The use of tuned-mass dampers is an alternative approach which involves the transfer of energy from the structure to an added mass with some energy dissipation occurring in a resilient element. Some applications of this principle have been described by McNamara [3].

This paper describes the investigation of severe vibration of the concrete roof slab of an aircraft engine test building and the application of tuned vibration absorbers to suppress the vibration.

## 2. DESCRIPTION OF THE TEST BUILDING

The test building was constructed in the early 1950s for the testing of Curtis-Wright piston engines and later Rolls-Royce Dart turbo-propeller engines. It is shown diagrammatically in Fig. 1.

The engine test space is 53 m long by 7 m wide and 7 m high. The walls originally were of brick cavity construction with an 0.22 m thick internal skin separated from an 0.11 m thick external skin by an 0.05 m cavity. Later, in order to provide for engines with increased power, such as the Allison A-14, the walls have been stiffened by filling the cavity with grout and connecting together the inner and outer walls with bolts. A very significant reduction in wall vibration was achieved this way.

The roof is of reinforced concrete slab and beam construction designed to withstand the quasi-steady pressure difference induced aerodynamically by air flow within the building.

Over the central region of the engine test space the beams at 2.74 m centres reinforce the slabs. The slabs are 0.16 m thick at the wall boundaries and increase to some 0.23 m at the centre line of the roof. Dimensions of a slab are typically 2.36 m between the beams and 7.5 m between the wall supports.

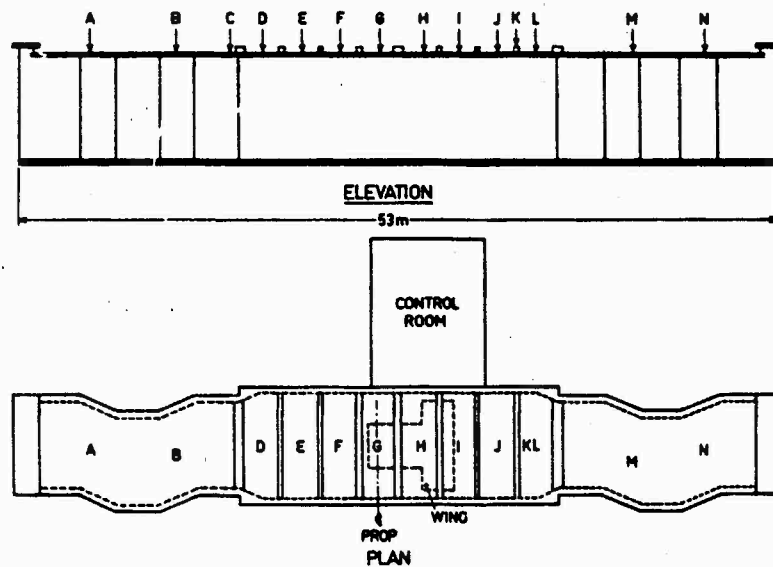


Fig. 1 - Elevation and plan of engine-test building.

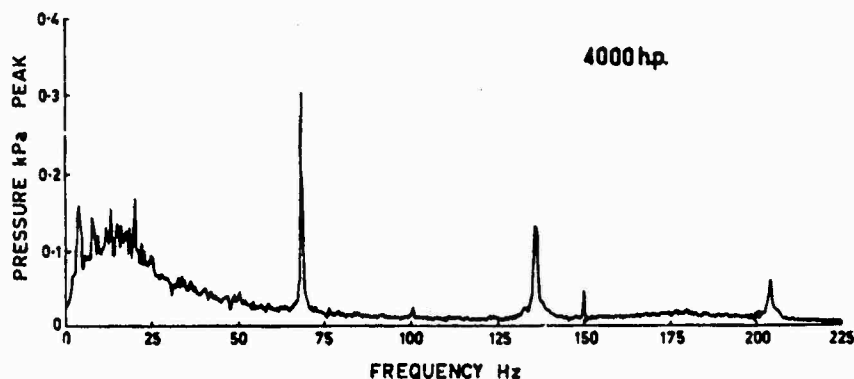


Fig. 2 - Frequency spectrum of dynamic pressure fluctuations inside building.

### 3. DYNAMIC PRESSURE AND VIBRATION MEASUREMENTS

The dynamic pressure fluctuations inside the building which are superimposed on the steady pressure have been measured and have the spectrum shown in Fig. 2.

The frequencies in the band from 0 to 25 Hz arise from turbulence and principally excite the walls of the structure. There is a strong component at 68 Hz with smaller harmonic components of this frequency which arise from the passage of a 4-bladed propeller which rotates at a constant speed of 1020 rpm. Increase in thrust is obtained by changing blade attitude.

The pressure fluctuations have been observed to increase with thrust, up to a maximum engine power of approximately 4500 h.p.

Measurement of the vibration at various positions on the roof slab directly over the propeller revealed a remarkably pure vibration mode at almost the same frequency as that of the propeller blade passage. The measured shape of this mode in the long and short directions of the slab is shown in Fig. 3. At the antinodes a very high velocity amplitude of 24 mm/sec was observed at 4000 h.p. Adjacent slabs showed a similar modal behavior but the velocity amplitude was not as great.

#### 4. VIBRATION CONTROL BY VIBRATION ABSORBER

The method of treatment involves placing damped vibration absorbers at some of the positions of maximum kinetic energy,  $G_1$ ,  $G_2$ ,  $G_3$  of Fig. 3. The mode can then be effectively suppressed if a significant part of the modal energy is transferred from the roof slab to the absorber masses and the remainder dissipated in the springs.

#### 5. EFFECTIVE MASS OF THE SLAB

The estimation of the energy transfer from slab to absorber requires a knowledge of the effective mass of the slab.

In Fig. 3 which refers to slab G of Fig. 1, if  $2a$  is the length and  $2b$  the width of the slab, the modal velocity  $v$  at angular frequency  $\omega$  of any point  $(x,y)$  is

$$v(x,y,t) = v_0 \cos \frac{3\pi x}{2a} \cos \frac{\pi y}{2b} \cos \omega t$$

where  $v_0$  is the maximum velocity amplitude. The mode shape is expressed in terms of velocity since this is the appropriate quantity when discussing potential levels for damage [6]. If  $\rho$  is the mass per unit area, here assumed to be constant, the total kinetic energy  $E$  averaged over one cycle of oscillation is

$$\begin{aligned} E &= \frac{1}{\pi} \int_0^\pi \int_{-b}^{+b} \int_{-a}^{+a} \frac{1}{2} \rho v^2 dx dy d(\omega t) \\ &= \frac{1}{32} \rho v_0^2 2a 2b \\ &= \frac{1}{2} \left( \frac{M}{16} \right) v_0^2 \end{aligned} \quad (1)$$

which shows that in terms of average kinetic energy per cycle, the effective mass  $M_e$  of the slab is 1/16 that of the actual mass  $M$ .

#### 6. ENERGY EQUATIONS

Let it be assumed that the mass, stiffness and damping characteristics of all absorbers are identical and that the masses move rectilinearly. The problem is then reduced to that of applying the well-known two-degree of freedom mass-spring system (Fig. 4).

If  $\alpha$  is the complex displacement amplitude of the main mass  $M_e$  and  $\beta$  is that of the absorber mass  $M_a$ , then at any excitation frequency  $\omega$ , the energy of the main mass expressed as a fraction  $R$  of the total energy of the system is

$$R = \frac{\frac{1}{2} M_e |\alpha|^2 \omega^2}{\frac{1}{2} M_e |\alpha|^2 \omega^2 + \frac{1}{2} M_a |\beta|^2 \omega^2 + 2s\zeta M_a |\beta - \alpha|^2 \omega^2}$$

where the third term of the denominator is the energy absorbed per cycle in springs of damping ratio  $\zeta$ . The energy loss is assumed for simplicity, to be the result of viscous damping. If  $\mu = M_a/M_e$ , is the mass ratio then

$$R = \frac{|\alpha|^2}{|\alpha|^2 + \mu [ |\beta|^2 + 4\zeta |\beta - \alpha|^2 ]} \quad (2)$$

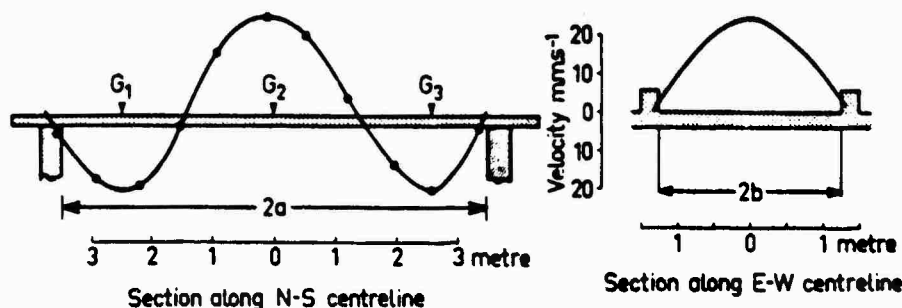


Fig. 3 - Mode shape of concrete roof slab showing nomenclature.

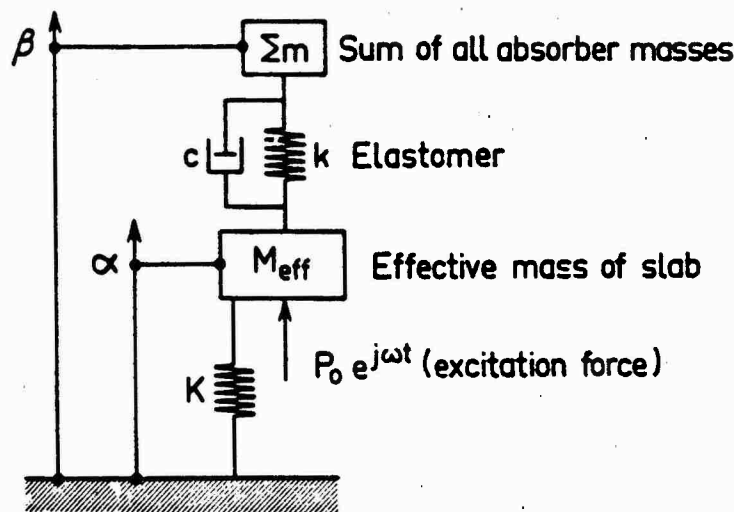


Fig. 4 - Two-degree of freedom mechanical system characterizing slab-absorber interaction.

According to Den Hartog [4]  $\alpha$  and  $\beta$  may be expressed in the following dimensionless forms:

$$\frac{\alpha}{\alpha_{\text{stat}}} = \frac{(\zeta^2 - q^2) + j 2 \zeta q}{[(q^2 - 1)(q^2 - \zeta^2) - \mu \zeta^2 q^2] + j 2 \zeta q [1 - q^2 - \mu q^2]} \quad (3)$$

$$\frac{\beta}{\alpha_{\text{stat}}} = \frac{\zeta^2 + j 2 \zeta q}{[(q^2 - 1)(q^2 - \zeta^2) - \mu \zeta^2 q^2] + j 2 \zeta q [1 - q^2 - \mu q^2]} \quad (4)$$

where  $f = \omega_s / \omega_n$

$q = \omega / \omega_n$

$\zeta = c / c_c$

$\omega_s$  = natural frequency of absorber system

$\omega_n$  = natural frequency of slab in the mode being suppressed

$\omega$  = excitation frequency

$\alpha_{\text{stat}} = P_0 / K$ ,  $P_0$  being the amplitude of the exciting force and  $K$  the spring constant of the slab.

Using Eqs. (3) and (4), Eq. (2) may be written

$$R = \frac{(\zeta^2 - q^2) + (2\zeta q)^2}{(\zeta^2 - q^2) + (2\zeta q)^2 + \mu [\zeta^4 + (2\zeta q)^2 + 4\zeta^2 q^2]}$$

Two sets of curves derived from Eq. (5) are shown in Fig. 5. Each curve set shows the energy ratio  $R$  as a function of the frequency ratio  $f$  for a specified mass ratio, and with  $q=1.02$  (approximately constant in this application). The three curves of each set show the effect of varying the damping ratio  $\zeta$ . Comparison of the curves indicates that if the effective mass of the slab is the same as the sum of the absorber masses, the slab energy is more effectively transferred than if the absorber mass ratio  $\mu$  is small. Also, for an absorber mass ratio of unity, the effect of the tuning frequency ratio on energy transfer is less critical for the values of damping ratio  $\zeta$  likely to be encountered with practical elastomeric materials. This is important in applications where the effects of temperature on tuning drift must be minimized.

## 7. VELOCITY OF ABSORBER MASS

An approximate but useful expression for absorber velocity can be obtained from energy balance considerations when the system is tuned.

If  $v_0$  is the slab velocity before treatment and  $\bar{v}_0$  the absorber mass velocity for a correctly tuned absorber, then approximately

$$\frac{1}{2} M_s v_0^2 = \frac{1}{2} M_a \bar{v}_0^2 + 2 \zeta M_a \bar{v}_r^2$$

where  $\bar{v}_r$  is the relative velocity between the absorber and slab masses.

At balance  $\bar{v}_r = \bar{v}_0$  and

$$\bar{v}_0 = v_0 \sqrt{\frac{M_s}{M_a (1 + 4\zeta^2)}} \quad (6)$$



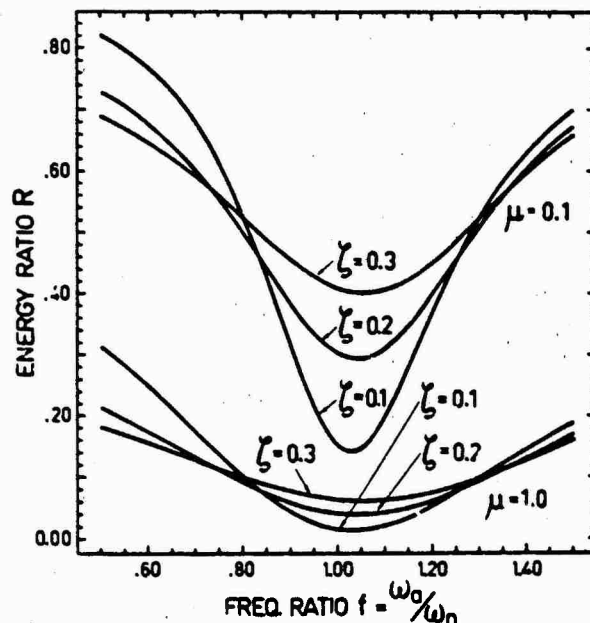


Fig. 5 - Energy ratio  $R$  as a function of the ratio of the natural frequencies of absorber and slab for different mass and damping ratios.

Expression (6) can be used to check that the velocity of the absorber mass corresponds, at the proper tuning frequency to an acceleration of less than 1 g. If the acceleration exceeds 1 g, an absorber mass system that depends on gravity constraint can chatter on its supports and this is unacceptable in practice.

If  $I_m = M_0$  and  $\zeta = 0.1$ , the velocity of the absorber masses becomes

$$V_0 = 0.66 v_0.$$

If  $v_0 = 24$  mm/sec then  $V_0 = 15$  mm/sec for the absorber masses; this corresponds to an acceleration of 0.65 g at 68 Hz, an acceptable value.

#### 8. CHOICE OF DAMPING FACTOR

It should be noted here that some authors, for example, Den Hartog [4] and Snowdon [5] have shown that the damping factor is critically related to tuning frequency ratio and mass ratio for optimum performance. However, in the practical case considered here this critical choice of damping factor is not only difficult to arrange in a spring, but also it is not necessary. The only criterion used here for choosing  $\zeta$  is that it should be large enough to permit an adequate energy loss without excessive mass and to accommodate possible thermal drift in the tuning frequency.

It has been seen that if  $I_m = M_0$ , a very

effective energy transfer takes place with convenient values of  $\zeta$ , say 0.1 which can be readily obtained with rubber elastomers.

The high value of absorber mass permits a relatively large area of ribbed rubber to be used as described in the next section and constitutes a convenient coupling to the slab mass.

#### 9. DESIGN OF THE RUBBER SPRINGS

The estimated slab mass  $M$  is 9080 kg so that the effective mass  $M_0$  is 568 kg. Suppose  $I_m$  is nominally 500 kg, which makes the mass ratio about unity. The mass is conveniently divided into two masses of nominal value 250 kg each, which can be positioned on two adjacent antinodal areas of the slab. The final value of mass used differs slightly from the nominal value as a result of experimental tuning adjustments carried out on the roof while the engine was running. The springs consist of pads of commercially available ribbed neoprene material between machined steel discs. The use of these pads enables the springs to be designed on a simple area basis once the dynamic properties of the rubber are known.

The static load-deflection characteristic of a sample of the material was found by loading it in a spring-testing machine and measuring the deflection with a dial indicator. Usually the procedure then is to estimate, from the slope of the load deflection curve at

If the above procedure is followed for a number of amplitudes at any one loading, an interesting phenomenon is observed. Although the static characteristic shows that the spring is stiffer for larger deflections (a hardening spring), under dynamic conditions the apparent stiffness is less for larger displacement amplitudes. Hence we have effectively a softening spring, and this result arises directly from the hysteresis.

We should therefore expect the frequency of resonance to vary inversely with the response amplitude, and this expectation was proven correct in the following test. To obtain a better estimate of resonance frequency, small samples were loaded with a measured mass and shaken on an electromagnetic vibration exciter.

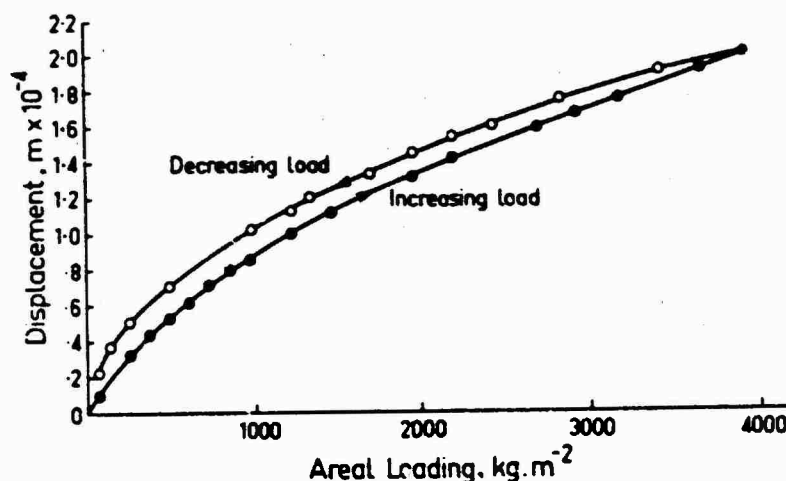


Fig. 6 - Static load deflection curve of ribbed rubber pad

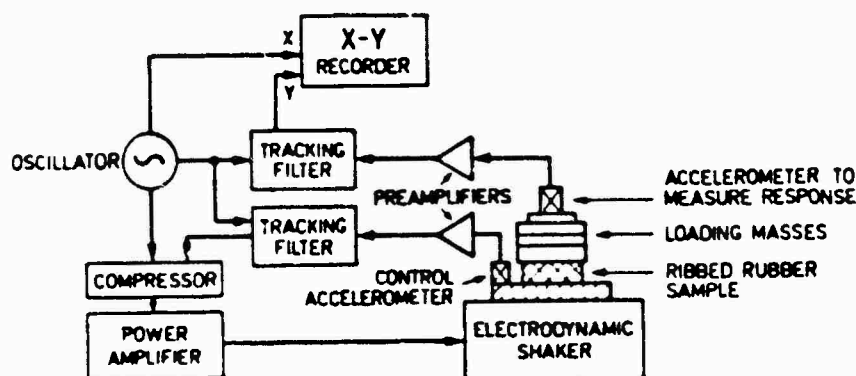


Fig. 7 - Test set-up to determine dynamic properties of ribbed rubber pad.

With the amplitude of excitation kept constant, the excitation frequency was swept, and the amplitude of response at the top of the loading mass was recorded as a function of frequency. The test setup is shown diagrammatically in Fig. 7 and typical response curves for various mass loadings are shown in Fig. 8.

From the 'Q' of the response curves the damping was estimated to be equivalent to approximately 0.1 of critical. The actual frequency of resonance (Fig. 8) is seen to decrease with increase in response amplitude, as predicted. Moreover, a settling effect was noticed; that is, when the load was first applied, the frequency of resonance was lower than the final steady value, probably indicating that the effective contact area was initially less.

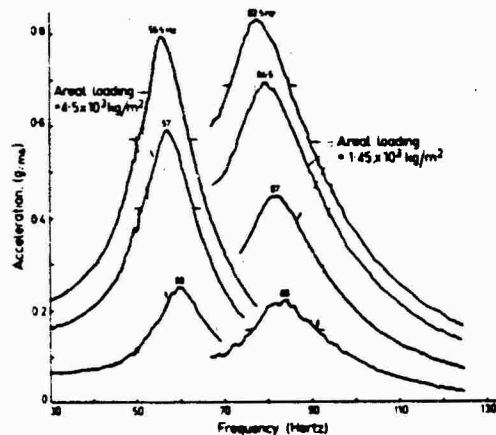


Fig. 8 - Typical response curves for various mass loadings.

The resonance frequency required for the dynamic absorber was 68 Hz. From the test results summarized in Fig. 9 it was deduced that this frequency would be obtained with an areal loading of about 2500 to 3000  $\text{kg.m}^{-2}$ .

In the final design the loading is 2700  $\text{kg.m}^{-2}$ . The total mass of 235 kg is made up of 8 concrete discs as shown in Fig. 10, and the actual area of rubber per spring is 0.013m. To ensure uniform loading, heavy machined steel discs are cemented to the upper and lower faces of each spring pad. The assembly is circular in plan view. A conical recess in the upper steel disc carries a steel ball, which locates in a similar seating under the lower concrete disc. The details and dimensions are shown in Fig. 10. The lower steel disc of each spring assembly is cemented to the upper surface of the concrete roof slab, and the three assemblies are symmetrically arranged over an antinode of the roof mode which is to be suppressed.

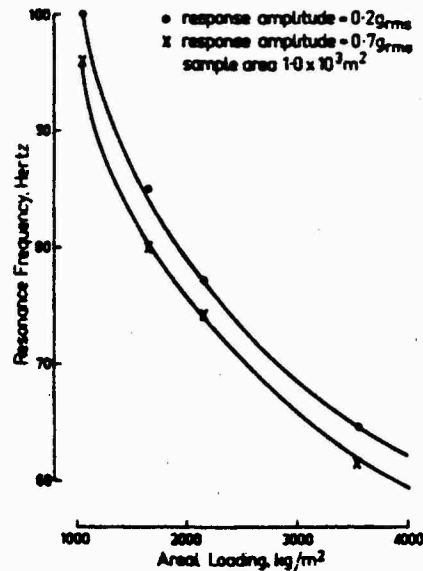


Fig. 9 - Resonance frequency versus loading curves for estimation of operating zone.

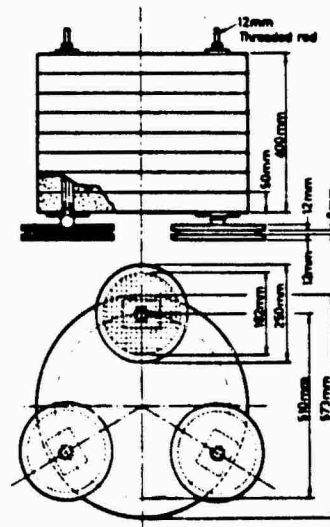


Fig.10 - Details of assembled absorber.

## 10. TESTING AND TUNING THE ABSORBER

An assembled absorber was first tested in the laboratory, on a very massive basement floor. Excitation was by a reaction shaker placed on the top of the absorber mass, with other instrumentation similar to that shown in Fig. 7. The absorber response, for a constant amplitude of excitation force, shows a slight hump at a frequency close to the vertical resonance frequency (Fig. 11). The hump was observed to be due to a coupled rocking mode, which in the final installation contributes to the damping of the roof vibration. Rocking occurs in practice because the vibration levels under the three springs are unlikely to be identical in amplitude. The absorber was tuned in situ on the roof by adding mass in increments of approximately 30 kg until the velocity amplitude of the slab was minimised.

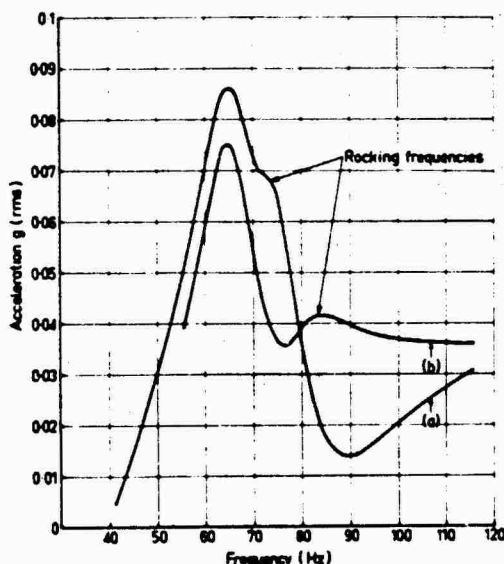


Fig. 11 - Frequency response of assembled absorber showing rocking frequencies for (a) nominally central and (b) highly eccentric excitation.

## 11. INSTRUMENTATION

The vibration survey of the test cell roof was carried out with six accelerometers. Inside the cell a piezo-electric transducer was used to monitor pressure fluctuations. The instrumentation system consisted of these transducers together with filter amplifiers, a high-speed chart recorder and a multi-channel instrumentation tape recorder.

The chart record indicated instantaneous values of acceleration and relative phase at each measuring point enabling mode shapes to be identified. Taped records were subsequently analysed for frequency and average velocity values using a real-time analyser.

## 12. THE EFFECTIVENESS OF MODE SUPPRESSION IN TERMS OF DAMAGE CRITERIA

Damage criteria are quantified in the Draft Document DP4866 [1975], of the International Organisation for Standardisation (ISO) [6]. This document sets out certain velocity ranges for concrete slabs which correspond to certain risks of damage. These ranges are illustrated in Fig. 12.

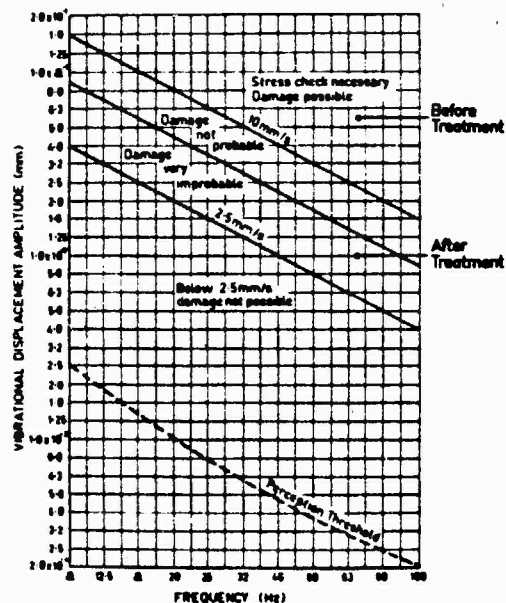


Fig. 12 - Graphical presentation of ISO damage criteria.

The degree of mode suppression achieved for slab G is shown in Fig. 13. With one absorber placed on the antinodal position nearest the north edge, partial suppression is obtained; the central antinode does not respond as dramatically as the outer ones because the kinetic energy of the slab is not uniformly distributed over the slab length; it will be recalled from section (1) that the slab tapers in depth from the centre to the edges in the direction of its longest dimension.

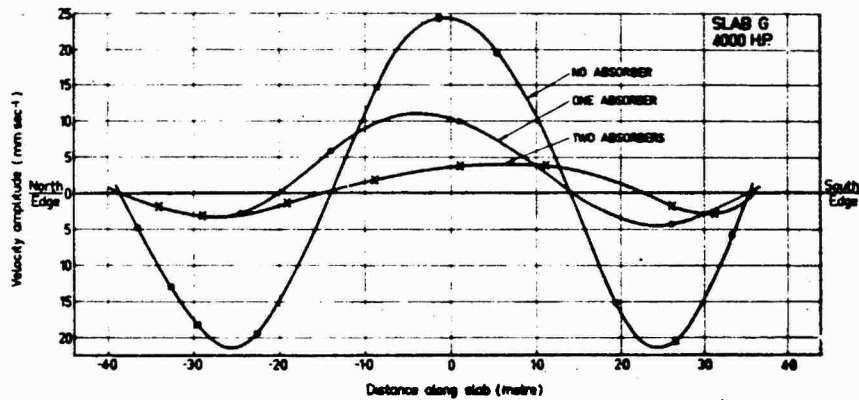


Fig. 13 - Mode suppression using one and two absorbers.

With two absorbers in position, however, there is no point on the slab which has a velocity amplitude higher than 4 mm/sec.

This final value and the unsuppressed value of modal velocity are displayed on the

graph of Fig. 12. In terms of the ISO criteria the degree of suppression achieved is seen to be adequate. Fig. 14 shows the absorbers mounted on the roof of the test building at Sydney airport.

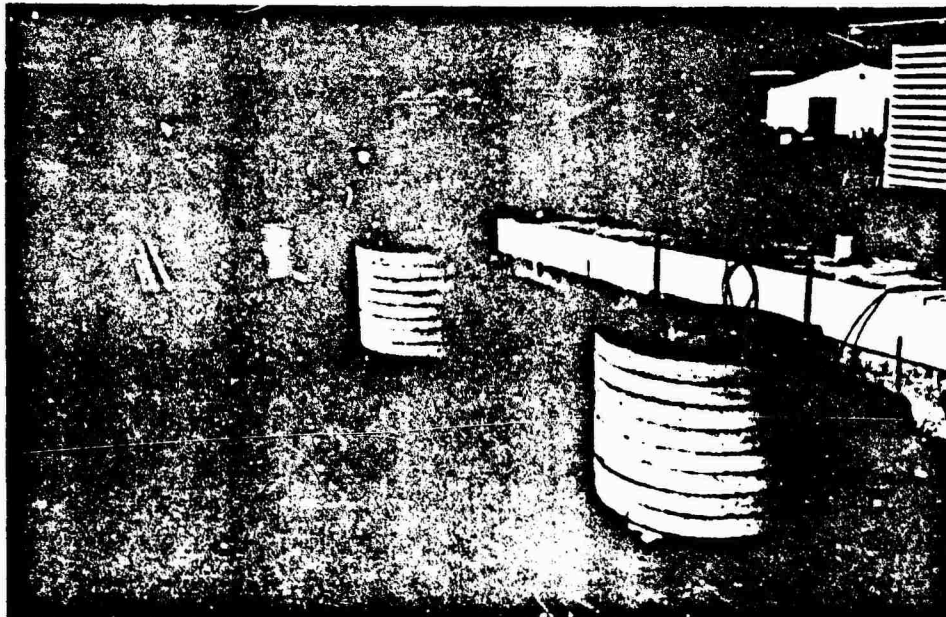


Fig. 14 - Photograph of absorbers mounted on roof of engine test building.

#### ACKNOWLEDGEMENTS

The authors would like to thank QANTAS Airways Ltd for practical help in completing this project. The assistance of K.M. O'Toole and P. Drew of this Laboratory is gratefully acknowledged.

#### REFERENCES

1. M.L. James, *et al.* "Dynamic Properties of Reinforced and Prestressed Concrete Structural Components".  
J. Amer. Concrete Inst. Vol. 61, No. 11,  
pp. 1359-1381, Nov. 1964.
2. P. Grootenhuys, "Sandwich Damping Treatment Applied to Concrete Structures".  
Phil. Trans. Royal Soc. Lond., Vol. 263 A.  
pp. 455-459, 1968.
3. R.J. McNamara, "Tuned Mass Dampers for Buildings".  
Proc. Amer. Soc. Civil Engrs, J. Structural  
Div. 103, No. ST9, pp. 1785-1798,  
Sep. 1977.
4. J.P. Den Hartog, Mechanical Vibrations,  
4th Ed. p. 93, McGraw Hill, New York, 1956.
5. J.C. Snowdon, Vibration and Shock in  
Damped Mechanical Systems. John Wiley,  
New York, 1968.
6. International Organisation for Standard-  
isation (ISO) Draft Proposal DP4866.  
Evaluation and Measurement of Vibration in  
Buildings, Sep. 1975.

## COMPARISON OF ANALYTICAL AND EXPERIMENTAL RESULTS FOR A SEMI-ACTIVE VIBRATION ISOLATOR

E. J. Krausnicki  
Lord Kinematics  
Erie, Pennsylvania

A single degree of freedom system employing an active damper, used as a semi-active vibration isolation device, has been successfully reduced to practice. A laboratory prototype has been fabricated and tested, and the test results of the active damper performance, subject to both sinusoidal and random vibrational input, will be discussed and compared to recent analytical simulations.

### INTRODUCTION

The concept of semi-active vibration isolation using the active damper was developed by M. Crosby of Lord Corporation and D. Karnopp of the University of California. The concept was patented (U.S. Patent No. 3,807,678) on April 30, 1974, with Lord Corporation being the assignee. The technical paper, "Vibration Control Using Semi-Active Force Generators", (ASME Paper No. 73-DET-122) June 6, 1973 [1], provides a detailed explanation of the active damper concept, its history, operation, and some potential hardware configurations.

Basically, the active damper can provide improved vibration and shock isolation, approaching that of a fully active system, by controlling the damping characteristics of a viscous damper independent of the relative velocity across the damper. The active damper is intended to be used in conjunction with passive vibration and shock isolators. In general, an active system is costly, complex, and requires an external power source. In contrast, the active damper requires no hydraulic power supply, only low level electrical power is needed for signal processing and valve actuation, and the implementation of its hardware is significantly simpler and less costly than a fully active system.

An active damper prototype using hydraulic fluid damping was assembled and tested at Lord Corporation in 1972. The design utilized standard industrial components in a breadboard configuration. This device demonstrated the feasibility of an empirical active damper. Its overall performance was significantly better than the results obtainable by a conventional system with sufficient damping to effectively damp the resonance. However, the experimental results did illustrate a compromise in high frequency performance due to several physical phenomena such as friction, slow response, etc.

The purpose of this paper is to demonstrate that a single degree of freedom system employing an active damper used as a semi-active vibration isolation device has been successfully reduced to practice. A laboratory prototype has been fabricated and tested, and the test results of the active damper performance, subject to both sinusoidal and random vibrational input, will be presented and compared to recent analytical simulations.

### CONVENTIONAL AND SKYHOOK DAMPER SYSTEMS

The conventional vibration control system discussed here is illustrated in Fig. 1a. It consists of a viscously damped, single degree of freedom vibration system excited by an oscillating motion of the base. The mass  $m$  simulates the mounted body, and the isolator is represented by the combination of a spring with constant  $k$ , and a damper with a constant  $b$ .

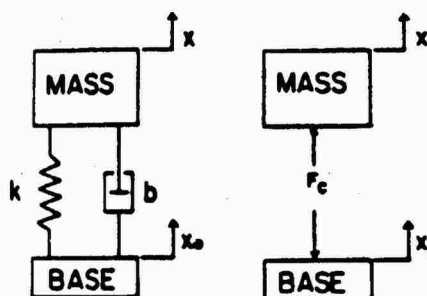


Figure 1  
a. Passive conventional vibration isolation system  
b. General isolation system,  $F_c$  may be generated by passive, active, or semi-active means.

The differential equation of motion for the mounted body in this conventional, passive, linear system is given by the following expression:

$$m\ddot{x} = -b(\dot{x} - \dot{x}_0) - k(x - x_0) \quad (1)$$

where compression of the damper and spring are defined as positive forces, illustrated in Fig. 1b. Only the equation parameters  $b$  and  $k$  can be varied to optimize the performance of this conventional passive system. If minimization of the relative displacement between the mass and the base  $x - x_0$  is desired, the suspension should be stiff. If minimization of the absolute displacement of the mass  $x$  is desired, a very soft suspension should be used at frequencies greater than  $\sqrt{2}$  times the undamped natural frequency.

The parameters  $b$  and  $k$  may be varied to obtain an optimized system delivering the desired performance throughout the required frequency range. This optimized passive suspension system will provide adequate system isolation in many situations. But many applications do exist where the desired combination of limited amplification at resonance and excellent high frequency isolation cannot be met with a passive system.

## INERTIAL REFERENCE

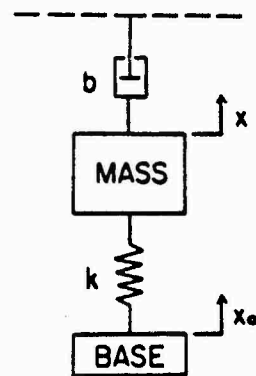


Figure 2  
The skyhook damper configuration

The "skyhook damper" system, illustrated in Fig. 2, can be constructed with passive elements and is represented by the following expression:

$$m\ddot{x} = -k(x - x_0) - b\dot{x} \quad (2)$$

The damper force is proportional to the absolute mass velocity  $\dot{x}$ , present across the damper connecting the suspended mass with the inertial reference. The implementation of this skyhook configuration is possible only in a limited number of applications. Vehicle suspension systems is just one category where it is not possible to use a skyhook damping scheme.

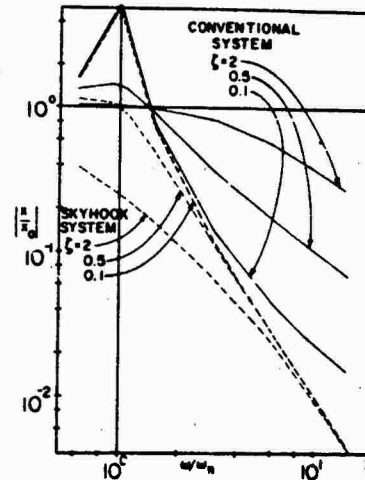


Figure 3  
Comparison of conventional and skyhook damping systems subject to sinusoidal base excitation.

In both the conventional and the skyhook damping systems, the value of the spring constant  $k$  determines the natural frequency  $\omega_n$  of the suspension, where  $\omega_n = (k/m)^{1/2}$ . The small relative displacements between the mass and base, observed at low frequencies below the natural frequency, are determined by the spring. In the vicinity of the natural frequency, the resonance of the system is controlled by the damper for both suspension systems. The major difference between these two dynamic systems becomes evident with changes in the damping parameter. Near the resonant frequency, an increase in the damping constant will decrease the mass response of both the skyhook configuration and the conventional system. An increase in the damping constant will slightly decrease the system response at high frequencies in the skyhook system, but will increase the high frequency system response (degrade isolation) in the conventional system. This difference is due to the fact that only the relative velocity between mass and base is reduced by the forces exerted in a conventional damper system, whereas the absolute velocity of the mass is reduced by the forces developed in the skyhook system. Therefore, an active system simulating a skyhook damper will provide superior performance at all frequencies, when compared with a conventional passive damper system which tends to stiffen the suspension at high frequencies, where a soft suspension is desired.

The damping ratio  $\zeta$  is defined as the ratio of the actual damping constant  $c$  to the critical damping constant  $c_c$ . The damping ratio may also be described by the following expression:

$$\zeta = \frac{b}{2(km)^{1/2}}$$



Fig. 3 illustrates transmissibility plots<sup>1</sup> of both conventional and skyhook damping systems for various values of the damping ratio  $\zeta$ .

Fig. 1b is a more general representation of the isolation suspension. The direction of the vectors illustrated are defined as positive for equation derivation purposes. The control force,  $F_c$ , represents the force generated by a combination of passive element, the actuator of an active system, or the active damper suspension system discussed in this paper.

The relationship between mass and base motion for the suspension systems discussed above apply only to linear systems. It is reasonable to assume that the comparison of non-linear passive and active suspensions would demonstrate the same qualitative effects.

#### THE ACTIVE DAMPER

The active damper is essentially a passive device, but capable of externally controlling the force across the damper, independently of the relative velocity across the damper. The varying damper force is generated by modulating the damping coefficient through modification of the damping orifice. The bandwidth of the orifice modulating device is high enough to allow drastic adjustments of  $F_c$  during a single cycle of vibration. If this active damper is substituted into the conventional isolation system configuration, the capability now exists to generate the skyhook damping force  $b\dot{x}$ , according to the control law given in Equation 2. This force can only be generated if the sign of the relative velocity is proper in relation to the absolute velocity, since no external power is supplied to the system. A schematic of the active damper used in a conventional configuration, forming a semi-active isolation system, is illustrated in Fig. 4.

The major difference between the active damper and a fully active system, both utilizing the skyhook control theory of Equation 2, can be seen in the following description. The fully active system can be described as one in which the

<sup>1</sup>The term transmissibility will be used for both linear and non-linear systems discussed here. For the active damper system the term is meaningful, but since its response is not linear, the normal implications associated with the transmissibility of a linear system do not hold for the active damper. For instance,  $|x/x_0| = |\dot{x}/\dot{x}_0| = |\ddot{x}/\ddot{x}_0|$  holds only for linear systems subject to harmonic excitation. Also, one cannot predict the exact response of the active damper subject to multiple sine wave or random inputs from the response predicted by single sine wave input. The point at which the device switches states changes with the amplitude and phase variations of a random input signal.

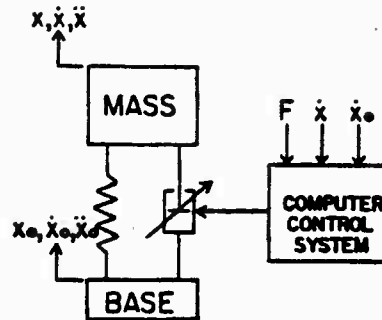


Figure 4  
An active damper isolation system

force  $F_c$  in Fig. 1b is generated by an actuator, powered by an external power source, and modulated by an adequate force-controlling device. This controlled actuator is a servomechanism that is capable of supplying or absorbing energy necessary to generate the skyhook damper force  $F_c$ , at all times, based on the control law given in Equation 2.

The active damper, being a passive device, is capable of generating a force  $F$ , where the power associated with  $F$  is always dissipated, as represented in the following equations:

$$F \cdot (\dot{x} - \dot{x}_0) \leq 0 \quad (3)$$

The desired value of the active damper force  $F$  is  $b\dot{x}$ , but because no external power is supplied to the active damper system, this force can only dissipate power; therefore, the following relationship exists.

$$F = F_d = b\dot{x}, \text{ if } \dot{x}(\dot{x} - \dot{x}_0) > 0 \quad (4)$$

When the situation exists where  $\dot{x}$  and  $(\dot{x} - \dot{x}_0)$  are of opposite sign, the active damper can only supply a force opposite to the desired force  $F_d$ . In this case, the best the active damper can do to approximate the desired force is to produce no force at all; therefore,

$$F = 0, \text{ if } \dot{x}(\dot{x} - \dot{x}_0) < 0 \quad (5)$$

The condition where the expression  $\dot{x}(\dot{x} - \dot{x}_0) = 0$  creates two special cases for the active damper. The first is if  $\dot{x} = 0$  then the desired force  $F_d = 0$ . The second case exists where  $(\dot{x} - \dot{x}_0) = 0$  and  $\dot{x} \neq 0$ . Here the active damper responds by attempting to generate the desired force  $F_d$ . If the quantities  $\dot{x}$  and  $(\dot{x} - \dot{x}_0)$  change so the criteria of equations 4 or 5 apply, normal control continues. If the desired force  $b\dot{x}$  is larger than the maximum available damper force, the active damper will lock up the

system resulting in  $(\dot{x}-\dot{x}_0) = 0$  for a finite time. During the lock up state the damper force is:

$$F = m\ddot{x}_0 + k(x-x_0) \quad (6)$$

Thus, the two conditions that must exist for the active damper to lock up are  $(\dot{x}-\dot{x}_0) = 0$  and the desired force  $F_d$  is larger in magnitude than the force determined in Equation 6. Therefore, three possible values of the damper force  $F$  exist: 1) the desired force  $F_d$ ; 2) zero force; or 3) the lock up force. Switching between the three possible force values is determined by the base input and resultant system response. This switching of states makes the active damper, programmed to simulate a skyhook damper, a non-linear element.

#### COMPARISON OF ANALYTICAL AND EXPERIMENTAL PERFORMANCE RESULTS FOR THE ACTIVE DAMPER

A new single degree of freedom, semi-active isolation system utilizing an active damper was developed and tested at Lord Corporation in 1970. The active damper consists of a hydraulic actuator used in conjunction with an electro-hydraulic servovalve modulating the controlling orifice area. The mass-spring-active damper test system consisted of a 213.6 kg (471 lbs.) mass resulting in an undamped natural frequency of 1.631 Hz measured at the point of a  $-180^\circ$  phase shift between base and mass displacement. The sensor signal processing and control of the electro-hydraulic servovalve were carried out with digital computer techniques. The performance testing of the active damper, using both sinusoidal and random vibration input, were conducted in a M.T.S. test machine. Transmissibility and signal/waveform data for sinusoidal base input were reduced from strip chart recordings. Random vibrational response was analyzed using a Hewlett-Packard 5420A digital signal analyzer.

Digital computer simulations were carried out duplicating the sinusoidal results obtained in reference [1]. This referred paper illustrates time history plots of mass and base displacement, velocity, acceleration, and damper force, as well as transmissibility plots comparing passive, skyhook, and semi-active systems for various damping values. These results were reproduced and will not be repeated here. But it is worth noting that the output time history plots generated by the nonlinear active damper do resemble those of a linear system as frequency increases. The computer model used in this study was modified to account for the non-ideal effects of Coulomb friction in the damper and the physical limitations of a maximum orifice opening. The following computer simulations were conducted with only sinusoidal vibration input.

All experimental and computer simulation transmissibility results were generated with the sinusoidal input frequencies and single amplitude displacements listed in Table I, for the purpose of consistency in dealing with nonlinear systems.

TABLE I

#### BASE INPUT FOR SINUSOIDAL PERFORMANCE TESTS OF THE ACTIVE DAMPER SYSTEM

Frequency Hz	Displacement $\pm$ m (in.)
1.0	$9.54 \times 10^{-3}$ ( $3.13 \times 10^{-2}$ )
1.2	$9.54 \times 10^{-3}$ ( $3.13 \times 10^{-2}$ )
1.4	$9.54 \times 10^{-3}$ ( $3.13 \times 10^{-2}$ )
1.5	$9.54 \times 10^{-3}$ ( $3.13 \times 10^{-2}$ )
1.631 $\omega_n$	$9.54 \times 10^{-3}$ ( $3.13 \times 10^{-2}$ )
1.8	$9.54 \times 10^{-3}$ ( $3.13 \times 10^{-2}$ )
2.0	$9.54 \times 10^{-3}$ ( $3.13 \times 10^{-2}$ )
2.5	$9.54 \times 10^{-3}$ ( $3.13 \times 10^{-2}$ )
3.0	$9.54 \times 10^{-3}$ ( $3.13 \times 10^{-2}$ )
5.0	$9.54 \times 10^{-3}$ ( $3.13 \times 10^{-2}$ )
7.0	$5.09 \times 10^{-3}$ ( $1.67 \times 10^{-2}$ )
10.0	$3.81 \times 10^{-3}$ ( $1.25 \times 10^{-2}$ )
15.0	$1.92 \times 10^{-3}$ ( $.63 \times 10^{-2}$ )

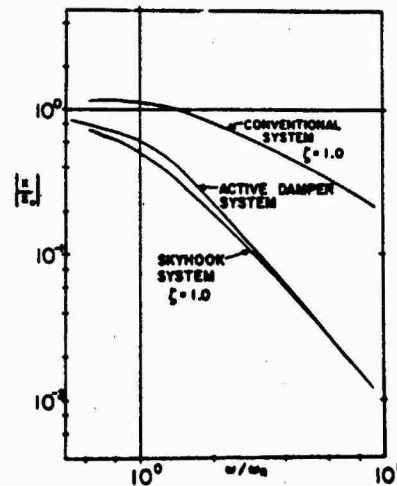


Figure 5

Comparison of the theoretical response of a critically damped skyhook system, a conventional isolation system and an active damper system.

Figure 5 compares the analytically predicted results of a critically damped passive conventional system, a critically damped skyhook system, and a conventional system utilizing an active damper simulating a critically damped skyhook system, subject to sinusoidal base excitation. The superior isolation performance of the active damper system is readily apparent in both the resonant and the high frequency regions. A comparison of the active damper and the theoretical skyhook damper reveals how closely the nonlinear active damper approaches the performance of the skyhook damper system.

In order to make the analytical model of the active damper more closely represent the actual hardware system, the non-ideal effects of Coulomb friction and a maximum orifice opening were included. Fig. 6 represents the theoretical performance of an ideal active damper, an active damper including only Coulomb friction, and a system with both Coulomb friction and a limited orifice opening. The Coulomb friction of the actual hardware was measured and a representative figure of 3.37N. (15 lbs.) was used in the analysis. The maximum orifice size used in the analysis was also representative of the actual hardware system. The most obvious effect of the addition of friction is the damper break-loose condition that exists in the vicinity of 5 Hz. This condition, discussed in reference [2], occurs when the resultant external force acting on the damper equals the dry friction force. Below this point, the displacement transmissibility is maintained at 1.0. In the absence of dry friction, the active damper provides system isolation even at extremely low input frequencies. The addition of friction does degrade system performance throughout the entire frequency range tested. The physical limitation of a maximum orifice opening has little effect at low frequencies, but performance does degrade with increasing excitation frequency. As the frequency is increased, the modulating orifice tends to remain at its maximum opening a greater percentage of the time in an attempt to generate the low desired force  $b\dot{x}$ . With increasing frequency and improving isolation, the reduction in the absolute velocity of the mass  $\dot{x}$  causes a further reduction in the desired force. As the active damper attempts to produce this force in spite of increasing relative velocity between the mass and the base, a limit is approached where the active damper orifice remains open to its maximum at all times. At these higher frequencies, the experimental active damper and the analytical model with orifice limitations approach a passive conventional constant orifice damper system. Fig. 6 clearly illustrates this performance limit. The transmissibility plot of the active damper system, including a maximum orifice, approaches a slope of -1, or 6 db per octave attenuation rate, as would a passive damper system with an equivalent damping coefficient. In contrast, the "ideal" active damper approaches an attenuation rate at 12 db per octave as would the theoretical skyhook damper.

Fig. 7 is a comparison of the performance response of the experimental active damper hardware and the response predicted by the analytical model including dry friction and a limited orifice opening, subject to sinusoidal base excitation. Both the experimental and analytical active damper utilize a control scheme simulating a critically damped skyhook damper. The damper break-loose condition and the 6 db per octave attenuation rate are evident in the response curves. A small discrepancy between the response of the experimental and analytical systems can be seen in the vicinity of the resonant frequency. The slightly degraded performance of the experimental hardware may be due to increased oil compliance,

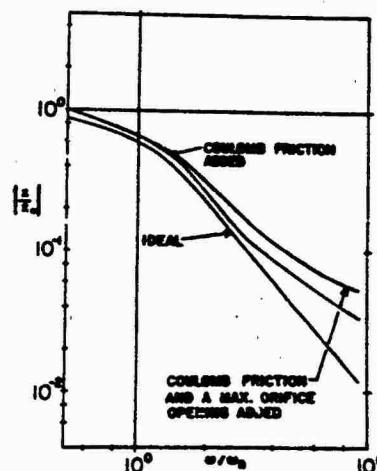


Figure 6  
Comparison of the theoretical simulation response of an ideal active damper system, simulating a critically damped skyhook damper, with that of two non-ideal, comparable active damper systems, subject to sinusoidal base excitation.

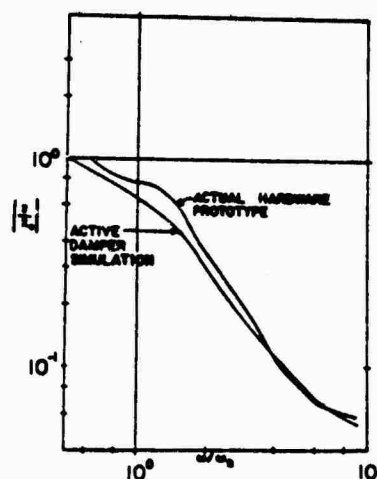


Figure 7  
Comparison of the theoretical simulation response and the experimental performance response of the active damper prototype hardware.

a non-ideal effect, possibly caused by air bubbles in the oil.

The experimentally determined performance response of the active damper, used in the conventional test system, is compared in Fig. 8 to the response of the test system, undamped and damped, with a constant orifice damper. Sinusoidal base excitation is being used with the active damper simulating a critically damped skyhook damper. This constant orifice damper is actually the active damper hardware held at its maximum orifice opening. In the region of the resonant frequency the superior isolation performance of the active damper is obvious. In the high frequency region, the active damper equals the isolation performance of the minimum damping coefficient passive system, and approaches the response of the undamped system.

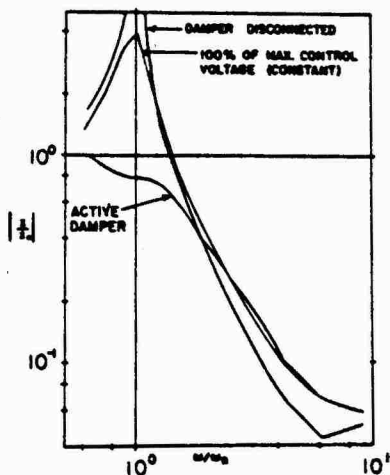


Figure 8  
Comparison of the experimental performance of the active damper, a constant orifice damper with maximum control voltage applied to the servovalve, and the test system with damper disconnected.

Fig. 9 compares experimentally determined performance response curves for the active damper system and several constant orifice damper systems with sinusoidal base excitation.

The sinusoidal testing of the active damper was very important for system development and comparative performance with computer simulations, but in real world applications the device must respond to input vibrations of very complex waveforms. For this reason, random vibration input was included in the test program. The performance response of all systems tested were analyzed using a Hewlett-Packard 5420A Digital Signal Analyzer. This instrument is a

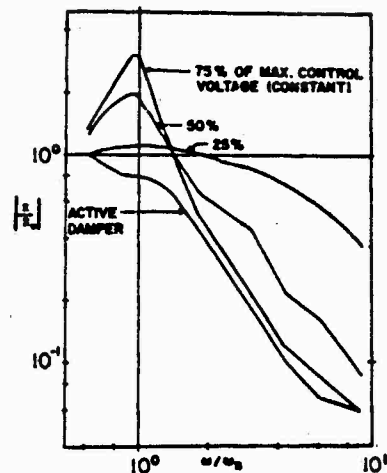


Figure 9  
Comparison of the experimental performance of the active damper simulating a critically damped skyhook damper, and constant orifice passive dampers of various damping coefficients (partial control voltage applied to the servovalve), subject to sinusoidal base excitation.

dual channel, digital instrument capable of executing a fast Fourier transform algorithm to perform time and frequency domain analysis of complex analog signals. The random signal generator internal to the HP-5420A was utilized to provide the random input signal applied to the M.T.S. test apparatus. The following analysis of the test results are plots, presented in the form of a transfer function  $|x/x_0|$  in the frequency domain, and plotted directly from the HP-5420A.

Figures 10-13 illustrate the performance response of the active damper compared to four constant orifice passive dampers, of a fixed damping coefficient, subject to random base excitation. Observation of these plots yields several interesting points. First, the performance response of the active damper, subject to random excitation, is slightly degraded from the system response curve made up of many single frequency, sinusoidal input data points. Non-linear system response, data sampling and averaging analysis techniques, and a damper force control algorithm that is independent of frequency, may contribute to this degradation of performance. Secondly, for a passive damper system with an equivalent constant orifice opening, the magnitude of the transmissibility at the resonant frequency is less for a random input signal as opposed to a single frequency sinusoidal base input. Again, non-linear system response and analysis may contribute to this response difference. Despite this slight degradation in the response of the active damper when random vibrational base excitation is applied, the active damper performance advantages are still

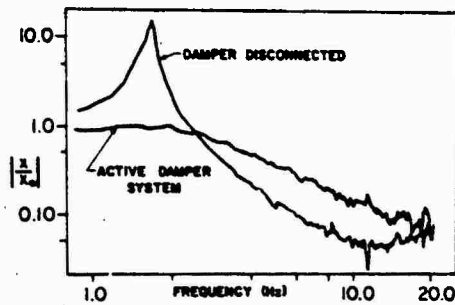


Figure 10

Comparison of the experimental response of the active damper system and the conventional test fixture with the damper disconnected (undamped).

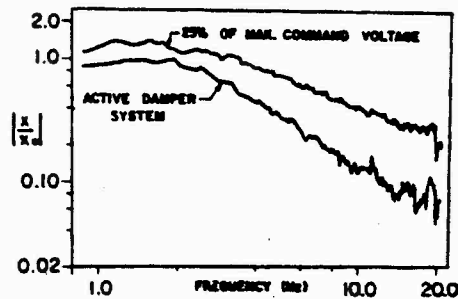


Figure 13

Comparison of the experimental response of the active damper system and a constant orifice, passive damper system. A constant 25% of the maximum command voltage is applied to the servovalve.

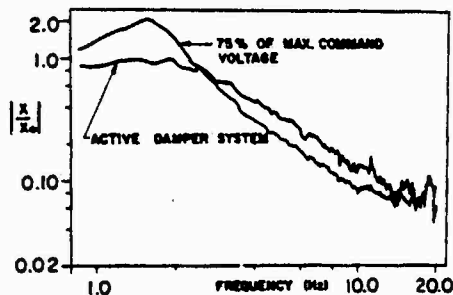


Figure 11

Comparison of the experimental response of the active damper system and a constant orifice, passive damper system. A constant 75% of the maximum command voltage is applied to the servovalve.

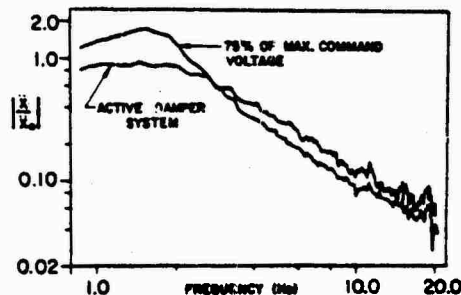


Figure 14

Acceleration transmissibility plots comparing the response of the active damper system and a constant orifice, passive damper system. Maximum command voltage applied to servovalve = 75%.

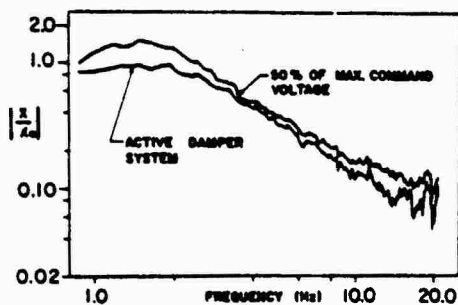


Figure 12

Comparison of the experimental response of the active damper system and a constant orifice, passive damper system. A constant 50% of the maximum command voltage is applied to the servovalve.

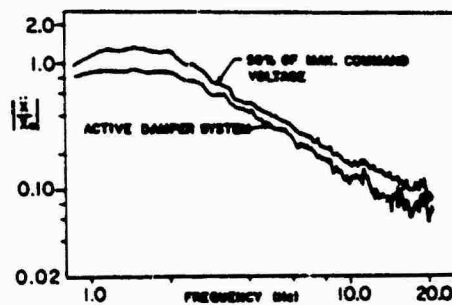


Figure 15

Acceleration transmissibility plots comparing response of active damper system and a constant orifice, passive damper system. Maximum control voltage applied to servovalve = 50%.

quite obvious. As the damping ratio of the passive damper increases in an attempt to limit the mass motion at resonance, the performance of the active damper surpasses that of the passive system in all frequency regions. This overall performance superiority becomes evident in Figures 12 and 13.

Acceleration transmissibility was experimentally measured with accelerometers on the base and the mass. Figures 14 and 15 are representative acceleration transmissibility plots for the active damper prototype, subject to random base vibration. These figures compare the acceleration response of the active damper and two constant orifice passive dampers. The passive damper orifice settings used in these two tests are identical to those used to obtain the results in Figures 11 and 12. When the corresponding displacement and acceleration transmissibility curves are compared, it can be seen that they closely resemble the linear system relationship  $|x/x_0| = |\ddot{x}/\ddot{x}_0|$ . In other words, the experimental results show the displacement transmissibility performance of the active damper is achieved without degrading the mass acceleration isolation.

The presented experimental and analytical performance of the active damper was determined using a single degree of freedom system. Analysis of semi-active vibration control for more complex systems is discussed in references [1] and [3]. A performance investigation of the active damper prototype used in more complex isolation systems is currently being pursued.

#### CONCLUSION

The active damper, used in a semi-active isolation system, has been successfully fabricated and tested with both sinusoidal and random vibrational base excitation. In suspension applications where both system isolation at the resonant frequency and excellent high frequency isolation are desired, the active damper has demonstrated its superiority over conventional passive systems, with performance approaching that of a fully active system. In contrast to the large cost, complexity, and power requirements of a fully active system, the active damper requires no hydraulic power supply, uses only low level electrical power for signal processing and valve actuation, and utilizes a hardware implementation significantly simpler and less costly than a fully active system.

A computer model simulating the active damper response to sinusoidal base excitation has been developed. This model includes several non-ideal effects actually encountered in system hardware, and predicts the performance response of the active damper device. The above-mentioned test results verify these analytical predictions that the operating hardware prototype active damper does indeed offer unique performance response, superior to that of a passive system in many suspension applications.

#### REFERENCES

1. Karnopp, D.C., Crosby, M.J., Harwood, R.A., "Vibration Control Using Semi-Active Force Generators," ASME Paper No. 73-DET-122, June 1974.
2. Ruzicka, J. E., Derby, T. F., "Influence of Damping in Vibration Isolation," The Shock and Vibration Information Center, Naval Research Laboratory, Washington, D.C., 1971.
3. Karnopp, D.C., Allen, R. R., "Semi-Active Control of Multimode Vibratory Systems Using the ILSM Concept," ASME Paper No. 75-DET-15, September, 1975.

6632A/djr

#### DISCUSSION

Mr. Henderson (Air Force Materiel Laboratory):  
Are we going to have mini computers on our automobiles and computer controlled shock absorbers?

Mr. Kraenicki: It is a definite possibility seeing that you can buy a computer for \$6.00 and eventually we may reach the point where we could do that. But in the meantime I see the application of this in heavy vehicle suspension systems where a fully active system, in order to get these parameters, would require a very large power supply in order to lift a tank. This system does not require that hydraulic power supply.

## AN EXPERIMENTAL INVESTIGATION OF NOISE ATTENUATING TECHNIQUES FOR SPACE-SHUTTLE CANISTERS\*

L. Mirandy  
General Electric Company  
Space Division  
P.O. Box 8555  
Philadelphia, Pennsylvania

and  
Frank On  
J. Scott  
NASA Goddard Space Flight Center  
Greenbelt, MD.

A model of the Space-Shuttle Thermal Canister has been acoustically tested to determine the amount of noise attenuation which could be derived using a simple, single-wall canister construction having rectangular shape. Acoustic testing was performed on the basic canister and with the following noise-attenuating design modifications: (a) an interior baffle; (b) with varying degrees of absorptive material covering on the interior surfaces; and (c) with constrained-layer viscoelastic damping strips bonded to the canister exterior.

The basic canister experienced noise amplifications at 56 and 80 Hz, which are attributed to the fundamental canister acoustic mode and local panel structural resonances, respectively. From 100 to 3000 Hz the Noise Reduction (NR) ranged from 1 to 6 dB, followed by a 6 dB/Oct increase above 3000 Hz. The overall NR was less than 1/2 dB for the test acoustic spectrum. Most of the energy in this spectrum is below 200 Hz, and hence the amplifications at 56 and 80 Hz had a particularly deleterious effect.

The standing wave response at 56 Hz was effectively suppressed by the incorporation of a cardboard baffle midway between the canister end-caps. This resulted in an additional overall noise reduction of 4 dB. The canister was next tested with 14%, 22.5% and 31% sound absorptive coverages on the interior walls. The coverage was effective between 400-3000 Hz; the maximum benefit (9 dB) occurring at 1600 Hz. Cross-plots of the data indicated that coverages beyond 31% would produce only small increases in NR. The damped configuration provided an additional 4 to 5 dB attenuation over much of the frequency range. It has an overall reduction of about 10 dB as compared to 4.4 dB without damping. A significant reduction of the resonant effect at 80 Hz was noted. Theoretical predictions of the canister NR frequency characteristics compare relatively well with the test results.

### INTRODUCTION

This investigation was undertaken to explore design modifications which could enhance the acoustic attenuation characteristics of the Space Shuttle Thermal Canister. The primary function of the Thermal Canister, developed by NASA-Goddard, is to provide an enclosure in which temperature can be accurately regulated; thereby providing a controlled environment for Space-Shuttle experiments. Protection from the high level shuttle acoustic environment represents a desirable secondary function. An inexpensive, but

representative, acoustic model of the Thermal Canister was designed and fabricated by General Electric for NASA. The design guidelines were simplicity, a rectangular shape which is the most conducive for thermal applications, and a single-wall construction. It is recognized that greater attenuations are possible using a double-wall construction, however, it was intentionally avoided in this initial study because of its additional weight and complexity, in favor of first finding the noise reduction possible with simpler approaches. Although this study was spawned by the Thermal Canister program, the results are equally applicable to other canister applications.

\*Work done under contract NAS 5-23412, MOD. 148.

The Thermal Canister Acoustic Model (TCAM; design evolved from analytical studies.<sup>(1)</sup> Therein, predictions of the noise reduction associated with various canister configurations were investigated using finite element models and noise reduction codes. The analytical results indicated that significant noise reduction could be achieved by: (a) stiffening the canister panel structure; (b) incorporating constrained layer damping strips; and, (c) partial coverage of the interior walls with sound absorptive material. Accordingly, stiffeners were incorporated in the basic TCAM design, while provision was made to bond on constrained layer damping strips. Acoustic testing was performed on the undamped and damped configurations. In addition, the model was configured with varying degrees of sound absorptive covering in order to assess its impact.

This paper highlights results of the experimental program. Additional details are contained in the test report.<sup>(2)</sup>

#### DESCRIPTION OF THERMAL CANISTER ACOUSTIC MODEL

A photo of the TCAM interior is shown in Figure 1. It is a rectangular container approximately 1 x 1 x 3 meters. It is of modular construction consisting of a welded aluminum angle framework with removable exterior panels. Each side of the TCAM has three panel assemblies; two identical panels of 0.081 cm (0.032 inch) aluminum sheet with stiffeners and a 0.32 cm (0.125 inch) aluminum center panel. The large side panel assemblies are stiffened by four riveted longitudinal "T" stiffeners that simulate the heat pipe installation and two exterior hat stiffeners riveted to the panel at right angles to the simulated heat pipes. Rivets connect the hat sections and T's at their intersections. The panel assemblies are bolted to the framework and can readily be replaced with modified panel assemblies if desired. The end panels are of 0.32 cm (0.125 inch) aluminum sheet with internal and external hat sections riveted to one another and the panel at right angles. A photo of the assembled TCAM in the acoustic chamber appears in Figure 2.

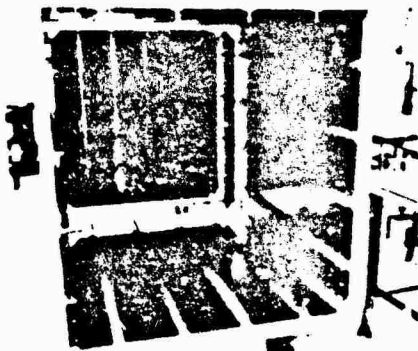


Fig. 1 - Interior Construction of TCAM



Fig. 2 - TCAM in Acoustic Chamber

Tap-tests were conducted to determine the fundamental resonances of the TCAM. A roving accelerometer was used to record motion near the tap locations. Figure 3 summarizes the resonant frequencies observed on the various sub-panels defined by the intersection of hat and T members. The center-section sub-panels appeared to move as a unit at 80 Hz, while the end-caps responded at 90 Hz. The fundamental mode of the gridwork of hat and T sections had a natural frequency of 180 Hz. This number was later supported by acceleration PSD's recorded during the acoustic test.

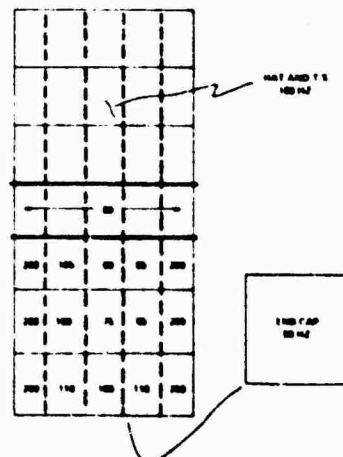


Fig. 3 - Principle Sub-panel Resonances Determined by Tap-Test



In order to increase the damping in the TCAM exterior wall panels, analytical studies were conducted to size constrained layer damping strips. The General Electric viscoelastic damping material SMRD was selected for this application. SMRD has a high loss factor (1.5 - 2.0), low density, is castable and has low outgassing characteristics. Integrally damped designs, incorporating SMRD, have been successfully implemented in circuit boards, a spherical gimbal, air-conditioners, and a variety of other applications. Perhaps, most germane, is the damped cylindrical acoustic enclosure reported by Ferrente, et. al. (3). Steel was selected as the constraining layer for the model program for economic reasons. It is envisioned that lighter weight graphite fibers would be used in actual applications, resulting in approximately a 70% weight savings.

The damping treatment was designed to provide a Composite Loss Factor (CLF) greater than 0.20 ( $Q = 5$ ) in the fundamental mode of the large side panels (i.e. the hat and T section gridwork at 180 Hz). A total of 3 strips per side panel were selected for TCAM application. General Electric computer codes were used to determine the CLF and natural frequency associated with the coupled damped mode. Results were determined as a function of: strip width, SMRD thickness, and constraining layer thickness. Figure 4 illustrates the variation in CLF with damping strip width for various thickness constraining layers and a SMRD thickness of 1.90 cm ( $\frac{3}{4}$  inch). It is evident that a constraining layer thickness of 0.635 cm (0.25 inches) is optimum; thicker and thinner constraining layers yield lower CLF's. The final selection was a strip width of 2.54 cm (1"), a constraining layer thickness of 0.635 cm (0.25 inches) and a SMRD thickness of 1.90 cm ( $\frac{3}{4}$  inch). The associated CLF was 0.23 with an increase in natural frequency from 180 Hz (no damping) to 250 Hz (damped configuration). After the undamped configurations were acoustically

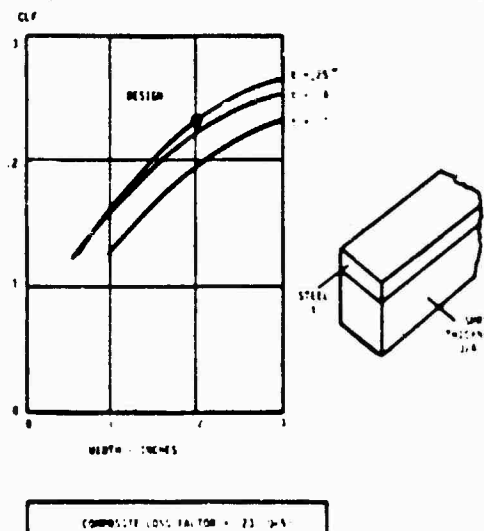


Fig. 4 - Damping Treatment Composite Loss Factor

tested, the damping strips were epoxied to the TCAM surface as shown in Figure 5. A total of 7 rows of damping strips (3 per large side panel and 1 center panel) encircle the canister girth. This amounts to 4-5% coverage of the TCAM surface.

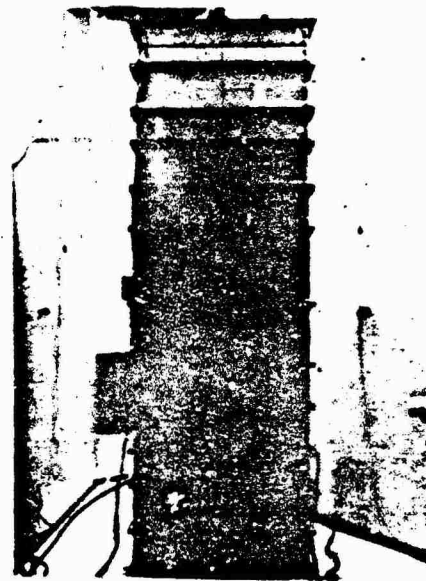


Fig. 5 - TCAM Damping Treatment

Although the damping treatment was designed to attenuate the overall panel mode of 180 Hz, it has the residual benefit of bisecting the sub-panels between the hats and T's. This raises the frequencies of the local sub-panel resonances, and provides some damping in these modes. The tap test was repeated after the SMRD damping strips were bonded to the panels. The response for all sub-panels was dead up to at least 200 Hz. If only the stiffening effect of the strips is considered, the now smaller sub-panels should, theoretically, have natural frequencies below 200 Hz. Evidently, damping quenched this response.

Johns-Manville "Microlite AA" was used as an acoustic absorptive cover for the interior of the TCAM during the acoustic tests. The blankets were 1.27 cm ( $\frac{1}{2}$  inch) thick and had a density of 37.5 grams/cm<sup>3</sup> (0.6 lb/ft<sup>3</sup>). Microlite is a good acoustic absorptive material that is space compatible and is currently being used in the GE Shuttle Waste Control System. The Microlite absorption coefficients, obtained from Johns-Manville, are plotted in Figure 6. The peak value of 0.80 occurs at 2000 Hz.

The first several acoustic modes of the rectangular canister have been computed. The fundamental end-to-end standing wave is at 56 Hz, while the first two side-to-side modes are at 166 Hz. A cardboard baffle was introduced during the test program in order to break up the fundamental standing wave.

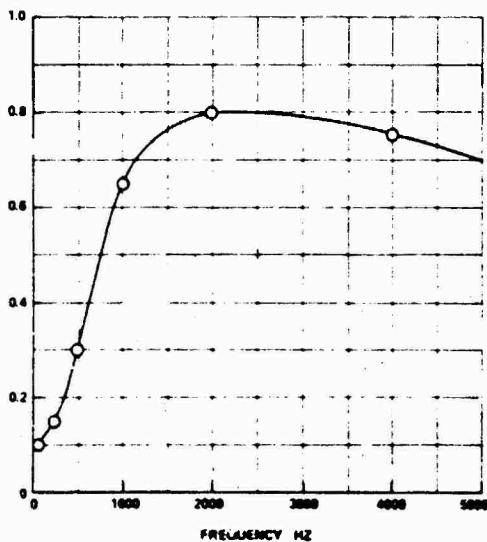


Fig. 6 - Microlite Absorption Properties

#### TEST PROGRAM DESCRIPTION

A total of 7 configurations, described below, were acoustically tested.

1. Bare Canister - The basic structure with no modifications.
2. Center Baffle - A cardboard baffle was inserted midway between and parallel to the end caps as shown in Figure 7. A circular hole, approximately 6 inches in diameter was cut in the center of the baffle in order to locate the center microphone.

Other internal microphones are also evidenced in Figure 6. The baffle was retained in the remainder of the test configurations.

3. Microlite on End-Caps - 1.27 cm ( $\frac{1}{2}$ " ) thick, Johns-Manville "Micro" 6-AA" sound absorptive covering was taped to both end-cap interiors. The total covering comprised approximately  $\frac{1}{3}$  of the interior canister area. The covered end-caps were retained in the remainder of the test configurations.
4. 10% Microlite Coverage of Side Walls - Six strips of Microlite approximately 38.1 x 12.7 cm (15" x 5") were taped to each side-wall between the simulated heat pipes. The strips, which were randomly spaced, are evident in Figure 7. The total interior coverage in this configuration (including end-caps) was approximately 22.5%.
5. 20% Microlite Coverage of Side Walls - Six additional strips of Microlite were added to

each of the side walls bringing the total interior coverage to 31%. This coverage was retained for the remaining two configurations.

6. & 7. SMRD Viscoelastic Damping Coverage - Seven 2.54 cm (1" ) wide strips of the GE viscoelastic damping material - SMRD, constrained by a layer of steel, were bonded to each of the side walls. Figure 5 contains a photograph of the configuration in the acoustic chamber. Because the damping material loss factor is temperature sensitive, test runs were conducted at 50°F (Configuration 6) and 68°F (Configuration 7). The particular SMRD compound used in this test (SMRD-100F90) is better suited for the higher temperature.

The test program was carried out at the NASA-Goddard Space Flight Center reverberant noise chamber in Greenbelt, Maryland. The chamber is an irregular-shaped five-walled room having a volume of approximately 68 m<sup>3</sup> and a total surface area of 102.1 m<sup>2</sup>. Approximately 50 kW of acoustic power are available for testing. The chamber is known to produce a diffuse reverberant noise field at frequencies above 160 Hz for test volumes less than 10% of the chamber volume.<sup>(4)</sup> (The TCAM occupied approximately 5% of the chamber.) At frequencies below 160 Hz, the chamber is still usable; however, spatial variations in the noise field will exist. The magnitude of these variations will increase with lower and lower frequencies. Thus, the measured noise reduction at low frequencies should be viewed with the knowledge that their absolute magnitudes could change if the TCAM were placed in a diffuse sound field. The comparative evaluation of the various test configurations, however, still has validity.

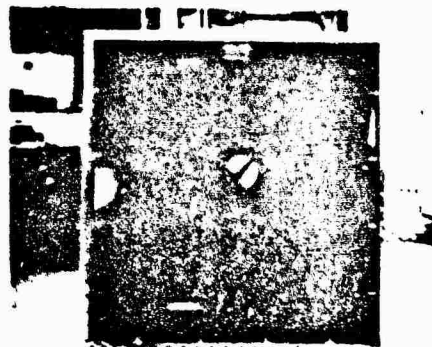


Fig. 7 - Baffle with 10% Side-Wall Microlite Coverage

The test instrumentation consisted of 6 external microphones, 9 internal (to the canister) microphones and 9 accelerometers. External microphones, which were suspended from the chamber ceiling, are visible in Figures 2 and 5. The average of 5 external micro-

phones were used to shape the chamber to the test acoustic spectrum and to define the external noise field in subsequent noise reduction computations. Internal microphones were secured to surgical tubing which was strung between eye-bolts located inside the canister. One microphone was located at the center of the canister, while four each were placed in the upper and lower halves of the canister. Internal microphones are evident in Figure 8. All microphone measurements were reduced to 1/2 octave spectra using both a "Real-Time Analyzer" and an off-line digital system. Comparable results were obtained with each method. Internal and external spatial averages were determined from the digitized individual microphone readings using the following standard formula:

$$SPL_{AVE} = 10 \log \left( \frac{1}{n} \sum_{i=1}^n 10^{SPL_i/10} \right)$$

where:

$SPL_{AVE}$  = Sound pressure level spatial average - dB

$SPL_i$  = Sound pressure level measured by  $i$ th microphone

$n$  = No. of microphones

The specified test acoustic levels are listed in Table 1. This spectrum represents the Goddard estimate of maximum flight levels anticipated on the STS. The test runs for each configuration were of one minute duration.

## EXPERIMENTAL RESULTS

Figure 8 displays the average internal and external sound pressures encountered during the bare canister run. The difference between these two curves was used to construct the noise reduction plot shown in Figure 9. Noise amplifications are noted at 60 and 80 Hz, followed by a noise reduction of about 5 dB from 100 to 500 Hz. There is a slight dip at 500 Hz after which the noise reduction ranges from 1 to 3 dB until 3150 Hz. Thereafter, it increases at 6 dB per octave which is consistent with the theoretical mass law. The amplification in the 50 Hz band is due to the fundamental longitudinal standing wave of the canister, which was computed to be 56 Hz. This conclusion is supported by the individual microphone data shown in Figure 10. Therein, the individual microphone test measurements have been converted to relative RMS pressure and are plotted versus location along the length of the canister. The measurements lie very close to the theoretical pressure distribution in the fundamental acoustic mode (1/2 cosine). The plot demonstrates that most of the energy in the 50 Hz band is indeed due to the first acoustic resonance. The amplification at 80 Hz (Figure 9) is attributed to the many local panel resonances in this frequency range. Local panel resonances in the 80-110 Hz range exist over approximately 60% of the external panel sheet areas (see Figure 3). The drop in noise reduction at 500 Hz is also likely due to a structural resonance. This conclusion was drawn from accelerometer data which indicated a structural resonance at 560 Hz.

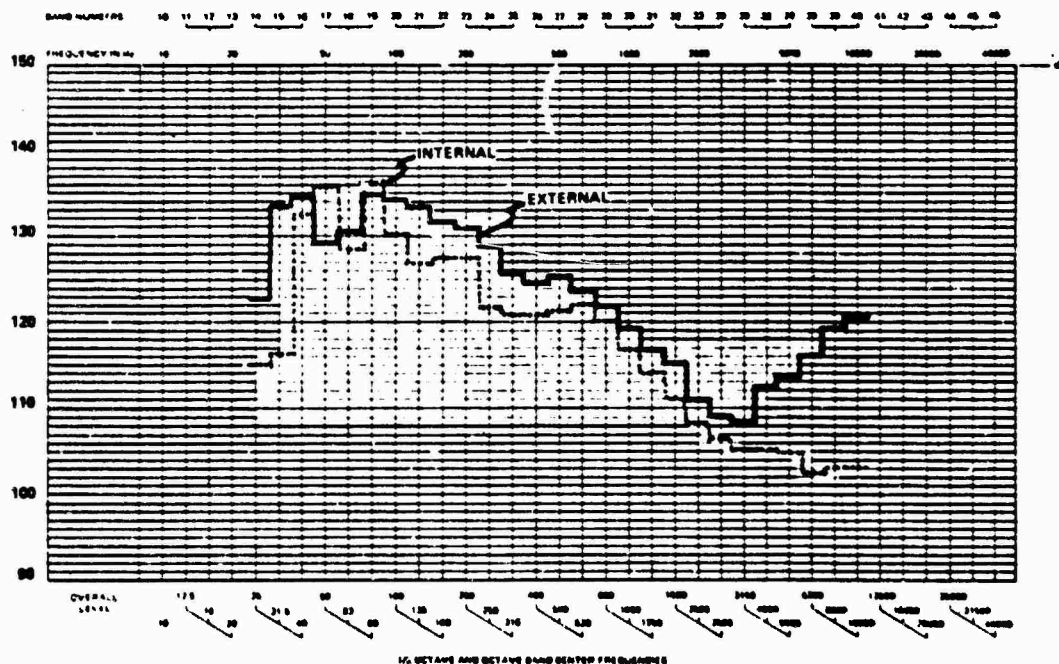


Fig. 8 - Average Internal and External SPL's With Bare Canister

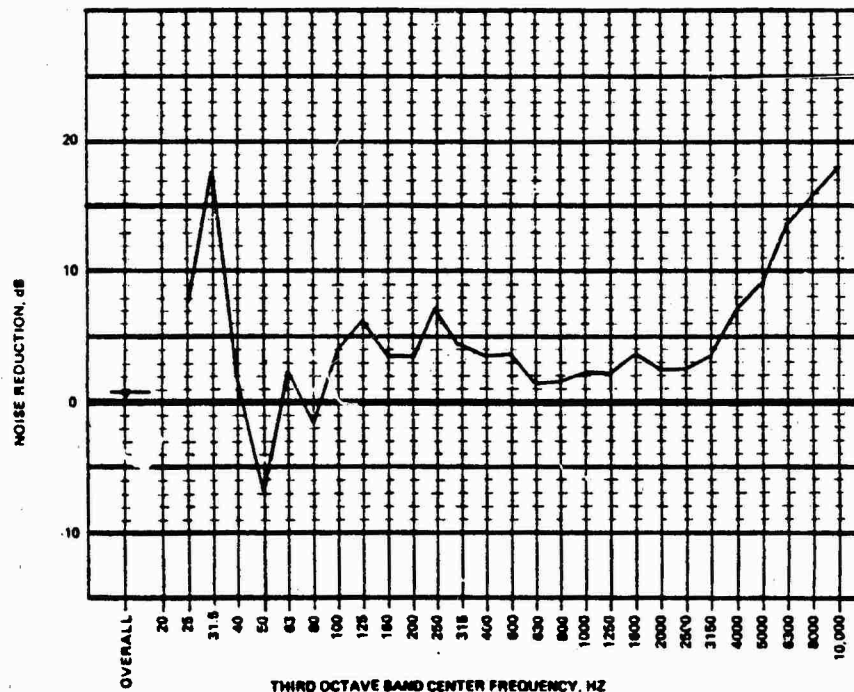


Fig. 9 - Noise Reduction for Bare Canister

In summary, the dominant structural modes of the basic canister from a noise reduction standpoint are - the local panel resonances around 80 Hz and a higher system mode at 560 Hz. Evidently, the side panel mode involving the network of hat and T sections did not produce a distinct trough in the noise reduction at its natural frequency (180-200 Hz). Response in this mode was, however, evident in the vibration data. The overall noise reduction of the bare canister was only 0.3 dB, largely due to the noise amplification at 50 and 80 Hz. (NOTE: The input (external) acoustic spectrum is such that most of its energy is below 200 Hz, and hence the overall noise reduction is primarily due to the low frequency response).

A cardboard baffle was placed midway between the end-caps (see Figure 7) in order to break-up the 56 Hz standing wave. The noise reduction obtained with the baffle is compared with that of the bare canister in Figure 11. The essential difference is as expected - large reductions of the noise levels at 50 and 63 Hz. In other frequency ranges, the configurations are similar. The baffle increased the overall noise reduction from 0.3 to 4.1 dB. The baffle was retained throughout the rest of the test program.

Figure 12 compares the noise reduction characteristics with varying degrees of Microlite coverage. Included are curves for: (a) bare canister (with baffle), (b) 14% coverage - end-caps, (c) 22.5% coverage - end-caps + 10% side walls, and (d) 31% coverage - end-caps + 20% side walls. Maximum attenuations

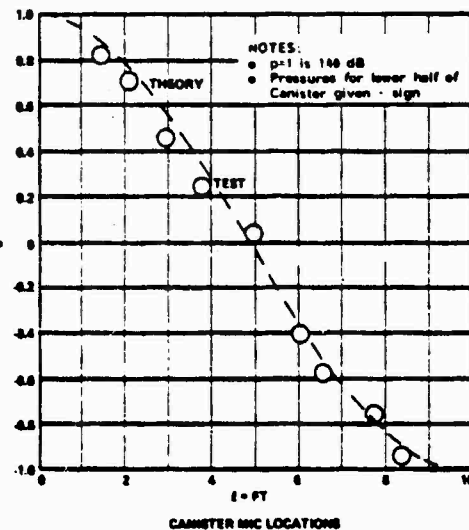


Fig. 10 - Spatial Distribution of Sound Pressure in 50 Hz Band

are seen to occur from 1600-2000 Hz, at which an increase in noise reduction of 9 dB is noted in going from the bare canister to the 31% coverage configuration. This frequency range corresponds to the maximum absorption coefficient shown in Figure 6. The coverage also suppresses the resonance effect at 560

Hz. Below 400 Hz the Microlite has negligible effect, while at the very high frequencies its effectiveness diminishes. Figure 13 shows the same data plotted against % interior coverage for discrete frequencies. It appears that some gain could be derived by increasing the coverage at 2000 Hz, however, not much additional benefit could be expected at the lower and higher frequencies. Because of Microlite's inefficiency at low frequency it had negligible impact on the overall noise reduction for the space shuttle environment.

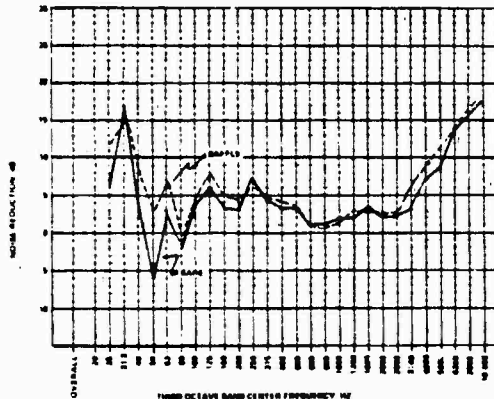


Fig. 11 - Effect of Baffle on Noise Reduction

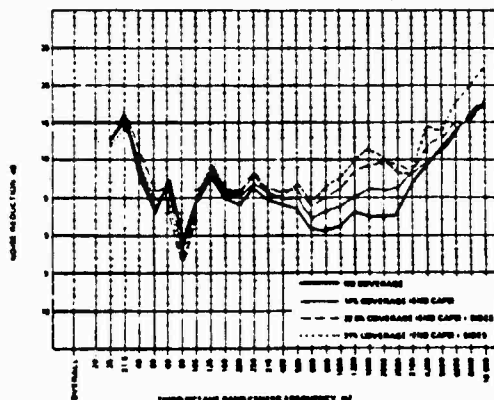


Fig. 12 - Effect of Microlite on Noise Reduction

Noise reduction curves for configurations with and without the damping strips are presented in Figure 14. The strips provide large attenuation of the resonance at 80 Hz, and produce a reduction of about 10 dB from 100-800 Hz. At 800 Hz the noise reduction increases at 6 dB per octave in accordance with the mass law. The overall reduction was about 10 dB, which is 6 dB higher than the undamped configuration. Data above 2500 Hz has not been plotted for the damped configuration because the internal microphone readings (90-95 dB) were near the lower limit of the system measurement capability, and thus could easily contain error. The noise levels at these higher frequencies are so low that their precise values are a

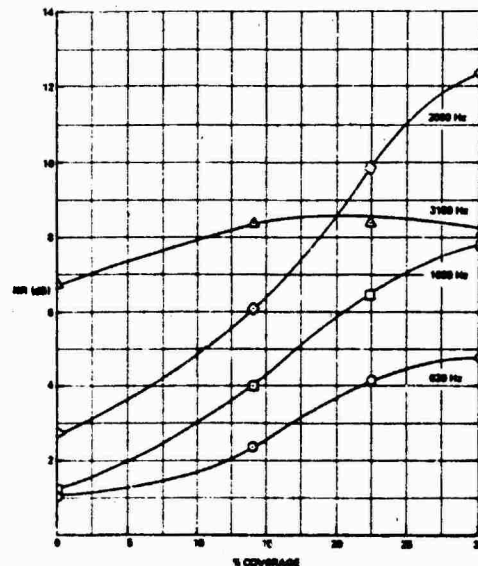


Fig. 13 - Noise Reduction Variations with % Microlite Coverage

moot point for practical shuttle design considerations.

The damped configuration was tested at two temperatures - 68°F for which the SMRD was designed, and 50°F at which the damping capability is reduced. Both runs are included in Figure 14. A 2 to 3 dB improvement is observed at the higher temperature for frequencies above 300 Hz. Below this frequency comparisons should be viewed with caution as the noise field is not diffuse. (In fact, the real time analyzer data (not shown) indicated that the higher temperature had slightly higher NR at the low frequencies).

While the stiffening effect of the damping strips was no doubt responsible for raising the sub-panel frequencies above 80 Hz, the absence of a pronounced resonant trough at a higher frequency indicates that the damping was also effective. It should be recalled that the damping treatment was designed to attenuate the 180 Hz overall panel mode involving motion of the hat and T sections, rather than to specifically damp the local panel resonances. It is felt that a significantly lighter damping treatment, which produces the same beneficial results, could be achieved by a design which directly attacks the local panel resonances.

Figure 15 contains curves of standard deviation from the spatial average for the internal and external microphone measurements versus frequency. A composite of the data from each test configuration is shown (i.e. 7 curves). The external and internal microphones exhibit a decrease in dispersion at 80 Hz, which is probably due to the chamber characteristics. It may, in part, have been influenced by "ringing" at canister local sub-panel resonances. (The higher inter-

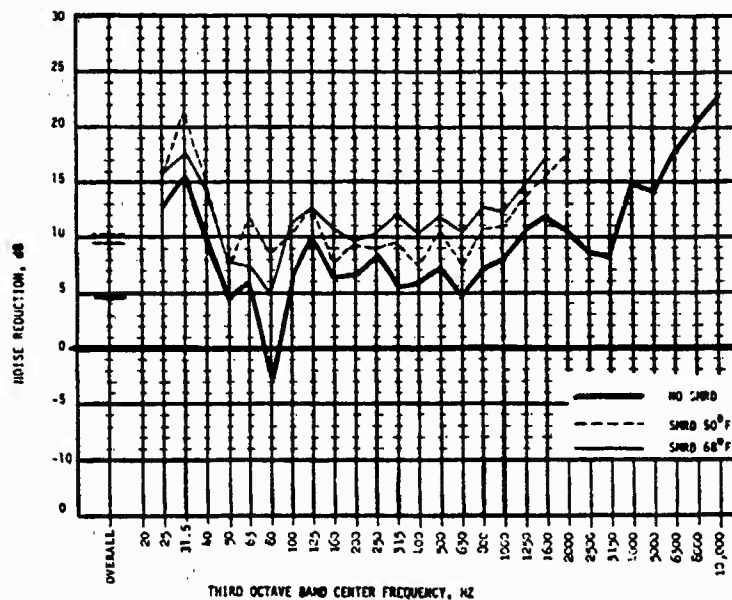


Fig. 14 - Effect of Damping Treatment on Noise Reduction

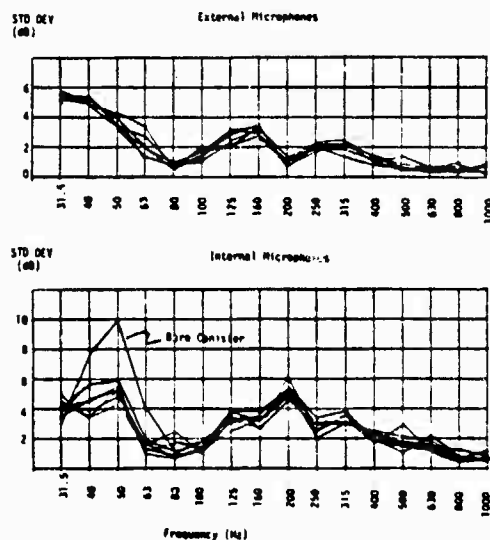


Fig. 15 - Average Internal and External SPL's with Bare Canister

nal standard deviations at 80 Hz are data points from the damped configuration). The external field displays a definite decrease in dispersion above 160 Hz which is in accordance with the known chamber characteristics. Internal dispersions depend on the number of canister acoustic modes present in each frequency band. The theoretical acoustic modal density for the canister is presented in Figure 16. As the number of modes within a frequency band increases, the sound

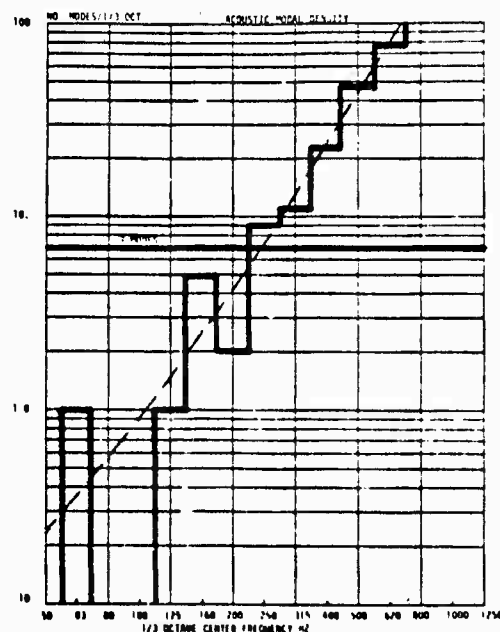


Fig. 16 - Acoustic Modal Density

field becomes more and more diffuse (i.e. spatial variations in pressure decrease). A modal density of 7 is generally accepted as a point at which reverberant conditions prevail. This occurs at 250 Hz, and it is noted that the internal dispersions in Figure 15 decrease at this point. The relative maximum in internal

standard deviation at 200 Hz is probably because only 2 acoustic modes lie in this bandwidth as compared to 5 and 9 at 160 Hz and 250 Hz, respectively (see Figure 16). The large low frequency dispersions in the bare canister run are due to the fundamental standing wave, which was suppressed in later test runs by the baffle. The standard deviations shown in Figure 15 were computed by:

$$\sigma = \sqrt{\frac{\sum_{i=1}^N (\text{SPL}_i - \text{SPL}_{\text{AVE}})^2}{N-1}}$$

where:

$\sigma$  = Standard deviation in dB

$\text{SPL}_i, \text{SPL}_{\text{AVE}}$  = The individual and space averaged sound pressure levels, respectively in dB.

$N$  = No. of microphones

#### CORRELATION WITH THEORY

Noise reductions have been analytically predicted for the configurations tested using architectural acoustic theory. An overview of the procedure used is presented in Figure 17. First the TCAM was separated

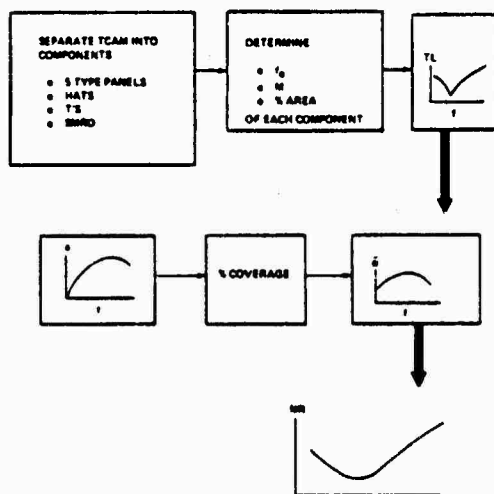


Fig. 17 - Overview of Noise Reduction Prediction Procedure

into generic components. The fundamental natural frequency,  $f_0$ , the weight per unit area,  $M$ , and the % of the total surface area occupied by each component were determined. This data was used to compute transmission coefficients for the individual components. The individual transmission coefficients were, in turn, summed to generate a composite

transmission loss as a function of frequency. Next, the average absorption coefficient for the canister interior ( $\bar{\alpha}$ ) was computed for the various test configurations. This was determined from the Microlite absorption characteristics (shown in Figure 6), the % Microlite coverage, and the absorption coefficient for aluminum (assumed equal to 0.05 at all frequencies). Finally the composite transmission loss and absorption coefficient were combined to furnish the noise reduction frequency characteristics. The mathematical details will be described next, followed by a comparison of test and predicted noise reductions.

The transmission coefficients were computed using the theoretical random-incidence mass law shown.<sup>(5)</sup>

$$\tau = 2 \int_0^{\pi/2} (\tau_\phi) \sin \phi \cos \phi \, d\phi \quad (1)$$

$$\tau_\phi = \frac{1}{1 + \frac{\pi M f \cos \phi}{\rho C}} \quad (2)$$

where:

$\tau$  = Random-Incidence Transmission Coefficient

$\phi$  = Incidence Angle

$f$  = Frequency (Hz)

$\rho C$  = Air Impedance (lb/ft<sup>2</sup>-sec). A value of 84 was used which is approximately sea-level conditions at 50°F (approximate test temperature)

$M$  = Panel Surface Weight Density (lb/ft<sup>2</sup>)

The integration in (1) was carried out numerically using 16 point Gaussian-quadrature. Stiffness effects were approximated by the method indicated in Reference 3. Mathematically, this is equivalent to modifying the transmission coefficient for frequencies below  $f_0$  by:

$$\tau = \tau(\text{EQ 2}) \cdot (f/f_0)^4, \quad f < f_0 \quad (3)$$

The above produces a 6 dB/OCT increase in transmission loss as frequency decreases below  $f_0$ . The composite transmission loss for the TCAM was computed by summing the effects of the individual components according to:

$$\text{TL} = 10 \log (1/\sum \tau_i p_i) \quad (4)$$

where:

$\text{TL}$  = Transmission loss (dB)

$\tau_i$  = Transmission coefficient for the  $i^{\text{th}}$  component

$p_i$  = Fraction of surface area occupied by the  $i^{\text{th}}$  component



Equations 1 thru 4 were used to compute a theoretical transmission loss for the undamped and damped configurations. Ten separate components (e.g. sub-panels shown in Figure 3) contributed to the total transmission loss. Natural frequency data were based on tap-test results, while mass and surface area properties were computed from the design drawings. The effect of damping was approximated indirectly by raising all the panel natural frequencies to 200 Hz. This was based on the tap test natural frequency results, which indicated that the sub-panels were "dead" at least up to 200 Hz. (Actually they may have had natural frequencies below 200 Hz, but the high degree of damping quenched this response). The major assumptions embodied in these calculations include: (a) consideration of only one resonant mode per component; (b) the indirect means of handling damping, just discussed; and, (c) no coincidence effect.

The theoretical noise reduction has been computed using an energy balance approach. The power input to the canister interior is equated to the power that "leaks" out of the container. That is:

$$P_{IN} = P_{DISS} + P_{OUT} \quad (5)$$

and,

$$P_{IN} = \bar{\tau} I_E \quad (6)$$

$$P_{DISS} = \bar{\alpha} I_I \quad (7)$$

$$P_{OUT} = \bar{\tau}(1-\bar{\alpha}) I_I \quad (8)$$

where:

$\bar{\tau}$  = Composite Transmission Coefficient

$\bar{\alpha}$  =  $10^{-TL/10}$

$\bar{\alpha}$  = Average absorption coefficient

$I_E$  = Intensity of the external field

$I_I$  = Intensity within the container

It has been assumed that the sound fields are diffuse and a steady-state has been reached, so that the intensities are constant. If Equations (6-8) are substituted into (5), there results after some rearrangement:

$$\frac{I_E}{I_I} = 1 - \bar{\alpha} + \bar{\alpha} / \bar{\tau}$$

and the noise reduction is defined as:

$$NR = 10 \log I_E / I_I = 10 \log (1 - \bar{\alpha} + \bar{\alpha} / \bar{\tau}) \quad (9)$$

Equation (9) has the following interesting features: (1) For  $\bar{\alpha} = 0$  (no dissipation), the noise reduction is zero, which would be expected on physical grounds; and, (2) For  $\bar{\alpha} = 1$  (anechoic room) the noise reduction is equal to the transmission loss, which is also

physically correct. Equation (9) was used to compute theoretical NR for the seven configurations tested. The equation is strictly correct only if the sound fields are diffuse. It cannot, for example, predict the effect of the baffle, which would require the use of wave acoustics.

Figure 18 compares theoretical and test noise reductions for the undamped 31% Microlite configuration. The theoretical prediction (shown as a  $\pm 3$  dB bandwidth) is in good agreement with the test at low and mid-frequencies. The theory overpredicts the noise reduction at high frequencies. This disagreement could stem from: (a) the coincidence effect (approximately 35% of the surface area was covered by panels having a coincidence frequency from 3000 to 4000 Hz); (b) higher structural modes not included in the analysis; (c) inaccuracies in the test measurements at higher frequencies (sound pressure levels were below 100 dB here, and the resolution is not as good as at the lower frequencies). Theoretical predictions are compared with test data from the damped configuration in Figure 19. The correlation is quite good for the entire

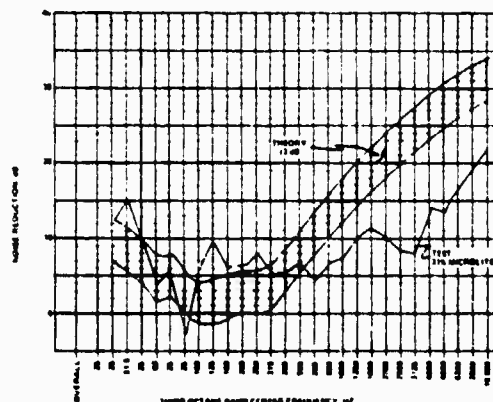


Fig. 18 - Noise Reduction Test/Theory Correlation for Undamped Configuration

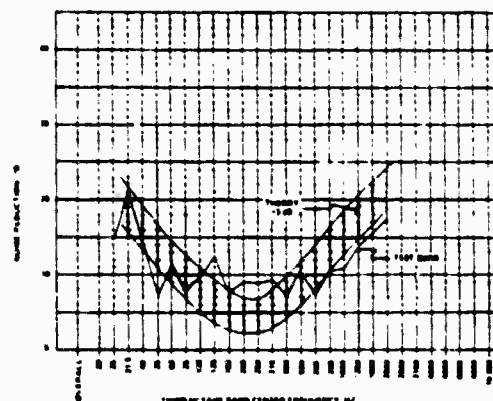


Fig. 19 - Noise Reduction Test/Theory Correlation for Damped Configuration



spectra. The test data only goes to 2000 Hz because the microphones measurements were too low to read accurately at higher frequencies. It is likely that the damping strips greatly reduced the coincidence effect noted above. Additional test/theory correlation data are contained in Reference (2).

## CONCLUSIONS

From this investigation, we draw the following conclusions.

- (1) The fundamental canister standing wave produced a significant sound amplification which was effectively suppressed with a baffle.
- (2) Local sub-panel resonances act as windows for acoustic energy. They produce a decided decrease in noise reduction at their natural frequency. Noise attenuation can be improved by stiffening the local panels (i.e. raising their natural frequency) and by damping treatment. The SMRD viscoelastic damping treatment applied in this test program was effective in quenching the local resonance effects.
- (3) Sound absorptive coverings were found to be effective in the mid-frequency range (500-3000 Hz). As much as 9 dB additional noise reduction was observed at 2000 Hz with approximately 30% interior surface coverage. It does not appear that substantial gains can be derived by increasing the coverage beyond 30%.
- (4) The overall noise reductions obtained with the various configurations were:

Bare Canister	0.3 dB
Baffle (With or Without sound absorptive coverage)	4.1-4.6 dB
SMRD Damping Treatment & Baffle	10 dB

Overall noise reduction in the shuttle acoustic environment is almost entirely dependent on the low frequency region of the spectrum (below 200 Hz). Thus, the effect of the sound absorptive material is not evidenced in the above.

- (5) Predictions based upon architectural acoustic theory correlate reasonably well with test results.

## REFERENCES

1. Gongloff, H., Rybacki, J., and Stahle, C., "Thermal Canister Mounted Instrument Acoustic Protection," GE Document No. 77SDS4237, Prepared for NASA-GSFC, (NAS 5-23412 MOD74), June, 1977.
2. Mirandy, L., "Thermal Canister Acoustic Model-An Experimental Investigation of Acoustic Attenuation Techniques," GE Document No. 79SDS4220, Prepared for NASA-GSFC (NAS 5-23412, MOD 148), April, 1979.
3. Ferrante, M., Stahle, C.V., and On, F.J., "Feasibility Study of An Acoustic Enclosure for Shuttle Payloads," Shock and Vibration Bulletin, August, 1976.
4. Cyphers, H.D., Munson, A., On, F., "Comparative Evaluation of Predicted and Measured Performance of a 68-Cubic Meter Truncated Reverberent Noise Chamber," NASA TND-7755, Jan., 1975.
5. Berenck, L. (Editor), Noise Reduction, McGraw-Hill Book Co., 1960.

TABLE 1  
Test Acoustic Spectrum

1/2 Octave Center Frequency (Hz)	Sound Pressure Level - dB <sub>2</sub> Re 20 $\mu$ N/M
25	132
31.5	133
40	133.4
50	134
63	134.5
80	134.2
100	134
125	134
160	133
200	131.8
250	129
315	127
400	125
500	124
630	123
800	122.5
1000	122
1250	119.8
1600	116.5
2000	113
2500	111.5
3150	110
4000	109
5000	107.8
6300	106.5
8000	105.4
10000	104
Overall	144

#### DISCUSSION

Mr. Nesbit (Lawrence Livermore Laboratory):

If most of the energy is coming in at several hundred Hz or less why did you chose the Microlite which has a maximum of 2,000 Hz?

Mr. Mirandy: Most sound absorbing materials have the same characteristics as Microlite in that when it is right against the wall it will not be very effective at lower frequencies. You could have drapes of material a little bit away from the walls but we didn't investigate this in this study.

DYNAMIC INTEGRITY METHODS INCLUDING DAMPING FOR  
ELECTRONIC PACKAGES IN RANDOM VIBRATION

J. M. Medaglia  
Spacecraft Development Dynamicist  
General Electric Space Division

Recent increases in electronic package size and increases in vibration qualification levels have emphasized the importance of design practices for dynamic integrity of printed wiring board and chassis assemblies of electronic piece-parts. Greater throw-weight capabilities of boosters has led to larger, more complex spacecraft with correspondingly larger electronic packages and experiments. The printed wiring boards (PWBs) now commonly span 17 to 20 cm on one side and require supplemental stiffening ribs to avoid excessive deflections even in moderate environments. Random vibration qualification levels derived by methods imposed in MIL-STD-1540B commonly reach  $0.5 G^2/Hz$  in the 100 to 1000 Hz range and an overall level of 25 Grms. These environments are 3 to 5 times the power spectral density and twice the energy of qualification levels in use only five years ago. They generate failures in 30 to 50% of packages designed without damping while the lower levels cause failures in 10 to 20% of packages tested. These data were collected from over 300 package tests on nine spacecraft programs. Although the large PWBs allow more efficient electronic design, ordinary stiffness design methods often fail to meet the response deflection and acceleration design criteria needed to minimize failure rates. In many cases, constrained layer viscoelastic damping can enhance other design practices by replacing ordinary ribs to produce adequate stiffness plus response magnifications of less than 10. Recently composite material graphite-epoxy constraining layers were applied to reduce the size and weight needed to ruggedize PWBs. This being a large departure from previous successful damping designs, tests were conducted to verify the performance of the new facets of the damping method and to verify simple techniques for assessing the integrity of PWBs. Also, the tests verified that the same techniques properly predict when damping is needed and what strip positions are effective.

#### INTRODUCTION

Some simple methods have been found effective in enhancing the reliability of electronic packages in sinusoidal and random vibration environments. The environments are more severe both in military applications and in civilian applications due to larger boosters and strict standards than can be sustained by obsolete designs which are sometimes as recent as five years old (Figure 1 and References 1, 2, 3, 11). The size and complexity of modern missions require a large number of package designs to be reviewed even with attempts at standardization of printed wiring boards (PWBs). To make matters worse, some trace-like RF-hybrid packages are incredibly complicated when considered as a structure required to survive a firm thrashing for nine minutes on a random vibration machine. Detailed modeling and analysis of some packages could take months and

is simply not done for economic reasons. In some cases a moderate amount of modeling by finite element methods is undertaken and supplemented by hand calculations and judgment. Most packages, however, do lend themselves to less sophisticated analytic approaches due to straightforward, boxy, and plate-like construction features. Hand calculations using beam and plate formulas (References 13, 14) with single degree of freedom response predictions are combined with simple deflection and acceleration criteria to assess the dynamic integrity of PWB assemblies and chassis assemblies of electrical and electronic parts. The scope of this paper is limited to the 75% to 95% of packages which are amenable to hand calculations. The specific examples cited are for random vibration environments lasting 3 minutes per axis. High cycle fatigue considerations for longer duration testing may cause a modification in the magnitude of allowable deflections and accelerations.

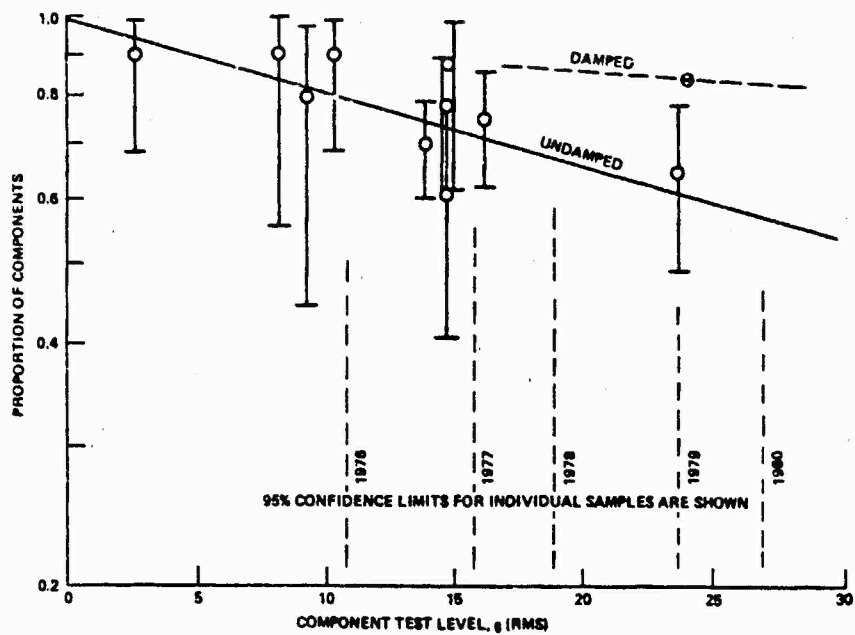


Fig. 1 - Proportion of Spacecraft Components That Pass Vibration Tests

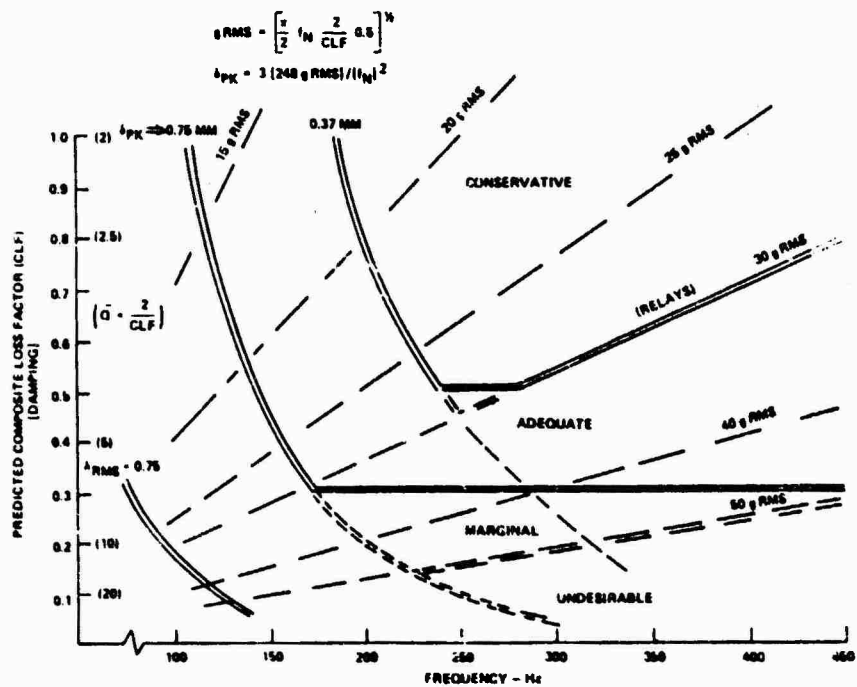


Fig. 2 - Design Risk Graph for 0.5 G<sup>2</sup>/Hz

### The Design Risk Graph

Figure 2 shows an evaluation tool for random vibration environments which combines natural frequency, response magnification, response deflection and response acceleration. The boundaries between regions are based on both analysis and experience. Once a criterion value has been accepted (i.e., 0.25 mm for maximum rms deflection) the location of the boundary with respect to structural damping and resonant frequency is intimately related to the applied vibration level. The random vibration profile in Figure 3 was used for the experimental work reported later in this paper and is the basis for the numerical configuration of Figure 2. The following formulas apply:

$$Grms = \sqrt{\frac{\pi}{2}} \cdot \frac{2}{CLF} \cdot f \quad (1)$$

$$\delta_{rms} = \frac{248 (Grms)}{f^2} \quad (2)$$

where:

$$\pi = 3.1415 \dots$$

$$G = \text{stimulus acceleration power spectral density (G}^2/\text{Hz)}$$

$$\frac{2}{CLF} = \bar{Q} = \text{response magnification factor (i.e., } \bar{Q} \approx 10 \text{ when } C/C_{CRIT} = 0.05 \text{ or } CLF = 0.1)$$

$$f = \text{resonant response frequency (Hz)}$$

$$\text{and } 248 = (9800 \text{ mm/sec}^2) \div (4 \pi^2).$$

It should be noted that Equation (1) is based on the Thompson-Barton formula (Reference 15), for the approximate response of a single degree of freedom oscillator to an acceleration PSD which is constant at all frequencies. Equation (1) differs from the T-B formula by a factor of  $\sqrt{2}$ . This is a deliberate attempt to mitigate the difficulty of predicting the amount of damping and to compensate for non-uniform PSD stimulus due to structural admittances or test control.

The boundaries of 0.37 mm and 0.75 mm for transition from conservative to adequate and from adequate to inadequate design regions are based on experience and some stress calculations. On review of past designs, it was found that designs having a deflection response of less than 0.75 mm generally survived well. This is reinforced by some simple calculations. Consider a glass-bodied part, 1/8-inch in diameter ( $p = 3.2 \text{ mm}$ ) staked to a PWB or chassis of span  $l$  so that it must bend as the substrate. The load intensity per unit length is  $q$ .

$$M = q l^2 / 8 \text{ (bending moment)} \quad (3)$$

$$\delta_{max} = 5 q l^4 / 384 EI \text{ (deflection)} \quad (4)$$

$$\delta_{max} = 5 M l^2 / 48 EI \quad (5)$$

$$\sigma = MC/I = \frac{648 E (D/2)}{5 l^2} \text{ (stress)} \quad (6)$$

$$\text{Let } E = 9.3 \times 10^8 \text{ psi; } D = 1/8 \text{ in}$$

$$\sigma = 5.58 \times 10^6 \delta / l^2 \text{ psi} \quad (7)$$

or

$$\sigma = 20.54 \delta / l^2 \text{ N/M}^2 \quad (7)$$

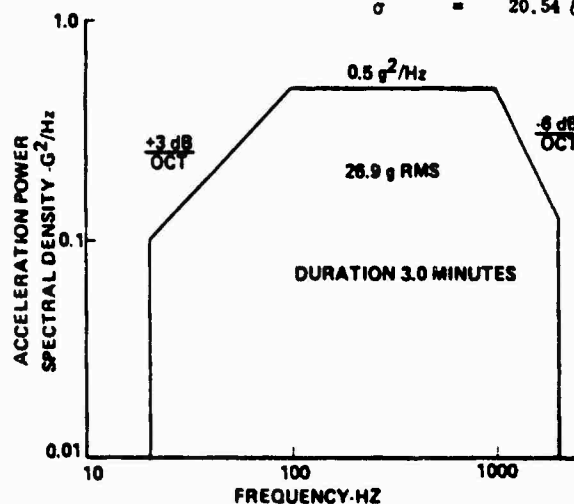


Fig. 3 - Typical Random Vibration Test Environment

TABLE 1.  
Stress in a 3.2 mm Diameter Glass Bodied Part

$l$ (inch)	$l$ (cm)	$\delta$ (mm)	$\sigma$ (N/M <sup>2</sup> )	$\sigma$ (PSI)
4	10	0.25	0.505	3487.5
		0.50	1.01	6975.
		0.75	1.515	10463.
6	15.25	0.25	0.225	1550.
		0.50	0.4493	3100.
		0.75	0.6739	4650.
8	20.3	0.25	0.1264	672.
		0.50	0.2527	1744.
		0.75	0.3791	2616.

Substitution of a few values into Equation (7) yields Table 1 which shows that larger boards provide a lower stress environment for a given deflection amplitude.

Similarly, bending stress in a lead-wire can be approximated. Consider the geometry of Figure 4 in which a resistor is at the mid-span of an assumed sinusoidal mode-shape, the classical solution for a simply supported beam or plate.

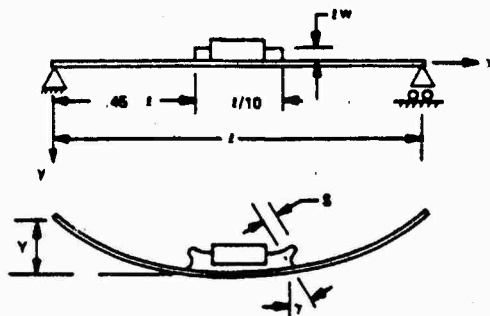


Fig. 4 - Hypothetical Resistor Lead Deformation

$$y = Y \sin \frac{\pi x}{l} \quad (8)$$

$$\gamma = \frac{dy}{dx} = \frac{Y\pi}{l} \cos \frac{\pi x}{l} \quad (9)$$

$$\delta = l_w \gamma = Y \pi \frac{l_w}{l} \cos \frac{\pi x}{l} \quad (10)$$

Let

$$x = 0.55 l$$

$$\delta = 0.49 Y \frac{l_w}{l} \quad (11)$$

$$M = 6EI \delta / l_w^2 \quad (12)$$

Let

$$E = 17 \times 10^6 \text{ psi}$$

$$\sigma = \frac{MD}{I_w} = \frac{6.36 \times 10^6 Y D}{l_w l} \quad (13)$$

Let

$$D_w = 0.005 \text{ inch (0.12 mm)}$$

$$l_w = 0.0625 \text{ inch (1.58 mm)}$$

$$\sigma = 6.888 \times 10^5 \frac{Y}{l} \text{ psi} \quad (14)$$

$$= 97 \cdot Y / l \text{ N/M}^2$$

Table 2 is compiled from Equation (14), again showing lower stress levels in larger spans for a given deflection. This is consistent with the larger radius of curvature (R) for a longer span at a specific deflection in comparison to the R of a shorter span.

Examination of Tables 1 and 2 show that at deflections as small as 0.25 mm the stress in the glass is disturbingly high on the 10 cm span. The lead wire stress is significant but not alarming; however, for wire only 2 or 3 times the illustrated diameter, the stress becomes a large fraction of the yield strength of some copper alloys. On large PWBs an rms deflection of 0.75 mm may still induce low stress, but such deflections consume all the sway space in some packages. Therefore, with some science and some

TABLE 2.  
Stress in a Lead-Wire

$l$ (inch)	$l$ (cm)	$Y$ (mm)	$\sigma$ (N/M <sup>2</sup> )	$\sigma$ (PSI)
4	10.16	0.25	0.244	1672
		0.5	0.488	3344
		0.75	0.732	5016
6	15.24	0.25	0.183	1254
		0.50	0.366	2508
		0.75	0.549	3762
8	20.32	0.25	0.122	836
		0.50	0.244	1672
		0.75	0.366	2508

judgment, 0.25 mm is recommended as a maximum rms allowable deflection. An alternate deflection rule is that deflection should be less than 0.003 times the length of the short side of the PWB, or 0.3 to 0.6 mm for 10 to 20 cm PWBs.

Acceleration boundaries must also be set since the Grms response is an indication of the overall severity of the environment that the piece-parts (relays, diodes, crystals, etc.) must endure. Heavy parts can be case off and relays chatter or transfer due to the oscillating acceleration level. On the Viking project, a PWB response environment of 60 Grms was regarded as the level at which damage becomes likely. Popular parts are today still bought to specifications of 50 to 100 Gs. Some relay types are screened with only 30 G since sweeps. Therefore, it is recommended that 50 Grms be the maximum predicted response for the PWB and chassis assemblies unless they carry relays or other fragile items in which case a maximum of 30 Grms is recommended. These criteria should be judged with the recollection that the rms response will be exceeded by a factor of 2 or more for about 3 to 4% of the duration of the test.

The final boundary to be established is based on the amount of structural damping expected. Figure 5 shows a few examples of response magnification measured on PWB and chassis assemblies having spans of 10 to 20 cm and fairly simple construction. A response magnification or "Q" of 20 to 30 is quite common. On some multi-level conglomeration assemblies with a huge amount of urethane used as both conformal coat (stucco by appearance) and staking adhesive a Q of 5 to 15 has been observed, even though specific damping treatments were not designed. On assemblies with a low-weight, thin (< 0.1 mm) application of urethane or other conformal coats, response magnification of 20 or more are usually observed. Of course, the coating is invaluable in securing items and is mandatory for all designs intended for a dynamic mech-

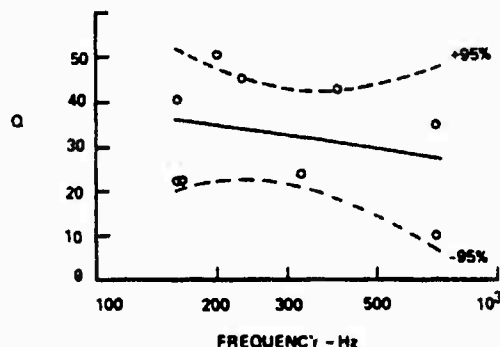


Fig. 5 - Typical Response Magnification

anical use. The damping boundaries are associated with designs in which some damping feature or treatment has been consciously installed. Although highly accurate predictions of damping can be made (References 10, 11), some simplifications in analytic approaches to package reviews warrant a nice margin in damping allowances. Through experience in correlating performance and prediction of damping, a minimum prediction of 0.3 composite loss factor (CLF) is necessary to justify the weight, space, cost, and complexity of a damping treatment. Strain energy analytically unaccounted for by the analytic mode shape usually raises the response magnification to 2 or 3 times that implied by the predicted CLF. Although the 0.3 CLF implies a Q of  $3 - 1/3$ , a measurement of the treated PWB or chassis often reveals a Q of 6 or 7 and sometimes a Q of 10. If the PWB or chassis carries something fragile like relays or crystals, then a CLF prediction of 0.5 is advisable.

Damping treatments are not always needed but are helpful. With a low stimulus, say 7 Grms and 0.05 G<sup>2</sup>/Hz, a structure with a Q of 20 or 30 and a resonant frequency of 200 Hz has a response within the



conservative region of design deflection and acceleration. But if a stiffening rib is needed to reach 200 Hz, one that also provides damping adds a comfortable margin. If the environment applied to the package is high as in Figure 3, then damping is needed to place the response predictions within low deflection and low acceleration design goals.

Further examination of Figure 2 shows the complexity accommodated by the graph. Having found the natural frequency by simple beam or plate formulas, one can deduce the amount of damping necessary (if any), or assuming a level of damping, the deflection response and acceleration response of the structure. If the analyst has a timesharing computer code or design charts for damping design, then the adequacy of the resultant design can also be clearly displayed for both development of the design and for reporting purposes. It can be seen that excessive stiffness requires the acceptance of high Grms responses, which is undesirable in that this can be damaging to crystals, filaments and relays and can cast off heavy parts. Further calculations for fatigue are needed for general derivation of the design risk graph. Miner's rule and the  $G^3t$  approximation (Reference 16) should be employed. Figure 2 was designed for nine minutes duration and for 15 to 20 cm PWB sizes.

#### Experimental Investigations

Early package designs which were found undesirably responsive were damped with a constrained layer of epoxy based viscoelastic material (References 4, 5, 6) of the same type now employed but the treatments were often 7 mm (1/4-inch) thick plus a 1.6 to 2.3 mm (0.063 to 0.09-inch) thick E-glass constraining layer. The damping was and still is applied in strips to allow maximum access to change out infant mortality parts or to make electrical design changes. Great success was achieved in rescuing responsive designs by additive damping or in preventing problems by integrally damped designs. The high environment of Figure 3 was therefore approached with respect but also confidence which turned out to be well-founded. But along the way of making the new packages, weight became extremely critical. The robust damping-stiffening strips were too heavy and too large. It was shown analytically that a thin (0.8 mm) graphite-epoxy constraining layer on a relatively thin (2.4 mm) damping material layer would work even with only 3 to 7% of the PWB area covered by the strip, but there was no data on such light treatment on such large (20 cm) PWB assemblies. Concerns were raised about panel-breaking effects and the response of the undamped panels. Tests were conducted to verify: (1) the need for damping, (2) the performance of the lightweight damping and (3) the merit of single degree of freedom integrity assessment. It was found for the environment of Figure 3 that damping is usually needed, the light

treatments can be effective if properly placed and single degree of freedom methods are adequate.

Figures 6, 7 and 8 show one of the development test specimens. Only responses normal to the PWB were measured. Figure 9 illustrates the natural frequency and response predictions for an undamped PWB. The semi-rigid boundary condition for such small boards is most appropriate. Considering this as the basic structure to be damped, a computer code based on now classical theory (Reference 9) was used to predict the composite natural frequency and composite loss factor for four light weight strip

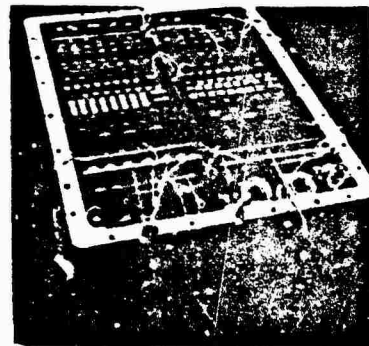


Fig. 6 - Test Article A, Cover Plate Removed



Fig. 7 - Test Specimens, Front

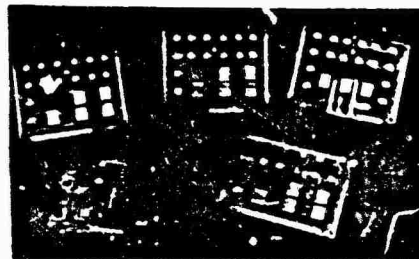


Fig. 8 - Test Specimens, Back

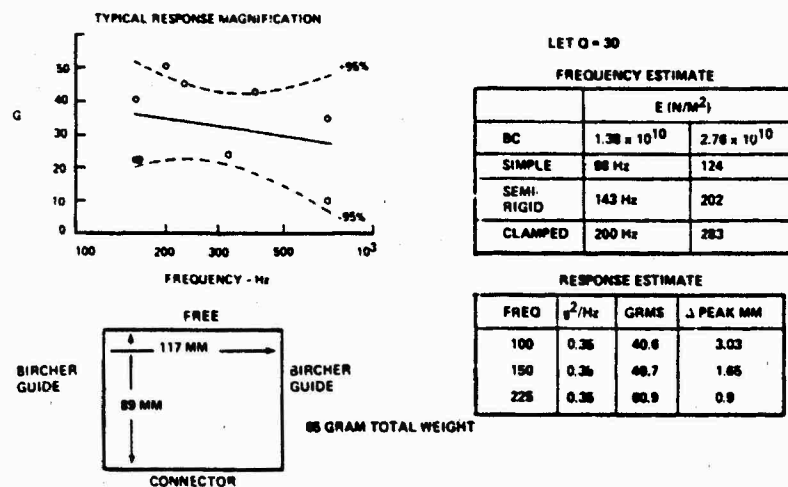


Fig. 9 - Undamped Response Prediction

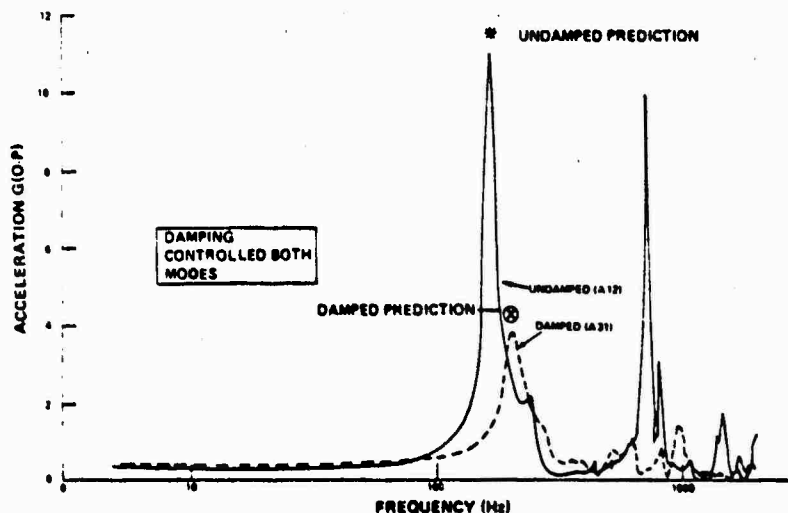


Fig. 10 - Effect of Edge Strip on Sine Vibration Response

configurations. Figures 10 and 11 show the measured sine and random vibration response of the undamped board "A12" and of the board "A31" which was damped and stiffened by one edge strip. All the boards showed a second mode. When the strip damping was properly placed and sized, the second mode was suppressed. This was accomplished on board numbers A31, A14 and A13. The first mode was nicely controlled on A32 but the second mode was uncontrolled because the free-edge strip was too stiff to be involved with that higher mode. Table 3 summarizes these results.

Figures 12 thru 15 show another test specimen. In this case, one PWB and the chassis were instru-

mented at a total of eight locations for 3 directions of response at each location. This was a large PWB (19 cm x 19 cm) assumed simply supported on all four sides and massing 320 grams while being only 1.6 mm thick. The damping-stiffening ribs were arranged in a cruciform as shown in Figures 12 and 13. A third strip at the connector minimized connector rocking modes. The cruciform strips raised the natural frequency from 65 Hz to 115 Hz (predicted and measured) and provided a CLF prediction of 0.37 and a measured CLF of 0.2 which is within the factor of 2 accounted for on the design risk curve, Figure 16. The in-axis response was found to dominate. Cross-axis responses were generally an order of magnitude lower. Chassis damping was

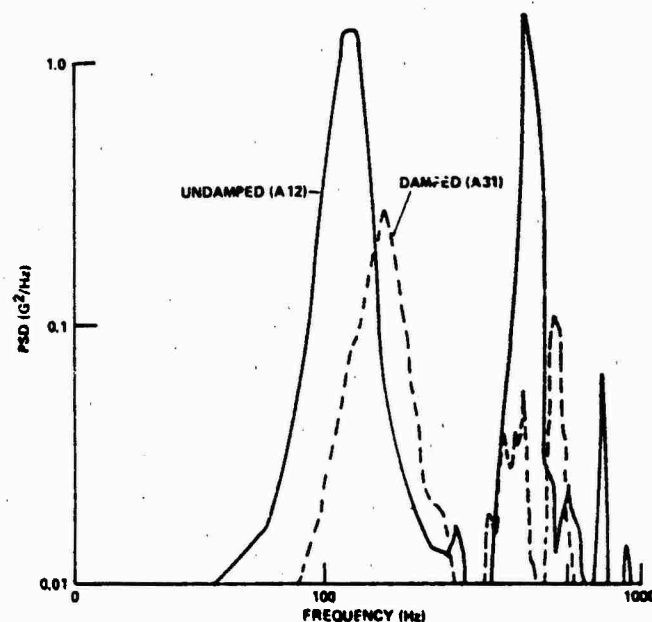


Fig. 11 - Effect of Edge Strip on Random Vibration Response

TABLE 3.  
Summary of Predictions and Measurements, Article A

Board	Configuration	Sine				Random*		Comment
		Predicted		Measured		Predicted	Measured	
		f	Q	f	Q	G <sub>rms</sub>	G <sub>rms</sub>	
A-12	Undamped	100-200	30	185	22	40-57	71	First mode good; Higher mode uncontrolled
A-31		180-258	8.7-7.95	200	7.6	24.6-28.4	33	Good
A-14		209-237	6.3-7.4	240	6.8	28-29.4	47	First mode good; Higher mode poorly controlled
A-13		258-309	7.98-6.25	285	8.2	28.4-34.6	29.5	Good
A-32		205-284	5.6-5.3	220	7.2	21-24.3	75	First mode good; Higher mode uncontrolled Edge strip too stiff to participate in 2nd mode

\* Scaled to full level

high due to friction in the Bircher guides and with the damping material (unconstrained) in the cover used for clamping and free-edge support. Higher modes were controlled on the PWB. The chassis exhibited only one mode in each direction (X and Z) parallel to the PWB. Figures 17, 18 and 19 and

Table 4 show the sine sweep response of the PWB in the axis of excitation. The X and Z responses (Figures 17 and 19) are chassis modes. Figures 20, 21 and 22 and Table 5 summarize the random vibration response which was adequately predicted (Figures 16 and 18) by the single degree of freedom

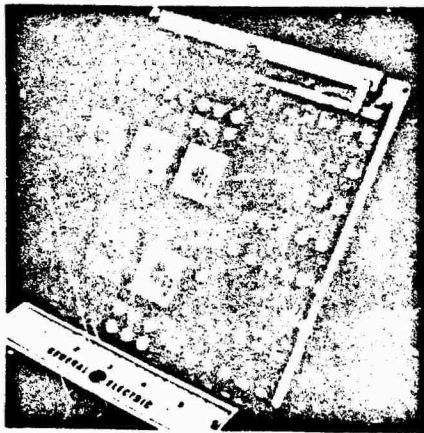


Fig. 12 - LSG Board, Conformal Coated and Damped

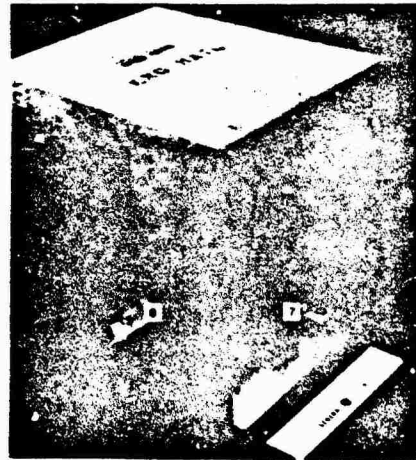


Fig. 14 - Chassis Measurement Locations 6 (Side Wall) and 7 (Cover)

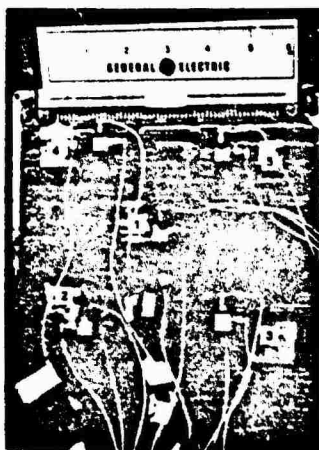


Fig. 13 - LSG Board Measurement Locations 1 thru 5

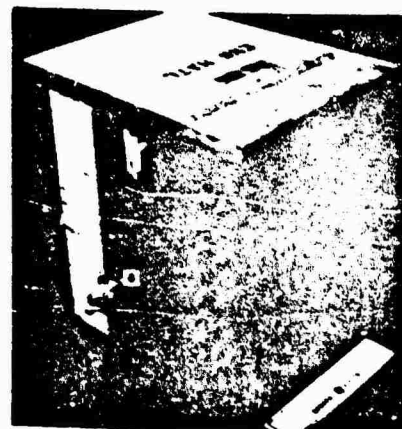


Fig. 15 - Chassis Measurement Location 8 (Side Wall)

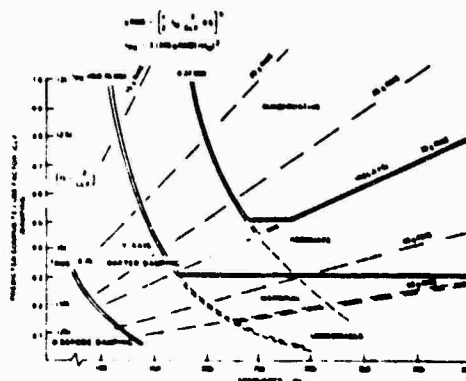


Fig. 16 - Predicted Performance of LSG Location 1 (center)

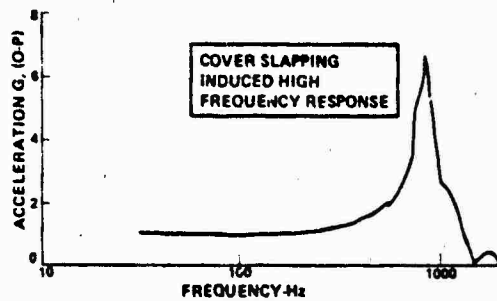


Fig. 17 - Worst PWB Sine Response to X-Sweep, Test Article B

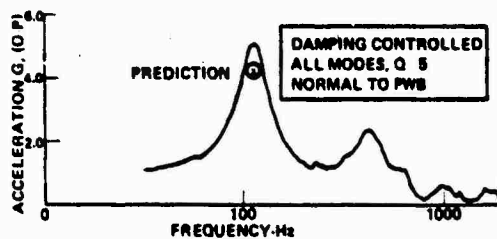


Fig. 18 - Worst PWB Response to Y-Sweep, Test Article B

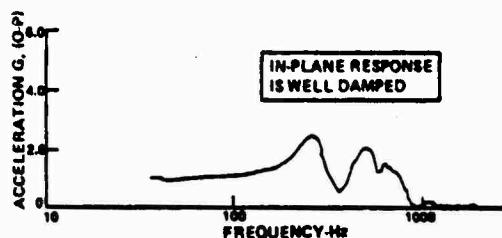


Fig. 19 - Worst PWB Response to Z-Sweep, Test Article B

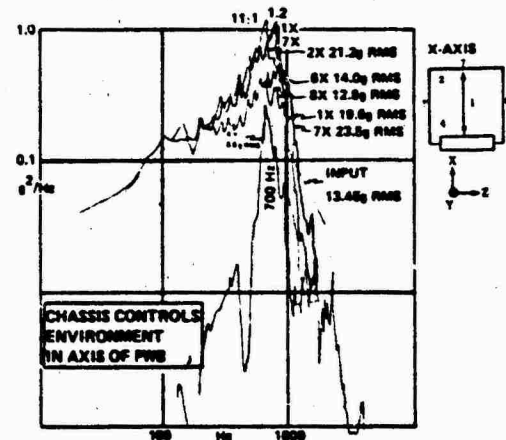


Fig. 20 - X-Axis PWB Random Vibration Environment, Test Article B

methods. The overall Grms response of Locations 1-8 are listed in Table 5 for two input levels at Location 9. Since a low frequency was expected, the development unit was subjected to only 1/2 qualification levels. The qualification unit passed the qualification level.

#### Analytic Approaches

Finite element model (FEM) of PWB assemblies as shown in Figure 23 have been employed to predict random vibration response as in Figure 24. Even when the numerical method is available and an experienced analyst uses it, the time required becomes excessive due to the natural desire to produce an accurate model and due to unique characteristics requiring origi-

TABLE 4.  
Sine Vibration Response to 1-G Sweep, Test Article B

Location	X Shake			Y Shake			Z Shake		
	X	Y	Z	X	Y	Z	X	Y	Z
1	5	0.7	0.4	0.0	5.0	0.1	0.3	0.5	2.4
2	0	1.4	1.2	0.0	3.0	0.4	0.0	0.4	2.5
3	5.4	0.9	1	0.4	3.4	0.0	0.4	0.3	2.4
4	5	1.7	0.0	0.0	2.3	0.0	0.4	0.5	2.6
5	0.7	1.7	1.4	1.2	3.7	0.0	0.7	0.4	2.5
6	3.2	0.5	0.5	0.4	1	0.0	0.2	0.7	2.7
7	6.9	1.0	0.9	1.2	1	0.5	0.0	0.5	1
8	2.0	0.0	0.7	0.2	1	-	0.2	0.0	2.0
Dominant Frequency	900	-	-	-	115	-	-	-	200

nal modeling for each case. For the PWB in Figure 23, eighteen modes were predicted below 2000 Hz. Damping was assigned to each mode as a function of frequency, related to previous PWB test data. No damping treatment was applied so the first mode at 155 Hz was assigned damping equivalent to a Q of 50. The 29 Grms of Figure 24 was integrated by the computer but the T-B formula also predicts it well.

$$\text{Grms} = \sqrt{\frac{\pi}{2}} 155 (50) 0.06 = 27$$

The fundamental frequency is also adequately estimated by hand methods as in Reference 13.

$$f = \frac{17 (0.062) 10^4}{(5)^2} \sqrt{\frac{2}{0.20} \frac{0.286}{29}} = 133 \text{ Hz}$$

$$= \frac{ct 10^4}{a^2} \sqrt{\frac{E}{\gamma} \left( \frac{Y}{E} \right)_{\text{REF}}}$$

where

17 is a shape factor related to the ratio of PWB length and width, in this case  $a/b = 5/6$

$t$  = thickness (inch)

$10^4$  = constant of proportionality

$a$  = length of short side

$E/\gamma$  = ratio of PWB modulus and density

$(\gamma/E)_{\text{REF}}$  = ratio of steel density and modulus

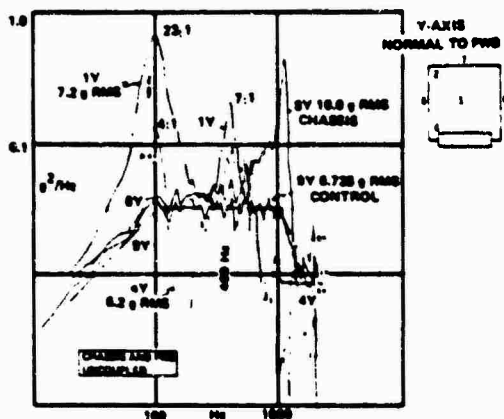


Fig. 21 - Y-Axis PWB Random Vibration Environment

Therefore the FEM is not really needed to predict the first mode and the first mode dominates the response, so single degree of freedom methods are adequate estimators of response. Similarly the deflections are largest in the first mode, so the integrity can be well estimated by hand in less than 1 hour versus the FEM which took 1 week.

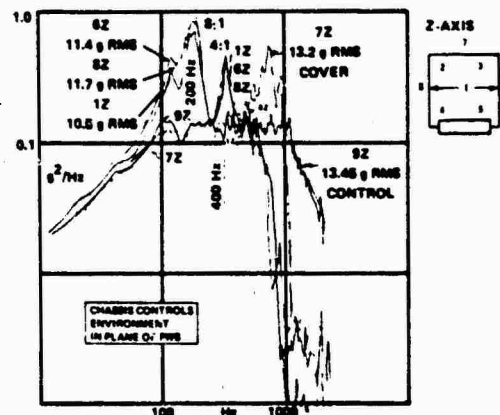


Fig. 22 - Z-Axis PWB Random Vibration Environment, Test Article B

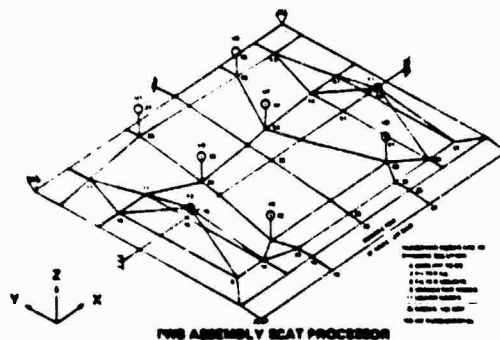


Fig. 23 - PWB Finite Element Model

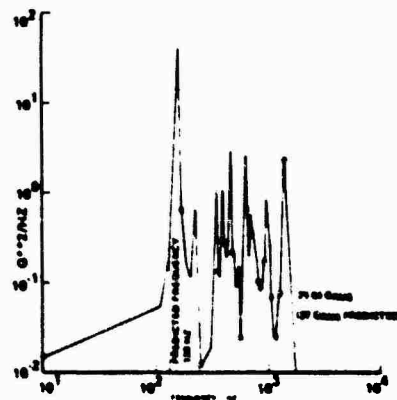


Fig. 24 - Acceleration PSD Response, Z-Axis of PWB FEM

TABLE 5.  
Random Vibration Environment Summary, Test Article B

Location	X Shake			Y Shake			Z Shake		
	X	Y	Z	X	Y	Z	X	Y	Z
1. Center PWB	19.6/ 12.0	5.7/ 2.8	1.7/ 1.1	3.0/ 1.75	15.8/ 7.2	1.5/ .72	1.65/ 1.08	1.9/ 1.05	10.5/ 8.0
2. +X-Z PWB	21.2/ 12.5	5.5/ 2.9	2.8/ 1.6	3.9/ 2.05	9.4/ 4.75	3.3/ 1.55	1.9/ 1.3	2.9/ 1.32	11.5/ 8.9
3. +X+Z PWB	18.5/ 11.5	3.0/ 2.2	2.8/ 1.8	3.3/ 1.85	10.8/ 5.6	3.4/ 1.7	1.8/ 1.05	2.3/ .95	10.8/ 8.5
4. -X-Z PWB	19.4/ 11.5	8.0/ 6.0	4.8/ 2.3	4.4/ 2.2	10.9/ 6.2	3.0/ 1.7	1.75/ 1.05	5.0/ 1.95	10.3/ 8.3
5. -X+Z PWB	21.5/ 13.5	5.8/ 3.1	5.4/ 3.1	5.7/ 3.3	9.0/ 5.2	3.8/ 2.0	2.2/ 1.85	2.1/ 1.13	10.4/ 8.3
6. Chassis +Z	14.0/ 6.8	2.2/ 1.2	3.3/ 1.5	1.9/ 1.07	18.3/ 8.7	4.7/ 2.5	1.45/ 0.75	8.2/ .86	11.4/ 8.9
7. Cover	23.5/ 14.5	9.0/ 3.3	3.2/ 2.0	4.4/ 2.35	18.5/ 8.7	1.85/ .82	2.4/ 1.2	1.9/ 1.18	13.2/ 7.0
8. Chassis -Z	12.8/ 7.0	4.0/ 2.3	2.6/ 1.8	1.2/ .82	1.2/ 1.0	18.0/ 1.0	5.7/ .78	1.5/ .85	11.7/ 7.0
9. Control	13.45/ 8.7	1.9/ .85	1.1/ .56	.60/ .34	13.4/ 8.7	1.5/ .74	1.8/ .72	2.3/ 1.08	13.45/ 8.7
	C-150			C-220			C-150		
PWB Dominate Frequency	In-Axis PWB Linearity 82% Chassis 89% 700 Hz			In-Axis Linearity PWB 96.2% Chassis 92.7% 100 Hz			In-Axis Linearity PWB 83.6% Chassis 86.5% 200 Hz		

(Linearity based on average in-axis response, e.g., 96.2% means the average response to the 13.4 Grms stimulus is 1.924 times the average response to the 8.7 Grms stimulus.)

#### Summary and Conclusions

The methods described were applied to several designs which have recently undergone qualification testing at 35 Grms. Less than 10% of the packages experienced failures in random vibration testing. In development testing, it was verified that the combination of the design risk graph, hand calculations, and simple damping strips positioned with some thought as to mode shape was highly effective in identifying and eliminating high risk PWB and chassis designs. The balance of the package design integrity procedures revolved around producing packages which were indeed analyzable and well-behaved structures.

Damping treatments can be plates or strips. Plates have the advantages of controlling all modes but have the disadvantages of obscuring the structure, rendering repairs or modifications difficult. Strips require a stiffer damping material than plate damping but

such materials are available (References 4, 5, 6, 10, 11). Strips occupy only about 5% of the surface but require some care in placement to control the desired modes. Fortunately, most PWB and chassis assemblies have only one or two strong modes to control and the mode shapes are fairly obvious.

It is therefore concluded that a few steps in package design can greatly enhance mechanical reliability. These steps include:

1. Make a design risk graph for the test environment.
2. Lay out packages which behave like plates and which minimize cross-coupled response.
3. Lay out design details which produce a recognizable boundary condition.

4. Use plate formulas for fundamental bending mode predictions.
5. Use test data for damping estimates when damping treatments are not discretely designed.
6. Design in damping strips for moderate stiffness and high damping when the test environment warrants. Remember to account for the temperature sensitivity of viscoelastic materials.
7. Avoid excessive stiffness especially if a high performance damping treatment is included.

Finally, it is recognized that a design risk graph can be made for sinusoidal test environments as well as random vibrations. Such a graph must consider duration of test and structure span as well as frequency, damping, and acceleration.

#### REFERENCES

1. Stahle, C. V., "A Method for Determining the Applicability of System Level Spacecraft Vibration Qualification Testing," Thesis for Drexel Institute of Technology, College of Engineering Graduate Studies, 1966.
2. Stahle, C. V., "Estimate of the Effect of Spacecraft Vibration Qualification Testing of Reliability," Shock and Vibration Bulletin No. 36 P7, February 1976.
3. Stahle, C. V., "Cost Effectiveness of Spacecraft Vibration Qualification Testing," Proc of IES 20th Annual Meeting, May 1974.
4. Stahle, C. V. and Tweedle, Dr. A. T., "A Layered Viscoelastic Epoxy Rigid Foam Material for Vibration Control," Shock and Vibration Bulletin No. 42, P4, January 1972.
5. Stahle, C. V., Tweedle, Dr. A. T. and Gresko, T. M., "Viscoelastic Epoxy Shear Damping Characteristics," Shock and Vibration Bulletin No. 43, P4, June 1973.
6. Stahle, C. V. and McCandless, W. H., "Controlling Vibration of Viking Lander Electronic Packages," 44th Shock and Vibration Symposium, December 1973.
7. Nashif, A. D., "Materials for Vibration Control in Engineering," 43rd Shock and Vibration Bulletin, 1973.
8. Ferry, J. D., "Viscoelastic Properties of Polymers," 2nd Ed., New York, John Wiley and Sons, Inc.
9. Rose, D., Ungar, E., and Kerwin, Jr., E., "Damping of Plate Flexural Vibrations by Means of Viscoelastic Laminas in Structural Damping," J. Ruzicka (Ed.), The American Society of Mechanical Engineers, 1959.
10. Medaglia, J. M., "Application of SMRD Damping to the IUE Scientific Instrument Structure," 75SD4268, November 21, 1975, with Stahle, C.V.
11. Medaglia, J. M., "SMRD Damping Applications," Conference on Aerospace Polymeric Viscoelastic Damping Technology for the 1980's, AFFDL-TM-78-78-FBA, July 1978.
12. Nashif, A. D. and Halvorsen, W. G., "Design Evaluation of Layered Viscoelastic Damping Treatments," Sound and Vibration Materials Reference Issue, July 1978.
13. MacDuff, J. N., and Felgar, R. P., "Vibration Frequency Charts," Machine Design, January 1957.
14. Steinberg, D. S., "Avoiding Vibration in Odd-Shaped Printed-Circuit Boards," Machine Design, May 20, 1976.
15. Thompson, W. T., Vibration Theory and Applications, Prentice-Hall Inc. © 1965, P319, Equation 10.3-8.
16. Stahle, C. V., Gongloff, H. R., Young, J. P. and Keegan, W. B., "Shuttle Payload Vibro-acoustic Test Plan Evaluation," Proc. of 3rd Aerospace Testing Seminar, IES, September 1976.



#### DISCUSSION

Mr. Rogers (Airforce Flight Dynamics Laboratory): When you add a strip like that or any kind of damping treatment, you also add stiffness and mass. How do you know that your before and after comparisons are valid? How do you know that you did not change mode shapes or introduce a mode line in the circuit board?

Mr. Medaglia: The analytical method accounts for the mass and stiffening effect of the damping strip and through experience and analytical procedures we developed the ability to not significantly change the mode shape. It is important to damp the mode you want to damp rather than to create a panel breaker. In the process we typically raise the natural frequency of those 17 cm. printed circuit boards from 50 Hz or less to well over 100 Hz. We are still damping the fundamental plate or the "oil canning" mode with that design.

Mr. Rogers: Do you feel in most cases that the mode shapes do not change and your before and after comparisons are valid?

Mr. Medaglia: That is correct. By looking at the data from experiments like that second test article, which had a fair distribution of accelerometers, you can see that the mode shape is the fundamental and it hasn't been changed.

## Shock and Blast

### AN OVERVIEW OF SHOCK ANALYSIS AND TESTING IN THE FEDERAL REPUBLIC OF GERMANY

K.-E. Meler-Dörnberg

Institut für Mechanik

Technische Hochschule Darmstadt

#### 1. INTRODUCTION

Differences in analysis or test conceptions are not so much an international problem but obviously more an interdisciplinary one. The "inside" information in the particular branches is fairly close despite of country borders but far less is the "outside" co-operation between different branches or even between numerical and experimental workers on the same subject.

Methods in earthquake engineering for example are the same in USA and Germany, just so as the handling of car crash or reactor safety problems. Environmental tests of electrical equipment were carried out by the same IEC standards even with identical test machines, and if there are some new ideas for naval shock test specifications, they will be discussed in the Netherlands as well as in USA and Germany.

Therefore it is really not necessary to cover the whole field of shock analysis and testing and it may be allowed to confine this presentation on some ideas of data reduction which might be of a more general interest. The ideas are realized in the German

#### "Shock Safety Requirements for Installations in Shelters"

which are used in the area of civil defense and with slight changes in the responsibility of the army, too.

The main object is a relevant approximation and classification of input shock pattern by sets of only few significant parameters, it allows

1. Definition of shock reliability classes as well as shock design loads and shock test parameters by the same values
2. Simplification of analysis and test procedures which might encourage a broader individual responsibility and will reduce the cost of sophisticated engineering.
3. Comparison of different methods or specifications by means of this approximation and acceptance of otherwise tested or designed equipment if the requirements are met.

## 2. THEORETICAL BACKGROUND

### 2.1 INTENTIONS AND CONCLUSIONS

The success of data reduction depends highly on the quality of the chosen reference parameters and the form of data presentation.

The main intentions are:

1. Evaluation and definition of system-relevant input quantities and of input-relevant system properties as reference parameters.
2. Uniform plotting of the various deduced shock data as input values, exposure limits, safety requirements, test and design parameters, standard Fourier and response spectra in terms of the defined reference parameters.

Obviously there are three different possibilities to reduce the variety of parameters:

- a) Reduction of the given input shock pattern to only few significant values.
- b) Reduction of the real object to a simple mathematical or structural model.
- c) Evaluation of input relevant properties of the affected system.

The proposed kind of data reduction which leads to coherent presentation of input and tolerance data, shall define a way of comparing the various design methods and to sum up the numerous research results.

The indicated reference parameters may be used in two levels of application,

1. as generalized research results or safety requirements.  
The proposed reference parameters themselves are approximate solutions of a shock problem. They represent the lowest level of approximation, i. e. the highest grade of data reduction which remains meaningful;
2. as reference parameters.  
In more detailed or sophisticated researches they may be used as reference parameters for uniform data presentation, because they expose the most significant characteristics of a shock problem.

### 2.2 FORMAT OF DATA PRESENTATION (the Shock Net)

The mechanical problems we have to deal with, have predominantly a multiplicative

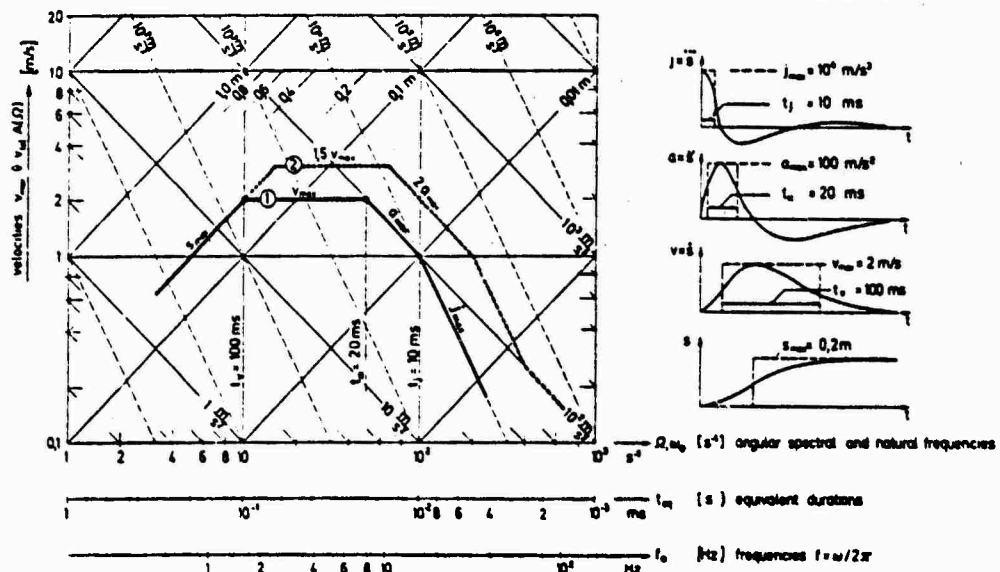


Fig. 1 - Classification of shock input parameters  
 (1) shock polygon and approx. Fourier spectrum  
 (2) shock response polygon of undamped simple systems

character, for instance relations between acceleration - velocity - or displacement amplitudes and frequency of a harmonic motion, or integral transformations from the time to the frequency domain. Therefore, it is evident to use logarithmic graphs. Figure 1 shows a graph of the suggested type. It is the wellknown multi-scaled logarithmic raster that already has found widespread application in the field of vibration and control techniques but has been adapted and completed for shock problems by some additional scales. In the following chapters we will see that these multiplicative connections will lead to approximate relations between values of time functions and their Fourier or response spectrum without further calculation and that they provide an overall view whether an input shock exceeds a given exposure boundary or meets a specified test requirement. The scales are:

- Abscissa:**  
inverted time axis, dimensions  $s^{-1}$ , scaled for spectral angular frequencies  $\Omega$  ( $s^{-1}$ ), natural angular frequencies  $\omega$  ( $s^{-1}$ ), equivalent durations  $t_{eq}(s)$  so that scale  $\Omega = \text{scale } \omega = \text{scale } 1/t_{eq}$ . Furthermore, a 2  $\pi$  shifted scale for frequencies  $f = \omega/2\pi$  (Hz) or natural periods  $T = 1/f$  may be provided for convenience.
- Ordinate:**  
velocity axis, dimensions m/s, scaled for spectral modulus  $A(\Omega)$  of acceleration histories  $a(t)$ , maximum velocities or total velocity changes of shock inputs  $v_{max}$ ; velocity response amplitude  $\dot{\phi}$  or tolerable velocities  $v_{tol}$ .
- Angled scales for the corresponding displacement values  $s$ , dimension (m); acceleration values  $a$ , dimension  $m/s^2$ ; and jerk values  $j$ , dimension  $m/s^3$ .**

#### EXAMPLES:

- A harmonic motion is represented by a point on the graph exhibiting the various amplitudes and frequency  $s_{\omega} = \dot{\phi} = s/\omega = j/\omega^2$ .
- A rectangular acceleration pulse is represented by the intersection of the velocity, acceleration and duration scales  $v = a \cdot t$ , i. e., each intersection of two lines represents an (equivalent) rectangular pulse.

### 2.3 CHARACTERISTIC FEATURES OF SHOCK FUNCTIONS (the Shock Polygon)

For all shock functions (functions having only values in the positive time range) Fourier and Laplace transform are identical when basing on the specific definition

$$X(\Omega) = \int_{-\infty}^{\infty} x(t) e^{-i\Omega t} dt = \int_0^{\infty} x(t) e^{-p t} dt$$

where  $\Omega$  is the spectral angular frequency and (the imaginary part of) the Laplace operator  $p = i\Omega$ , respectively.

Using the limit theorems of Laplace theory we find the asymptotic modulus values if  $x(0)$  and  $x(\infty)$  exist

$$\lim_{p \rightarrow \infty} [p X(p)] = \lim_{t \rightarrow 0} [x(t)]$$

$$\lim_{p \rightarrow 0} [p X(p)] = \lim_{t \rightarrow \infty} [x(t)]$$

Taking for example the shock function  $a(t)$  of Figure 1, these asymptotic relations can be applied to the derivative  $j$ , because  $j(0) = j_{max}$ , and to the double integral  $s$ , because  $s(\infty) = s_{max}$  with the resultant asymptotes [1,2]

$$\Omega \rightarrow \infty : \Omega J(\Omega) = j_{max}$$

$$\Omega \rightarrow 0 : \Omega S(\Omega) = s_{max}$$

Because  $J(\Omega) = \Omega A(\Omega)$  and  $S(\Omega) = A(\Omega)/\Omega^2$ , the final results are the asymptotic modulus values  $A(\Omega)$

$$\Omega \rightarrow \infty : A(\Omega) = j_{max}/\Omega^2$$

$$\Omega \rightarrow 0 : A(\Omega) = s_{max} \cdot \Omega$$

as lines  $j_{max}$  and  $s_{max}$  in the proposed format.

Approximations in the medium frequency range in setting  $t_j \rightarrow 0$  and  $t_a \rightarrow 0$  are:

$$t_j \rightarrow 0 : A(\Omega) = a_{max}/\Omega$$

$$t_a \rightarrow 0 : A(\Omega) = v_{max}$$

The polygon, Figure 1, line (1), which is formed by the values  $s_{max}$ ,  $v_{max}$ ,  $a_{max}$  and  $j_{max}$  of a given function  $a(t)$  is therefore an approximate solution of the Fourier transform  $a(t) \leftrightarrow A(\Omega)$ . Let us call it the SHOCK POLYGON.

The intersections of this polygon exhibit very informative relations between a time function and its spectrum. The ratios of two maximum values of two successive time functions define certain time values which may be defined as equivalent durations, e.g.

$$\text{eq. duration of jerk } t_j = \frac{a_{max}}{j_{max}}$$

$$\text{eq. duration of acceleration } t_a = \frac{v_{max}}{a_{max}}$$

eq. duration of velocity  $t_v = \frac{s_{\max}}{v_{\max}}$

They represent the duration of an area equivalent rectangular pulse.

The polygon intersections in the frequency domain exhibit another group of relations.

corner frequency  $\Omega_j = \frac{j_{\max}}{a_{\max}}$

corner frequency  $\Omega_a = \frac{a_{\max}}{s_{\max}}$

corner frequency  $\Omega_v = \frac{v_{\max}}{s_{\max}}$

The above definitions establish very close connections between the time and frequency domain

$$t_j = \frac{1}{\Omega_j}; \quad t_a = \frac{1}{\Omega_a}; \quad t_v = \frac{1}{\Omega_v},$$

which lead to the stated interrelation between the abscissa scales  $\Omega_{eq} = 1/t_{eq}$ .

Besides, the corner frequencies or equivalent durations mark per se the validity range of approximation in which a shock function can be replaced alternatively by an acceleration, velocity or displacement step.

The approximation of a Fourier spectrum by the maximum values of time derivatives is very close for all functions with only one discontinuity, for example all combinations of e-functions without time lags (phase minimum functions). It gradually becomes less precise for rougher or more oscillating histories.

#### Construction of an upper spectrum limitation.

The upper limits of a Fourier spectrum may be of special interest for acoustics and structural design work where linear, small-damped systems have to be investigated. In contrast, mean spectral values which are represented by the shock polygon are more significant for safety or statistical performance applications.

The upper limit of a spectral modulus can be found by summing up all changes (ups and downs) of the time functions instead of using the simple maxima values.

Figure 2 shows as an example a double-sine acceleration pulse, its exact Fourier spectrum (1), the shock polygon formed by the simple maxima  $s_{\max}$ ,  $a_{\max}$ ,  $j_{\max}$  (2), and the upper limit formed by the sums  $s_{\max}$ ,  $2v_{\max}$ ,  $4a_{\max}$ ,  $8j_{\max}$ .

#### Valuation of the deduced reference parameters

We must ascertain now that the deduced reference parameters not only exhibit plain relations between time functions and their spectra but that they are also relevant input parameters with respect to system responses or tolerance limits.

#### The convolution integral

Linear system analyses, using approximate solutions of the Duhamel or convolution integral lead directly to the same result and show that the exhibited maxima of a shock input and its derivatives are predominant and response relevant values of a shock input [1].

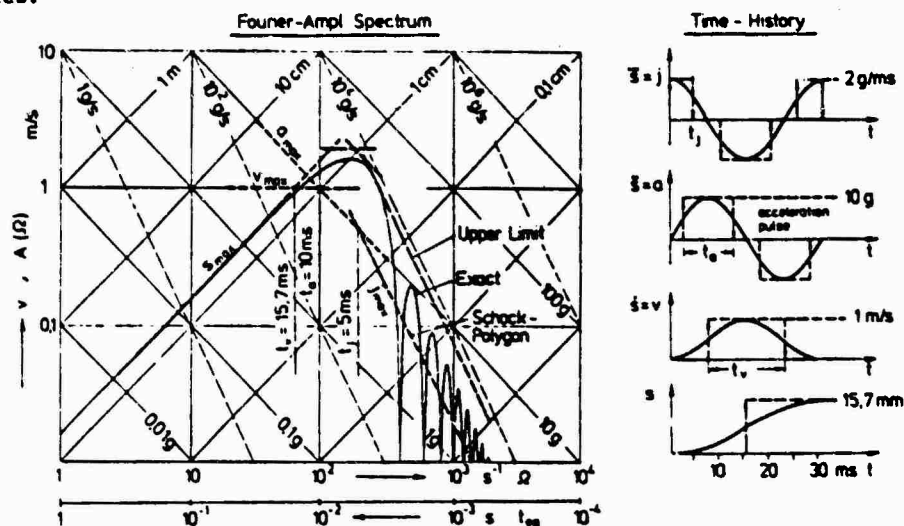


Fig. 2

## 2.4 SHOCK RESPONSE SPECTRA (the Shock Response Polygon)

The simplest response spectrum is that of the oscillatory parts of the residual response of an undamped simple linear system.

A comparison of the Fourier spectrum with this residual response spectrum by means of the Fourier integral and the convolution integral confirms the well-known similarity of both solutions. The corresponding values are

spectral modulus and velocity response amplitude  $A(\Omega) \rightarrow \dot{Q}$ ,

spectral angular frequency and natural system frequency  $\Omega \rightarrow \omega$ .

Conclusion: In the proposed format of the shock net, where scale  $\Omega$  = scale  $\omega$ , and scale  $A(\Omega)$  = scale  $\dot{Q}$ , the Fourier spectrum and this residual response spectrum have exactly the same curve, thus, the shock polygon is not only an approximation to the Fourier spectrum but also to this response spectrum.

Generalized (approximate) response spectra can be obtained from the shock polygon by calculating the various step response of the specific type of systems (e.g. damped, undamped) and the response of interest (e.g. max. relative displacement, absolute acceleration). A generalized shock response diagram, thus originates in the polygon by weighting each range. It may be called SHOCK RESPONSE POLYGON.

Figure 1 line (2) shows the standard shock spectrum for relative displacement and absolute acceleration of single-degree-of-freedom systems with small or no damping as used in the field of shock testing and isolation. The weighting factors are  $1 s_{\max}$ ;  $1.5 v_{\max}$  and  $2 a_{\max}$  up to  $\omega = 2/t_j$ .

### Summary and instructions

The quantifying of an input shock is based on typical peak values of a shock function and its appropriate derivatives and integrals, e.g. max. displacement, velocity, acceleration, and jerk if applicable, see Figure 1. They form the SHOCK POLYGON from which several important relations can be deduced as under:

- The time coordinates of the intersections indicate the equivalent pulse durations  $t_v$ ;  $t_a$ ;  $t_j$ .
- The shock polygon approximates a given shock by a couple of step functions, e.g. an acceleration step  $a_{\max}$ , a velocity step  $v_{\max}$ , and a displacement step  $s_{\max}$ . The intersections indicate the validity range of approximation.

- The shock polygon is an approximation to the modulus of the Fourier spectrum  $A(\Omega)$  of the acceleration  $a(t)$ , i.e. it approximates the Fourier transform of  $a(t)$ . Thus it is a generalized Fourier spectrum.

- It also approximates the residual response spectrum of undamped single-degree-of-freedom systems with natural angular frequencies  $\omega$ . The responding vibration amplitudes  $\dot{s}$ ;  $\dot{Q}$  or  $\dot{s}$  can be read off the corresponding scales for displacement, velocity or acceleration.

If some of the values, e.g.  $j_{\max}$ ,  $a_{\max}$  or  $s_{\max}$  are not known (or are infinite), the polygon reduce to a straight line, e.g.  $v_{\max}$  which indicates that all other values are assumed to be infinite.

Shocks having the same shock polygon, have approximately the same frequency content but may differ more or less in phase characteristics. The remaining additional information of an actual pulse shape has only second-order quality.

In the case of transient vibrations (e.g. earthquake motions) the generalized Fourier spectrum of a polygonal type is a shock polygon and thus defines the basic parameters of an equivalent shock.

## 2.5 SHOCK RELEVANT SYSTEM PROPERTIES (the Exposure Polygon)

Relations between response spectra and tolerance limit boundaries.

In linear systems the relations between a maximax response spectrum and the corresponding exposure limit boundary is evident. Both solutions are merely inverse interpretations of the same problem.

A maximax response spectrum exhibits the maximum response values of a set of equal systems excited by one specific shock input as function of the system frequency  $\omega$ . Figure 3a shows the max. acceleration response  $\ddot{x}_{\max}$  of damped linear simple systems ( $\omega$ ) to a double-sine acceleration input which is defined by the value  $v_{\max}$  and the equivalent duration,  $t_a$ .

An exposure limit boundary exhibits the limit values of a set of equally shaped input shocks which excite a specified tolerable response value of the given system as function of the shock durations. Figure 3b shows the input tolerance values  $v_{\text{tol}}$  of all double-sine input shocks of various equivalent durations  $t_a$ . The tolerance criterion is the tolerable system response  $\ddot{x}_{\text{tol}}$ .

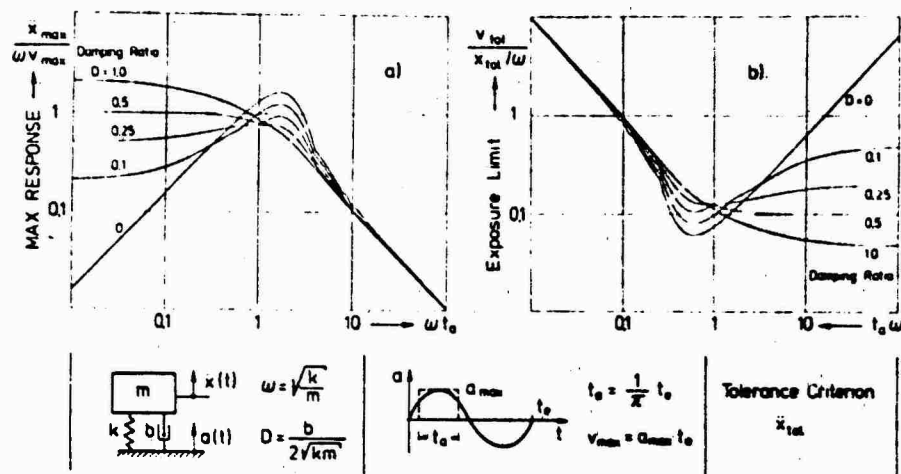


Fig. 3 - Equivalence of response spectra a) and exposure limit boundaries b) in linear systems

For linear systems and logarithmic plotting the two results in Figure 3a, b are reciprocal congruent curves.

The ensemble of shock inputs of the same pattern (e.g. all double-sine-acceleration pulses, Figure 3b) affecting the same response value (e.g. tolerable relative displacement or stress) form a specific exposure limit boundary. Each specific tolerance criterion creates another special limit boundary.

In general, the exposure limit boundary for a specific system with one criterion considering all various types of shock inputs is a multi-dimensional envelope area which can be obtained by means of modelling techniques or numerous series of shock tests.

A useful approximation which reduces the envelope area to a simple line, is the envelope of all tolerable shock groups represented by their shock polygons. As further approximation, which represents the highest grade of meaningful data reduction, this boundary can be approximated by a polygonal line, see Figure 4, which may be called the EXPOSURE POLYGON.

The exposure polygon requires the following relevant shock properties of the affected system:

- a) Steady acceleration limit  $a_{tol}$  (static load capacity):  
the asymptotic value for tolerable long-duration shocks with low jerk values ( $j_{max} \rightarrow 0$ ).
- b) Acceleration step limit,  $a_s tol$ :  
the value of the tolerable acceleration step (sudden applied load,  $j_{max} \rightarrow \infty$ )

which is related to the steady acceleration limit by means of the dynamic load factor DLF ( $=$ )  $= a_{tol}/a_s tol$ . The transition range from the steady acceleration limit  $a_{tol}$  to the acceleration step limit  $a_s tol$  is given by the tolerable jerk  $j_{tol}$  which creates no significant overshooting.

- c) Velocity step limit  $v_s tol$ :  
the shock tolerance for relatively short acceleration pulses which is related to the energy capacity or the wave resistance of the system.
- d) Displacement step limit  $s_{tol}$ :  
the shock tolerance value in the case of sudden displacement changes which is related to the deflection ability of the system. In viscous damped or continuous systems  $s_{tol}$  is zero.

The shock exposure polygon applies approximately to all types of shock, and thus is a shock relevant property of the system and its tolerance criterion.

#### SUMMARY AND INSTRUCTIONS

The exposure polygon as an approximate tolerance boundary is a useful tool in orientation and planning for more detailed theoretical or experimental studies. It defines typical criteria related system properties and the range of their relevance;

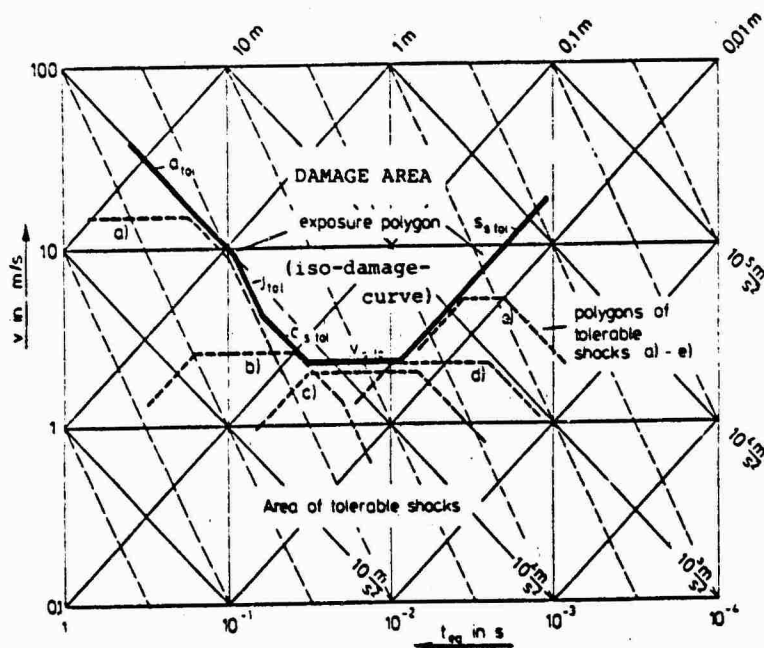


Fig. 4 - Definition and elements of the exposure polygon

- static load capacity ( $t_j > 10/\omega_0$ )
- step load capacity ( $t_a > 1/\omega_0$ )
- impulse load capacity ( $t_a < 1/\omega_0$ )
- deflection ability ( $t_v < 1/\omega_0$ )
- dynamic load factor ( $1 < \omega_0 t_j < 10$ )

In linear systems the term  $\omega_0$  represents the lowest system frequency, in nonlinear systems an equivalent corner frequency.

### 3. SHOCK SAFETY REQUIREMENTS FOR INSTALLATIONS IN SHELTERS 3

#### 3.1 SOURCES OF INPUT DATA

Weight and stiffness of protective concrete structures normally are much higher than those of the installed equipment. Therefore interaction phenomena between structure and installations can be neglected and the motion of the structure can be assumed as the Shock input. A reasonable number of calculated structure responses in subjection to different weapon loadings, structure design and location, behaviour of soil were collected from literature, and additional calculations were performed. The

results were compared by means of their significant values both in the time and frequency domain, using the above explained reference parameters in order to get a reliable picture of the intensity and frequency range of the Shock excitations to be considered.

#### 3.2 CLASSIFICATION OF SHOCK PERFORMANCE

With respect to this standard, the required shock input is sufficiently defined by a shock polygon, exhibiting the following time history values

- max displacement  $s_{\max}$
- max velocity (change)  $v_{\max}$
- max acceleration  $a_{\max}$
- max jerk  $j_{\max}$

The parameters of the shock polygon specify both, the maximum values of the applied shock to be considered, and the minimum values of the test or design parameters to be required. An upper tolerance limit for test or design parameters is not fixed.

Two series of standard reliability classes RK were defined:

1. Series "10 ms" having equivalent pulse durations

$$t_a = v_{\max}/a_{\max} = 10 \text{ ms}$$

and equivalent rise times

$$t_j = a_{\max}/v_{\max} = 4 \text{ ms.}$$

It represents nuclear blast induced shocks.



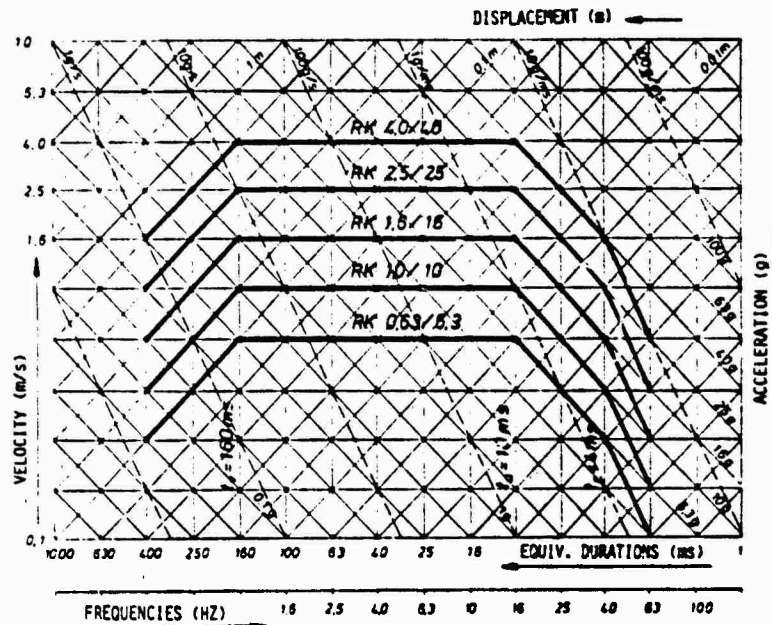


Fig. 5 - Standard classes of shock reliability (RK) and shock test parameters for equipment in shelters (series "10 ms").

2. Series "4 ms" with equivalent pulse durations

$$t_a = v_{\max}/a_{\max} = 4 \text{ ms}$$

and equivalent rise times

$$t_j = a_{\max}/r_{\max} = 1.6 \text{ ms}$$

as a necessary adaption to the effect of conventional weapons.

Both series have the same equivalent duration of the velocity shape

$$t_v = s_{\max}/v_{\max} = 160 \text{ ms}.$$

A standard class of shock performance (RK) is denoted by the values of its main parameters  $v_{\max}$  (in m/s) and  $a_{\max}$  (in g). The standard classes of series "10 ms" are listed in the following table and plotted in Figure 5.

The increments of all parameters follow the standard series  $10^{0.2}$  with steps of 1,6 (or 4 dB), they have the numerical values 0.63; 1.0; 1.6; 2.5; 4.0; 6.3; 10; ...

Generally, the following classes of shock reliability are to be applied, if no other classes are required by the user by reason of importance, situation or economy of the structure.

- RK 0.63/6.3 - publish shelters for basic protection;
- buried shelters S 3\* and basements of above-ground shelters, if situated in stiff subsoil;
- RK 1.0/10 - buried shelters S 3 if situated in soft subsoil;
- RK 1.6/16 - private shelters S 3 (light constructions);

Series "10 ms"		Main Parameters		Related Parameters	
class		$v_{\max}$	$a_{\max}$	$s_{\max}$	$j_{\max}$
Rk	0.63/6.3	0.63 m/s	6.3 g	10 cm	1.6 g/ms
RK	1.0 /10	1.0 m/s	10 g	16 cm	2.5 g/ms
RK	1.6 /16	1.6 m/s	16 g	25 cm	4.0 g/ms
RK	2.5 /25	2.5 m/s	25 g	40 cm	6.3 g/ms
RK	4.0 /40	4.0 m/s	40 g	63 cm	10 g/ms

- cover-plates of public shelters S 3;
- above-ground stories of shelters S 3;

- RK 2.5/25 - cover-plates of shelters S 3;
- RK 4.0/40 - shelters S 9 \*)
- outside walls of above-ground shelters S 3;
  - cover-plates of shelters S 9.

\*) S 3; S 9: specification of shelters with higher protection levels, to resist blast overpressures of 3 and 9 bar respectively.

### 3.3 SHOCK TEST EVALUATION

The values of the shock motions of the anchor-points of the equipment are the relevant parameters in respect to the shock reliability.

The evaluation has to be based on the smoothed histories (faired curves) of the recorded functions. See Figure 6.

According to the given definition the maximum faired values  $s_{\max}$ ,  $a_{\max}$ ,  $v_{\max}$ ,  $r_{\max}$  are to be plotted as shock polygon.

Additionally the maximum relative displacements of the equipment have to be measured in order to define the necessary installation clearance and to provide sufficient flexibility of connections, pipes, cables, etc.

The required grade of shockproofness is obtained if all test parameters at least reach the required values and if the specimen has passed the test without major damage or reduced functional reliability.

The functional reliability should be proven by a continuous performance test under conditions of normal use of at least 14 days.

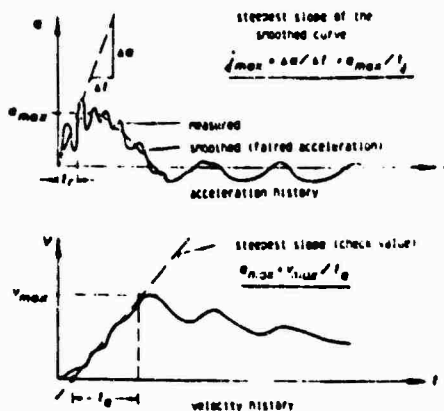


Fig. 6 - Evaluating of the test record

### 3.4 EXCEPTIONAL CASES

In specific cases, auxiliary tests, test of components, analyses of shock resistance or modelling research could be requested and performed instead of the required shock test. These exceptions have to be agreed upon by the ministry.

In performing an auxiliary test, it must be ensured, that all parameters of the auxiliary test reach or exceed the parameter set of the required reliability class.

A simple auxiliary test, for example, is a free-drop test of the specimen onto a rigid surface. It must be ensured, that the specimen strikes the base plate with all its mounting points simultaneously. The free-fall-height  $s_{\max}$  and the impact velocity  $v_{\max} = \sqrt{2 g s_{\max}}$  are the characteristic parameters of the drop test.

If the equipment is composed of single units, the units can be tested separately. It must be proved by means of dynamic design analysis, that the single units of the assembly could not collide or tear off. Deflection and stress responses of the mounting racks and fastenings have to be indicated.

Modelling investigation is indicated, if high-value or large specimens could not be tested for economical or technical reasons.

The model has to be built to the largest possible scale; representative material and construction should be used. Modelling research has to be supported by dynamic analysis.

### 3.5 SIMPLIFIED DESIGN ANALYSIS METHODS

Equivalent static load analysis: The equivalent static load analysis is the most simple dynamic design method. The actual dynamic load has to be substituted by an equivalent static design load, and a static stress analysis has to be performed. The equivalent static load  $F_e$  is the product of the required acceleration value  $a_{\max}$ , the mass  $m$  of the specimen or its parts, and the dynamic loadfactor. The required minimum value of the dynamic load-factor is 1.6:

$$F_e = 1.6 m \cdot a_{\max}$$

The design load  $F_e$  acts in addition to the normal loads, weights and operating forces, its origin is the center-of-gravity of the system or parts considered. Stress analysis has to be performed with design loads  $F_e$  acting in any of the six directions to be considered.

The diagram lines in Figure 7 show, that the equivalent static load analysis leads to reasonable results in the polygon



- The intensity of the applied shock, which is given by the value  $v_{\max}$  of the required shock reliability class and is to be applied as an input velocity step.
- Data concerning the shock tolerance limit of the system to be isolated.

Figure 8, line (1) shows the required shock performance, line (2) the actual exposure limit of an equipment outlined by its acceleration step limit (step load capacity)  $a_s \text{ tol}$  and its velocity step (impulse load capacity)  $v_{\text{tol}}$ .

The exposure limit of the system can be lifted by two measures as it is indicated in Figure 8.

- Hardening, that is increasing the static load capacity resp. acceleration step limit up to the value  $a_1 > a_{\max}$
- Shock isolation, that is increasing the energy capacity resp. velocity step limit up to the value  $v_2 > v_{\max}$ .

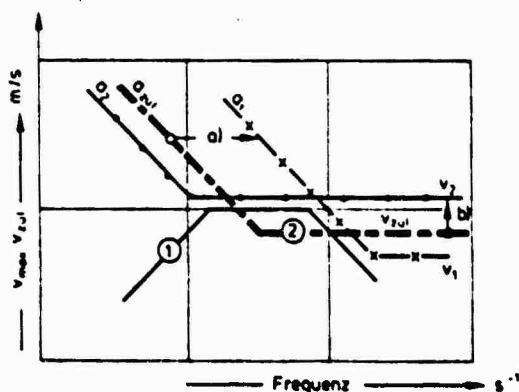


Fig. 8 - Measures of rising an exposure limit  
(1) required shock performance  
(2) actual exposure limit  
a) hardening  
b) shock isolation

Shock isolators, particular nonlinear ductile mounts easily can be designed by means of the energy balance of the kinetic input energy and the deformation energy of the system including the isolator.

$$\frac{1}{2} m v_{\max}^2 = I E_1,$$

and the maximum tolerable input force resp. yield force, which depends on the static load capacity resp. acceleration limit of the actual system

$$a_s < a_s \text{ tol}.$$

#### 4. SHOCK TEST MASHINES

By preference three shock test machines are used for standard acceptance tests and research activities on building components (concrete beams, plates, bunks) and fastenings (isolators, pipe coupling, dowels) and installation units.

The machines are designed as horizontal impacted shock tables.

##### 1. Small machine

table dimensions	0,5 m x 0,9 m
max. weight of specimen	200 kg
max. acceleration	250 kg
max. velocity	10 m/s
max. displacement	2 m

The equivalent pulse duration is adjustable from  $t_a = 1 \text{ ms} - 40 \text{ ms}$ .

By impulse transfer to an auxiliary mass, short and high intensity displacement steps (acceleration double pulses) can be produced, too.

##### 2. Medium machine

Table dimensions	1,2 m x 2,2 m
max. weight of specimen	2000 kg
max. acceleration	160 g
max. velocity	8 m/s
max. displacement	2 m
pulse durations	$t_a = 2,5 - 30 \text{ ms}$

##### 3. Large machine

Table dimensions	2,6 m x 4,3 m
max. weight of specimen	6000 kg
max. acceleration	100 g
max. velocity	6 m/s
max. displacement	2 m
pulse durations	$t_a = 6 - 30 \text{ ms}$

#### REFERENCES

- [1] KLOTTER, K.: "Schwingungslehre", Band I A, Neuauflage, Springer-Verlag 1978
- [2] MEIER-DÖRNBERG, K.-E.: "Das Schockpolygon und das Verträglichkeitspolygon, eine Basis zur Bewertung von Stoßeinwirkungen und Verträglichkeitsgrenzen", VDI-Bericht Nr. 221, VDI-Verlag 1974
- [3] Federal Ministry for Building (BMBau): "Shock Safety Requirements for Installations in Shelters", Bonn-Bad Godesberg 1975
- [4] MEIER-DÖRNBERG, K.-E.: "Reference Parameters for Shock Inputs and Shock Tolerance Limits. AGARD Conference Proceedings No. 253, Models and Analogues in Human Biodynamics, NASA, Langley Field, Virginia 1978

## CONSERVATISM IN SHOCK ANALYSIS AND TESTING

Thomas L. Paez  
The University of New Mexico  
Albuquerque, New Mexico

When a structure is to be subjected to mechanical shocks in the field, it is desirable to test that structure using a shock test which is conservative with respect to the field shock inputs. When we say that a test is conservative we mean that it excites a more severe response in a structure than the inputs it is meant to represent. The method of shock response spectra can be used to obtain a shock test which is conservative, in some sense, with respect to multiple field shocks measured in the past. But when the adequacy of a structure is to be proven for inputs which will occur in the future, and when the shock source under consideration is random, then any given test may or may not be conservative with respect to the future inputs. For a particular shock test there exists a probability of conservatism. This paper shows how the probability of conservatism of a shock test can be approximately calculated when some shocks measured from the random field source are available.

### 1.0 Introduction and Objectives

To obtain adequate designs for engineering structures, we analyze them and perform laboratory tests on their prototypes. If our analysis techniques were a perfect representation of the phenomena that occur in nature, and if there were no randomness in structural loads and material behavior, then we could measure loads and material properties and judge the sufficiency of a structure for a given environment through the use of analysis. Or in the laboratory, we would generate an input which is the correct, deterministic field input, test a structural prototype and infer the sufficiency of a structure from the results of a test. In reality, though, our analytical methods are approximate, field excitations and material properties are random, and it is impossible to generate a specific load with perfect accuracy in the laboratory. Therefore, when we test a structure through analysis or a physical test, we must somehow allow for the variations which prevent a loading and structural responses from being perfectly represented. We often do this in structural tests by increasing the test load beyond the level of average loading to a level which is conservative, in some sense. When a test input excites a less severe response than a collection of field inputs, the test is not conservative. It is desirable to test structures using conservative tests and yet it is undesirable to severely overtest structures.

The subject of the present investigation is shock testing and, in particular, shock testing through use of the method of shock response spectra. We wish to develop a probabilistic criterion to quantitatively measure the level of conservatism of a shock test specified by the method of shock response spectra. Especially, we wish to consider random shock signal sources and find the probability that a shock test, which is based on samples from the random shock source, is conservative with respect to another random signal which is drawn from the source.

The method of shock response spectra is the technique most commonly used for the specification of shock tests. It is a load specification technique which allows us to use dynamic shock loads measured in the field to derive a shock test which can be used to excite a structure to judge its sufficiency to survive inputs similar to those measured in the field. A shock response spectrum is a frequency domain measure of a shock signal and is defined as follows. The ordinate of a shock response spectrum at a frequency,  $\omega$ , is the peak response of a single-degree-of-freedom (SDF) system, with natural frequency,  $\omega_n$ , to a shock signal. An entire shock spectrum for a given shock is a collection of shock spectral ordinates over the range of frequencies in which the shock signal has power. The SDF system used in the peak response analysis has a specific damping, and since this damping influences the peak response, each shock

response spectrum has associated with it a damping value.

We obtain a shock test which represents an ensemble of field shocks in the following way. First, we collect the ensemble of field shocks. Second, we find the shock response spectrum of each shock. Third, we draw these response spectra on a single graph and determine an exact envelope for the spectra. Fourth, we find a shock whose response spectrum closely matches or envelopes the exact envelope of the ensemble of shock spectra. This shock, obtained in the fourth step, is the test shock and the method of obtaining it is known as the method of shock response spectra.

The method of shock response spectra is a useful means for shock test specification since it usually provides a test which is conservative with respect to the underlying field shocks which were used to derive it and since that single test can be used to prove a structure for several different environments. It would be favorable if the method of shock response spectra produced a shock test which is guaranteed to be conservative with respect to the underlying shocks used to derive the test, even if this guarantee were restricted by all the linearity assumptions used in the analysis. But it does not. There are at least two major reasons for this. Briefly, the first reason is the method of shock response spectra can only provide a conservative test for each frequency mode of a multi-degree-of-freedom (MDF) structure and a conservative test of the entire structure is not guaranteed simply because each mode is conservatively tested. We will amplify this statement in Section 3.0. The second reason is that the true damping in each of the modes of a MDF structure is neglected in deriving the shock test. Usually, in the implementation of the procedure described in the previous paragraph, the shock spectra of the field shocks are found using a single value of damping at all frequencies and the test is specified using this same damping value. It can happen that a test which conservatively exercises a structural mode when one value of damping is used in the analysis does not conservatively exercise the same mode when the true modal damping value is used in the analysis. In spite of these problem areas, the method of shock response spectra has been used widely and has usually provided trustworthy results. Therefore, the potential inability of the method of shock response spectra to provide a conservative test with respect to shock signals measured in the past is usually a matter of secondary importance. A matter of greater importance is the intended use of the method of shock response spectra in practice.

In practice, we often gather random signals from a shock source in the field. We then generate a test based on these signals and we

\*Numerical superscripts refer to a list of references appended to this report.

use this test, either in the laboratory or analytically, to judge the sufficiency of a structure. Our hope is that if the structure under consideration survives the test, then we can conclude, at least in a qualitative sense, that the structure is durable enough to survive any excitation which comes from the shock source. This assumption has been used previously. This hope cannot always be realized, though, particularly with regard to shocks which are taken from the shock source in the future since the shock source is random and some shocks, which have a nonzero probability of occurrence, will cause a more severe response than any test we specify. Therefore, any shock test which we specify has only a nonzero probability of being conservative when we apply the test to a structure.

The purpose of this investigation is to estimate the probability of conservatism of a shock test in light of the fact that the method of shock response spectra is not strictly guaranteed to provide a conservative test for any ensemble of inputs. We pursue this objective in a two part investigation. In the first part we find the probability distribution of each shock spectral ordinate of a shock which comes from a random source. This information enables us to find the probability that the shock spectral ordinate of a test at a particular frequency is greater than the shock spectral ordinate of a random shock at that frequency. Then we make the important assumption that any test shock whose response spectrum envelopes the response spectrum of a field shock is conservative with respect to that field shock. Based on this assumption, and the fact that the response of a multi-degree-of-freedom (MDF) structure depends heavily on the input at the modal frequencies, we define a methodology for estimating the probability of conservatism of a shock test input. In the second part of the investigation we assess the validity of the primary assumption which was necessary to the first part of the investigation. That is, we consider the probability that the response to a test at each degree of freedom of a structure is conservative when each structural mode is conservatively tested. Finally, we present a discussion on the accuracy of the probabilistic shock test specification procedure proposed in this paper.

## 2.0 Conservatism Probability of a Mechanical Shock Test

In this section we define an easy-to-use technique for the approximate computation of the probability of conservatism of a test specified using the method of shock response spectra. Application of the technique requires the collection of data which can be used to statistically characterize the random shock signal source under consideration. We pursue this objective by first characterizing the probability distribution of a shock spectral ordinate for a random signal. In a two-part study in Sections 2.1a and 2.1b, we show that the shock spectral ordinate of a random signal can be approximated

using a lognormal probability distribution function. In Section 2.2 we assume that if the response spectrum of a test shock envelops the response spectrum of a shock realized in the field, then the test shock is conservative with respect to the field shock. Since the response of a MDF structure depends primarily on the character of an input at the modal frequencies of the structure, the assumption allows us to compute the probability of conservatism of any test shock.

## 2.1a Peak Response of SDF Systems--Analysis

We summarize a study of the probabilistic character of the peak response of a SDF system to stationary and nonstationary random inputs in this subsection. Ultimately, we show that the probability distribution function of the SDF system response to a random shock input is approximately lognormal. The peak response of a SDF system is important to consider, with respect to the method of shock response spectra, since the shock response spectrum of a shock signal is defined as the collection of peak responses of SDF systems to the shock input where the SDF systems have natural frequencies which vary over a specified range of frequencies. By determining the probability distribution of the peak response of a SDF system to a nonstationary random input, we are able to specify the probability distribution of the shock response spectrum for the class of random input considered. We use the shock spectrum of a base-excited SDF system in this report. This is the shock spectrum which should properly be used in the design and analysis of a base-excited structure or component.

We introduce the following notation.  $\ddot{X}(t)$ ,  $-\infty < t < \infty$ , is a random process used to represent the acceleration obtained from a random shock signal source.  $Y(t)$ ,  $-\infty < t < \infty$ , is the random process which represents the displacement response of the mass of a SDF system relative to its base, when the system is excited through its base by  $\ddot{X}(t)$ . The system has natural frequency,  $\omega$ , and damping factor,  $\zeta$ . We define the random variable,  $A(\omega, \zeta)$  as

$$A(\omega, \zeta) = \max_t |Y(t)|. \quad (1)$$

The random variable,  $A(\omega, \zeta)$ , is the shock spectral ordinate of the random signal,  $\ddot{X}(t)$ , at frequency,  $\omega$ , with damping factor,  $\zeta$ . We wish to find the probability distribution of  $A(\omega, \zeta)$ .

This study shows how the peak response probability distribution can be found analytically in a special case. When the input random process,  $\ddot{X}(t)$ , is a time modulated, normal, zero mean, band-limited, white noise, the probability distribution of  $A(\omega, \zeta)$  can be found using the following three step approach.

1. Completely specify  $\ddot{X}(t)$ ,  $t \in T$ , in terms of its autocorrelation function or spectral density, and its modulating function. Find the

moments of the SDF system response,  $Y(t)$ , using a standard procedure.<sup>4</sup>

2. Use the moments of  $Y(t)$  to express the average crossing rate of a barrier with level "a" by the random process,  $|Y(t)|$ . This is done using Rice's procedure.<sup>5</sup>

3. Assume that the peaks in the nonstationary response random process which are higher than the level "a" can be counted using a Poisson random process.<sup>2,3</sup> This yields an expression for the cumulative distribution function (cdf) of  $A(\omega, \zeta)$ .

We implement this procedure in the following paragraphs and obtain the cdf of  $A(\omega, \zeta)$  for some specific shock inputs.

The shock random processes to be used in the present portion of this investigation have the following form.  $\ddot{X}(t)$ ,  $t \geq 0$ , is an acceleration random process defined by the product

$$\ddot{X}(t) = a(t) W(t), \quad -\infty < t < \infty, \quad (2)$$

where  $W(t)$ ,  $-\infty < t < \infty$ , is a band-limited white noise random process, and  $a(t)$  is a deterministic function of time. We assume that the input has a cutoff frequency which is high compared to the characteristic frequencies of the systems to be excited, therefore, the white noise random process has an autocorrelation function which can be approximated as

$$R_{WW}(\tau) = 2\pi K \delta(\tau), \quad -\infty < \tau < \infty, \quad (3)$$

where  $\delta(\tau)$  is the Dirac delta function,  $\tau$  is a time lag, and  $K$  is the random process spectral density. In this study we use three envelope functions,  $a(t)$ . They are

$$a_1(t) = B e^{-\alpha t} H(t), \quad -\infty < t < \infty, \quad \alpha > 0, \quad (4a)$$

$$a_2(t) = B (e^{-\alpha t} - e^{-\beta t}) H(t), \quad -\infty < t < \infty, \quad \beta > \alpha > 0, \quad (4b)$$

$$a_3(t) = B H(t), \quad -\infty < t < \infty, \quad (4c)$$

$B$ ,  $\alpha$  and  $\beta$  are constants, and  $H(t)$  is the Heaviside unit step function. These envelopes correspond to decaying exponential, earthquake and steady random inputs. When Expression 4a is used in Equation 2, we find the autocorrelation function of the input to be

$$R_{\ddot{X}\ddot{X}}^{(1)}(t, s) = 2\pi K B^2 e^{-\alpha(t+s)} \delta(t-s), \quad t, s \geq 0, \quad (5)$$

where the superscript "1" refers to the fact that this is the autocorrelation function of the decaying exponential random input, and  $t$  and  $s$  are time points. The autocorrelation functions

can also be found when Expressions 4b and 4c are used in Equation 2, and these functions are written out in Appendix A.

To find the cdf of the peak response of a SDF system it is necessary to find the moments of the response of the system to the inputs described above. Particularly, we must find the variance of the response random process, the variance of the derivative of the response random process, and the crosscorrelation between the response random process and its derivative. (It can be shown that this derivative exists in a mean square sense.) In the following, we will obtain expressions for the moments of the response random process for the case of the decaying exponential input. In Appendix A we will use these expressions to compose the moments of the response random process for the case of the earthquake input and the steady input. The equation governing the response of a base-excited SDF system is

$$\ddot{Y} + 2\zeta\omega_n \dot{Y} + \omega_n^2 Y = -\ddot{X}(t), \quad (6)$$

where dots denote differentiation with respect to time,  $\omega_n$  is the natural frequency of the system,  $\zeta$  is the system damping factor, and  $Y(t)$ ,  $t \geq 0$  is the response random process of the SDF system mass relative to the base. For this analysis we will take the initial conditions to be zero, i.e.,  $Y(0) = 0$ ,  $\dot{Y}(0) = 0$ . We can express the response using the convolution integral.

$$Y(t) = \int_0^t \ddot{X}(t-\tau) h(\tau) d\tau \quad t \geq 0 \quad (7)$$

where

$$h(t) = \begin{cases} \frac{e^{-\zeta\omega_n t}}{\omega_d} \sin \omega_d t & t \geq 0 \\ 0 & t < 0 \end{cases} \quad (7a)$$

and

$$\omega_d = \omega_n \sqrt{1-\zeta^2}, \quad (7b)$$

$h(t)$  is the impulse response function of the SDF system, and  $\omega_d$  is its damped natural frequency. By taking the expectation of the response random process at  $t$ , times the response random process at  $s$ , we obtain an expression for the autocorrelation function of the response. This is

$$\begin{aligned} \rho_{YY}(t, s) &= E[Y(t)Y(s)] \\ &= \int_0^t d\tau \int_0^s d\gamma R_{XX}(t-\tau, s-\gamma) h(\tau) h(\gamma) \end{aligned} \quad (8)$$

$t, s \geq 0$

By using the expression for the impulse response function, Equations 7a and 5 in Equation 8, we obtain the autocorrelation function of the

response random process. We denote this  $R_{YY}^{(1)}(t, s, \alpha)$ , and note that this function depends on  $t, s, \alpha, B, K, \zeta$ , and  $\omega_n$ . The superscript "1" refers to the fact that this is the autocorrelation function of the response due to the decaying exponential input. The argument  $\alpha$  is included to show special dependence of this function on it. To obtain the variance of the response we set  $s = t$  in  $R_{YY}(t, s, \alpha)$ . This yields

$$\begin{aligned} R_{YY}^{(1)}(t, t, \alpha) &= \frac{\pi K B^2}{\omega_d^2} \left[ e^{-2\alpha t} \left\{ \frac{\omega_d^2}{2(\alpha - \zeta\omega_n)(\alpha^2 - 2\alpha\zeta\omega_n + \omega_n^2)} \right\} \right. \\ &\quad + e^{-2\zeta\omega_n t} \left\{ \frac{1}{2(\alpha - \zeta\omega_n)} \right. \\ &\quad \left. \left. - \frac{(\alpha - \zeta\omega_n) \cos 2\omega_d t + \omega_d \sin 2\omega_d t}{2(\alpha^2 - 2\alpha\zeta\omega_n + \omega_n^2)} \right\} \right] t \geq 0 \end{aligned} \quad (9)$$

This function will be denoted  $\sigma^2$  in the following. We note that this expression always depends on  $t$  since the response random process is nonstationary.

Next, we must determine the crosscorrelation between the response random process and its first derivative. This is

$$R_{\dot{Y}Y}^{(1)}(t, s) = \frac{\partial}{\partial s} R_{YY}^{(1)}(t, s). \quad (10)$$

We obtain this by differentiating the autocorrelation function,  $R_{YY}(t, s, \alpha)$ , with respect to  $s$ . The crosscorrelation is denoted  $R_{\dot{Y}Y}^{(1)}(t, s, \alpha)$ , and depends on  $t, s, \alpha, B, K, \zeta$ , and  $\omega_n$ . Evaluation of this expression at  $s = t$  results in

$$\begin{aligned} R_{\dot{Y}Y}^{(1)}(t, t, \alpha) &= \frac{\pi K B^2}{\omega_d^2} \left[ e^{-2\alpha t} \left\{ \frac{\omega_d^2 \alpha}{2(\alpha - \zeta\omega_n)(\alpha^2 - 2\alpha\zeta\omega_n + \omega_n^2)} \right\} \right. \\ &\quad + e^{-2\zeta\omega_n t} \left\{ -\frac{\zeta\omega_n}{2(\alpha - \zeta\omega_n)} \right. \\ &\quad \left. \left. + \frac{\omega_n(\alpha - \zeta\omega_n) \cos 2\omega_d t + \omega_d \sin 2\omega_d t}{2(\alpha^2 - 2\alpha\zeta\omega_n + \omega_n^2)} \right\} \right] \end{aligned}$$

$t \geq 0 \quad (11)$



When we divide this expression by  $\sigma_1 \sigma_2$  ( $\sigma_2$  to be defined in the following paragraph) we obtain the expression which will be denoted  $\rho$ .

Finally, we must determine the variance of the derivative of the response random process. We first obtain its autocorrelation function using the definition

$$R_{\dot{Y}\dot{Y}}(t, s) = \frac{\partial^2}{\partial s \partial t} R_{YY}(t, s) \quad (12)$$

The autocorrelation function of the velocity response is denoted  $R_{\dot{Y}\dot{Y}}(t, s, a)$  and depends on  $t, s, a, B, K, \zeta$ , and  $\omega_n$ . Evaluation of this expression at  $s = t$  yields the variance of the derivative of the response random process.

$$\begin{aligned} (1) \\ R_{\dot{Y}\dot{Y}}(t, t, a) &= -\frac{\pi K B^2}{\omega_d^2} \left[ e^{-2\alpha t} \left\{ \frac{\omega_d^2 (-2\alpha^2 + 2\alpha\zeta\omega_n - \omega_n^2)}{2(\alpha - \zeta\omega_n)(\alpha^2 - 2\alpha\zeta\omega_n + \omega_n^2)} \right\} \right. \\ &+ e^{-2\zeta\omega_n t} \left\{ \frac{\omega_n^2}{2(\alpha - \zeta\omega_n)} \right. \\ &+ \frac{\omega_n^2 (\alpha(1 - 2\zeta^2) + \zeta\omega_n) \cos 2\omega_d t}{2(\alpha^2 - 2\alpha\zeta\omega_n + \omega_n^2)} \\ &\left. \left. + \frac{\omega_n \omega_d (\omega_n - 2\alpha\zeta) \sin 2\omega_d t}{2(\alpha^2 - 2\alpha\zeta\omega_n + \omega_n^2)} \right\} \right] t \geq 0 \quad (13) \end{aligned}$$

This function will be denoted  $\sigma_2^2$ .

In Appendix A we use the expression derived above to find the moments of the responses to the earthquake and the steady inputs.

It is now necessary to use the moments of  $Y(t)$ , derived above and in the Appendix, to find the average crossing rate of a barrier with level "a" by the random process,  $|Y(t)|$ . The average barrier crossing rate of a nonstationary, zero mean, normal random process is  $v_a(t)$ . This is the average rate at which a random process,  $Y(t)$ , passes outside the barrier  $|Y(t)| = a$ , at time  $t$ . By assuming that the fraction of the total number of members of the ensemble of a random process,  $Y(t)$ , which pass outside the barrier  $|Y(t)| = a$  in the time interval  $(t, t + dt)$ , is equal to the expected number of crossings,  $v_a dt$ , of the random process outside the barrier in  $(t, t + dt)$ , Rice<sup>6</sup> obtained the following formula for  $v_a(t)$ .

$$v_a(t) = 2 \int_0^\infty v_{PY}(a, v) dv \quad t \geq 0 \quad (14) \\ a \geq 0$$

where  $v$  is the velocity variable,  $P_{YY}(a, v)$  is the joint pdf of the random process  $Y(t)$ , and its time derivative,  $\dot{Y}(t)$ , and is a function of time since we have assumed the random process to be nonstationary. The joint pdf of a zero mean, normal random process and its time derivative is given by

$$P_{YY}(y, v) = \frac{1}{2\pi\sigma_1\sigma_2\sqrt{1-\rho^2}} \exp \left[ -\frac{1}{2(1-\rho^2)} \left( \frac{y^2}{\sigma_1^2} - \frac{2\rho yv}{\sigma_1\sigma_2} + \frac{v^2}{\sigma_2^2} \right) \right] \\ -\infty < y, v < \infty \quad (15)$$

where  $\sigma_1^2$  is the variance of  $Y(t)$ ,  $\sigma_2^2$  is the variance of  $\dot{Y}(t)$ ,  $\rho$  is the crosscorrelation coefficient between the random variables  $Y(t)$  and  $\dot{Y}(t)$ , and all these moments are functions of time. By substituting Equation 15 into Equation 12 and using a square completion technique and a change of variables we obtain

$$v_a(t) = \frac{\sigma_2}{\pi\sigma_1} e^{-a^2/2\sigma_1^2} \left\{ \sqrt{1-\rho^2} \exp \left( \frac{-\rho^2 a^2}{2\sigma_1^2(1-\rho^2)} \right) \right. \\ \left. + \frac{\sqrt{2\pi}\rho a}{\sigma_1} \left( 1 - \Phi \left( -\frac{\rho a}{\sigma_1\sqrt{1-\rho^2}} \right) \right) \right\} a \geq 0, t \geq 0 \quad (16)$$

where  $\Phi(\cdot)$  is the cdf of standard normal random variable. For the special case of a stationary random process  $\rho = 0$  and  $v_a(t) = v_a$  is no longer a function of time. Equation 16 becomes

$$v_a = \frac{\sigma_2}{\pi\sigma_1} e^{-a^2/2\sigma_1^2}, \quad a \geq 0 \quad (16a)$$

This result agrees with the expression given in the literature.<sup>5</sup>

The moments derived in Equations 9, 11, and 13, and in Appendix A, can be used in the above equations to find the average barrier crossing rate for each response random process.

Now we use the assumption that the peaks in the response random process,  $|Y(t)|$ , which are higher than the level "a", can be counted using a Poisson random process, to find the cdf of the peak response of the SDF system. The response of a SDF system to a random input is a narrowband random process if the input contains power in the band of frequencies in the near vicinity of the natural frequency of the SDF system. A narrowband random process is one which contains power only within a small band of frequencies. A narrowband random process resembles a harmonic signal with frequency equal to the central frequency of the narrowband, and with slowly

varying amplitude. A nonstationary input random process is usually composed of components with power over a wide range of frequencies, therefore, the response of a lightly damped SDF system to a nonstationary input is narrowband in character. Because of this, the response contains a sequence of separate, identifiable peaks. We are interested in finding the probabilistic character of the highest peak in a narrowband response. The collection of peaks and troughs in a random response compose a random process and we can describe one aspect of this random process, in some sense, by using a counting process. To be precise, we are interested in counting the number of peaks in a random response process which surpass a given level. For this application we use a Poisson counting process.

Let  $N(t)$ ,  $t \geq 0$ , be a nonnegative, integer valued random process and let it count the number of "events of interest" occurring in the time interval  $(0, t]$ . We assume that the events to be counted follow these rules: (a) the events arrive independently of one another, i.e., the occurrence of one event within a time interval has no influence on the occurrence of later events, (b) the chance of a simultaneous occurrence of events is negligible, and the chance of occurrence of one event in the time interval  $(t, t + dt]$  is  $\lambda(t)dt$ , where  $dt \ll 1$ . To completely characterize the random process,  $N(t)$ , we must find expressions for all its joint cdf's. For the present, though, we are only interested in finding a first order description of the random process.

This is done in Reference 4 and we find that

$$P_N(k, t) = \frac{\left[ \int_0^t \lambda(\tau) d\tau \right]^k}{k!} \exp \left[ - \int_0^t \lambda(\tau) d\tau \right] \quad (17)$$

$t \geq 0, \quad k = 0, 1, 2, \dots$

$P_N(k, t)$  is the probability that  $k$  "events of interest" occur in the time interval  $(0, t]$ , where  $\lambda(t)$ ,  $t \geq 0$ , is the mean rate of occurrence of events as a function of time. The random process,  $N(t)$ , is known as a Poisson counting process with nonstationary increments when it has the probability mass function of Equation 17. One case of particular interest to us is that in which  $\lambda(t)$ , the mean rate of occurrence in the Poisson counting process, equals  $v_a(t)$ , the average barrier crossing rate of the response random process for a barrier with level "a". In that case,  $P_N(0, \infty)$  is the chance that the random process,  $|Y(t)|$ , does not cross the barrier level "a" at any time. This indicates that the largest value of the absolute value of the response,  $Y(t)$ , is equal to or less than "a". Let the random variable  $A = A(\omega, \zeta)$ , be the peak value of the absolute value of the response. Then the cdf of  $A$  can be written

$$P_A(a) = \exp \left[ - \int_0^\infty v_a(\tau) d\tau \right], \quad a \geq 0 \quad (18)$$

This is the approximate chance that the peak value in the absolute value of the response is equal to or less than "a". This is a function of  $v_a(t)$ , the average rate at which the response random process,  $Y(t)$ , crosses outside a barrier,  $|Y(t)| = a$ . The expression for  $v_a(t)$  is complicated, therefore, the integration in the above equation is carried out numerically in the numerical examples which follow.

To show how the procedure described above can be used to find the probability density function (pdf) of the peak response of a SDF system we present a numerical example. (Reference 7 gives additional numerical examples.) In the example we consider an input shock of the type described in Equation 2 where  $e(t)$  is given by Equation 4a. We choose  $\alpha = 20 \text{ sec}^{-1}$  and  $B = 2738$ . We choose  $K = 1.0 \text{ (cm/sec}^2\text{)}^2/\text{rad/sec}$ . The pdf of the peak responses of two SDF systems will be shown here. These systems have natural frequencies 5027 rad/sec and 9425 rad/sec, and damping factor, 0.03. Equations 9, 11, and 13 were used to find the moments of the response random processes. These were used in Equation 18 to find the cdf of the peak responses,  $A(\omega, \zeta) = A(5027, 0.03)$  and  $A(\omega, \zeta) = A(9425, 0.03)$ . The pdf's of these random variables are graphed in Figures 1a and 1b. The mean, variance and coefficient of variation of each peak response is given in the graph.

In an attempt to simplify the representation of the peak response pdf we compared the pdf's in Figures 1a and 1b to Type I extreme value and lognormal pdf's using probability paper. The straightest lines were achieved on lognormal paper and the graphs of  $A(5027, 0.03)$  and  $A(9425, 0.03)$  plotted on lognormal paper are shown in Figure 2. Other examples are presented in Reference 7. We conclude from this comparison that the pdf of  $A(\omega, \zeta)$  can be adequately approximated using a lognormal pdf.

All results indicate that the probabilistic behavior of the peak response of a SDF system is approximately governed by a lognormal distribution and this is significant for the following reason. Shock signals from a random field source can be collected in the field and their shock spectra can be computed. The logarithm of each shock spectral ordinate can be computed, and the average and the variance of the logarithm of shock spectral ordinate can be estimated at each frequency. Then using the estimated mean and variance, and the fact that the logarithm of the shock spectral ordinate has approximately normal distribution, we can estimate the probability that the logarithm of a future random shock spectral ordinate will fall within certain bounds. This procedure is much simpler and more direct than the three-step procedure described at the beginning of this section. Use of that procedure was essential,

though, in showing that the lognormal distribution is a good approximation for  $P_A(a)$ .

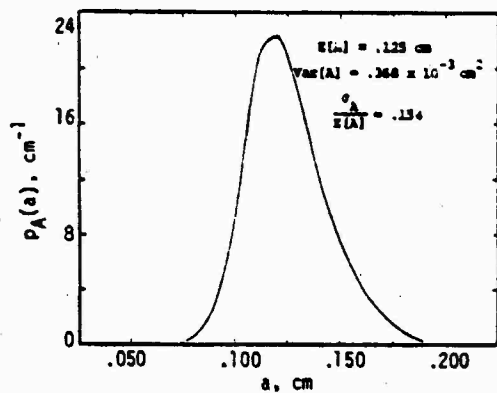


Figure 1a pdf of peak response of SDF system to decaying exponential input,  $\omega_n = 5027$  rad/sec

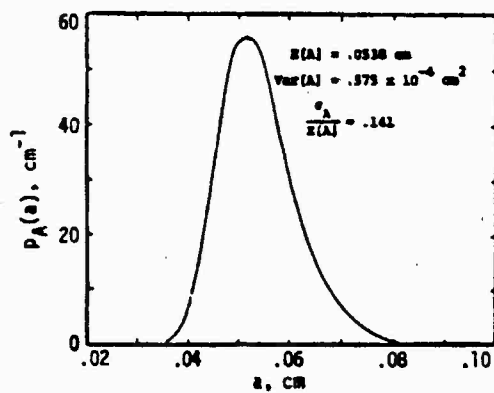


Figure 1b pdf of peak response of SDF system to decaying exponential input,  $\omega_n = 9425$  rad/sec

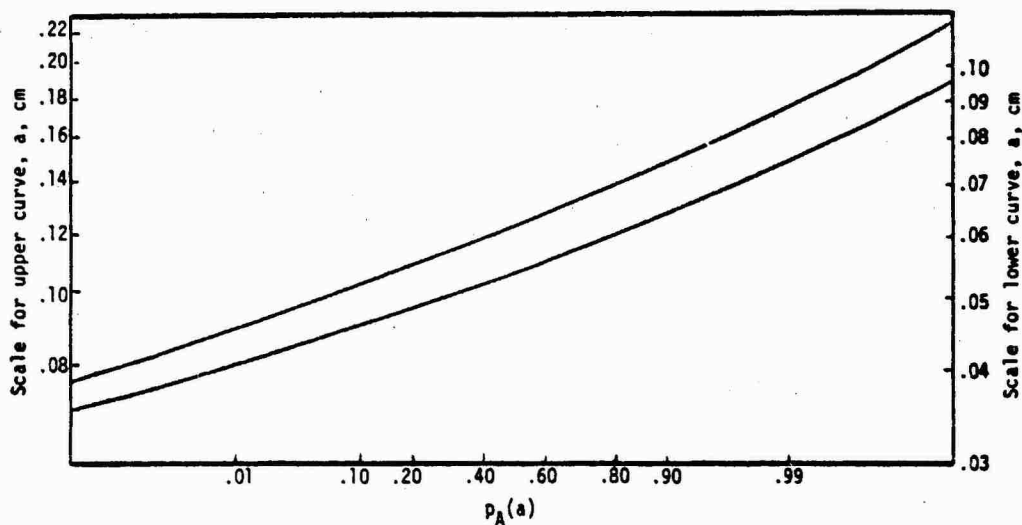


Figure 2 Plot of cdf of peak response of SDF system to decaying exponential input on lognormal probability paper,  $\omega_n = 5027$  rad/sec (top),  $\omega_n = 9425$  rad/sec (bottom)

## 2.1b Peak Response of SDF Systems--Monte Carlo

In this subsection we wish to verify the conclusion reached in the previous subsection, that is, that the peak response of a SDF system to a shock input is approximately governed by a lognormal probability distribution. This conclusion, reached in the previous subsection, is restricted by many assumptions. Most important is our assumption that an input shock random process can be represented as a product between a deterministic function and a white noise random process. It is probable that, although most shock sources can realistically be represented as the product between a deterministic function and a stationary random process, that random process is not usually a white noise type random process. To determine whether the probability distribution of peak response of a SDF system to nonstationary random input is approximately lognormal, for more general inputs, we conducted a Monte Carlo study.

In the Monte Carlo study, three varieties of input are generated. The inputs are defined as the product of a mean zero, stationary, normal random process,  $X_0(t)$ ,  $-\infty < t < \infty$ , and a deterministic function of time,  $e(t)$ . The input random process,  $\ddot{x}(t)$ ,  $-\infty < t < \infty$ , is an acceleration random process and is defined

$$\ddot{x}(t) = e(t) \ddot{x}_0(t), \quad -\infty < t < \infty. \quad (19)$$

The time functions defined in Equations 4a, 4b, and 4c are used to create the nonstationarity. Realizations,  $x_i(t)$ , of the random process,  $X_0(t)$ , are generated, in the standard manner,<sup>8</sup> by summing harmonic signal components with random phases. The component amplitudes are chosen to simulate random processes with non-white spectral densities.

In each Monte Carlo analysis we first generate 20 random signals based on Equation 19. Second, we find the shock spectrum of each input. To do this, we use a recursive filter technique such as that described in Reference 9. Finally, at preselected frequencies, we plot the shock spectral ordinates on lognormal probability paper to judge whether or not the ordinates are governed by a lognormal probability distribution.

We summarize some of the results of one of the Monte Carlo analyses. The input is chosen to be a decaying exponential-oscillatory type random shock. This type of shock might be realized in connection with an explosive environment, for example, near a separation joint on a missile. This shock is described by Equations 4a and 19. The underlying, mean zero, stationary, normal random process,  $X_0(t)$ ,  $-\infty < t < \infty$ , has the spectral density shown in Figure 3a. The parameters of the shock source are  $B = 1.0$ ,  $\alpha = 36.84 \text{ sec}^{-1}$ . A typical shock generated by the random source described here is shown in Figure 3b. Its shock spectrum is shown in Figure 3c. The shock spectral ordinates of the 20 shocks generated in this analysis at frequencies,

$\omega = 1500$ , and  $7500 \text{ rad/sec}$ , are plotted on lognormal probability paper in Figure 4. In these cases, the data form a relatively straight line on the lognormal probability paper.

Several other Monte Carlo analyses were performed,<sup>8</sup> and from all these we conclude that the lognormal probability distribution provides a satisfactory fit to the peak response data. In view of this, we now proceed to define a method for specifying shock tests with a particular probability of conservatism.

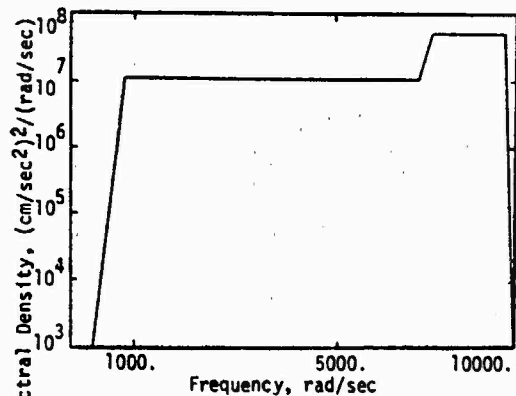


Figure 3a Underlying Spectral Density for Decaying Exponential Random Input

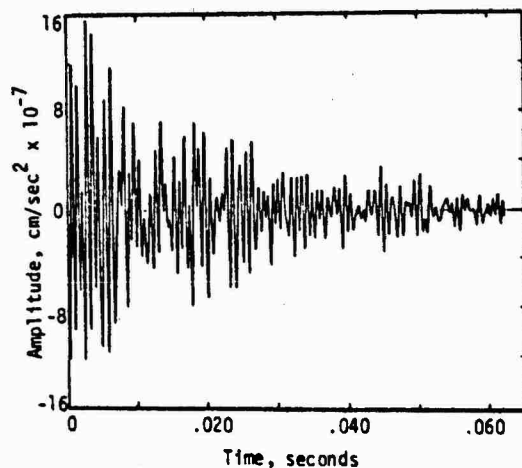


Figure 3b Typical Decaying Exponential Random Shock

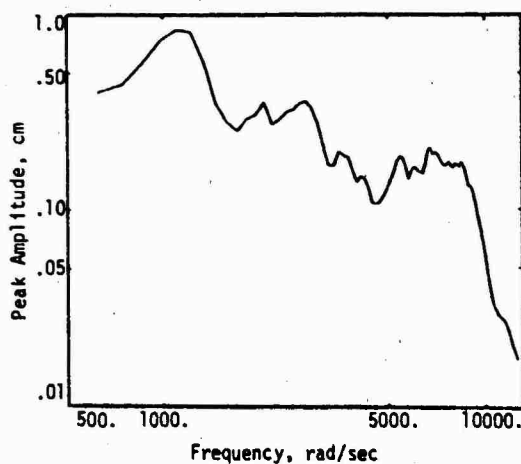


Figure 3c Shock Response Spectrum of Input in Figure 3b

## 2.2 Shock Test Specification

The early part of this study showed that shock spectral ordinates are approximately governed by a lognormal probability law. We now show how this information can be used to approximately compute the probability of conservatism of a shock test. Our primary assumption is that when a shock test is specified so that all modes of a MCF structure are conservatively tested, then the entire structure is conservatively tested. This assumption is only approximate, primarily since conservatism of a test at any point on a structure is not guaranteed even if all modes of the structure are conservatively tested. Moreover, conservatism of a test at all points on a structure is certainly not guaranteed if conservatism at one point is not guaranteed. Nevertheless, the assumption should be relatively safe in most cases.

For present purposes, we assume that four degrees of structural information might be available for a structure which is to be tested. These are a) no information, b) number of structural modes, c) number of modes plus location of modal frequencies, and d) modal frequencies plus modal damping factors. In the following, we show how the probability of test conservatism can be approximated in each of the above cases. With the assumption given in the previous paragraph, the probability of test conservatism is the probability that each structural mode is conservatively tested. This latter is simply the probability that a shock drawn from a random shock signal source will have a shock spectral ordinate which is equal to or lower than the shock spectral ordinate of the test shock, at a modal frequency of a structure, where the correct modal damping has been used in the shock spectrum analysis.

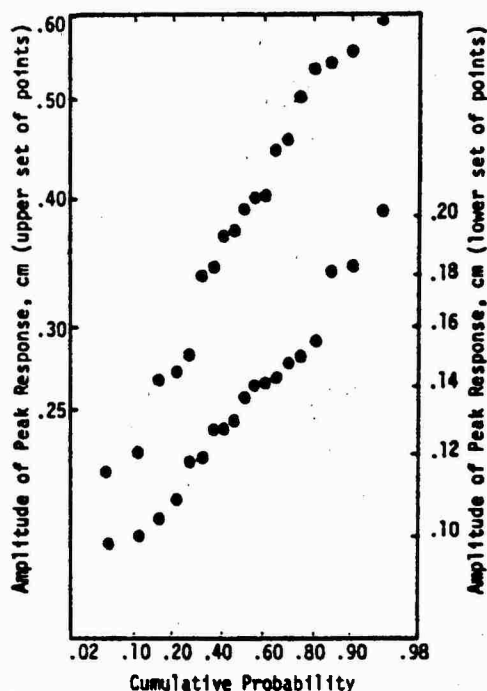


Figure 4 Peak Values of SDF System Response to Decaying Exponential Input. Case 1:  $\omega = 1500$  rad/sec,  $\zeta = 0.03$ . Case 2:  $\omega = 7500$  rad/sec,  $\zeta = 0.03$

For the purpose of computing the probability of conservatism of a shock test, we assume that several shock signals are available for analysis. We find the shock response spectrum of each signal and take the natural logarithm of each shock spectral ordinate at each frequency. Next, we estimate the mean and variance of the logarithm of the shock spectral ordinate at each frequency. This statistically characterizes the underlying random shock source. Let  $\mu(\omega, \zeta)$  be the mean and  $\sigma(\omega, \zeta)$  the standard deviation of the logarithm of the shock spectral ordinate at frequency,  $\omega$ , where damping factor,  $\zeta$ , is used in the shock spectrum analysis. Let  $V(\omega, \zeta)$  be the test shock spectrum level at frequency,  $\omega$ , with damping,  $\zeta$ . And let  $\omega_j$  and  $\zeta_j$ ,  $j = 1, \dots, m$  be the modal frequencies and modal damping factors for the structure to be tested.

When no structural information is available, we can bound the probability of test conservatism with the probability that the test shock spectrum is greater than the random field shock spectrum at every frequency. Our reasoning here is that if the test shock spectrum is greater than the random field shock spectrum at every frequency, then it is certainly greater at the modal frequencies. However, this bound on the probability of conservatism is a loose lower bound. Therefore, in this case, we choose to specify an index of conservatism,  $k$ , for obtaining a test. Here the test shock spectrum is

specified by

$$V(\omega, \zeta) = \exp(u(\omega, \zeta) + k\sigma(\omega, \zeta)), \quad (20)$$

where  $k$ , the index of conservatism, is chosen large enough so that any mode in a response is unlikely to have a peak greater than  $V(\omega, \zeta)$ . In this case, we know neither the modal frequencies nor the damping factors, so we choose  $\zeta$  to be a small damping and we generate a value of  $V(\omega, \zeta)$  at each value of  $\omega$ . Any single structural mode has a probability of approximately

$$P_1 = \Phi(k) \quad (21)$$

of being conservatively tested. Here,  $\Phi(\cdot)$  is the cdf of a standard normal random variable. Note that the probability given here is only approximate since the shock spectra are computed using a damping factor which is probably not equal to the true modal damping. (In this case, we assume that the true modal damping is unknown.) We try to conservatively account for this lack of knowledge through use of a damping factor which is small in magnitude. The reason for using a small damping factor is this: typically, random inputs tend to excite responses with greater variability in systems with light damping. If we compute all shock spectra using low damping values, then we derive a test which allows for the greatest possible random variability and, on the average, this increases the conservatism of a test. Analyses conducted during this investigation show that the mean and standard deviation of a shock spectral ordinate vary as  $\zeta^b$ , where  $-0.5 \leq b \leq 0$ .

When we know the number of structural modes,  $m$ , excited by a shock input, but not the modal frequencies, we must still resort to a technique for test specification such as that described with Equation 20. The test must be specified at every frequency where the input has power. However, in this case, we can approximately compute the probability of conservatism of the test according to the criterion defined at the beginning of this section. The probability of test conservatism,  $P_c$ , is given by

$$P_c = [\Phi(k)]^m. \quad (22)$$

We have assumed that the conservatism of a test at one modal frequency is independent of the test conservatism at all other modal frequencies. This is a reasonably accurate assumption when structural modes of vibration are widely separated in frequency and it is a conservative assumption when they are not. This estimate is only approximate because the true modal damping factors are not used in the analysis.

When modal frequencies are available, we can specify the test shock spectrum at each modal frequency using the formula

$$V(\omega_j, \zeta) = \exp(u(\omega_j, \zeta) + k_j \sigma(\omega_j, \zeta)), \quad j = 1, \dots, m, \quad (23)$$

where  $\zeta$  is chosen to be a small damping value, as before. We choose the values of  $k_j$ ,  $j = 1, \dots, m$ , so that the natural logarithm of the peak response of a SDF system with natural frequency,  $\omega_j$ , excited by a random input is unlikely to surpass,  $u(\omega_j, \zeta) + k_j \sigma(\omega_j, \zeta)$ . Variation of the values of  $k_j$ ,  $j = 1, \dots, m$ , from one mode to another allows us to specify different factors of conservatism for the test at different modal frequencies. The probability of conservatism of the test specified using Equation 23 is approximately

$$P_c = \prod_{j=1}^m \Phi(k_j). \quad (24)$$

This is only approximate since damping has not been accurately accounted for. Note that the shock spectral levels away from the modal frequencies are not important in the test specification. The reason for this is that shock test conservatism is defined in terms of modal response.

When both modal frequencies and modal damping factors are available, we can specify test shock spectrum levels using the following formula

$$V(\omega_j, \zeta_j) = \exp(u(\omega_j, \zeta_j) + k_j \sigma(\omega_j, \zeta_j)), \quad j = 1, \dots, m. \quad (25)$$

This equation states that the test shock must have a shock spectrum with magnitude equal to or greater than  $V(\omega_j, \zeta_j)$  at the frequency,  $\omega_j$ , when the shock spectral analysis is performed using a damping factor,  $\zeta_j$ . Again, it is only necessary to match the shock spectrum near the modal frequencies,  $\omega_j$ . Note that a test shock derived using Equation 25 cannot be derived in the standard manner. In fact, a shock spectrum of the test shock must be computed using each value of modal damping,  $\zeta_j$ , and at a frequency,  $\omega_j$ , this must envelop the quantity on the right-hand side of Equation 25. To find the quantities used on the right side of Equation 25, we must compute the shock spectrum of each field shock using each value of modal damping. The probability of conservatism of a test derived using Equation 25 is given by Equation 24. This is the best estimate of test probability of conservatism we can obtain when the conservatism criterion is that given at the beginning of this section.

Given the test shock spectrum function,  $V(\zeta, \omega)$ , from Equation 20, 23 or 25, we can now specify a shock test following the standard procedure, except as noted in the previous paragraph. When enough information is available, it is desirable to use Equation 25 for test specification since maximum shock and system data are used in this case. When less information is available, then Equation 23 should be used. A technique such as that used in Reference 10 can be used to find a shock which matches the test shock spectrum. In all cases, it is desirable

to match the function,  $V(\omega, \zeta)$ , as closely as possible with the actual test shock spectrum.

In addition to assuring that a test shock is conservative, it is desirable to know the structural reliability of a structure which will be placed in the field. This is the probability that a structure will survive the environment to which it is subjected. It is possible to relate the probability of conservatism of a test to structural reliability in the following way. If a shock test is specified and a structure is subjected to that test and survives, then this implies that the structure would survive any less severe test. But the probability of conservatism of a test is the chance that a test is more severe than a random field input. Therefore, the probability that a structure will survive a random field input is related to the probability that the random field input is less severe than the test. In fact, the probability of test conservatism forms a lower bound on the structural reliability. The reason it is simply a lower bound is that in order to know the exact structural reliability, we must know the exact level at which a structure will fail. When a structure simply survives a test, we do not know the failure level.

Our assumption that the probability of conservatism forms a lower bound on the structural reliability can be interpreted in the following way. Since the probability of conservatism of a test shock is the chance that all modes in a structure are conservatively tested, the lower bound on structural reliability is the probability that all modes are conservatively tested. This is only an approximation, but it serves the purpose of providing guidance in test level specification.

One of the shortcomings of the test specification techniques defined above is that we assume the mean and variance of the logarithm of the shock response spectrum of a random shock source are known exactly. In fact, we only have estimates for these functions. If an increased degree of accuracy is desired, it is possible to perform a confidence analysis on these functions. Then we could use parameters which reflect any degree of confidence we wish.

When insufficient data are available to compute the moments of the logarithm of the shock spectral ordinates of a random source, the following information may prove valuable. Studies performed during the current investigation show that the coefficient of variation of the shock spectral ordinate (i.e., the quotient  $\sigma(\omega_j, \zeta_j)/\mu(\omega_j, \zeta_j)$ ) is usually a number in the interval (0.15, 0.30). If we have confidence in our estimate of the mean, then we could conservatively assume that  $\sigma(\omega_j, \zeta_j) = 0.30 \cdot \mu(\omega_j, \zeta_j)$ . This may permit an analysis when the amount of data available appears insufficient.

The present shock specification technique can be used in more general ways than previously shown. First, when a structure is excited by

multiple exposures which come from a single random shock source, then a shock test level can be specified using Equation 25, but the probability of conservatism of the test becomes approximately  $(p_c)^N$ , where  $N$  is the number of exposures. The values of  $k_j$ ,  $j = 1, \dots, m$ , in Equation 25 can be adjusted to yield the desired value of  $(p_c)^N$ . Second, a shock test which represents several different random shock source environments can be specified. The shock test is specified using the following procedure.

- a. Gather the data for each environment. Compute all shock spectra. Take natural logarithms. Estimate the mean and variance of this quantity for each environment,  $\mu_z(\omega_j, \zeta_j)$ ,  $\sigma_z(\omega_j, \zeta_j)$ ,  $j = 1, \dots, m$ ,  $z = 1, \dots, n_e$ . The  $z$  subscript refers to the individual environment and there are  $n_e$  different environments.

- b. Specify a test for each environment using the formula

$$V_z(\omega_j, \sigma_j) = \exp(\mu_z(\omega_j, \zeta_j) + k_{jz} \sigma_z(\omega_j, \zeta_j))$$

$$j = 1, \dots, m, \quad z = 1, \dots, n_e \quad (26)$$

- c. Compute the probability of conservatism of each test.

$$(p_c)_z = \prod_{j=1}^m \Phi(k_{jz}) \quad (27)$$

- d. Plot all of the  $V_z(\omega_j, \zeta_j)$  functions on one graph. The shock test should be one whose shock spectrum closely matches the exact envelope of all the  $V_z(\omega_j, \zeta_j)$ ,  $z = 1, \dots, n_e$ , at each of the modal frequencies,  $\omega_j$ ,  $j = 1, \dots, m$ .

- e. A lower bound on the probability of conservatism of the shock test is given by

$$p_c^* = \prod_{z=1}^{n_e} (p_c)_z \quad (28)$$

The value of  $p_c^*$  can be adjusted by a suitable variation of the values of the  $k_{jz}$ ,  $j = 1, \dots, m$ ,  $z = 1, \dots, n_e$ .

### 3.0 Shock Spectral Conservatism Versus Structural Response Conservatism

The assumption which allowed approximate computation in the previous section of the probability of conservatism of a shock test was the following: if the shock response spectrum of a test shock envelopes the shock response spectrum of a field shock at every frequency where the structure of interest has a mode, then the test

shock is conservative with respect to the field shock for the structure of interest. This assumption is not always correct since a test shock spectrum may be conservative in the sense defined above, but the actual structural response may not be conservative at one or more points on the structure. In this section we investigate this problem. Our objective is to determine what level of shock spectral test conservatism is required to insure that the structural response excited by a test is conservative. To complete this objective a study was performed and some of the results are presented in the following.

We evaluate the test factor of conservatism with an experiment that has the following format. First, we simulate a random field, shock signal source using a burst of white noise. Second, using the same type of input, we generate shock tests with various average levels of conservatism. Third, we excite a MDF structure using the field and test inputs. Finally, we compare measures of the average structural response excited by the test inputs. From this comparison we can determine how the shock spectral level of conservatism compares to the overall structural response level of conservatism.

The equation governing the dynamic response of a linear MDF structure to a lateral base input is

$$[M](\ddot{z}) + [C](\dot{z}) + [K](z) = -[M](R) \ddot{x}, \quad (29)$$

where  $[M]$ ,  $[C]$ , and  $[K]$  respectively, are the mass, damping and stiffness matrices of the structure;  $(R)$  is a vector composed of ones and zeros, with a one in each position corresponding to a lateral motion degree of freedom;  $(z)$  is the structural response;  $\ddot{x}$  is the base acceleration input; and dots denote differentiation with respect to time. All vectors in the equation have dimension  $n \times 1$  and matrices are square and dimensioned  $n \times n$ .  $\ddot{x}(t)$  is taken to be the random process defined by using Equation 4c in Equation 2. We assume that the response vector random process is mean square continuous and two mean square derivatives exist. The structural response can be obtained through a modal analysis. In the modal analysis we obtain the system modal frequencies,  $\omega_j$ ,  $j = 1, \dots, m$ , where  $m$  is the number of modes analyzed in the system and we require  $1 \leq m \leq n$ . And we obtain the matrix of normal modes of the system,  $[u]$ , with dimensions  $n \times m$ . The matrix of normal modes (or modal matrix) is that matrix which is characterized by the following two relations.

$$[u]^T [M] [u] = [I] \quad (30a)$$

and

$$[u]^T [K] [u] = [\omega^2], \quad (30b)$$

where  $[I]$  is an  $m \times m$  identity matrix and  $[\omega^2]$  is the diagonal matrix with the elements,  $\omega_j^2$ ,  $j = 1, \dots, m$ . We assume that the damping matrix can be diagonalized, and we let

$$[u]^T [C] [u] = [2\zeta\omega]. \quad (30c)$$

The values  $\zeta_j$ ,  $j = 1, \dots, m$ , are known as the modal damping factors of the structure.

We now let

$$(z) = [u](y) \quad (31)$$

and use this in Equation 29. Next, we premultiply the resulting equation by  $[u]^T$ . The result is

$$(\ddot{y}) + [2\zeta\omega](\dot{y}) + [\omega^2](y) = -[u]^T [M] (R) \ddot{x}. \quad (32)$$

This is a set of  $n$  uncoupled equations in matrix form. The  $j^{\text{th}}$  equation in this set can be written

$$\ddot{y}_j + 2\zeta_j \omega_j \dot{y}_j + \omega_j^2 y_j = \ddot{x} \left[ -\sum_{k=1}^n u_{kj} M_k R_k \right], \quad j = 1, \dots, m, \quad (33)$$

where  $u_{jk}$  is the  $j^{\text{th}}$  row  $k^{\text{th}}$  column element in the matrix,  $[u]$ ,  $M_k$  is the  $k^{\text{th}}$  element in the diagonal matrix,  $[M]$ , and  $R_k$  is the  $k^{\text{th}}$  element in the vector,  $(R)$ . We have already found the moments of the response for a system governed by this equation. For present purposes we use the stationary response moments. These are given in Equations A-4a through A-4c of Appendix A. For the mean square value of the modal displacement response we write

$$\sigma_{y_j}^2 = \frac{\pi \omega_j^2}{2\zeta_j \omega_j^3}, \quad j = 1, \dots, m. \quad (34)$$

where

$$\omega_j^2 = -\sum_{k=1}^n u_{kj} M_k R_k, \quad j = 1, \dots, m. \quad (34a)$$

The mean square value of the modal velocity response can be written

$$\sigma_{\dot{y}_j}^2 = \frac{\pi \omega_j^2}{2\zeta_j \omega_j}, \quad j = 1, \dots, m. \quad (35)$$

We now define the peak response in the  $j^{\text{th}}$  mode as

$$A_j = \max_t |y_j(t)|. \quad (36)$$

Since we are considering the stationary state of response, Equations 34 and 35 can be used in Equation 16a, and Equation 16a can be used in Equation 18 to obtain the cdf of  $A_j$ . It is

$$P_{A_j}(a) = \exp \left[ -\frac{a^2}{\pi} \frac{\sigma_{\dot{y}_j}^2}{\sigma_{y_j}^2} \exp \left( -\frac{a^2}{2\sigma_{y_j}^2} \right) \right], \quad a > 0, \quad j = 1, \dots, m. \quad (37)$$



where  $\sigma_{y_j}^2$  and  $\sigma_{\dot{y}_j}^2$ , the mean squares of the modal displacement and velocity responses, come from Equations 34 and 35. This is the probability that  $|Y_j(t)|$  remains below the value of  $\alpha$  during the entire time interval  $(0, t)$ . The expected value and variance of  $A_j$  can be found by determining the pdf of  $A_j$  and using the definitions of mean and variance. The pdf of  $A_j$  is found by differentiating  $P_{A_j}(\alpha)$  with respect to  $\alpha$ . Reference 11 shows that the first two moments of  $A_j$  are

$$E[A_j] = \sqrt{2 \ln \left[ \left( \frac{2}{\pi} \frac{\sigma_{\dot{y}_j}^2}{\sigma_{y_j}^2} \right) t \right]} \sigma_{y_j}, \quad j = 1, \dots, n, \quad (38a)$$

$$V[A_j] = \frac{\pi^2}{12 \ln \left[ \left( \frac{2}{\pi} \frac{\sigma_{\dot{y}_j}^2}{\sigma_{y_j}^2} \right) t \right]} \sigma_{y_j}^2, \quad j = 1, \dots, n. \quad (38b)$$

The variance of the peak response in the  $j^{\text{th}}$  mode is a measure of the degree of variability of the peak modal response.

We now proceed to compute the moments of the response at each degree of freedom. Based on Equation 31 the response at the  $k^{\text{th}}$  structural degree of freedom is given by

$$z_k(t) = \sum_{l=1}^n u_{kl} y_l(t), \quad k = 1, \dots, n. \quad (39)$$

Based on our computations for modal response autocorrelation functions (Appendix A), and the fact that the modal crosscorrelation functions are zero, we can determine the autocorrelation functions for the structural responses,  $z_k(t)$ ,  $k = 1, \dots, n$ . These can be used to find the mean square value of the stationary structural displacement response at the  $k^{\text{th}}$  degree of freedom. It is

$$\sigma_{z_k}^2 = \sum_{l=1}^n u_{kl}^2 \sigma_{y_l}^2, \quad k = 1, \dots, n. \quad (40)$$

where  $\sigma_{y_l}^2$  is given in Equation 34. Similarly, the mean square value of the stationary structural velocity response at the  $k^{\text{th}}$  degree of freedom is

$$\sigma_{\dot{z}_k}^2 = \sum_{l=1}^n u_{kl}^2 \sigma_{\dot{y}_l}^2, \quad k = 1, \dots, n. \quad (41)$$

where  $\sigma_{\dot{y}_l}^2$  is given in Equation 35. It is also possible to evaluate the crosscorrelation between the structural displacement and velocity responses. This is zero. Equations 40 and 41 define the second order moments of the stationary response random process at each degree of

freedom. These are used in the following paragraphs to define the peak response cdf at each degree of freedom.

Using the same assumption we did in the SDF case, we can write the cdf which governs the peak response of the structure at each of its degrees of freedom. The primary assumption is that the response executes a stationary motion during the time interval  $(0, t)$ . We define the peak response at the  $k^{\text{th}}$  degree of freedom as

$$Z_k = \max_t |z_k(t)|, \quad k = 1, \dots, n. \quad (42)$$

The cdf of  $Z_k$  is

$$P_{Z_k}(\alpha) = \exp \left[ - \frac{t}{\pi} \frac{\sigma_{\dot{z}_k}^2}{\sigma_{z_k}^2} \exp \left( - \frac{\alpha^2}{2\sigma_{z_k}^2} \right) \right], \quad \alpha \geq 0, \quad k = 1, \dots, n. \quad (43)$$

where the mean square values of the structural displacement and velocity responses,  $\sigma_{z_k}^2$  and  $\sigma_{\dot{z}_k}^2$ , are given in Equations 40 and 41. This is the probability that the peak absolute structural response at the  $k^{\text{th}}$  degree of freedom is lower than  $\alpha$  during the time interval  $(0, t)$ . We can obtain the mean and variance of peak structural response by finding the pdf of  $Z_k$  and using the definitions. These were obtained in Reference 12 and are given by

$$E[Z_k] = \sqrt{2 \ln \left[ \left( \frac{2}{\pi} \frac{\sigma_{\dot{z}_k}^2}{\sigma_{z_k}^2} \right) t \right]} \sigma_{z_k}, \quad k = 1, \dots, n \quad (44a)$$

$$V[Z_k] = \frac{\pi^2}{12 \ln \left[ \left( \frac{2}{\pi} \frac{\sigma_{\dot{z}_k}^2}{\sigma_{z_k}^2} \right) t \right]} \sigma_{z_k}^2, \quad k = 1, \dots, n \quad (44b)$$

These values characterize the central location and spread in the pdf of  $Z_k$ .

Using the information derived in this section, it is now possible to compare, in a probabilistic sense, the levels of conservatism of the modal responses (these reflect shock spectral conservatism) to the levels of conservatism of the structural responses. One possible means for comparing the former to the latter is to choose a particular structure and a particular variety of random input, predict the level of conservatism in each mode and at each degree of freedom and compare these. The problem with this approach is that it is tedious since it attempts to consider each mode and degree of

freedom, and these may be numerous.

A better way to compare modal to structural conservatism is to define measures of modal and structural conservatism which incorporate information from each mode and degree of freedom, and compare the measures of conservatism. Many measures of response conservatism exist, and each must be defined for a particular structure, and with reference to a particular field input. In the following, we use the structural notation defined previously. The field input which we wish to represent in a test is denoted,  $\tilde{X}(t)$ . We assume that the field input excites a response in each structural mode,  $Y_{Fj}(t)$ ,  $j = 1, \dots, m$ , and that the field input excites the structural response,  $Z_{Fk}(t)$ ,  $k = 1, \dots, n$ , at the  $k$ th degree of freedom. The peak modal responses excited by the field input are  $A_{Fj}$ ,  $j = 1, \dots, m$ , and the peak structural responses excited by the field input are  $Z_{Fk}$ ,  $k = 1, \dots, n$ . An arbitrary input, which might possibly be a test input, is denoted,  $\tilde{X}(t)$ . It excites the modal responses,  $Y_j(t)$ ,  $j = 1, \dots, m$ , and the structural responses,  $Z_k(t)$ ,  $k = 1, \dots, n$ . The absolute peak modal responses excited by this input are  $A_j$ ,  $j = 1, \dots, m$ , and the absolute peak structural responses excited by this input are  $Z_k$ ,  $k = 1, \dots, n$ . We now define the probability of modal conservatism in the  $j$ th mode for the arbitrary input as

$$P_{mj} = P\{A_j \geq A_{Fj}\}, j = 1, \dots, m. \quad (45a)$$

This is the probability that the peak modal response excited by the input,  $\tilde{X}(t)$ , is greater than the peak modal response excited by the field input,  $\tilde{X}_F(t)$ . We define the probability of response conservatism at the  $k$ th structural degree of freedom as follows:

$$P_{sk} = P\{Z_k \geq Z_{Fk}\}, k = 1, \dots, n. \quad (45b)$$

This is the chance that the peak structural response at the  $k$ th degree of freedom excited by  $\tilde{X}(t)$ , is greater than the response excited by the field input,  $\tilde{X}_F(t)$ . This is the probability that the test input is conservative with respect to the field input at the  $k$ th mode.

A first measure of modal response conservatism can now be defined. It is

$$G_m = \left[ \prod_{j=1}^m P_{mj} \right]^{1/m}. \quad (46a)$$

This is the geometric mean probability of modal conservatism. This quantity reflects a typical probability that the response in any mode is conservative. If the responses in all structural modes are independent, then we can raise  $G_m$  to the power  $m$  to obtain the chance that the responses in all modes are conservative. An analogous measure of structural response conservatism can be specified; it is

$$G_s = \left[ \prod_{k=1}^n P_{sk} \right]^{1/n}. \quad (46b)$$

This is the geometric mean probability of structural conservatism. These geometric mean probabilities of conservatism can be computed when the characteristics of a random source are known, and a test to represent that source is specified.

The actual factor by which the peak response excited by a test input exceeds the peak response excited by a field input, provides a measure of response conservatism. Let this factor be denoted  $R_{mj}$ ,  $j = 1, \dots, m$ , in the modal case, and  $R_{sk}$ ,  $k = 1, \dots, n$ , in the structural degree of freedom case. Then we have

$$R_{mj} = \frac{A_j}{A_{Fj}}, j = 1, \dots, m \quad (47a)$$

and

$$R_{sk} = \frac{Z_k}{Z_{Fk}}, k = 1, \dots, n. \quad (47b)$$

A second pair of measures of response conservatism can be defined in terms of the above quantities. An averaged measure of the modal response factor of conservatism can be defined

$$C_m^* = \frac{1}{m} \sum_{j=1}^m R_{mj}. \quad (48a)$$

and an averaged measure of the structural response factor of conservatism can be defined

$$C_s^* = \frac{1}{n} \sum_{k=1}^n R_{sk}. \quad (48b)$$

This pair of measures of the factor of conservatism of a shock input indicates, in an average sense, whether or not a test is conservative. We note that the modal or structural response may be unconservative at one or several points, and this measure will provide no indication of that. However, in using this measure of input conservatism we eliminate the need to observe each mode and each degree of freedom in a structural response. In the following we use  $C_m^*$  and  $C_s^*$  to derive some variables which are indicators of the level of conservatism at a typical mode in the system or at a typical degree of freedom in the system, and for various levels of test input, we estimate the means and variances of these variables. To do this we first estimate the mean and variance of  $C_m^*$  and  $C_s^*$ .

The formulas for the mean and variance of a sum of random variables are well known and are given in Reference 13. For the sums of random variables,  $C_m^*$  and  $C_s^*$ , these are

$$E[C_m^*] = \frac{1}{m} \sum_{j=1}^m \frac{E[A_j]}{A_{Fj}}, \quad (49a)$$

$$E[C_m^*] = \frac{1}{n} \sum_{k=1}^n \frac{E[Z_k]}{Z_{mk}}, \quad (49b)$$

$$\text{Var}[C_m^*] = \frac{1}{n^2} \left[ \sum_{j=1}^n \frac{\text{Var}[A_j]}{A_{mj}^2} + \sum_{j \neq k} \frac{\text{cov}[A_j, A_k]}{A_{mj} A_{mk}} \right] \quad (49c)$$

$$\text{Var}[C_s^*] = \frac{1}{n^2} \left[ \sum_{k=1}^n \frac{\text{Var}[Z_k]}{Z_{sk}^2} + \sum_{j \neq k} \frac{\text{cov}[Z_j, Z_k]}{Z_{sj} Z_{sk}} \right] \quad (49d)$$

For the analytical purposes of this investigation we assume that the peak modal responses and peak structural responses are uncorrelated. Therefore, the double summation terms on the right-hand side of the latter two equations written above are zero. In the above equations, the averages,  $E[C_m^*]$  and  $E[C_s^*]$ , can be taken as representative of the mean of a typical underlying factor of conservatism. The variance of an average equals the variance of an underlying random variable divided by the averaging constant ( $m$  or  $n$ ), when all the underlying random variables are identically distributed. Therefore, we can take  $m \cdot \text{Var}[C_m^*]$  and  $n \cdot \text{Var}[C_s^*]$  as representative of the variances of typical underlying factors of conservatism above. In view of these factors, we define the random variables,  $C_m$  and  $C_s$ , in terms of  $C_m^*$  and  $C_s^*$ .  $C_m$  and  $C_s$  are random variables with means and variances defined below.

$$E[C_m] = E[C_m^*] \quad (50a)$$

$$E[C_s] = E[C_s^*] \quad (50b)$$

$$\text{Var}[C_m] = m \cdot \text{Var}[C_m^*] \quad (50c)$$

$$\text{Var}[C_s] = n \cdot \text{Var}[C_s^*] \quad (50d)$$

These random variables represent the random factor of conservatism in a typical mode or at a typical degree of freedom of a structure. The probability distribution of the random variables  $C_m$  and  $C_s$  are unknown. Nevertheless, these random variables still indicate the factor of conservatism associated with the structural response to a test relative to the structural response to a field input. A measure of the relative degree of variation of the modal and structural factors of conservatism is given by the coefficient of variation of each random variable. This is defined as the standard deviation of the random variable divided by the mean. These are

$$\rho_m = \frac{\sqrt{\text{Var}[C_m]}}{E[C_m]} \quad (51a)$$

$$\rho_s = \frac{\sqrt{\text{Var}[C_s]}}{E[C_s]} \quad (51b)$$

When  $C_m$  and  $C_s$  are taken as quantities representative of the modal and structural factors of conservatism of a structure, then  $\rho_m$  and  $\rho_s$  reflect the relative normalized degree of variation of conservatism in the structure. The measures of peak structural response presented in this section can be used in a limited way to compare the peak structural response at a structural degree of freedom to the shock spectral response excited by a shock input. In the following, a numerical example is performed to show how the geometric mean probabilities of modal and structural conservatism vary as functions of the average factor of shock spectral conservatism.

In the example we consider the shock response of the conic shell shown in Figure 5. This is a thin walled shell made from aluminum.

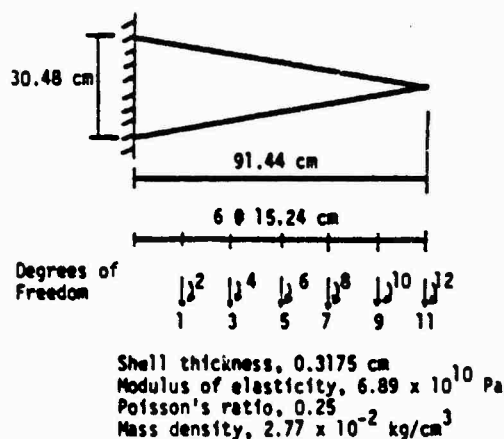


Figure 5 Conical shell

The mass density has been increased by a factor of ten to account for nonstructural mass appended to this shell. The shell is fixed at the end and is excited through its base. This structure was modeled using a finite element model and was analyzed using CAL. Six elements and twelve degrees of freedom were used in the model. The model parameters are given in Table 1. Included are modal frequencies and structural masses. The modal damping factors presented in Table 1 were used in the analysis. It was assumed that the excitation is a band limited white noise with cutoff frequency, 30,000 rad/sec, therefore, only five structural modes respond to the input. The duration for each input used to excite the structure was 0.045 sec. Ten white noise inputs with the

Table 1

## Conical Shell Parameters

Mode No. j	Modal Frequency, $\omega_j$ , (rad/sec)	Modal Damping Factor, $\zeta_j$	Degree of Freedom No.	Structural Mass $M_j$ , (kg)
1	2824	0.1	1	1.068
2	4809	0.01	2	3.205
3	10554	0.005	3	0.855
4	20184	0.005	4	2.562
5	23346	0.005	5	0.641
6	39502	-	6	1.923
7	58320	-	7	0.427
8	72576	-	8	1.284
9	96278	-	9	0.214
10	129178	-	10	0.641
11	162230	-	11	0.053
12	204269	-	12	0.159

spectral density levels listed in Table 2 were used to excite the conic shell. These were taken as the test input levels. The field input was a burst of white noise with frequency cutoff, 30,000 rad/sec, duration 0.045 sec, and spectral density  $25.8 \times 10^4 \text{ cm}^2/\text{rad-sec}^3$ . The peak response excited by the field input was taken as the average peak response which the given random input excites. The modal and structural degree of freedom responses to the field input are listed in Table 2. For each input, the stationary state mean square response in each mode was calculated using

Equation 34, and the mean square value of the derivative of the modal response was calculated using Equation 35. These were used, in turn, to calculate the mean square structural response and mean square of the derivative of the structural response at each degree of freedom using Equations 40 and 41. The four mean square quantities calculated above were used to find the modal and structural probabilities of conservatism expressed in Equations 45a and 45b using Equations 37 and 43. The mean and variance of peak modal response in each mode and peak structural response at each degree of

Table 2

Cone  
Spectral Density Input Levels  
Structural Response to Field Inputs

Input No.	Spectral Density Level ( $\text{cm}^2/\text{rad-sec}^3$ )	Mode No.	Modal Resp. to Field Input, (cm)	Structural Degree of Freedom No.	Structural Resp. to Field Input, (cm)
1	$25.8 \times 10^4$	1	$2.95 \times 10^{-3}$	1	$3.81 \times 10^{-3}$
2	$28.5 \times 10^4$	2	$3.53 \times 10^{-3}$	2	$1.37 \times 10^{-2}$
3	$31.2 \times 10^4$	3	$1.65 \times 10^{-3}$	3	$2.69 \times 10^{-2}$
4	$34.1 \times 10^4$	4	$4.32 \times 10^{-4}$	4	$4.14 \times 10^{-2}$
5	$37.2 \times 10^4$	5	$2.79 \times 10^{-4}$	5	$6.60 \times 10^{-2}$
6	$40.3 \times 10^4$			6	$1.72 \times 10^{-1}$
7	$43.6 \times 10^4$				
8	$47.0 \times 10^4$				
9	$50.6 \times 10^4$				
10	$54.3 \times 10^4$				

freedom were also calculated using Equations 38 and 44. Using Equations 46a and 46b, the geometric mean probabilities of modal and structural conservatism were calculated for each input level. These are listed in Table 3. And using Equations 50 and 51, the mean, variance and coefficient of variation of the typical peak modal and structural responses were calculated for each input level. These are also listed in Table 3.

Figure 6 includes two curves. The first graphs the geometric mean probability of modal conservatism versus the mean level of conservatism of a typical structural mode, where use is made of Table 3. The second curve is similar to the first except that the geometric mean probability of structural conservatism is used. Figure 6 shows that the probability of conservatism of the response at a typical mode varies in nearly the same way as the probability of conservatism of the response at a typical degree of freedom on the structure.

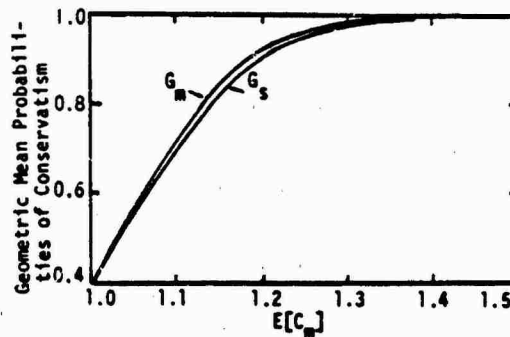


Figure 6 Cone--Geometric mean probabilities of modal and structural conservatism versus average factor of conservatism at a typical mode

Table 3

Cone  
Geometric Mean Probability of Conservatism  
Moments of Peak Response in Typical Mode or at  
Typical Degree of Freedom

Modes

Input No.	Input Ratio*	$G_m$	$E[C_m]$	$Var[C_m]$	$\rho_m$
1	1.00	0.394	1.00	0.0142	0.119
2	1.05	0.568	1.05	0.0156	0.119
3	1.10	0.730	1.10	0.0171	0.119
4	1.15	0.851	1.15	0.0187	0.119
5	1.20	0.926	1.20	0.0204	0.119
6	1.25	0.965	1.25	0.0221	0.119
7	1.30	0.984	1.30	0.0239	0.119
8	1.35	0.992	1.35	0.0258	0.119
9	1.40	0.997	1.40	0.0277	0.119
10	1.45	0.998	1.45	0.0296	0.119

Structural Degrees of Freedom

Input No.	Input Ratio*	$G_s$	$E[C_s]$	$Var[C_s]$	$\rho_s$
1	1.00	0.393	1.00	0.0155	0.124
2	1.05	0.554	1.05	0.0171	0.124
3	1.10	0.707	1.10	0.0187	0.124
4	1.15	0.828	1.15	0.0205	0.124
5	1.20	0.911	1.20	0.0223	0.124
6	1.25	0.959	1.25	0.0242	0.124
7	1.30	0.983	1.30	0.0261	0.124
8	1.35	0.993	1.35	0.0282	0.124
9	1.40	0.998	1.40	0.0303	0.124
10	1.45	0.999	1.45	0.0325	0.124

\*The input ratio is the square root of the ratio of the test input spectral density to the field input spectral density.

The results of this example and some similar examples summarized in Reference 1 show that as the average factor of shock spectral conservatism increases, the probability that the test specified is conservative also increases. When a shock spectral factor of conservatism of 1.4 or greater is used in specifying a test, the probability of conservatism of the response at a degree of freedom is within a few percent of the shock spectral probability of conservatism. Since the factor, 1.4, is small relative to shock spectral factors of conservatism which might be used in practice, we conclude that the assumption used in Section 2.2 is reasonable. That is, the fact that a shock test is specified so that all modes in a MDF structure are conservatively tested does imply that the entire structure is conservatively tested.

#### 4.0 Conclusion

In this paper we have defined a method which can be used for the probabilistic specification of mechanical shock tests. The method is easy to use, and its accuracy depends, in part, on the accuracy of the assumption that the peak response probability distribution of a randomly excited SDF system is lognormal. The analysis presented in this paper and other studies show that, for a wide variety of inputs, this is a reasonable assumption. Further, the accuracy of this method depends on the assumption that when one shock spectrum envelops another, any test corresponding to the enveloping shock spectrum is conservative with respect to any input corresponding to the second shock spectrum. We have shown in a special application that this assumption is reasonable. There may, however, be circumstances under which this assumption is invalid. When these circumstances exist, the effectiveness of the method of shock response spectra, itself, is greatly diminished.

In the majority of cases we can certainly conclude that the method for probabilistic shock test specification presented in Section 2.2 of this paper will yield accurate and useful results.

#### Appendix A

##### Input and Response Moments

In this Appendix we write the expressions for the autocorrelation functions of some non-stationary random acceleration inputs. These inputs have zero mean and are normal. Then we write the expression for some moments of the response of SDF systems to these inputs. In Equation 5 in the text we gave the autocorrelation function of the random process obtained by using Equation 4a in Equation 2. We now present the autocorrelation functions of the random processes defined by using Equations 4b and 4c in Equation 2. These are

$$R_{XX}^{(2)}(t,s) = 2\pi KB^2(e^{-\alpha(t+s)} + e^{-\beta(t+s)} - e^{-\alpha t - \beta s} - e^{-\beta t - \alpha s}) \delta(t-s), t,s \geq 0 \quad (A-1a)$$

$$R_{XX}^{(3)}(t,s) = 2\pi KB^2 \delta(t-s), t,s \geq 0 \quad (A-1b)$$

The moments of the SDF system response to the earthquake input (Equation 4b) are given by

$$R_{YY}^{(2)}(t,s) = R_{YY}^{(1)}(t,s,\alpha) + R_{YY}^{(1)}(t,s,\beta) - 2 \cdot R_{YY}^{(1)}\left(t,s, \frac{\alpha+\beta}{2}\right) \quad (A-2a)$$

$$R_{YY}^{(2)}(t,s) = R_{YY}^{(1)}(t,s,\alpha) + R_{YY}^{(1)}(t,s,\beta) - 2 \cdot R_{YY}^{(1)}\left(t,s, \frac{\alpha+\beta}{2}\right) \quad (A-2b)$$

$$R_{YY}^{(2)}(t,s) = R_{YY}^{(1)}(t,s,\alpha) + R_{YY}^{(1)}(t,s,\beta) - 2 \cdot R_{YY}^{(1)}\left(t,s, \frac{\alpha+\beta}{2}\right) \quad (A-2c)$$

These are the autocorrelation function of the response random process (Equation A-2a), the crosscorrelation function of the response random process and its derivative (Equation A-2b), and the autocorrelation function of the derivative of the response random process (Equation A-2c). The superscript "2" shows that these expressions refer to the earthquake response random process.

The moments of the SDF system response to the steady input (Equation 4c) can be written as follows:

$$R_{YY}^{(3)}(t,s) = R_{YY}^{(1)}(t,s,0) \quad (A-3a)$$

$$R_{YY}^{(3)}(t,s) = R_{YY}^{(1)}(t,s,0) \quad (A-3b)$$

$$R_{YY}^{(3)}(t,s) = R_{YY}^{(1)}(t,s,0) \quad (A-3c)$$

The "3" superscripts show that these functions refer to the steady input. We note that as  $t$  and  $s$  become large, in the above expressions, the moments approach the following limits.

$$R_{YY}^{(3)}(\infty, \infty) = \frac{\pi KB^2}{2\zeta\omega_n^3} \quad (A-4a)$$

$$R_{YY}^{(3)}(\infty, \infty) = 0 \quad (A-4b)$$

$$R_{YY}^{(3)}(\infty, \infty) = \frac{\pi KB^2}{2\zeta\omega_n^3} \quad (A-4c)$$

These are the response moments once the system has reached the stationary state. For typical systems, the response moments nearly equal the limits given above after twenty cycles of response have been executed.

#### Acknowledgement

The author gratefully acknowledges the support of Sandia Laboratories. This project was supported through a Sandia University Research Program contract numbered 281-617-3.

#### References

1. Paez, T. L., "Shock Response Spectra: Conservatism of Structural Tests," Report No. CE-48(79)SURP-729-3, Bureau of Engineering Research, The University of New Mexico, Albuquerque, NM, June 1979.
2. Yang, J.-N., "Nonstationary Envelope Process and First Excursion Probability," Journal of Structural Mechanics, Vol. 1, No. 2, 1972, pp. 231-248.
3. Yang, J.-N., "First Excursion Probability in Nonstationary Random Vibration," Journal of Sound and Vibration, Vol. 27, No. 2, 1973.
4. Lin, Y. K., Probabilistic Theory of Structural Dynamics, McGraw-Hill Book Company, New York, 1967.
5. Crandall, S. H., and Mark, W. D., Random Vibration in Mechanical Systems, Academic Press, New York, 1973.
6. Rice, S. O., "Mathematical Analysis of Random Noise," Bell System Technical Journal, Vols. 23 and 24, reprinted in Selected Papers on Noise and Stochastic Processes, N. Wax, Ed., Dover, 1954.
7. Paez, T. L., "Conservatism in Shock Analysis and Testing: Peak Response of Randomly Excited Systems," Report No. CE-44(78)SURP-617-3, Bureau of Engineering Research, The University of New Mexico, Albuquerque, NM, July 1978.
8. Paez, T. L., "Conservatism in Shock Analysis and Testing: Probability of Test Conservatism," Report No. CE-46(78)SURP-617-3, Bureau of Engineering Research, The University of New Mexico, Albuquerque, NM, October 1979.
9. Kelley, R. D. and Richman, G., Principles and Techniques of Shock Data Analysis, Shock and Vibration Monograph-5, Naval Research Laboratory, 1969.
10. Scanlan, R. H. and Sachs, K., "Earthquake Time Histories and Response Spectra," Journal of the Engineering Mechanics Division, ASCE, Vol. 100, pp. 635-655.
11. Paez, T. L., "Conservatism in Shock Analysis and Testing," Report No. CE-43(78)-SURP-617-3, Bureau of Engineering Research, The University of New Mexico, Albuquerque, New Mexico, February 1978.
12. Meyer, S. and Paez, T. L., "Measurement of Suspension Loads and Determination of Suspension Reliability for a Store in the F-111 Weapons Bay," Proceedings of the Aircraft/Stores Compatibility Symposium, Ft. Walton Beach, Florida, 1977.
13. Brownlee, K. A., Statistical Theory and Methodology in Science and Engineering, John Wiley & Sons, New York, 1967.
14. Wilson, E. L., "CAL-Computer Analysis Language for the Static and Dynamic Analysis of Structural Systems," Report No. UC SESM-77-2, University of California, Berkeley, California, 1977.

#### DISCUSSION

Voice: What do you consider to be sufficient data? You said something like five items of data and I certainly agree that you might be lucky to ever have that much data. With only five items of data the statistics, using the standard distribution tables and the lab tests to give a high probability of conservatism, will raise your levels excessively. If we could ever have 50 pieces of data I am sure we could come up with very reasonable tests using your techniques. I am a little concerned when you say five items of data are enough.

Mr. Pezz: I think you are right. If you have little data then you will have low confidence and you can extend this to include a confidence analysis of the statistics that you compute. If you have very little data then you will have wide confidence intervals around the statistics and that tends to diminish the accuracy of what you are doing or it will raise the specified levels. I think that there is no way around that except to try to collect as much data as you can. If you only collect one piece of data then that is all you have to work with and you have to be satisfied with whatever you can get from that; but if you have a few pieces of data, as many as you think are necessary to compute the statistics, then you are increasing your information or increasing your knowledge of what this test means by using a probabilistic approach like this, for example.

Mr. Warner (Westinghouse): What was the size of your Monte Carlo sample?

Mr. Pezz: I did a lot of Monte Carlo tests. I think the slide I showed had about 20 peak responses on it. I did a lot of others and I think 20 was the minimum and I think 30 was the maximum, but I used a lot of different sources.

Voice: Did you try the Rayleigh distribution and the plain normal distribution on your Monte Carlo simulation?

Mr. Pezz: No, I have the feeling that those probably would have fit well but the two that I tried were the type one extreme value distribution and the log normal distribution. Later on, after I finished this, I tried a normal distribution. The log normal distribution looked better than both of those but neither of those other ones looked bad.



## MEASUREMENT OF DYNAMIC STRUCTURAL CHARACTERISTICS OF MASSIVE BUILDINGS BY HIGH-LEVEL MULTIPULSE TECHNIQUES

D.G. Yates and F.B. Safford  
Agbabian Associates, El Segundo, California

Experimental determination of the responses of large structures has become a necessary tool for structural design verification and analysis. The structural integrity of offshore oil platforms and the seismic risks in nuclear power plants and other large structures require much greater safety assurance. Multipulsed High-Level Structural Testing is an innovative approach to high-level transient testing. A portable impulse device of recent development produces large force time histories that can be controlled to satisfy multimode system response. The pulse shapes provide an input Fourier spectrum concentrated in the desired frequency region with input force amplitude as high as 60,000 pounds-force. This testing machine is a metal-cutting device in which a multiple-blade cutter cuts through a series of metal projections called nubbins. Judicious design of the cutter, nubbin shapes, cutting velocity, and energy source produces various pulse amplitudes, shapes, and durations. The force pulse generates high output forces for time durations sufficient to mobilize structural modes and compatible with digital signal capture.

Experimental determination of the response of large structures has become necessary for structural design, verification, and analysis. This is especially true today with the increasing emphasis on such problems as nuclear power plant safety, structural integrity of offshore oil platforms, and all large structures placed near potential earthquake activity. Testing is undertaken as a validation of computer simulations (finite element models) or as a direct indication of dynamic structural responses.

The type of testing undertaken is normally that in which modal frequencies, mode shapes, and damping are extracted. In the last few years, however, testing results have also been used to directly calculate structural systems response motions to a variety of dynamic forcing functions. This has been partly due to the rapid advances of the digital signal capture and processing technology [1, 2, 3].

There are many different types of tests performed today, with varying degrees of success, and they are usually designated by the input forcing function used in the program. The following test methods are commonly performed today:

- Slow sine sweep
- Sine dwell
- Rapid sine sweep (chirp)
- Random input
- Initial displacement
- Transient low level
- Transient high level

Extensive work has been accomplished using the slow sine sweep and dwell test efforts, and they are still considered, in many engineering circles, to be the baseline which all other test methods must equal.

These steady-state tests require hydraulic, electromechanical, hybrid shaker devices or some form of mechanical device, such as counterrotating weights, in order to subject the system to slowly sweeping sinusoidal forces or resonance-dwell sinusoidal excitations. The dynamic response data obtained from the system, as motions, can then be analyzed by standard techniques to provide the modal properties of the system--mode shapes, natural frequencies, and damping. Rapid sine

sweep (or chirp functions) and random inputs have not been used as extensively on very large structures, as they require complex control systems and can only be used for low-level testing. Initial displacement, or snap-back, tests have been used on tall thin structures such as chimneys and oil distillation chambers to determine the first mode information. There appears, however, to be an excessive amount of error in this latter case when second or third mode determination is attempted.

Transient tests are conducted by applying non-steady-state, or impulsive, forces to a system and measuring the dynamic response in the form of motions. Complex pulses as inputs produce complex system responses. The method is amenable to analysis by modal methods, but one can also determine the overall transfer-function characteristics of the system by relating the system response-frequency spectrum to the input force-frequency spectrum. The measured transfer function in the frequency domain may be readily inverse transformed to the time domain to obtain the impulse function of the structure. The response of the structure to any input can then be determined by convolving the impulse response function with the expected inputs.

Transient tests have been performed with low-level impact devices, shakers, and high-explosive devices that can produce quick-energy release over an extended frequency band. With the emergence of good quality, field applicable, digital capture data acquisition and analysis system (DAAS), the transient type of testing has become even more popular. The advent of these portable mini- and microcomputers has greatly facilitated the application of transient testing techniques by allowing on-site data reduction and processing and direct communication between the small mini system and large main frame computers, thereby enhancing data accuracy and testing and analysis speed. In the past, electrical and mechanical noises have often severely limited the quality of mode shapes and transfer functions determined from transient testing. Multiple transient tests performed within the framework of modern digital DAAS technology permit data averaging and other signal processing techniques to greatly minimize the noise contribution [1].

A portable impulse device recently developed produces large force time histories that can be controlled to satisfy multimode system response. This device is an innovative approach to high-level transient testing, which will be referred to as a multipulsed high-level structural exciter (or pulsar). The pulse shapes can be designed to provide a near-flat input Fourier transform in the desired frequency regions of interest or other spectra shapes as desired. These force pulse trains

generate high output forces for time durations sufficient to mobilize structural modes and for time durations compatible with digital signal capture.

The high-level multipulse system has been used successfully on several large structures, exciting the response frequencies in each. Due to its simplicity, a number of tests can be run at any position in a short period of time. This allows for the determination of statistical invariance in the data and/or rapid retesting in case of errors in the preceding test.

## THEORETICAL PRINCIPLES

There are two principles utilized in the design of the multipulse exciter. The first involves the spectral energy in a series of force pulses. The second involves the energy required to cut metal.

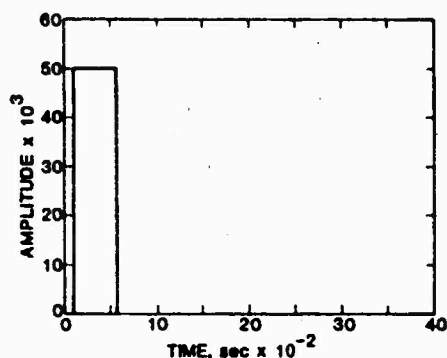
### SPECTRAL ENERGY CONSIDERATIONS

The Fourier spectrum of a single pulse has a large frequency region of energy associated with it. Fig. 1 illustrates both a single pulse time history and its Fourier transform amplitude. If a series of pulses makes up the time history, the influence of each pulse will contribute to the energy in the total Fourier transform. By judicious design of these pulses, various spectral curves can be obtained for a desired frequency region as illustrated in Fig. 2. The spectrum of Fig. 2 for the input function is a desirable criteria for broad-frequency band vibration testing. There are a number of papers concerning the techniques used to optimize a pulse train to provide a particular spectral input [4, 5, 6], but these techniques will not be dealt with in this paper. The optimization can provide either an input with constant spectral amplitude or an input to cause a required response to take place at several output locations.

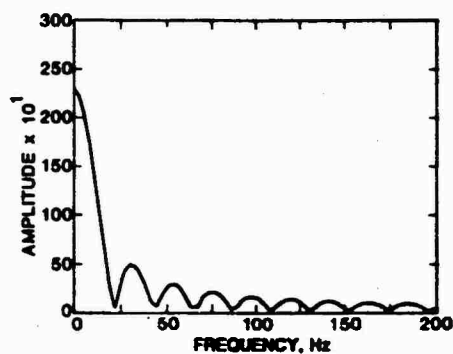
### CUTTING ENERGY CONSIDERATIONS

To physically produce the desired optimized pulse train, a metal cutting technique has been employed. A cutter is driven with great force through a series of metal projections called mubbins. The proper design of and specifications for the cutter, projection shapes, cutting velocity, and energy source are essentials to produce the various input force pulse amplitudes, shapes, and durations desired.

Past studies [5] have revealed that over a large cutting velocity range [ $v > 1.27 \text{ m/s}$  (50 ips)], the output force produced by the cutting of aluminum stock can be predicted by the following equation:

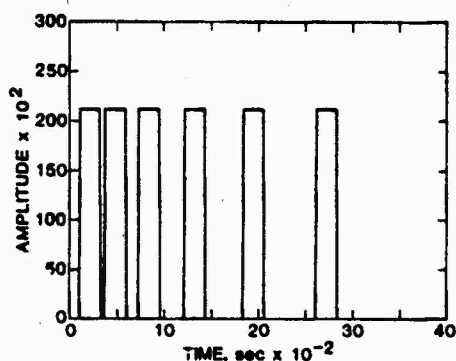


(a) Pulse time history

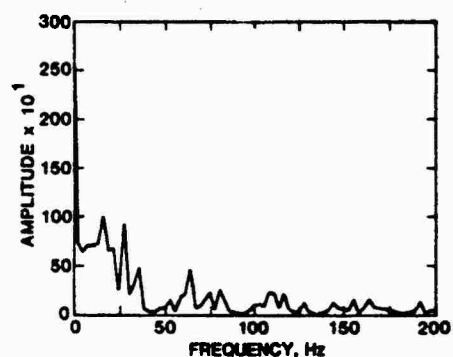


(b) Fourier transform

FIG. 1. SINGLE PULSE TIME HISTORY WITH ASSOCIATED FOURIER TRANSFORM



(a) Pulse time history



(b) Fourier transform

FIG. 2. MULTIPULSE TIME HISTORY AND ASSOCIATED FOURIER TRANSFORM  
ROUGHLY DESIGNED TO POPULATE SPECTRAL ENERGY FROM 0 TO 40 Hz

$$F = 43.11 \times 10^4 [\tanh(wt) - 0.006] \pm 5\% \quad \text{Newtons}$$

$$F = 9.58 \times 10^4 [\tanh(wt) - 0.006] \pm 5\% \quad \text{Pounds-force}$$

for

$$0.41 \text{ mm (0.016 in.)} < t < 25.4 \text{ mm (1.0 in.)}$$

$$3.18 \text{ mm (0.125 in.)} \leq w \leq 12.7 \text{ mm (0.50 in.)}$$

where

$F$  = Force output produced by cutting aluminum

$t$  = The total cut depth

$$t = t'_1 + t'_2 + \dots + t'_N$$

$t'_N$  = depth of cut of  $N^{\text{th}}$  cutter blade

$w$  = Width of the cutter blades (width is same for  $N$  cutters)

The limitations on  $t$  and  $w$  are included only as the ranges of present experimentation.

### DESIGN

The design of the multipulse structural exciter or pulser, implementing the above principles, involves a power source, cutting tool, cutting medium, and various support assemblies that are discussed below. Certain basic criteria were set forth at the initiation of design and are presented as follows:

- Force output capability allowing for a minimum of six pulses to be no less than 225,000 N (50,000 lbf)

- Vertical and horizontal inputs to be simultaneously produced with both inputs to be adjustable
- Physical portability to be used for field application
- Variable height to be used for field applications

An assembly drawing of the pulser design is shown in Fig. 3.

#### POWER SOURCE

The power required for this high-speed metal cutting is developed from the kinetic energy of a steel weight or carriage that is allowed to effectively fall 1.22 m (4 ft) prior to cutting. Actually, the "fall" is not vertical but at an angle to the vertical; the carriage is supported on Thompson linear ball bearings running on hardened and ground steel rods.

The size of the box-shaped steel carriage is 546 mm wide, 546 mm high, and 838 mm long (21.5 in. by 21.5 in. by 33 in.). It is made from 25.4 mm (1 in.) and 54.8 mm (2 in.) steel plates. Two large steel arms to support the linear bearings are bolted on the front and back. The front plate holds the cutter and cutter housing. The total weight of the carriage is 726 kg (1600 lb), which is increased by the addition of steel plates inside

the carriage. The maximum attainable carriage weight using these steel plates is 2180 kg (4800 lb). If lead plates are used, then a maximum weight of 3175 kg (7000 lb) can be attained.

#### RAIL ASSEMBLY

The carriage, through the linear bearings, rides on two 51 mm (2.1 in.) diameter hardened steel rods 3.91 m (12.8 ft) long. These rods, in turn, are supported on I-beams, which prevented excessive bending of the rods while the carriage traveled. The rails are attached at one end through the pivot shaft and anvil assembly for precise alignment. The placement of the cutter housing on the front carriage plate is based on the alignment of the bearings and mandrel to ensure that the reaction forces on the carriage are along the centroid. This minimizes any couple-induced loads on the carriage that might put additional forces on the linear bearings, thereby slowing its velocity.

The other end of the rail assembly is attached by a steel channel to which a manual release mechanism for the carriage and a pulley bracket is attached. The manual release is a hook catch assembly with a clevis pin attached to the carriage. To release the carriage at its highest point, a safety is removed before the hook can be rotated to release from the clevis pin. The carriage is raised and lowered along the rail system by a power winch through a double-strand pulley system.

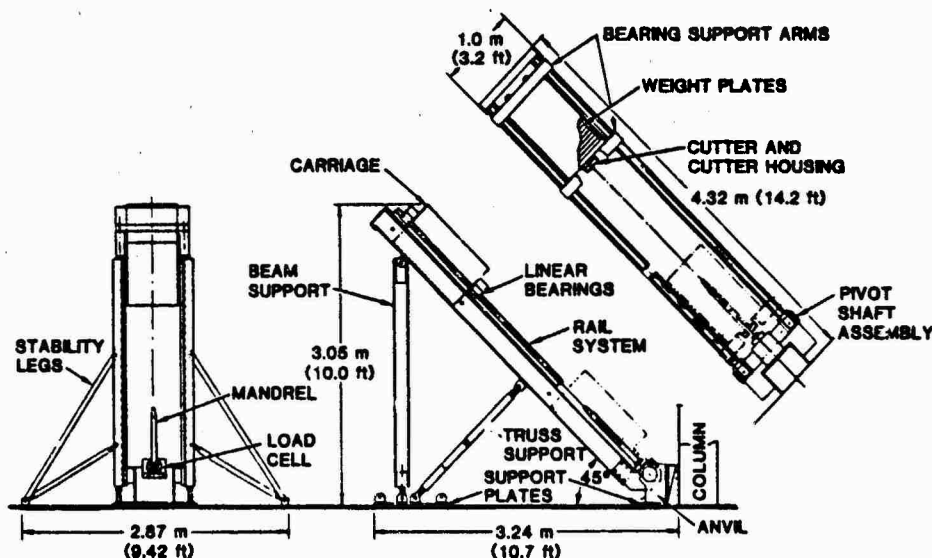


FIG. 3. ASSEMBLY - IMPULSE TESTER

When the rail assembly is raised to its proper angle, it is supported by adjustable beam-truss assemblies. These consist of aluminum channels as the main support beams at the far end of the rail assembly and cylindrical turnbuckles for additional support and alignment. For portability, these assemblies are attached by quick-disconnect pins. The power winch is bolted to a crossplate on the channel support beams. Both the beam and

truss members are attached to a common support plate epoxied on the floor. Attached to the channel support beams are stability legs made from aluminum channels. These absorb any rocking produced at release due to the offset alignment of the release hook. These features are illustrated in the assembly drawing (Fig. 3) and in photographs (Figs. 4 through 8).

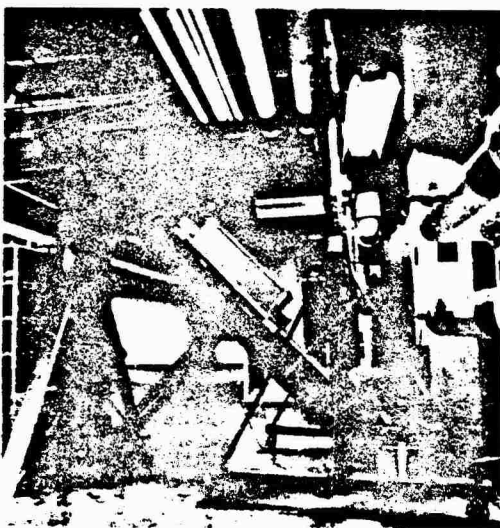


FIG. 4. SIDE VIEW OF HIGH LEVEL PULSER WITH GANTRY (ON SITE)



FIG. 5. REAR VIEW OF PULSER ON SITE



FIG. 6. IMPULSE DEVICE SHOWING MANDREL AND CUTTERS

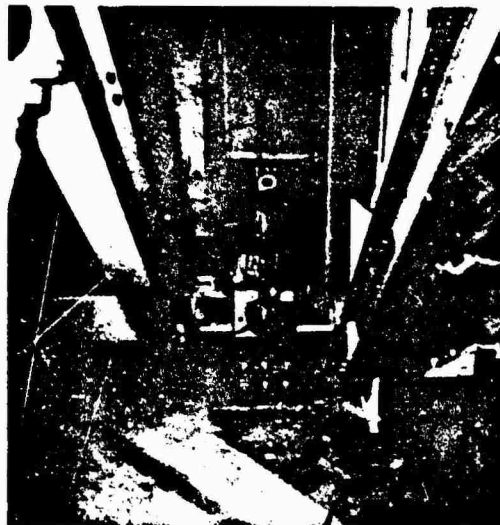


FIG. 7. FRONT VIEW OF PIVOT-SHAFT-ANVIL ASSEMBLY

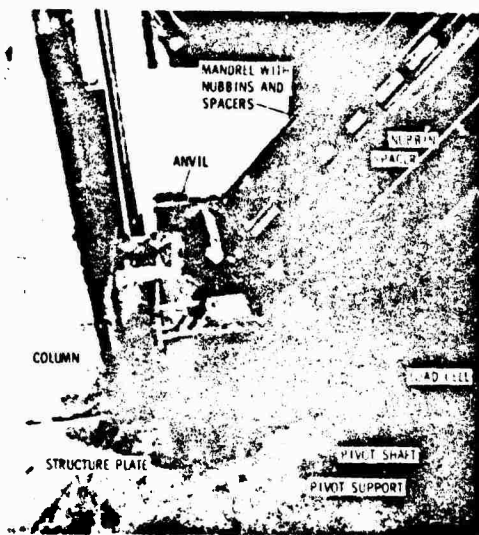


FIG. 8. VIEW OF PIVOT-SHAFT-ANVIL ASSEMBLY

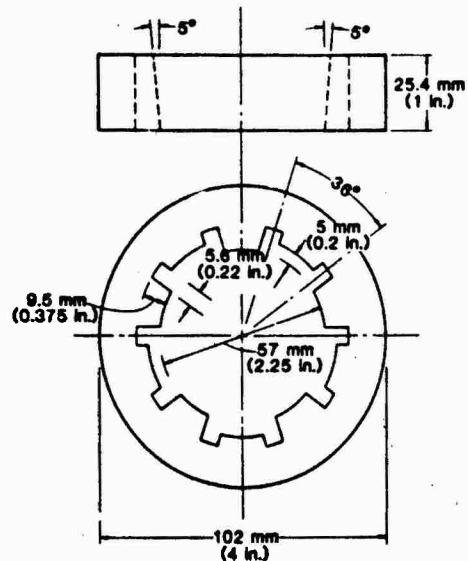


FIG. 9. CUTTER FOR MULTIPULSE EXCITATION

#### CUTTER AND CUTTER HOUSING

The cutter is a circular disc made from AISI-S4 shock resistant tool steel. The basic size is 102 mm (4 in.) outside diameter and 25.4 mm (1 in.) thick. The cutter blades are made by drilling a 57 mm (2.25 in.) diameter hole into the cutter with 5.6 mm (0.22 in.) slots cut at 38-deg angles to form the blades. The blade rake angle is 0 deg with a 5-deg relief angle. In the configuration described above, 10 cutting blades were formed. However, it was determined that 10 blades would decrease the force range variation desired. Therefore, every other blade was cut back an additional 5 mm (0.20 in.). The cutter is shown in Fig. 9.

The cutter housing is also a circular disk of 146 mm (5.75 in.) diameter and 44.5 mm (1.75 in.) thickness. A hole of 79.4 mm (3.125 in.) was drilled through the housing to allow free travel of the mandrel through it. The cutter is loosely secured in a 108 mm (4.25 in.) diameter and 25.4 mm (1 in.) deep area milled out of the housing. This allows for 3.2 mm (0.125 in.) circular self-adjustment by the cutter. The cutter is held in the housing by a thin circular cover plate.

#### MANDREL, NUBBINS, AND SPACERS

The mandrel for cutting is a hardened steel shaft 51 mm (2 in.) in diameter, 850 mm (33.5 in.) long. The mandrel is threaded into the force measuring system (load cell), which in turn is attached

to the pivot-anvil assembly. To produce the force pulse input, aluminum rings, or nubbins, and steel spacers are sandwiched on the mandrel. A locking nut at the end of the mandrel then secures the ring-spacer assembly. The locking nut is bullet-nosed to provide initial alignment of the cutter. The cutter traveling on the carriage will cut through each nubbin, producing the force pulse output, while the spacers allow the time delay between pulses and realign the cutter for the next nubbin. The aluminum rings and steel spacers are each a different length (as required for uniform cutting time with a cutting velocity decreasing with each successive cut). The spacers have an outside diameter approximately 0.12 mm (0.005 in.) smaller than the cutter diameter. This prevents cutting of the hardened steel spacer but allows for alignment changes. The outside diameter of the nubbins depends on the depth of cut required for the desired input force. The inside diameters of the nubbins and spacers are just large enough to allow the ring to slide over the mandrel.

#### PIVOT SHAFT AND ANVIL ASSEMBLY

The pivot shaft is a 152 mm (6 in.) diameter by 832 mm (32.75 in.) steel shaft that takes the main dynamic loading during cutting and allows for erection of the rail assembly by the pivoting action. The center length of the shaft has a milled flat area to allow attachment of the load cell support plate. The load cell and mandrel are bolted to this support plate. At each end of the shaft are the dowel holes for the 51 mm (2 in.) rails. The

perpendicularity of the dowel hole center line and the flatted surface was machined to be no greater than 0.005 in. TIR. This precision allows for ease of alignment of the carriage rail assembly and mandrel.

The anvil is the main force transfer block. It is a 254 mm (10 in.) wide, 330 mm (13 in.) long, and 373 mm (14.7 in.) high steel block with a semicircular bored-out corner that holds the pivot shaft. It weighs 190 kg (417 lb). The pivot shaft is mated to the bored corners and is held to the anvil by a welded support structure bolted to each side of the anvil. The anvil also has 10 holes drilled through it for attachment to a structure plate. The structure plate is a 406.5 mm (16 in.) sq angle plate made from 25.4 mm (1 in.) steel plate. It is epoxied to a structure at the driving point location. A number of support plates can be epoxied to different locations on a structure before testing. The rail system with pivot-anvil assembly attached can then be easily positioned at any of the desired test locations. Once the anvil is bolted to the structure plate and the carriage attached to the rail assembly, the rail assembly can be lifted to its proper position by a portable gantry crane. The support assemblies can then be attached and testing initiated.

#### STRUCTURE ANALYSIS

The basic sizing of the material was based on portability and dimensional requirements. A computer model (SAP) was developed to check that the basic design was structurally safe. It was found that there were no static and dynamic strain levels greater than 25% of allowable. Although this is very conservative and a redesign would be justified, time constraints and certain dimensional requirements dominate the decision to stay with the basic design.

#### DIGITAL DATA ACQUISITION AND ANALYSIS SYSTEM

With the use of a transient input source, in-place digital data capture becomes a desirable feature. With the microcomputer technology of today, field processing can also be accomplished. This became part of the testing philosophy used.

The Zonic Technical Labs Data Memory System (DMS) is the hub of the data-gathering activity. It provides simultaneous digitization of up to 16 channels of data derived from response accelerometers and the load cell. The captured data can then be viewed on a CRT as time histories or as frequency

domain data after processing by the built-in Fourier transform array processor. The Fourier processor is rapid enough to make on-site verification that the data capture is of proper quality before the sensors are moved or the test setup is torn down.

The total system consists of a bank of programmable antialiasing filters, individual channel data memory units that work simultaneously, an FFT array processor, a microcomputer that permits data processing and can also be batch programmed for operator-prompted test sequencing, and finally a cartridge tape recorder that can record either raw or processed data, or both (sequentially).

The full specifications of the Zonic equipment are too extensive to list here, but some of the cogent items include:

- Sampling intervals from 20 msec to 5  $\mu$ sec
- 10-bit digitization ( $\pm 512$  points full scale)
- Pretrigger recording mode
- Internal-external trigger modes
- 4096 point recirculating memory
- 1024 point array processor
- Twin tape drives for 3M-100A cartridges

The setup to record data consists of connecting signal cables from the installed sensors to the input channels of the programmable antialiasing filters. The low-pass filters are set to a desired cutoff frequency. The filter design is a Cauer-elliptical with an 80 dB/octave rolloff. The filters are phase matched to within 2 deg out to the cutoff frequency. A variable gain capability offers gains of 1, 2, 5, and 10.

The output of each filter channel is connected to the input of a separate Zonic DMS channel. Here additional gain is available up to 100:1, along with the calibration values. All of the DMS channels start digitizing at the same instant in response to the timing and control module. The module is triggered by an external source sensing the falling carriage just prior to contact with the first ring element to be cut. After the data are captured, they can be displayed and recorded as called for by a sequence programmed into the microcomputer. Additional investigations of the data can be performed at the discretion of the project engineer. Fig. 10 shows various components of the data acquisition system.

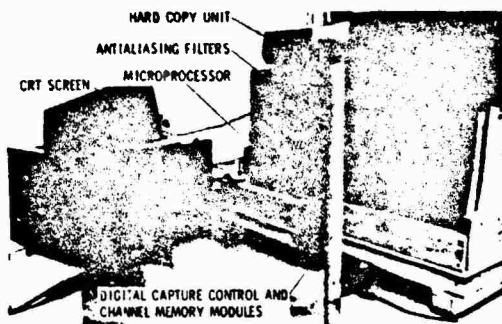


FIG. 10. DIGITAL DATA ACQUISITION SYSTEM ON SITE

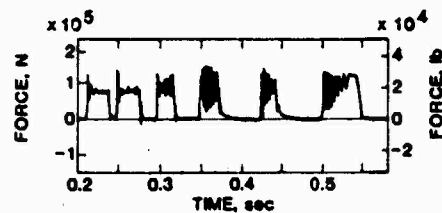
### INITIAL EXPERIMENTS

Initial tests uncovered some minor problems with cutter alignment and carriage-bearing friction. The cutter that was loosely secured in the cutter housing required some constraints on the adjustment freedom originally designed for. The solution was to provide a rubber elastic band between the cutter and housing. This allowed for the required self-alignment but provided the necessary restrictive reaction forces. Inspection of the 51 mm (2 in.) diameter rails, after the first tests, revealed some indenting of the top of the rails by the ball bearings on the top race. This proved to be due to a lack of adjustment of the compression set screw on the bearing housing. Once the adjustments were made, there were no further indenting difficulties. A second problem with the bearings concerned the change in velocity of the carriage at each test. Apparently there was additional friction buildup in the bearings during the testing due to misalignment after a test. The solution to the problem was to allow the bearings to self-adjust laterally. The bearing housings had originally been tightly secured to the carriage-bearing support arms. By loosening the securing bolts, the bearing could slide and rotate slightly on the support arm surface. This alleviated the problem, and after that the velocities just prior to cutting were consistent. This technique also provided very low friction, and velocity losses were less than 1% of theoretical.

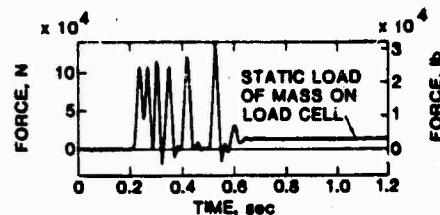
Overall, the design worked quite well. The assemblies went together easily, and the use of quick-disconnect pins proved very beneficial for rapid assembly. It was found that the testing gear could be set up in less than a day even though the equipment was relatively large and heavy.

Fig. 11 shows the type of data acquired. Fig. 11a shows a typical six-pulse train as a raw time history. The high frequencies in the pulse amplitudes are artifacts of the cut chip failure

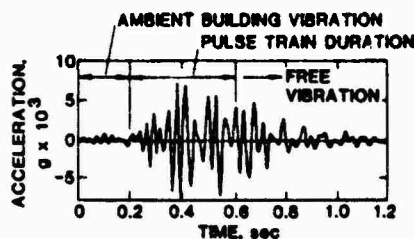
during the cutting action. Notice that as the pulses progress, the chip frequencies become lower. This is due to the decreasing velocity of cutting. Fig. 11b is the same basic signal as Fig. 11a but the data has been filtered at 20 Hz. Fig. 11c illustrates a typical response acceleration function, and Fig. 11d is the calculated inertance function  $\ddot{X}/F(\omega)$ .



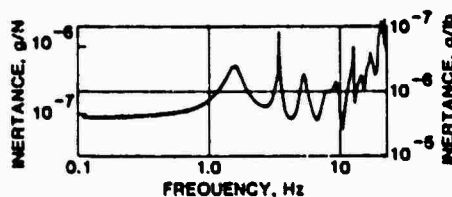
(a) Raw input force-time history



(b) Filtered input force-time history (0 to 20 Hz)



(c) Acceleration-time history (0 to 20 Hz)



(d) Transfer function (acceleration divided by force)

FIG. 11. TYPICAL DATA RECORDS FROM PULSE TRAIN TESTS AND RESULTING TRANSFER (INERTANCE) FUNCTIONS COMPUTED FROM DATA



## FIELD ACTIVITY

The high-level pulser has been used to excite the structural modes on a number of nuclear processing facilities. These facilities are two-story steel reinforced concrete structures. They have large stiffness parameters, with the first modal frequencies in the range of 6 Hz to 10 Hz. The testing was performed as part of a validation of computer finite element models that were developed for seismic analysis. The pulse train was designed for 0.5 Hz to 40 Hz spectral amplitude optimization, which is the maximum useful range for seismic validation. Fig. 12 shows a view of a typical tested structure. The accelerometers were placed along a transverse column plane and in the soil outside the structure. Fig. 13 shows typical input and output time histories and their respective Fourier transforms. The spectral amplitude of the input force function over the frequency region of interest can be seen in Fig. 13b. Typical inertia functions are shown in Fig. 14.

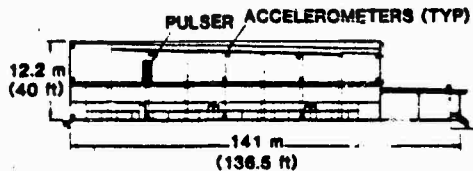
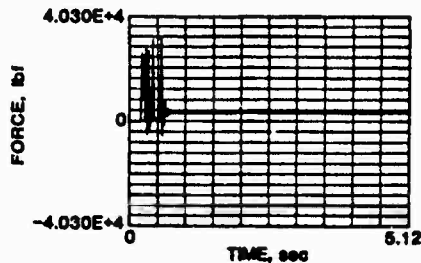


FIG. 12. CROSS SECTION OF NUCLEAR PROCESSING PLANT SHOWING ACCELEROMETER AND PULSER LOCATIONS (PULSER EXCITATION NORMAL TO SECTION SHOWN)

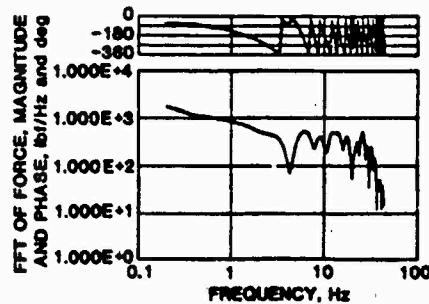
The results of these programs have been very encouraging in terms of both the test techniques developed and the computer model development. For one typical structure, the test model frequencies and analytic model frequencies are tabulated below:

Analytic Frequency, Hz	Experimental Frequency, Hz	Experimental Damping, %
9.2	9.7	7
10.0	10.45	10.7
12.8	13.13	9.3
13.3		
13.85	15.1	8.9
18.0	18.5	4.8
18.2		

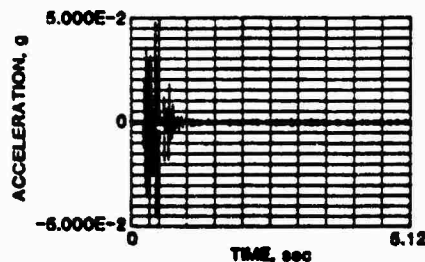
The mode shapes were also determined, and a typical shape is shown in Fig. 15. The experimental frequencies, damping, and mode shapes were determined through the use of a modal extraction program called PARET. This program has



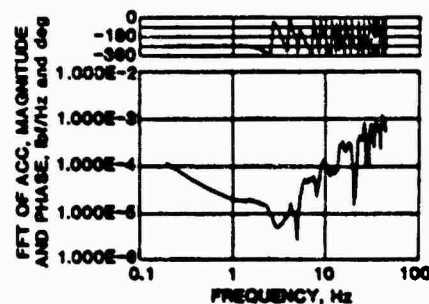
(a) Input force pulse



(b) FFT of input force pulse

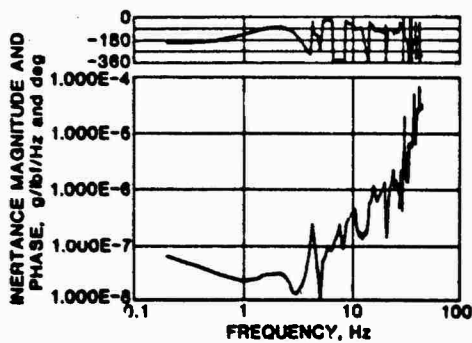


(c) Output response acceleration

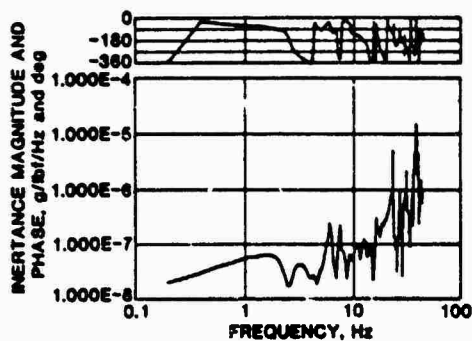


(d) FFT of output response acceleration

FIG. 13. TYPICAL INPUT FORCE PULSE AND OUTPUT RESPONSE TIME HISTORIES WITH RESPECTIVE FOURIER TRANSFORMS



(a) Building A



(b) Building B

FIG. 14. TYPICAL INERTANCE FUNCTIONS OF TEST DATA

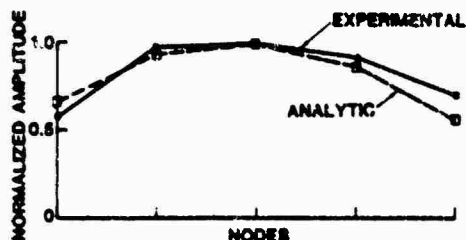


FIG. 15. TYPICAL MODE SHAPE PLOT FROM EXPERIMENTAL AND ANALYTIC DATA (Frequency: 9.2 Hz)

been developed by the Lawrence Livermore Laboratory (LLL) through a Nuclear Regulatory Commission (NRC) contract. PARET is a systems identification code utilizing transfer function parameter estimation by use of Lorentz functions, i.e.,

$$H(f) = \sum_{k=1}^N \frac{S_k}{B_k + 2\pi i(f - f_k)}$$

where

$H(f)$  = Transfer function

$S_k$  =  $K^{\text{th}}$  residue for mode shapes (complex)

$B_k$  =  $K^{\text{th}}$  modal damping parameter

$f_k$  =  $K^{\text{th}}$  modal frequency parameter

## CONCLUSIONS

The high-level pulser developed is a viable cost-effective field testing apparatus for large structural systems. With the present microprocessor technology and parameter estimation techniques, the testing community has gained a new useful tool for dynamic structural applications.

There are a number of applications that lend themselves well to this type of testing, including:

- Structural validation testing
- Equipment shock testing to required standards
- Fragility testing
- Impact damage assessment of building substructures
- Force-controlled impacts for required responses of on-site structures or equipment
- Model testing
- Nonlinear testing applications

## REFERENCES

1. D.E. Hudson, "Dynamic Tests of Full-Scale Structures," Dynamic Response of Structures, Instrumentation, Testing Methods, and System Identification, G.C. Hart, ed., ASCE/EMD Specialty Conference, UCLA, Los Angeles, 30-31 Mar 1976.
2. F.B. Safford, R.E. Walker, and T.E. Kennedy, "Impedance Techniques for Scaling and for Predicting Structural Response to Air Blast," Shock & Vibration Bull. No. 48, Pt. 2, Sep 1976, pp 193-214.

3. Agabian Associates, Impedance-Based Motion Prediction, Scaling, and Environmental Simulation for Shock Applications, NRL-MR-3676. Washington, DC: Naval Res. Lab., Nov 1977.
4. F.B. Safford and S.F. Masri, "Analytical and Experimental Studies of a Mechanical Pulse Generator," Jnl. of Eng. for Industry, Trans. ASME, Series B, 96:2, May 1974, pp 459-470.
5. S.F. Masri and F.B. Safford, "Dynamic Environment Simulation by Pulse Techniques," Jnl. Eng. Mech. Div., ASCE, 102:EM1, Feb 1976, pp 151-169.
6. S.F. Masri, G.A. Bekey, and F.B. Safford, "Adaptive Random Search Method for Identification of Large-Scale Nonlinear Systems," 4th Symp. for Identification and System Parameter Estimation, Int. Federation of Automatic Control, Tbilisi, USSR, Sep 1976 (to be published in Automatica).
7. M. Richardson and J. Kuiskern, "Identifying Modes of Large Structures from Multiple Input and Response Measurements," Paper No. 760875. Nat'l Aerospace Engineering and Manufacturing Meeting, San Diego, CA, Nov 29-Dec 2, 1976.
8. A. Klosterman and R. Simmerman, "Modal Survey Activity via Frequency Response Functions," Paper No. 751068. Nat'l Aerospace Engineering and Manufacturing Meeting, Culver City, CA, 17-20 Nov, 1975.
9. A.J. Poggio, PARET: A Parameter Estimation Technique for Physical Application. Livermore, CA: Lawrence Livermore Lab, 1976.

CONSIDERATION OF  
AN OPTIMAL PROCEDURE FOR TESTING THE OPERABILITY  
OF EQUIPMENT UNDER SEISMIC DISTURBANCES

C.W. de Silva\*  
Carnegie-Mellon University  
Pittsburgh, PA 15213

and

\*\* F. Loceff and K.M. Vashi\*\*\*  
Westinghouse Nuclear Energy Systems  
Pittsburgh, PA 15230

An optimal single-shaker test procedure is developed for the seismic qualification of Class 1E multicomponent electrical equipment. The method comprises a single test that uses an uniaxial excitation having certain minimum intensity applied at the equipment support location in a predetermined optimal direction. Analytical expressions for the optimal test parameters are obtained by maximizing the risk of component failure during testing. The apriori evaluation of these parameters requires a frequency response test. The optimization problem is expressed as a matrix eigenvalue problem. The primary advantages of the proposed method over the currently employed four-rotation test simulating tri-axial input are reduction of the test duration, minimization of the excitation intensity and elimination of unnecessary overtesting in the vertical direction. The test procedure may be fully automated. The decision logic for testing and the computational procedure for the optimal test parameters can be pre-programmed.

#### INTRODUCTION

Seismic reliability of nuclear power plants is a heavily discussed issue today. The public awareness of the matter centers around the hazards of possible radioactive contamination and exposure. The reliability of modern electric power systems including non-nuclear facilities is also vital from the view point of socio-economic impact due to major power failures.

The operability of individual equipment is probably as crucial as the size and complexity of the entire system in determining the power system reliability. The manufacturers and the users usually devote a major effort on a seismic qualification program to ensure the operational capability of Class 1E equipment. The primary objective of such a program is to establish that the future equipment of that category will not malfunction during and following one safe shutdown earthquake (SSE) preceded by a number of operating basis earthquakes (OBE) [1].

The three basic methods for seismic qualification are: analysis, testing, and combined analysis and testing. Qualification by analysis is done using a satisfactory analytical model of the particular electrical equipment. Once the model is developed, a digital computer with suitable memory and processing speed must be employed to simulate the equipment response to synthesized support excitation inputs. Possible component failure and equipment malfunction may be predicted in this manner provided the correlation between the component response and its likelihood of failure is known. In general, this procedure must be supplemented by the judicious use of the past experience concerning the operation of the equipment and frequently testing is also necessary. The present paper is concerned with the seismic qualification by testing.

\*Assistant Professor of Mechanical Engineering, Consultant to Structural Technology Systems

\*\*Manager, Structural Technology Systems

\*\*\*Fellow Engineer, Structural Technology Systems

## State-of-the-Art

For Class 1E equipment, seismic qualification by testing is accomplished using a shake table apparatus. The equipment to be qualified is secured to the shake table in a manner representative of its installation during the actual service and its support location is excited by operating the electro-hydraulic actuators attached to the table. The dynamic response of the equipment at critical component locations is usually monitored using properly positioned accelerometers. The excitation input must characterize the anticipated seismic disturbances at the equipment locations. From the accelerometer outputs at the equipment support points the test response spectrum (TRS) is determined. The amplitude and frequency components of the excitation input are adjusted until the TRS envelopes one or several required response spectra (RRS) normally provided by the user. During the test, the normal operating environment of the equipment must be simulated as closely as possible. By monitoring the functional outputs of the equipment, its operability can be established. The simulation of the operating conditions might not be always feasible particularly for very complex equipment consisting of many components. In such situations, the equipment mainframe could be tested first with the critical components replaced by dummies. Subsequently, the individual components are tested using the response levels at their location on the mainframe during the dummy test. The qualification test is usually preceded by a resonance search test. The excitation input for this test is a sinusoidal wave of constant amplitude or a white noise. From this test, vital information such as the resonant frequencies and the system damping can be determined.

The IEEE recommended practice [1] for seismic qualification favors the use of three uncorrelated excitation inputs applied simultaneously in the vertical and two orthogonal horizontal directions to provide a more realistic characterization of the earthquake motions. In view of the difficulty in realizing such triaxial testing, the IEEE standards have also recommended a biaxial alternative with simultaneous inputs in a principal horizontal and the vertical axes. In general, two or four tests are performed depending upon whether biaxial inputs are uncorrelated or correlated. In another available test procedure that is essentially equivalent to this biaxial test procedure with correlated inputs, a uniaxial excitation is first applied along the line of symmetry with respect to the equipment principal axes. This is followed by three more tests with the equipment rotated through 90°, 180°, and 270°, respectively, about the vertical axis from the initial orientation. In this test, input intensity along the drive axis is conventionally made larger than the intensity of each of the three individual components for the triaxial test by a factor of  $\sqrt{3}$ .

## PROBLEM FORMULATION

### Excitation Input Characterization

The classical response spectrum concept [2] has been widely used to characterize seismic motions. The response spectrum is based on the peak response of a linear, hypothetical, single-degree-of-freedom, damped system subjected to a representative seismic disturbance time history. Clearly, the response spectrum lacks direct physical interpretation in the case of multi-degree-of-freedom and distributed parameter systems for which the peak response cannot be directly determined from the response spectrum. If the modal participation factors are known, however, a conservative upper bound for the peak response can be determined. Since only the peak values of the time response are considered, the correlation with the actual response time history is limited and the cyclic (fatigue) behavior requires separate treatment. Further, the classical response spectrum concept is based on the deterministic system theory rather than a more appropriate random characterization of the seismic motions.

Seismic disturbances are essentially random processes and a statistical description would be quite appropriate in representing them [3,4,5]. In view of this, the present theoretical development is based on a stochastic foundation. Once the test procedure is developed, the response spectra may be used, if so desired, to characterize the actuator input signals during the proposed seismic qualification test program. The specific statistical representation used in the present development is the power spectral density (psd) of the excitation input. For the psd to exist, the signal has to be covariance stationary. This property does not strictly hold for earthquake motions because they possess the time decaying characteristic with a definite beginning and an ending. Their correlation functions depend on the time origin as well as the time interval. But, as proposed by Tajimi [3] it is possible to construct a stationary process that retains the important characteristics such as the intensity and the frequency content of a given seismic motion. To accomplish this, a significant segment of the actual motion, over which the major energy content occurs is chosen. The statistical characteristics of the random process are not expected to vary significantly over this time interval. Consequently, the selected record segment may be thought of as a finite length cut from a stationary sample function. Next, simulated stationary sample functions having approximately the same statistical properties as the chosen principal sample segment are continuously repeated before and after the principal segment. The result is a sample function from a stationary process. The stationary processes normally encountered in engineering practice are at least weakly ergodic [6]. In numerical terms, the spectral error introduced by this process of input synthesis is negligible provided the record length used in the digital processing is not

much larger than the principal interval of the synthesized record.

For a realistic qualification, the equipment must be tested for the seismic floor motions at its location in the building. Due to the structural dynamics of the building, the floor motions will have different characteristics from the ground motions. In addition, due to coupled motions of the building, the floor response in the principal directions correlate to some extent even if the ground motions in these directions are uncorrelated.

#### Testing Criteria

The objective of this paper is to develop a procedure whereby a single uniaxial test performed in a certain optimal direction with least excitation intensity can subject the critical components of the equipment to the levels of acceleration that will maximize the risk of component failure. It is appropriate to mention at this point that a sequence of four qualification tests as currently employed can produce significant fatigue in the equipment at least in some directions. To avoid such overtesting is an obvious advantage of a single, uniaxial test.

#### Performance Index

The optimization problem is formulated in terms of a performance index (PI) or an objective function, which reflects the test objective. This index is a function of the parameters that are variable during the process of optimization. The primary purpose of a seismic qualification test is to ensure that the component failure does not occur during the normal operation in a seismic environment. Consequently, it is desired to maximize the risk of component failure during testing so that, under service conditions the chances of failure are less. Two candidate performance indices are:

$(PI)_1$  = expected value of the acceleration psd at the component that failed first, assuming that the component failure is a certainty.

$(PI)_2$  = total probability of equipment malfunction.

In either case, the PI may be expressed as

$$PI = \sum_{i=1}^N p_i \phi_i(\omega) \quad (1)$$

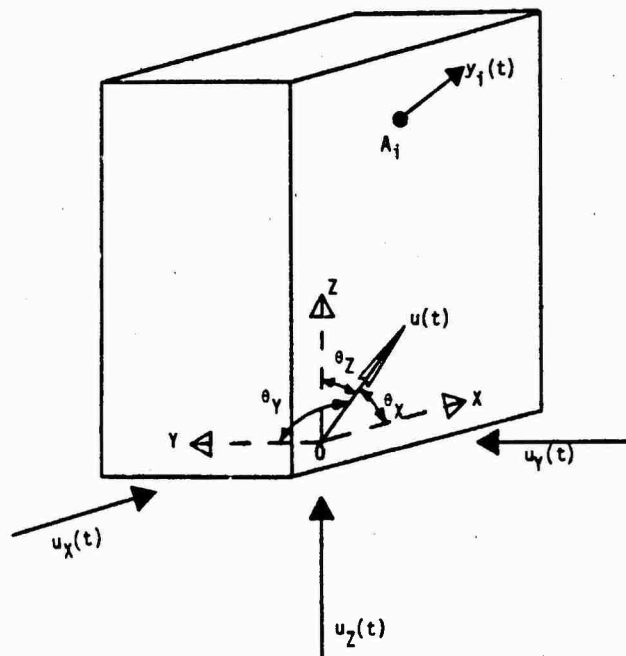


Figure 1. Excitation Input-Output Nomenclature

where

$N$  = the number of critical components in the equipment

$\phi_i(\omega)$  = acceleration psd at the  $i$ th component along its direction of maximum sensitivity.

In the first case  $p_i$  is interpreted as the conditional probability that the  $i$ th component fails first assuming that the equipment malfunction occurs during the test. These probabilities must add up to unity. In the second case,  $p_i$  is the probability of failure for the  $i$ th component when that component is subjected to a given excitation for a specified period of time. In the latter case, it is assumed that the different components fail independently and the probability of failure is proportional to the acceleration psd at the component location. If the direction of maximum sensitivity of a particular component is not known in certainty, probabilities must be assigned to all independent directions of possible failure for that component. Consequently, such a component is represented by more than one term in the summation of equation (1). The test objective is achieved by maximizing the PI.

The cartesian frame OXYZ is fixed in the equipment as shown in Figure 1. The origin O is the base point at which the single uniaxial input acceleration  $u(t)$  is applied. The direction cosines  $\alpha_x, \alpha_y$  and  $\alpha_z$  of the excitation input vector are given by  $\alpha_x = \cos \theta_x, \alpha_y = \cos \theta_y$  and  $\alpha_z = \cos \theta_z$ . The Fourier transform of acceleration time history  $y_i(t)$  at the  $i$ th component is given by

$$F[y_i(t)] = [\alpha_x H_{xi}(\omega) + \alpha_y H_{yi}(\omega) + \alpha_z H_{zi}(\omega)] F[u(t)] \quad (2)$$

where  $H_{xi}, H_{yi}$ , and  $H_{zi}$  are the frequency response functions [6] between the output  $y_i(t)$  and the input components in the X, Y and Z directions, respectively, and  $F[\ ]$  denotes the Fourier integral transform operator. This input-output configuration is shown by the block diagram in Figure 2. With the usual assumptions of linear, time-invariant system behavior [5] the psd of  $y_i(t)$  is given by

$$\phi_i(\omega) = |\alpha_x H_{xi}(\omega) + \alpha_y H_{yi}(\omega) + \alpha_z H_{zi}(\omega)|^2 \phi_{uu}(\omega) \quad (3)$$

where  $\phi_{uu}(\omega)$  is the psd of the input acceleration  $u(t)$ .

The real and imaginary parts of the frequency response functions are defined by

$$\begin{aligned} H_{xi}(\omega) &= R_{xi}(\omega) - j I_{xi}(\omega) \\ H_{yi}(\omega) &= R_{yi}(\omega) - j I_{yi}(\omega) \\ H_{zi}(\omega) &= R_{zi}(\omega) - j I_{zi}(\omega) \end{aligned} \quad (4)$$

where  $j = \sqrt{-1}$ . By substituting equation (3) in (1) and using (4), one obtains:

$$\begin{aligned} J &= \sum_{i=1}^N p_i [\alpha_x R_{xi}(\omega) + \alpha_y R_{yi}(\omega) + \alpha_z R_{zi}(\omega)]^2 \\ &+ \sum_{i=1}^N p_i [\alpha_x I_{xi}(\omega) + \alpha_y I_{yi}(\omega) + \alpha_z I_{zi}(\omega)]^2 \end{aligned} \quad (5)$$

subject to

$$\alpha_x^2 + \alpha_y^2 + \alpha_z^2 = 1$$

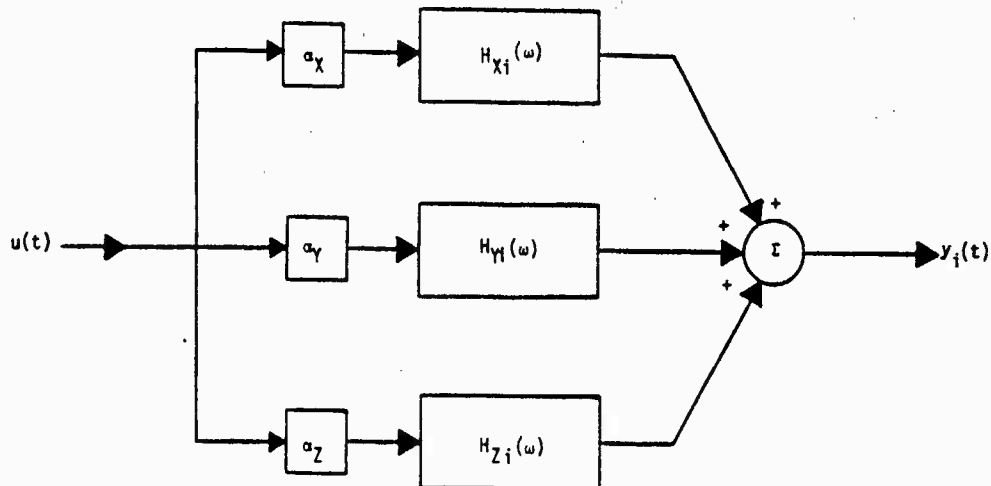


Figure 2. Input-Output Configuration for the Uniaxial Test.

## OPTIMAL SOLUTION

### Solution Using Matrix-Eigenvalue Formulation

The optimization problem consists of selecting the direction cosine vector  $\underline{a} = [a_x, a_y, a_z]^T$  so as to maximize the objective function in equation (5) subject to the condition in equation (6). This constrained optimization is accomplished by applying the Lagrange multiplier method. The augmented function to be maximized is

$$\begin{aligned} \tilde{J} = & \sum_{i=1}^N p_i [a_x R_{xi}(\omega) + a_y R_{yi}(\omega) + a_z R_{zi}(\omega)]^2 \\ & + \sum_{i=1}^N p_i [a_x I_{xi}(\omega) + a_y I_{yi}(\omega) + a_z I_{zi}(\omega)]^2 \\ & + \lambda (1 - a_x^2 - a_y^2 - a_z^2) \end{aligned} \quad (7)$$

where  $\lambda$  is the Lagrange multiplier. At this stage, it is shown that the optimization problem can be reduced to a matrix eigenvalue problem. The eigenvalues of a certain real symmetric matrix are the stationary values of  $\tilde{J}$ . The normalized eigenvector corresponding to the maximum eigenvalue gives the optimal direction cosines for the test input. To show this, the necessary conditions for optimization

$$\frac{\partial \tilde{J}}{\partial a_x} = \frac{\partial \tilde{J}}{\partial a_y} = \frac{\partial \tilde{J}}{\partial a_z} = 0$$

are determined. The resulting three equations may be written as the matrix equation

$$[\underline{P} - \lambda \underline{I}] \underline{a} = \underline{0} \quad (8)$$

where

$$\begin{aligned} \underline{P} = & \begin{bmatrix} \sum_{i=1}^N p_i (R_{xi}^2 + I_{xi}^2) & \sum_{i=1}^N p_i (R_{xi} R_{yi} + I_{xi} I_{yi}) & \sum_{i=1}^N p_i (R_{xi} R_{zi} + I_{xi} I_{zi}) \\ \sum_{i=1}^N p_i (R_{xi} R_{yi} + I_{xi} I_{yi}) & \sum_{i=1}^N p_i (R_{yi}^2 + I_{yi}^2) & \sum_{i=1}^N p_i (R_{yi} R_{zi} + I_{yi} I_{zi}) \\ \sum_{i=1}^N p_i (R_{xi} R_{zi} + I_{xi} I_{zi}) & \sum_{i=1}^N p_i (R_{yi} R_{zi} + I_{yi} I_{zi}) & \sum_{i=1}^N p_i (R_{zi}^2 + I_{zi}^2) \end{bmatrix} \end{aligned} \quad (9)$$

and  $\underline{I}$  is the identity matrix. The matrix  $\underline{P}$  is termed the test matrix. For nontrivial  $\underline{a}$ , the determinant of the left hand side matrix in equation (8) must vanish. The corresponding solutions for  $\lambda$  are in fact the eigenvalues of  $\underline{P}$ . For each distinct solution for  $\lambda$ , the direction cosine vector  $\underline{a}$  is determined up to a single unknown parameter. The unknown parameter is obtained using the normalizing relation (6). These solutions  $\underline{a}$  are the normalized eigenvectors of  $\underline{P}$ .

### Significance of Eigenvalues

To verify that the eigenvalues of  $\underline{P}$  are the values of  $\tilde{J}$  that correspond to the stationary points of  $\tilde{J}$ , the three equations denoted

by (8) are multiplied by  $a_x$ ,  $a_y$  and  $a_z$  respectively, and the resulting equations are added together. This gives

$$\begin{aligned} & \sum_{i=1}^N p_i (a_x R_{xi} + a_y R_{yi} + a_z R_{zi}) a_x R_{xi} \\ & + \sum_{i=1}^N p_i (a_x I_{xi} + a_y I_{yi} + a_z I_{zi}) a_x I_{xi} \\ & + \sum_{i=1}^N p_i (a_x R_{xi} + a_y R_{yi} + a_z R_{zi}) a_y R_{yi} \\ & + \sum_{i=1}^N p_i (a_x I_{xi} + a_y I_{yi} + a_z I_{zi}) a_y I_{yi} \\ & + \sum_{i=1}^N p_i (a_x R_{xi} + a_y R_{yi} + a_z R_{zi}) a_z R_{zi} \\ & + \sum_{i=1}^N p_i (a_x I_{xi} + a_y I_{yi} + a_z I_{zi}) a_z I_{zi} \\ & - \lambda (a_x^2 + a_y^2 + a_z^2) = 0 \end{aligned}$$

In view of equation (6) the desired result is obtained following straightforward manipulation of the last expression.

$$\lambda = \left[ \sum_{i=1}^N p_i (a_x R_{xi} + a_y R_{yi} + a_z R_{zi})^2 + \sum_{i=1}^N p_i (a_x I_{xi} + a_y I_{yi} + a_z I_{zi})^2 \right]_{st} \quad (10)$$

The subscript  $[ ]_{st}$  denotes the stationary values because the equations (8) correspond to the stationary values of  $\tilde{J}$ . It follows that the maximum eigenvalue of the test matrix  $\underline{P}$  correspond to the constrained global maximum  $\tilde{J}_{max}$  of  $\tilde{J}$  subject to equation (6). The associated normalized eigenvector gives the optimal direction cosines  $\underline{a}_{opt}$ .

### Existence of a Global Maximum

In the foregoing it has been assumed that a well defined global maximum exists for  $\tilde{J}$  subject to equation (6). It is established in this section that the assumption holds for the present problem.

The parameter vector  $\underline{a}$  is defined in the



the finite domain D described by equation (6) which is the unit sphere centered around the origin of the cartesian frame (OXYZ). The objective function J is a continuous function of  $\underline{a}$  and has continuous derivatives as evident from equation (5). Furthermore, in the domain D the following inequality is satisfied:

$$\begin{aligned} J &= \sum_{i=1}^N p_i |a_x H_{xi} + a_y H_{yi} + a_z H_{zi}|^2 \\ &\leq \sum_{i=1}^N p_i (|a_x| |H_{xi}| + |a_y| |H_{yi}| + |a_z| |H_{zi}|)^2 \\ &< \sum_{i=1}^N p_i (|H_{xi}| + |H_{yi}| + |H_{zi}|)^2 \end{aligned} \quad (11)$$

Consequently, a conservative upperbound exists for J. This guarantees a well defined global maximum. Note that the formulation itself assumes that the component transfer functions  $H_{xi}(\omega)$ ,  $H_{yi}(\omega)$  and  $H_{zi}(\omega)$  have finite magnitudes. This is necessarily satisfied in the practical range of frequencies. As a design requirement for the equipment, the peak values of the transfer functions must not be large. This is usually guaranteed by adequate system damping.

#### Minimum Excitation Intensity

To determine the minimum allowable intensity of the excitation input, the proposed test procedure is compared with the tri-axial qualification test with uncorrelated inputs [1]. Suppose the uncorrelated excitation inputs  $u_x(t)$ ,  $u_y(t)$  and  $u_z(t)$  are applied simultaneously in X, Y and Z directions at the equipment support location (Figure 1). The Fourier transform of the time response  $y_i(t)$  at the  $i$ th component is given by

$$\begin{aligned} F[\tilde{y}_i(t)] &= H_{xi}(\omega) F[u_x(t)] + H_{yi}(\omega) F[u_y(t)] + \\ &\quad H_{zi}(\omega) F[u_z(t)] \end{aligned} \quad (12)$$

The psd of  $\tilde{y}_i(t)$  may be expressed as

$$\begin{aligned} \bar{\phi}_i(\omega) &= |H_{xi}(\omega)|^2 \phi_{u_x u_x}(\omega) + |H_{yi}(\omega)|^2 \phi_{u_y u_y}(\omega) \\ &\quad + |H_{zi}(\omega)|^2 \phi_{u_z u_z}(\omega) \end{aligned} \quad (13)$$

The criterion for assuring that in the proposed test the disturbance at the component expected to fail is not less than that in the triaxial test with uncorrelated input is

$$\sum_{i=1}^N p_i \bar{\phi}_i(\omega) \geq \sum_{i=1}^N p_i \hat{\phi}_i(\omega) \quad (14)$$

The inputs  $u(t)$ ,  $u_y(t)$ ,  $u_z(t)$  and  $u_z(t)$  must be identically distributed because they are generated by necessarily the same random process. However, their intensities need not be identical. Consequently,

$$\phi_{uu}(\omega) = k^2 \phi(\omega) \quad (15)$$

$$\phi_{u_x u_x}(\omega) = a_x^2 \phi(\omega) \quad (16)$$

$$\phi_{u_y u_y}(\omega) = a_y^2 \phi(\omega) \quad (17)$$

$$\phi_{u_z u_z}(\omega) = a_z^2 \phi(\omega) \quad (18)$$

where  $k$ ,  $a_x$ ,  $a_y$  and  $a_z$  are the corresponding scaling factors for the input intensities. The minimum intensity  $k_{min}$  is determined by substituting equations (3) and (13) into (14) in conjunction with equations (15) to (18). Finally, in view of equation (10)

$$\begin{aligned} k_{min} &= \left[ \sum_{i=1}^N p_i \{ (R_{xi}^2 + I_{xi}^2) a_x^2 + (R_{yi}^2 + I_{yi}^2) a_y^2 \right. \\ &\quad \left. + (R_{zi}^2 + I_{zi}^2) a_z^2 \} / \lambda_{max} \right]^{1/2} \end{aligned} \quad (19)$$

where  $\lambda_{max}$  is the maximum eigenvalue of the test matrix  $\underline{P}$ . For most situations it is sufficient to use  $a_x = a_y = a_z = 1$ . On the other hand, if the critical frequency band is less than 3.5 Hz, it is recommended [1] that  $a_z$  be given a value smaller than unity, but greater than 0.67.

#### SEISMIC QUALIFICATION PROCEDURE

##### Determination of the Critical Frequency

The transfer functions  $H_{xi}(\omega)$ ,  $H_{yi}(\omega)$  and  $H_{zi}(\omega)$  are dependent on the frequency of excitation  $\omega$  in general. Consequently, the value of the objective function J depends on the frequency point at which it is computed. For a given transfer function, the critical magnitude is not necessarily its peak. For example, if the peak falls outside the frequency band of interest, the highest magnitude in the critical frequency band has more significance than the peak value of the transfer function.

The frequency at which the optimal test parameters are computed must reflect the influence of the severity of the transfer functions at the individual components in various orientations. Also, the critical frequencies of the components must be weighted according to their likelihood of failure during the test. A suggested way of accomplishing this is as follows:

To each transfer function component, a critical frequency is assigned. This is typically the resonance frequency if it falls within the frequency band of interest. Otherwise, a choice must be made using engineering judgment, past experience and available data. Let  $\omega_{xi}$ ,  $\omega_{yi}$  and  $\omega_{zi}$  be the critical frequencies of the  $i$ th component associated with the transfer functions  $H_{xi}$ ,  $H_{yi}$  and  $H_{zi}$ . The corresponding maximum values of the objective function (5), that is, the maximum eigenvalues of the test matrices  $\underline{P}$ , are  $\lambda_{xi}$ ,  $\lambda_{yi}$ , and  $\lambda_{zi}$ , respectively. Then, the critical test frequency  $\bar{\omega}$  is determined using

$$\bar{\omega} = \frac{1}{\sum_{n=1}^N p_n} \sum_{i=1}^N p_i \left[ \frac{\lambda_{xi} \omega_{xi} + \lambda_{yi} \omega_{yi} + \lambda_{zi} \omega_{zi}}{\lambda_{xi} + \lambda_{yi} + \lambda_{zi}} \right] \quad (20)$$

This frequency favors the component that is most likely to fail. It is also biased towards the excitation input orientation that produces the largest response in the frequency range of interest. The optimal direction cosines and the minimum input intensity scaling factor for performing the qualification test are computed using  $\bar{\omega}$ .

#### Test Plan

The major steps of the seismic qualification test procedure developed in this paper are given below:

- Step 1: Assign probabilities of failure to each component or component orientation.
- Step 2: Locate accelerometers at these component locations or orientations.
- Step 3: Using a frequency response test determine the transfer functions  $H_{xi}(\omega)$ ,  $H_{yi}(\omega)$ , and  $H_{zi}(\omega)$  at each critical component location or orientation.
- Step 4: By examining the transfer functions choose the critical frequencies  $\omega_{xi}$ ,  $\omega_{yi}$  and  $\omega_{zi}$  and note the corresponding real and imaginary parts of the transfer functions. Form the test matrix  $P$  (equation (9)) for each chosen frequency and compute the corresponding maximum eigenvalues  $\lambda_{xi}$ ,  $\lambda_{yi}$  and  $\lambda_{zi}$ .
- Step 5: Compute the test frequency  $\omega$  using equation (20). Note the corresponding values of the transfer functions. Form the test matrix  $P$  and compute its maximum eigenvalue  $\lambda_{\max}$  and the associated normalized eigenvector  $\underline{a}_{\text{opt}}$ .
- Step 6: Using equation (19) compute the minimum intensity scaling factor  $k_{\min}$ .
- Step 7: Synthesize the excitation input using the procedure for a standard triaxial test [1]. Scale it by  $k_{\min}$ . Conduct the uniaxial test using this input in the  $\underline{a}_{\text{opt}}$  direction.

#### General Discussion

The preliminary frequency response test mentioned in the previous section may be performed either by a sinusoidal input sweep [6] or using a white noise. In the latter case the transfer function is obtained simply as the ratio of the cross psd of the output and input signals to the input psd [7]. If this preliminary test is not conducted at the qualification test intensity, the system non-

linearities can have a significant influence on the optimal test parameters. On the other hand, fatigue effects become serious as the test intensity increases. If the nonlinearities are known to be weak, the input intensity of the preliminary test may be reduced without noticeably affecting the accuracy of the test results.

The present test procedure is based on the assumptions of asymptotically stable, linear time-invariant parameter system behavior. In the presence of strong nonlinearities the analytical development is valid for a narrow band of parameter variations about an operating point. In such cases, the results are usually reliable provided the test input intensity is of the same order of magnitude as the anticipated earthquakes at the equipment location. At lower input intensities the damaging effects of the seismic disturbances are negligible even though the accuracy of the analytical results is lost under these conditions.

Fatigue effects due to testing must be given due consideration. Increasing the test duration increases the fatigue of the equipment due to prolonged stressing of various components. This is the case when the test is repeated one or more times at the same intensity as that prescribed for a single test. For instance, the four-rotation test simulating triaxial input as presently performed, employs four separate tests at an input intensity that is higher by a factor of  $\sqrt{3}$  than that recommended for the triaxial test with uncorrelated input. Due to the particular test input configuration, overtesting results in the vertical direction. The degree of overtesting can be minimized if only three tests were performed in orthogonal directions. In any event, care must be exercised to avoid overtesting or overfatiguing in sequential tests. In this respect, the single uniaxial test has an obvious advantage over the sequential tests.

A flow diagram of the test set-up for the proposed seismic qualification test procedure is shown in Figure 3. The input synthesizer generates an excitation input signal that has the required frequency content and the intensity. The dynamic filtering effect caused by the support structure under service conditions may be taken into account by passing the signal through a suitable filter network. A tunable filter may be used to ensure that the signal is restricted to the frequency band of interest. The signal is then amplified and applied to the electro-hydraulic actuator attached to the shake table. The accelerometer outputs are usually integrated twice prior to processing. This is necessary when the excitation input is specified as a displacement rather than an acceleration. An analog spectrum analyzer is used to evaluate the spectral properties of the input and the outputs. For example, the transfer functions required for determining the optimal test parameters may be obtained using the spectral analyzer simply by computing the psd of the input signal and the cross psd's of

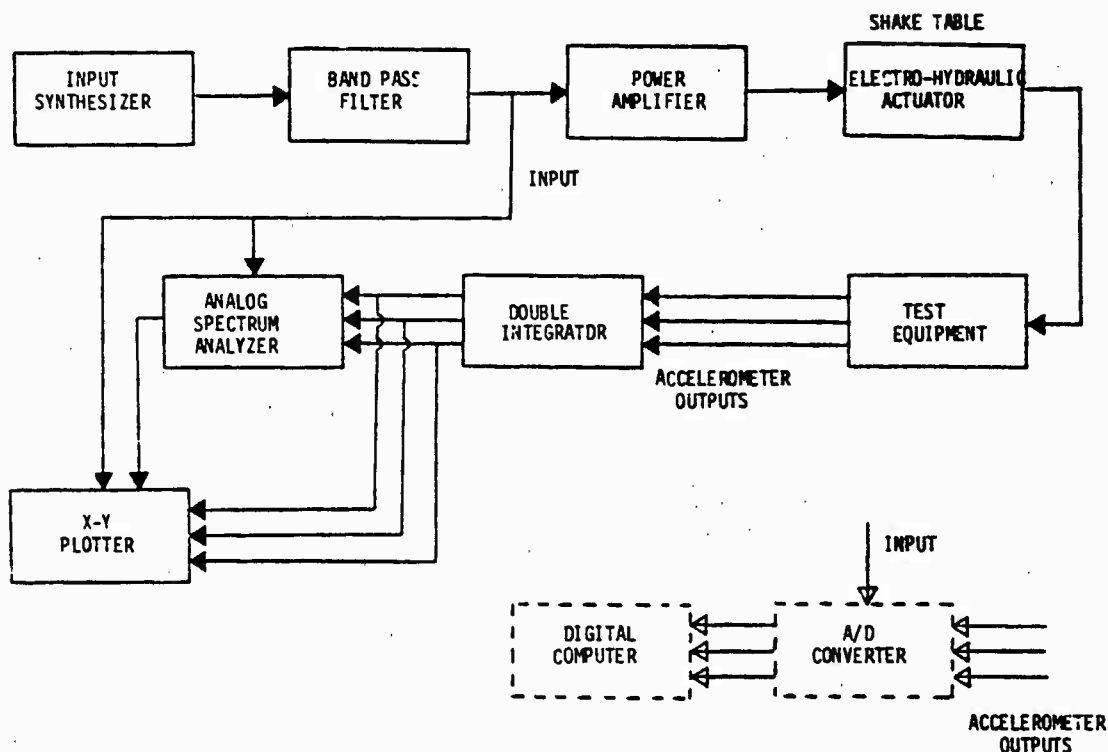


Figure 3. Flow Diagram of the Seismic Qualification Test Procedure.

the input and the output signals. If the response spectrum is employed as the criterion of signal specification, a special purpose analyzer may be employed to compute the response spectra and to check whether the TRS conforms to the RRS. Alternatively, the psd's computed during the previous stage may be employed to verify that the signal possesses the required frequency content and the intensity. On the other hand, an extensive digital analysis could be performed off-line by first recording the input and output signals on a magnetic tape and subsequently reading the data into a properly programmed digital computer via an analog/digital (A/D) converter. Alternatively, the analog spectrum analyzer could be replaced by an on-line A/D converter and a digital microcomputer (dotted lines in Figure 3). In a microcomputer based fully automated set-up, the optimization procedure and the associated decision logic are stored in the read only memory (ROM) chip of the microcomputer. Data acquisition, transfer function evaluation, selection of the test frequency and the determination of the optimal test input direction and the minimum input intensity are accomplished in real-time. These results are then used to position the actuator and to set the intensity of the excitation signal automatically. A feedback sensor loop may be used to improve the accuracy of the positioning process. Synthesis of the excitation input signal may also be accomplished digitally with improved accuracy.

The assignment of the probabilities of failure to the individual components of the

equipment is a major step in the present test procedure. This must be done with great care. If no past information is available, the probabilities may be assigned using engineering judgment. If this is not possible, equal probabilities may be assigned. These probabilities should be updated as more and more test results on component failure are available.

#### EXAMPLES

##### Example 1

Consider an equipment possessing fully symmetric dynamic characteristics with respect to the cartesian frame (OXYZ). For this case

$$\begin{aligned} H_{X1} &= H_{Y1} = H_{Z1} = H_1 \\ \text{or} \quad R_{X1} &= R_{Y1} = R_{Z1} = R_1 \text{ and } I_{X1} = I_{Y1} = I_{Z1} = I_1 \end{aligned}$$

The test matrix for this case becomes

$$\underline{P} = \begin{matrix} & \begin{matrix} N & 2 & 1 & 1 & 1 \end{matrix} \\ \begin{matrix} \Sigma \\ i=1 \end{matrix} & \begin{matrix} p_i & |H_i|^2 & 1 & 1 & 1 \end{matrix} \end{matrix}$$

The eigenvalues of  $\underline{P}$  are

$$\lambda_1 = \lambda_2 = 0, \lambda_3 = 3 \sum_{i=1}^N p_i |H_i|^2$$

Consequently,

$$J_{\max} = \lambda_{\max} = 3 \sum_{i=1}^N p_i |H_i|^2$$

The normalized eigenvector corresponding to  $\lambda_{\max}$  is determined as

$$\underline{a}_{\text{opt}} = \left[ \frac{1}{\sqrt{3}}, \frac{1}{\sqrt{3}}, \frac{1}{\sqrt{3}} \right]^T$$

This gives the optimal direction of testing. The minimum excitation intensity scaling factor is obtained using equation (19).

$$k_{\min} = \left[ \sum_{i=1}^N p_i |H_i|^2 (a_x^2 + a_y^2 + a_z^2) / \lambda_{\max} \right]^{1/2}$$

i.e.,

$$k_{\min} = [(a_x^2 + a_y^2 + a_z^2) / 3]^{1/2}$$

If equal intensities are specified for the standard triaxial test with uncorrelated-input, then  $a_x = a_y = a_z = 1$ . Then  $k_{\min} = 1$ . This tells us that the optimal uniaxial test must be performed at the same intensity as the uncorrelated input triaxial test. This intensity is lower by a factor of  $\sqrt{3}$  than that used in the current four-rotation test simulating triaxial input.

#### Example 2

As the second example consider an equipment that is sensitive to excitation in one direction (say the X-direction) only. The corresponding test matrix is

$$\underline{P} = \sum_{i=1}^N p_i |H_{xi}|^2 \begin{bmatrix} 1 & 0 & 0 \\ 0 & 0 & 0 \\ 0 & 0 & 0 \end{bmatrix}$$

The maximum eigenvalue of  $\underline{P}$  is

$$\lambda_{\max} = \sum_{i=1}^N p_i |H_{xi}|^2$$

The corresponding normalized eigenvector is

$$\underline{a}_{\text{opt}} = [1, 0, 0]^T$$

From equation (19), with equal intensities being stipulated for the standard triaxial test with uncorrelated-input, one obtains:

$$k_{\min} = a_x = 1$$

Thus, the optimal uniaxial test input must be applied in the direction of sensitivity (X-direction for this example). Furthermore, the test intensity need not be greater than the intensity of one input component in the triaxial test with uncorrelated-input. As in the previous example, an intensity reduction by a factor of  $\sqrt{3}$  over the four-rotation test simulating triaxial input is obtained.

#### CONCLUSIONS

An optimal test procedure for the seismic qualification of a class of multi-component electrical equipment has been developed. The procedure comprises a single uniaxial test conducted in an optimal direction using a test excitation input having certain minimum intensity. The optimal test parameters are determined using a frequency response test which is essentially similar to the sine sweep test currently employed in the industry to determine the resonant frequencies of the equipment being tested.

The objective function for the optimization has been expressed as the risk of component failure during testing. The implication of maximizing this performance index is to minimize the likelihood of component failure during actual service conditions. The optimal test parameters should be updated as more reliable information is available concerning the probabilities of failure for the individual components. In this manner, the past experience and the engineering judgment are directly incorporated in the test procedure.

A single uniaxial test can effect considerable savings in time and effort needed in comparison to the currently employed four-rotation test simulating triaxial input. Another advantage of the proposed test procedure is the elimination of unnecessary overtesting in the vertical direction caused by the four-rotation test. For the examples based on extreme equipment configurations, the required test input intensity is lower by a factor of  $\sqrt{3}$  than that for the currently employed four-rotation test.

The proposed test procedure can be fully automated. The decision logic and the precomputing to determine the optimal test parameters such as the direction cosines and the intensity of the test input can be conveniently programmed.

#### ACKNOWLEDGEMENT

This work was carried out at the Nuclear Technology Division, Westinghouse Nuclear Energy Systems, Pittsburgh, Pennsylvania.

#### REFERENCES

1. IEEE Recommended Practices for Seismic Qualification of Class 1E Equipment for Nuclear Power Plants, IEEE Std. 344-1975, Inst. Electrical and Electronics Engineers, Inc., New York, 1975.
2. Young, D., "Response of Structural Systems to Ground Shock," Shock and Structural Response, American Society of Mechanical Engineers, New York, 1960.
3. Tajimi, H., "A Statistical Method of Determining the Maximum Response of a Building Structure During an Earthquake," Proc. 2nd World Conference on Earthquake Engineering,

Tokyo and Kyoto, Japan, pp.781-796, 1960.

4. Bolotin, V.V., "Statistical Theory of the Aseismic Design of Structures," Proc. 2nd World Conference on Earthquake Engineering, Tokyo and Kyoto, Japan, pp.1365-1374, 1960.
5. Cornell, C.A., "Design Seismic Inputs," Seismic Design for Nuclear Power Plants, R.J. Hansen (Editor), MIT Press, Cambridge, MA, pp.114-137, 1972.
6. Newland, D.E., Random Vibrations and Spectral Analysis, Longman Ltd., London, 1975.
7. Bendat, J.S. and Piersol, A.G., Random Data: Analysis and Measurement Procedures, Wiley-Interscience, New York, 1971.

## DYNAMIC LOADING OF METAL RIVETED JOINTS\*

R. L. Sierakowski, C. A. Ross and J. Hoover  
Department of Engineering Sciences  
University of Florida, Gainesville, FL 32611

and

W. S. Strickland  
Vulnerability Branch  
USAF Armament Lab  
AFATL/DLYV Eglin AFB, FL 32542

This study presents the results of a series of tests to determine the effects of dynamic loading on riveted joints of thin metal structures. Dynamic tests were performed on strain gage instrumented tensile specimens with a precut central hole to determine the effect of stress concentrations. Results showed that dynamic stress concentrations are of the same order of magnitude as the corresponding static stress concentrations. Dynamic tests were also conducted on riveted tensile specimens of various types. The same general fracture (failure) modes observed in failed static specimens were also observed in the dynamic tests. Comparison of the results of the dynamic tensile test data with results of blast loaded riveted panels showed very good qualitative agreement. These full scale tests on flat panels with riveted edges and instrumented with strain gages were conducted using a fuel-air-explosive (FAE) device as the dynamic loading. Strain-time histories for interior points of the panel as well as along the rivet lines were recorded. Experimental techniques used introducing the blast loading and strain gage instrumentation are included in the discussion.

### INTRODUCTION

The principle requirement of any structural component when used in a complex structural system is to insure that the structural configuration remain intact when subjected to the static and dynamic design loads. This necessitates an understanding of the load transfer mechanism between and within structural components, and more importantly the load transfer mechanisms at the attachment points between adjacent components. In order to identify attachment or joint techniques, two general attachment classes can be inferred, specifically a mechanical or bonded joint type. To differentiate between these two classes, the mechanical joints as defined herein are those requiring a cutout or hole in the parent material for placement of a fastener device. The absence of this removed material reduces the potential useful component strength below that of the tested ultimate strength of the material. In addition the very nature of the type of loading is found to play an important role in characterizing the observed resultant attachment fracture. Fracture in this case and as used in this study is defined as actual material rupture or separation of one part of the attachment from the other. Bonded types of structures on the other hand, require the introduction of an adhesive type of material to insure structural continuity. Thus, the

inherent shear strength of the adhesive as well as the surface condition of the parent materials play an important role in characterizing attachment failure.

In the present study attention has been focused on only mechanical riveted connections found typically in sheet stiffener combinations of semi-monocoque structures. This study was initiated to establish qualitatively the fracture mechanisms for dynamically loaded riveted joint assemblies and to determine dynamic load factors based on measured strains at near field and far field positions relative to the rivets. To obtain this information a series of experiments was conducted on various sheet-rivet combinations and struts containing a single hole, using a drop weight device. In addition, full scale blast loaded instrumented panels were tested in cooperation with the USAF Armament Laboratory, Eglin AFB, Florida. The experimental tests and discussion of results are described in the following sections.

### EXPERIMENTAL TESTS AND DISCUSSION

The influence of stress concentrations for a static loaded infinitely wide plate with a circular hole as shown in Figure 1 has been discussed in detail in such classical elasticity tests as that of Timoshenko [1] and the general solution to such analysis shown graphically in Figure 2 with the intercept of the ordinate axis at  $K_t = 3.0$ . In order to establish equivalent

\*Funded by the USAF Armament Laboratory through USAF Office of Scientific Research Grant No. 76-3157.

stress concentration data for the case of dynamic loadings, a drop weight tester as shown in Figure 3 was used to load struts of various thicknesses. It was assumed that if strain measurements made near the circular hole were compared to strain measurements made at positions several hole diameters away, then their values would be indicators of the induced stress concentrations. Typical 2024T-3 aluminum test samples as shown in Figure 4 were tested in the drop weight tester and strain histories were recorded using MMEP-08-031AP-120 strain gages and a high speed recorder. The strain gages were trimmed and placed as close to the hole and to each other as possible (see Figure 4). While recognizing that the strains may not be uniform over the gage areas selected, measurements taken were intended to be comparative and not absolute. Similar geometrical specimens without holes were also tested to insure that a relatively uniform stress field existed across the sample at the far field gage position (position 1, Figure 4). The maximum strain readings of gage positions 2 and 3 were then compared to the maximum readings of the far field gage and strain ratios of gages 2 and 3 formed relative to those values measured at gage station 1. The ratios as determined for all the tests are shown in Figure 5. Static data were also taken for similar geometrical specimens as used in the dynamic tests. The static test data are also shown in Figure 5. The solid curve shown in Figure 5 represents the analytical prediction for static loading of a tensile specimen corrected for width effect as given by Peterson [2].

A comparison of these results as shown in Figure 5 indicates that there is very little difference between the static stress concentration as measured and calculated and compared with the dynamic experimental values. These results are in good agreement with dynamic stress concentration data generated by Dally [3,4] for birefringent materials using flash photography and photoelastic measuring equipment.

The above data has been used as a basis to examine the question of failure at the mechanical joint attachments. Classically, static loaded rivet/sheet combinations fail in one of the several failure modes as shown in Figure 6. In addition, rivet shear failure occurs with little damage to the sheet material. Static fracture loads for protruding head rivet/sheet combinations may be calculated using the material properties of the rivet and sheet material; however fracture loads for flush head rivets must be determined experimentally.

In order to observe rivet/sheet fracture under dynamic loads, a series of single and double lap tensile specimens were again tested using the drop weight tester. The specimens were instrumented with strain gages as close to the rivet head as possible. Drop heights were increased to produce increased strain levels at positions of uniform stress similar to the far field gage positions of the tensile struts with circular holes. Strains were recorded in the

same manner as in the previous case and strain ratios are shown in Figure 7. The ordinate of Figure 7 is an indication of the strain or stress level in the uniform stress section of the specimen. The abscissa is the ratio of strain at gage positions 2 and 3 to that of position 1 with negative values indicating the strains at positions 2 and 3 are in compression since gage position 1 is always tension or positive. As shown by the curves, the strains at positions 2 and 3 of the single lapped specimens are always in compression indicating a rotation at the rivet for all loads. However, for the double lapped specimens at low drop heights the gage positions 2 and 3 are in tension indicating that there is much less rotation taking place at the rivet than in the comparable single lapped specimens. Intuitively this would appear to be true due to the nature of the load misalignment of the single lapped specimens however, at the higher drop heights (increased uniform stress) rotation of the double lapped specimens is observed and as indicated by the curves of Figure 7 rivet and sheet rotation are noted at the higher loads with corresponding magnitudes appearing to be independent of rivet lap geometry. Rivet and sheet rotation was found to occur before fracture for all tests with the exception of sheet thicknesses of 0.1 in. (.25cm) and higher.

Various rivet and sheet combinations were tested using the drop weight tester. These tests are summarized in Tables I, II, and III. In almost all cases the trends were observed to be the same. For a given rivet diameter rivet shear was observed to be the dominating failure mode for the thicker sheets tested, however, as either leg of the tensile specimen was decreased a critical value was approached where rivet/sheet rotation began to predominate. This reduction in thickness reduces the bending stiffness and the resultant rotation combined with yielding under the bearing load produces greater deformation and distortion within the specimen. This increased distortion may be the reason for the increased drop height required to produce fracture with decreasing specimen thickness as indicated in Table II. However, as the sheet thickness continues to decrease a reduction in drop height necessary to produce fracture can occur accompanied by a change in the fracture mode. It may be argued that the increased drop height required for thinner specimens is due to the change in fracture toughness of the material, however, fracture toughness is generally accepted to be independent of the material and its geometrical properties. Further observations of this phenomenon are indicated in Table I where both legs of the specimen were of .025 in. (.064 cm) sheet material. Here a change in fracture mode from rivet/sheet rotation followed by rivet shear to rivet/sheet rotation followed by sheet tear out occurred as the sheet thickness was reduced from .32 in (.081cm).

As an application of these data, full scale blast tests were performed on several flat panels using a fuel-air-explosive (FAE) device for the loading. The FAE device has been used previously

and has been described in detail elsewhere by Ross and Strickland [5,6]. This loading method produces a plane and uniform blast loading over a large area. The panels as used in these tests were riveted to 0.25 inch (.64cm) thick side stiffeners which were in turn bolted to a massive frame using a 1.0 inch (2.54cm) thick front plate. Pressure time histories recorded in previous experiments [5,6] have been used as a data base and a well documented panel loading history for the experiments as used in this paper.

A typical test panel and location of strain gages used are shown in Figure 8. The BLH<sup>®</sup> foil gages used were cemented with EPY 150 epoxy adhesive cured at 150° F for one hour. Some gage debonding during testing was noted when using Eastman 910 adhesive or EPY 150 epoxy adhesive cured at temperature. The leads were always carefully taped to the plate to prevent breakage at the gages and at lead wire terminal strips. Strain time histories were recorded using a Honeywell Model 118 strain gage control and amplifier and a Bell and Howell VR3700 Recorder.

The results of all the full scale tests conducted were found to yield similar results with three cases presented in some detail here. In general, the areas of interest were the rivet lines and the area of the panel adjacent to the rivet line. For this particular study three plate thicknesses for a given size rivet configuration and loading history were examined. For analysis a point, 1.0 in (2.54cm) from the rivet line as shown by strain gage positions 5 and 6 of Figure 8, were chosen as the test strain monitoring positions. A 100 psi (.69 MPa) uniform pressure was chosen as the load intensity since rivet line fracture occurred in one of the three plate thicknesses at this load level. Even though rivet line fracture occurred the observed strain levels at the strain gage positions 5 and 6 were still elastic. As an analytical check of the data obtained, using only the unit deformations at these points (shear strain was found to be negligible) the load per unit length was determined using the elastic modulus and sheet thickness. The values are shown as functions of time in Figures 9, 10 and 11. For comparison with the engineering analysis above, bounded analytical results were obtained using a model analysis code DEPROM [7] for plates having simply supported/fully clamped edge boundary conditions. The code data obtained was then converted to an equivalent load per unit length in order to make the comparisons shown in Figures 9, 10 and 11.

The code used is an elastic-plastic analysis based upon an incremental theory for plasticity. Since only classical boundary conditions were available with this code, such conditions impose a rigidity for membrane action at the edges for both the pinned and fixed boundaries. This gives zero membrane flexibility at the boundaries and any yielding will be evidenced only in the panel. For all three plate thick-

nesses the stress level across the entire center line of the plate was greater than the yield stress. This is in disagreement with the experiment which showed elastic strains for all the plates tested.

Upon post-test examination of the riveted boundaries both rivet rotation and yielding of the plate near the rivet line has occurred. This rivet line deformation gives boundary flexibility which can not be accounted for in the analytical code. It appears that the riveted boundary flexibility gives sufficient stress relief in all cases tested to produce the experimentally observed elastic strains. This indicates that panel analyses that incorporate only classical boundary conditions, cannot be used for riveted or flexible boundaries which may deform at low stress levels, even though the analyses may allow for plastic behavior within the interior of the panel.

#### GENERAL CONCLUSIONS

Dynamic stress concentrations associated with mechanical joint attachments, that is fastener holes and rivet joints, are approximately equal to the corresponding static stress concentration values. The fracture/failure modes of riveted joints subject to dynamic loads are essentially the same as those of riveted joints subjected to static loadings however, the corresponding dynamic response of panels with riveted metal joints at or near the fracture load are very dependant on joint stiffness. Analytical models used to establish the fracture/failure load should include the stiffness of the real boundary and not those of either the standard simple or fully clamped boundary conditions.

#### REFERENCES

1. S. P. Timoshenko and J. N. Goodier, *Theory of Elasticity*, pp. 78-81. McGraw Hill Book Co., New York, Third Ed., 1970.
2. R. E. Peterson, *Stress Concentration Factors*, p. 9 #150, J. Wiley & Sons, 1974.
3. A. J. Durelli and J. W. Dally, "Stress Concentration Factors Under Dynamic Loading Conditions," *J. Mech. Eng. Sci.*, Vol. 1, No. 1, pp. 1-5, 1959.
4. J. W. Dally and W. F. Halbleib, "Dynamic Stress Concentrations at Circular Holes in Struts," *J. Mech. Eng. Sci.*, Vol. 7, No. 1, pp. 23-26, 1965.
5. C. A. Ross and W. S. Strickland, "Response of Flat Plates Subject to Mild Impulsive Loads," *Shock and Vibration Bulletin* No. 43, pp. 103-116, 1973.
6. W. S. Strickland and C. A. Ross, "The Plastic Response of Rectangular Membrane Plates to Mild Explosive Loading Functions," *U. S. Air*



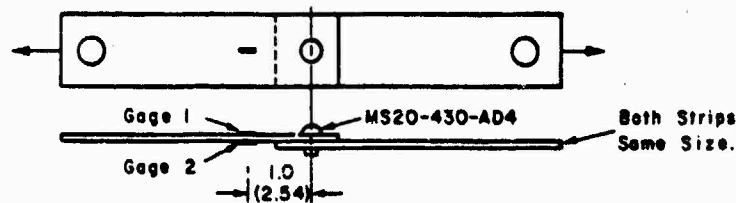
Force Armament Lab., Eglin AFB, FL, AFATL-TR-74-181, 1974.

7. L. J. Mente and W. N. Lee, "DEPROP - A Digital Computer Program for Predicting Dynamic Elastic-Plastic Response of Panels to Blast Loadings," U. S. Air Force Armament Lab., Eglin AFB, FL, AFATL-TR-76-61, 1976.

TABLE 1

MAXIMUM STRESSES AND LOADS FOR MS20-430-AD4 RIVET AND 2024-T3 SHEET

Sheet Thickness in(cm)	Fracture Drop Ht. in(cm)	Maximum Strain, $\epsilon$ $\mu$ Units		Ave. Strain $(\epsilon_1 + \epsilon_2)/2$ $\mu$ Units	Ave. Max. Stress KPSI (MPa)	Ave. Max. Load Lbs.	Type of Failure
		Gage 1	Gage 2				
.063(.160)	9.0(22.86)	636	1213	925	9.71(66.97)	612	Rivet rotation followed by rivet shear
.040(.102)	10.0(25.40)	1144	1440	1292	13.57(93.59)	517	Rivet rotation followed by rivet shear
.032(.081)	14.0(35.56)	1768	2366	2067	21.70(149.66)	695	Rivet rotation, bearing yielding, and elongation of hole followed by rivet shear
.025(.064)	11.0(27.94)	1411	1454	1433	15.05(108.79)	376	Severe rivet rotation and bearing yielding followed by shear tear out

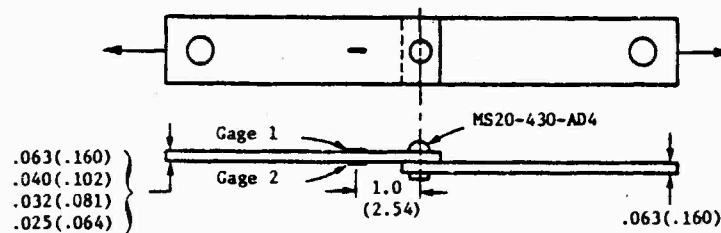


\*Static Shear fracture load for the rivet is 388 pounds

TABLE II

MAXIMUM STRESSES AND LOADS IN SPECIMENS WITH DIFFERENT THICKNESS IN THE TWO STRIPS OF THE SPECIMENS. MS20-430-AD4 RIVET AND 2024T3 SHEET

Sheet Thickenss in (cm)	Fracture Drop Ht. in (cm)	Maximum Strain, $\epsilon$ $\mu$ Units		Ave. Strain $(\epsilon_1 + \epsilon_2)/2$ $\mu$ Units	Ave. Max. Stress KPSI (MPa)	*Ave. Max. Load Lbs.	Type of Failure
		Gage 1	Gage 2				



\*Static shear fracture load for the rivet is 388 pounds

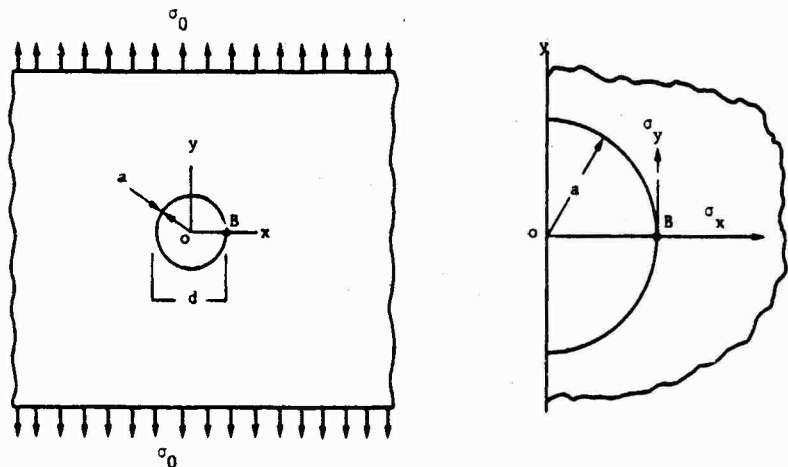
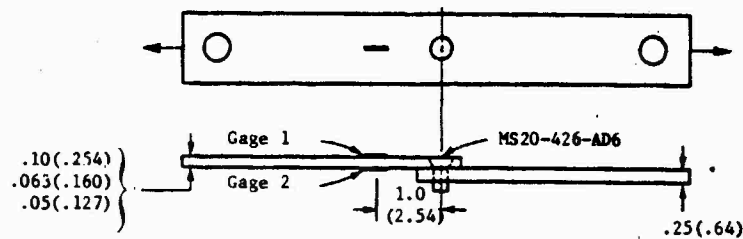


Figure 1. Circular Hole in Flat Plate of Infinite Width with Applied Far Field Stress  $\sigma_0$ .

TABLE III

MAXIMUM STRESSES AND LOADS IN SPECIMENS WITH DIFFERENT THICKNESSES IN THE TWO STRIPS OF THE SPECIMENS. MS20-426-AD6 RIVETS AND 2024-T3 SHEET

Sheet Thickness in (cm)	Fracture Drop Ht. in (cm)	Maximum Strain, $\epsilon$ $\mu$ Units		Ave. Strain $(\epsilon_1 + \epsilon_2)/2$ $\mu$ Units	Ave. Max Stress KPSI (MPa)	*Ave. Max. Load Lbs.	Type of Failure
		Gage 1	Gage 2				
.1(.254)	5.5(13.97)	Broken Lead	1530	----	----	----	Rivet shear with very little deformation
.063(.160)	9.0(22.86)	792	1317	1054	11.07(76.34)	698	Bearing and elongation of hole followed by rivet shear
.05(.127)	11.5(29.21)	1500	1790	1645	17.27(119.12)	864	Severe rotation of rivet and sheet. Severe hole elongation followed by shear tear out



\*Maximum static shear load 862 pounds

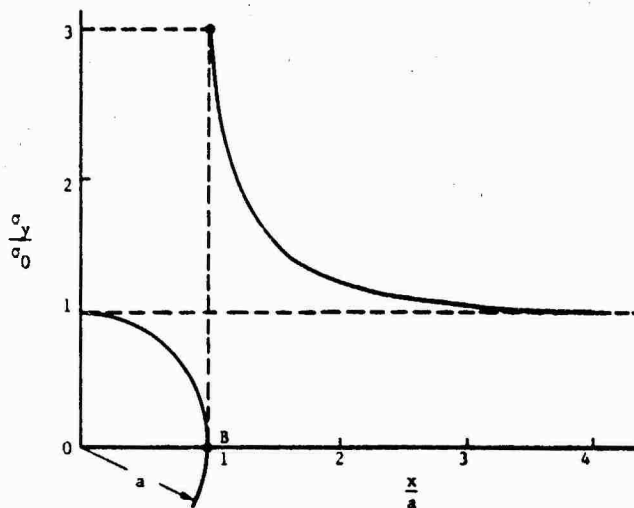


Figure 2. Ratio of Stress (Stress Concentration Factor) Along  $Bx$  for Plate Shown Figure 2.

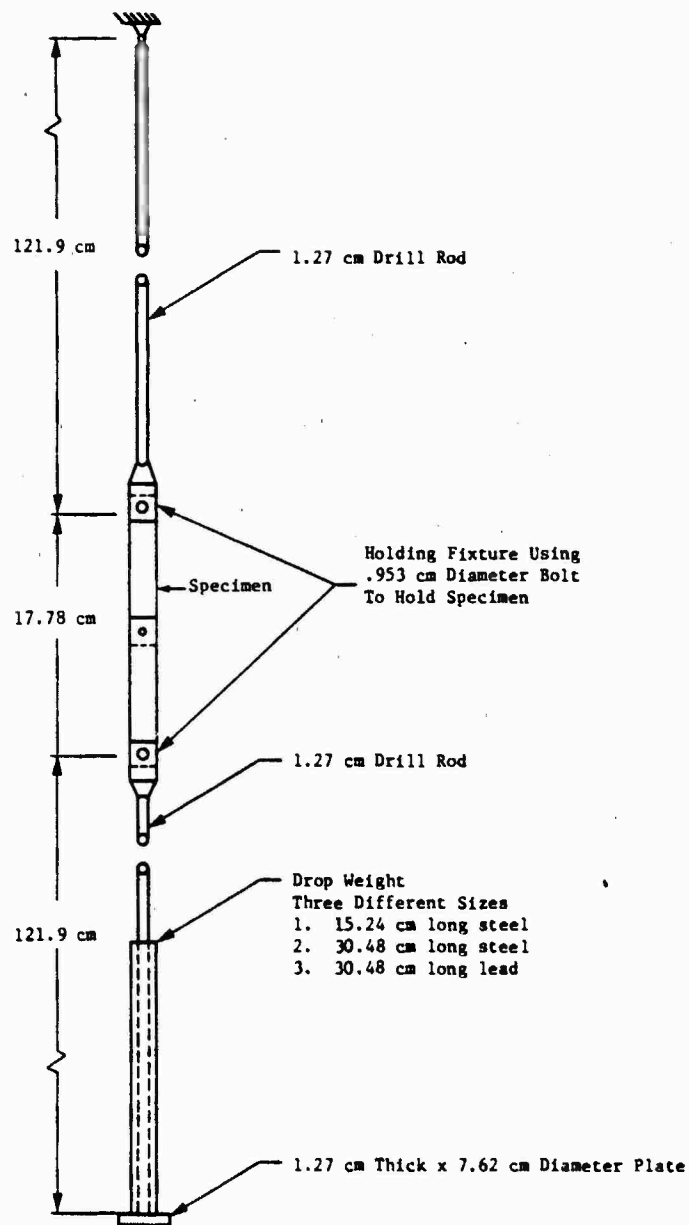


Figure 3. Drop Weight Device Used in Various Tests.

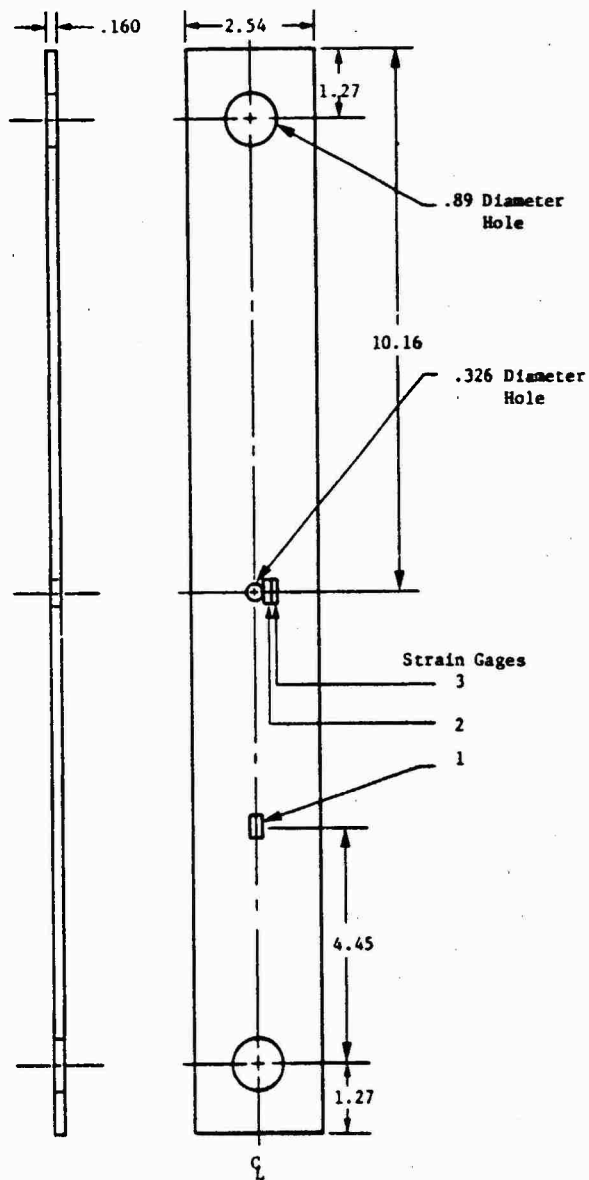


Figure 4. Strut with Central Hole used for Determining Dynamic Stress Concentrations. All Dimensions in Centimeters.

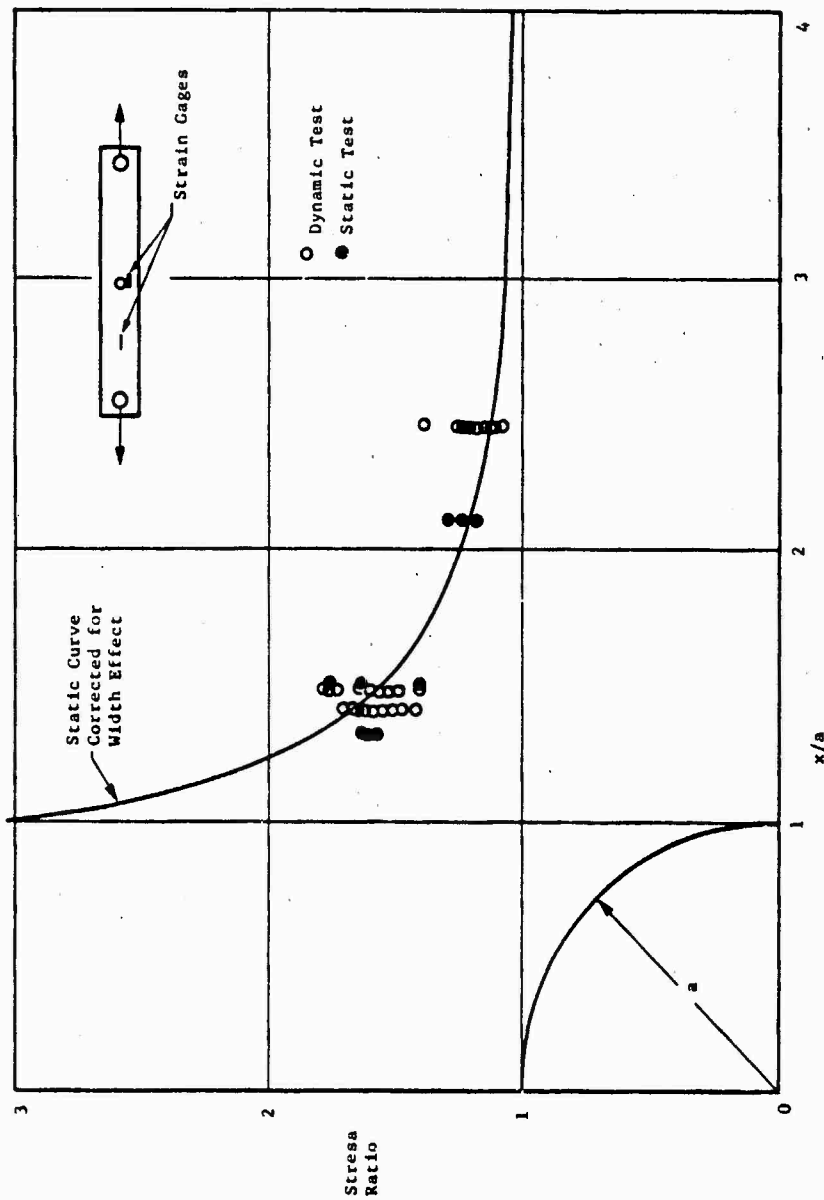
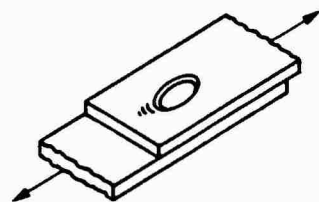
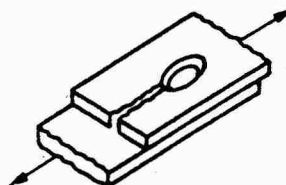


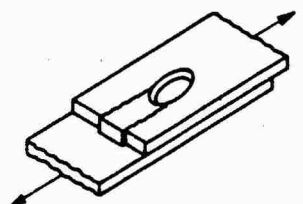
Figure 5. Stress Concentration Factors for Specimen Shown in Figure 4. Stress Ratio Same as Shown in Figures 1 and 2.



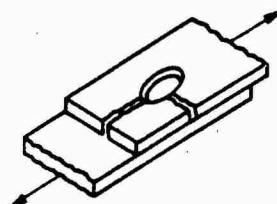
Bearing Failure



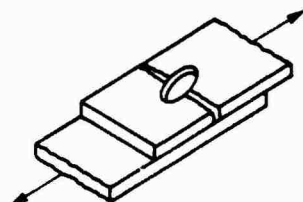
Cleavage Fracture



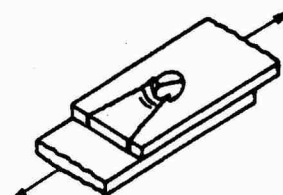
Shear Out Fracture



Combination Fracture



Net Tension Fracture



Shear Tear Out Fracture

Figure 6. Rivet Failure/Fracture Modes for Static Loads.

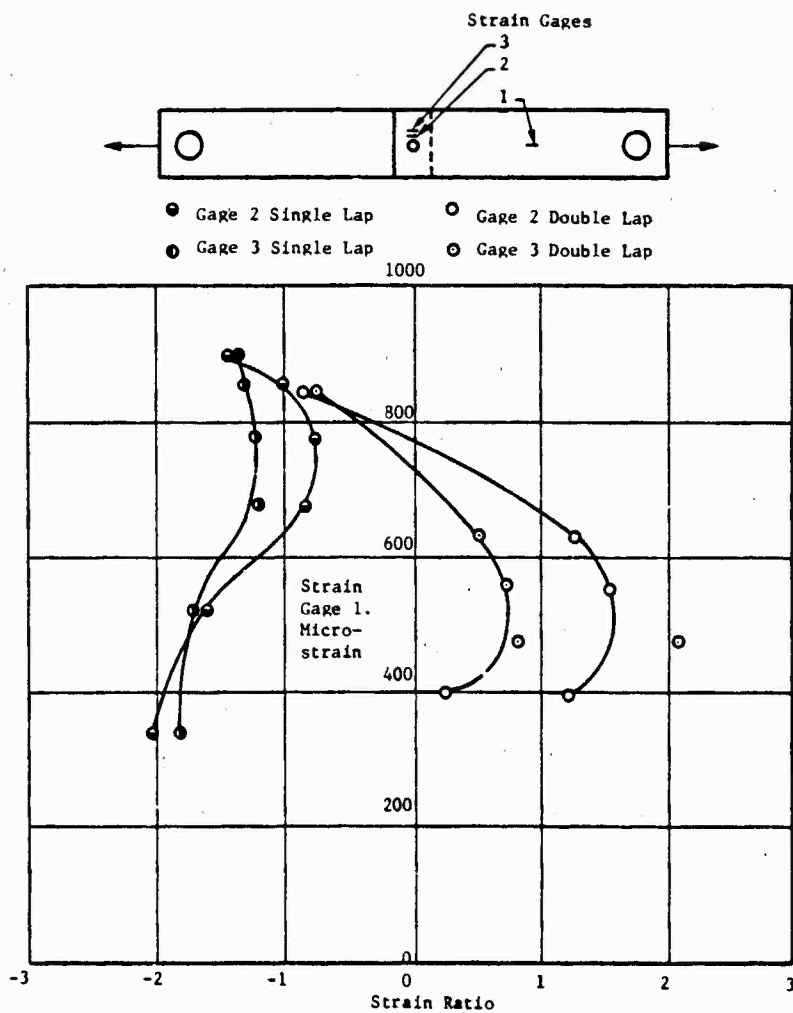


Figure 7. Strain Ratios for Lapped Flush Head Riveted Specimens Vs Strain at Gage 1.



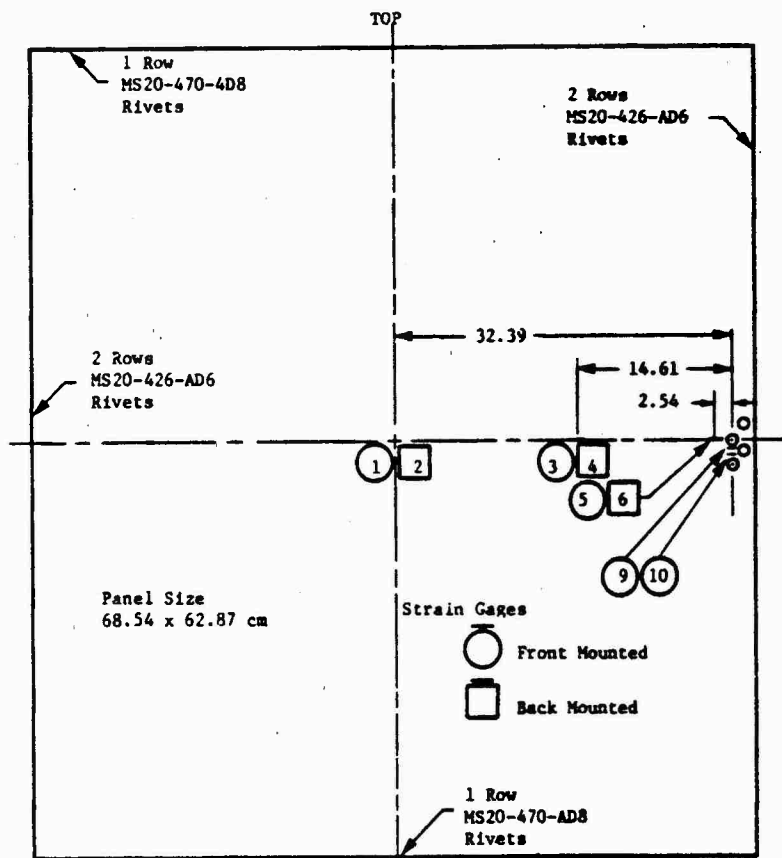


Figure 8. Rivet Arrangements and Strain Gage Positions for Full Scale Blast Tests. Panel Dimensions in Centimeters.

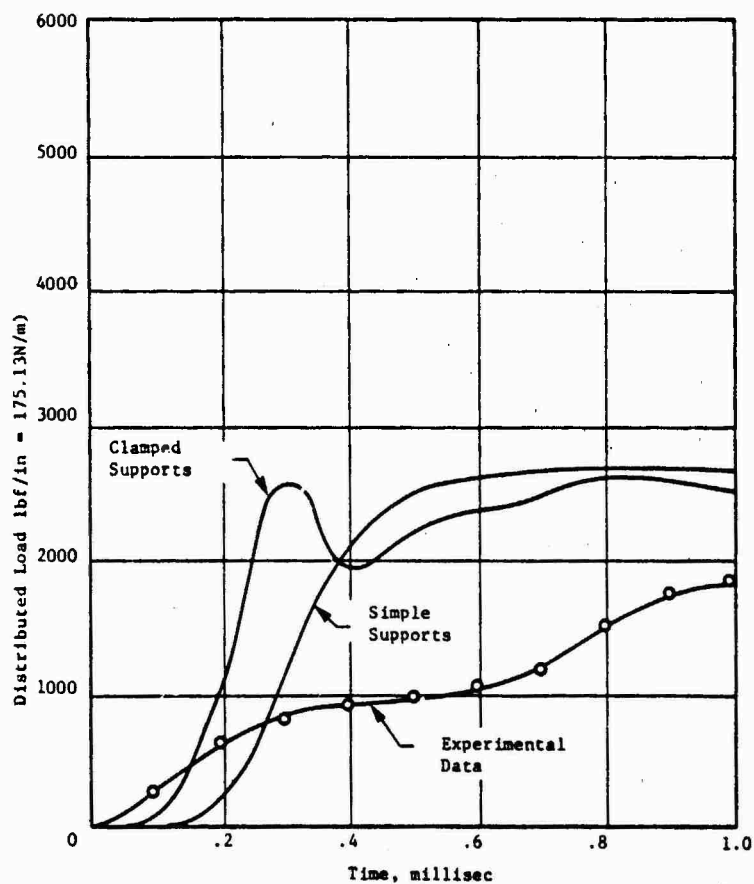


Figure 9. Distributed Normal Load Vs Time for a Point One Inch from Edge of Rivet Line at the Midpoint of the Side of Panel Shown in Figure 10. (Gage Positions 5 and 6) Panel Thickness 0.05 in(.127 cm).

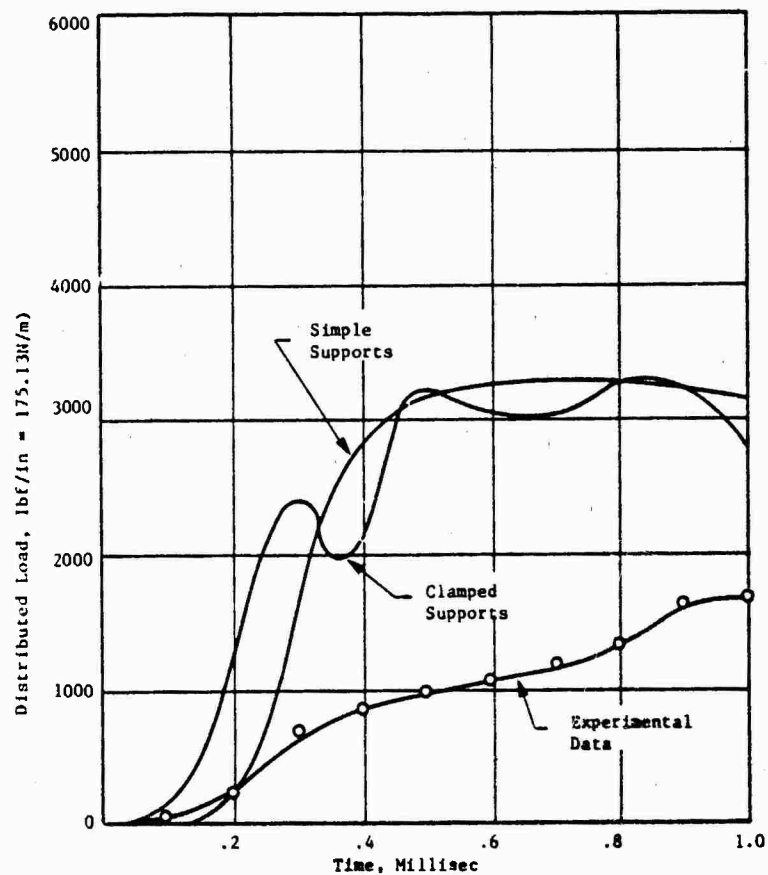


Figure 10. Distributed Normal Load Vs Time for a Point One Inch From Edge of Rivet Line at Midpoint of the Side of the Panel Shown in Figure 10. (Gage Positions 5 and 6) Panel Thickness 0.063 in (0.160 cm).

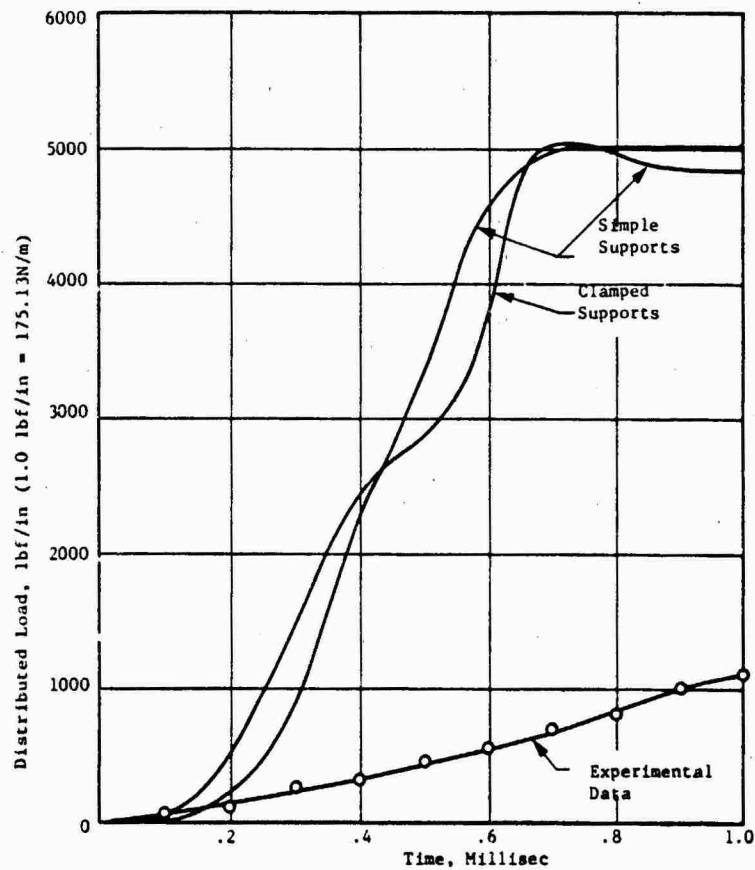


Figure 11. Distributed Normal Load Vs Time for a Point One Inch From Edge of Rivet Line at Midpoint of the Side Panel Shown in Figure 10. (Gage Positions 5 and 6) Panel Thickness 0.10 m (.254 cm)

#### DISCUSSION

Mr. Salive (David Taylor Naval Ship Research and Development Center): What kind of material did you use in your test?

Mr. Ross: All of the plates were 20-24 or 60-61 aluminum alloy and the rivets, if I remember, were 20-14 aluminum alloy.

Mr. Salive: Was there any anisotropy or directional strength in those plate materials?

Mr. Ross: Very little.

Mr. Westine (Southwest Research Institute): You talked about the two different loading techniques. You talked about the drop test then before you started showing figures 7 through 11, you talked about explosive loading. Then I saw what you call an analysis. I am partially confused because I am not sure which loading technique you used and you did not say why you felt that you had much lower rise times relative to the analysis. Was it because you applied the loads instantaneously in your analysis? What was your explosive loading?

Mr. Ross: The slide previous to the last three was a picture of a full scale panel which is instrumented with strain gages. Maybe I needed to have a slide to show you the loading technique in that particular case. It was a fuel air explosion which is contained in a large plastic bag which is detonated at one end; then a moving wave passes through that bag and at the aft end of that bag there is a pretty good planar explosion or planar wave. That was the type of loading device we used on the full scale test. We used the pressure loads that we measured from that full scale test for the analysis. I can't understand why the analysis shows the rise time to be that much higher, but that was exactly what we used. We used this fuel air explosion technique many times before and we have a good idea what the pressure is and what the rise times are.

GENERALIZED GRAPHICAL SOLUTION FOR ESTIMATING RECOILLESS  
RIFLE BREECH BLAST OVERPRESSURES AND IMPULSES

P. S. Westine, G. J. Friesenhahn, J. P. Riegel, III  
Southwest Research Institute  
San Antonio, Texas

The breech blast from recoilless rifles produces a severe transient blast field that can damage weapon carriers and cause gun crew hearing loss. This paper culminates a three-year program in which similitude theory and experimental test results from gun firings have been used to develop a generalized graphical solution for predicting both blast pressures and impulses forward as well as aft of recoilless rifle nozzles. Experimental test data from the literature on various recoilless rifles and a special series of tests on a variable nozzle and chamber recoilless rifle test fixture demonstrate the validity of this solution.

INTRODUCTION

This paper is an expansion on a previous one published in the 1978 Shock and Vibration Bulletin[1]. In that paper, the model laws for scaling breech blast pressure and the blast pressure field aft of a recoilless rifle nozzle were presented. This paper extends this previous work by permitting breech blast overpressures to be estimated now both forward as well as aft of the nozzle. In addition, the impulse field, which was previously overlooked, can now be predicted both forward and aft of the

breech. Both the breech blast overpressure and impulse solutions have been generalized in such a fashion that they should work for any caliber recoilless rifle, with any size propelling charge, with various expansion ratios in the nozzles, and with either kidney-shaped or central orifice nozzles.

The breech blast overpressure equation which results and will be discussed is given by Equation (1) and the impulse breech blast field is given by Equation (2).

$$\ln [\bar{P} \times 10^{4.3}] = 7.579 - 0.03433 \theta - 1.2134 \ln \bar{L} + 0.005526 \theta \ln \bar{L} \quad (1)$$

$$\bar{I} = \{45.71 - 45.40 [\tanh^{0.3}(\frac{\theta}{30})]\} \bar{I} [-0.851 + 0.766 \tanh^{1/2}(\frac{\theta}{30}) + 0.1e^{-\theta/5.2}] \quad (2)$$

where

$$\bar{P} = \frac{P}{mP_c} \left(\frac{A_E}{A_t}\right)^2$$

$$\bar{I} = \frac{Ia_o}{\sqrt{P_c P_o} A_t} \left(\frac{A_E}{A_t}\right)^2$$

$$\bar{L} = \frac{NL}{A_E}$$

$$\bar{I} = \frac{L}{A_E}$$

and where  $\theta$  = the angle in degrees from center line of rifle ( $0^\circ$  is directly aft)

$A_E$  = effective nozzle exit area--can be less than actual  $A_E$  if nozzle is poorly designed so flow cannot fully expand.

$A_t$  = nozzle throat area

$P_C$  = maximum propellant chamber pressure

$P$  = maximum side-on blast overpressure

$I$  = side-on specific impulse

$L$  = distance from breech

$m$  = shape factor associated with chamber pressure time history. Approximately equals average chamber pressure divided by maximum chamber pressure

$N$  = shape factor associated with type of nozzle. Equals 1.0 for central orifice nozzle but equals  $e^{0.001287\theta^{3/2}}$  for kidney nozzles

$P_0$  = ambient atmospheric pressure

$a_0$  = speed of sound in air

Both Equations (1) and (2) are fairly complicated functions. Fortunately, both equations are three-parameter spaces of scaled quantities. In functional format, the blast overpressure solution can be written as:

$$\frac{P}{mP_C} \left( \frac{A_E}{A_t} \right)^2 = f_P \left[ \theta, \frac{N(\theta)L}{\sqrt{A_E}} \right] \quad (3)$$

and the impulse solution can be written as:

$$\frac{I a_0}{\sqrt{P_C P_0 A_t}} \left( \frac{A_E}{A_t} \right)^2 = f_I \left[ \theta, \frac{L}{\sqrt{A_E}} \right] \quad (4)$$

This observation means that, if rectangular rather than polar coordinates are used, an easy graphical presentation results. Either a nondimensional pressure

$\frac{P}{mP_C} \left( \frac{A_E}{A_t} \right)^2$  or a scaled impulse

$\frac{I a_0}{\sqrt{P_C P_0 A_t}} \left( \frac{A_E}{A_t} \right)^2$  can be plotted as contours

versus one's position in space

$\frac{L_1}{\sqrt{A_E}}$  and  $\frac{L_H}{\sqrt{A_E}}$ , where  $L_1$  is the distance

from the nozzle perpendicular to the line of fire and  $L_H$  is the distance

from the nozzle parallel to the line of fire. Any self-consistent set of units can be used as all terms are nondimensional.

These plots are shown in Figure 1 for predicting breech blast overpressure and Figure 2 for predicting impulse. The solid contour constant overpressure or constant impulse lines cover regions where pressures and impulses were measured, and dashed contours cover regions where pressure and impulse have been extrapolated. The inserts in the upper right hand corners of Figures 1 and 2 expand the graphical solution in the regions forward of the breech, where the gunner's head is located.

The overpressure contours, seen in Figure 1, have the elliptical shape which is typical of recoilless rifle firings. On the other hand, the impulse contours, seen in Figure 2, exhibit "fingers" radiating away from the source. Over the region which was mapped, scaled impulse is much closer to being constant than is scaled pressure. Along any radial line at a constant angle from the breech, scaled impulse changes very little. This observation will become apparent in subsequent plots when pressures and impulses are compared to test data in plots along radial lines at a constant angle from the breech.

#### COMPARISON WITH TEST RESULTS

Experimental breech blast overpressure data were taken from the literature for such guns as 57mm T66E6, 57mm M18A1, 75mm T21, 90mm T219, 105mm modified M27, 105mm T/19, and 106mm T170E1. This breech blast pressure data base was supplemented with SwRI-measured breech blast pressures obtained using a special chamber on which nozzles, chamber volume, quantities of propellant, and type of propellant could all be changed independently or in combination. This special test device will not be described further in this paper as it is presented in detail in Reference 1.

Figures 3 through 13 present test results in polar plots of scaled pressure versus scaled standoff distance for constant angular directions from the breech. Each plot is along a radial line rotated 15° further forward than its predecessor. The shape of the symbol in all figures indicates the sources of the data and the reference from which the data were taken. The solid line through all of the data points is Equation (1) which is a curve fit to the test results. Of the weapons included in these comparisons, the 57mm T66E6,

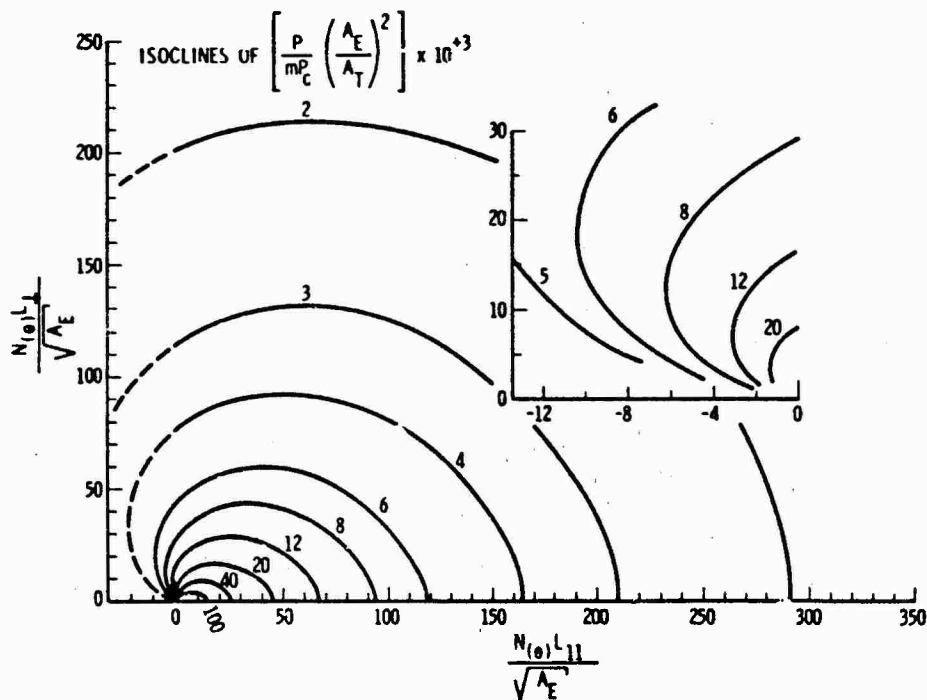


FIGURE 1  
Free Field Blast Pressures Around the Breech of Recoilless Rifles

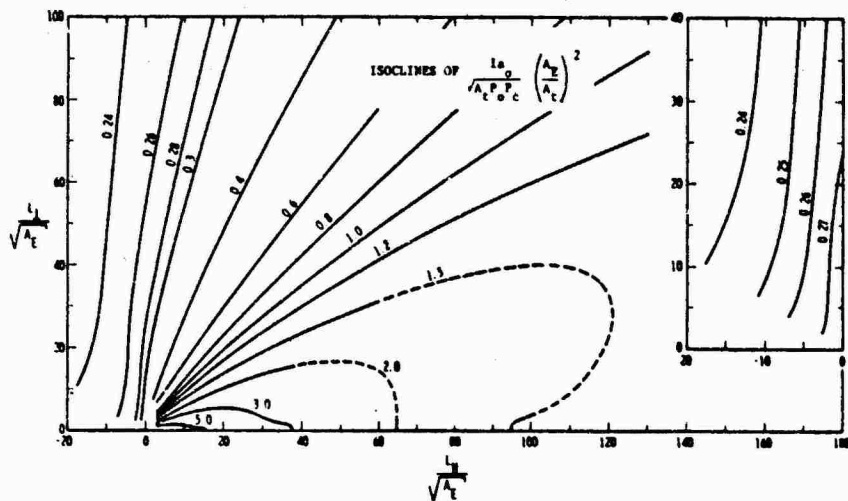


FIGURE 2  
Free Field Impulse Around the Breech of Recoilless Rifle



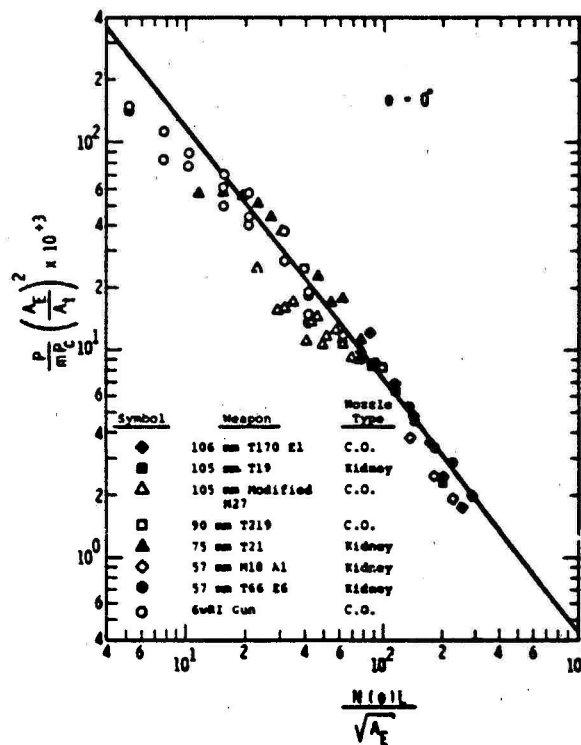


FIGURE 3  
Scaled Pressure Versus Scaled Standoff for  $\theta = 0^\circ$

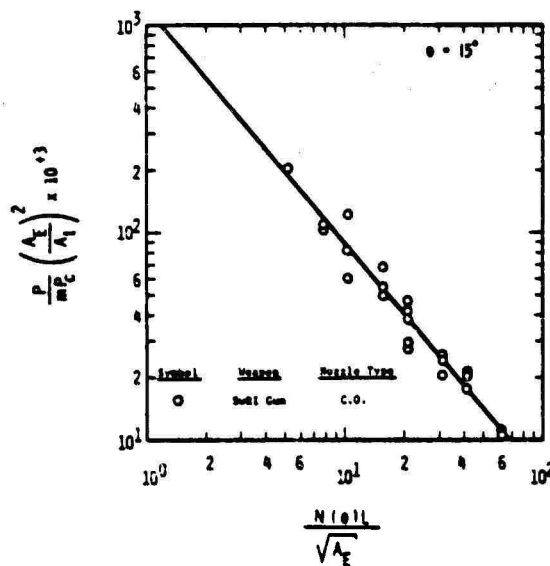


FIGURE 4  
Scaled Pressure vs Scaled Standoff for  $\theta = 15^\circ$

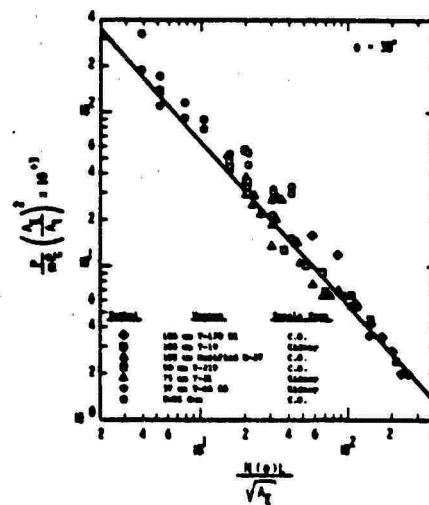


FIGURE 5  
Scaled Pressure vs Scaled Standoff for  $\theta = 30^\circ$

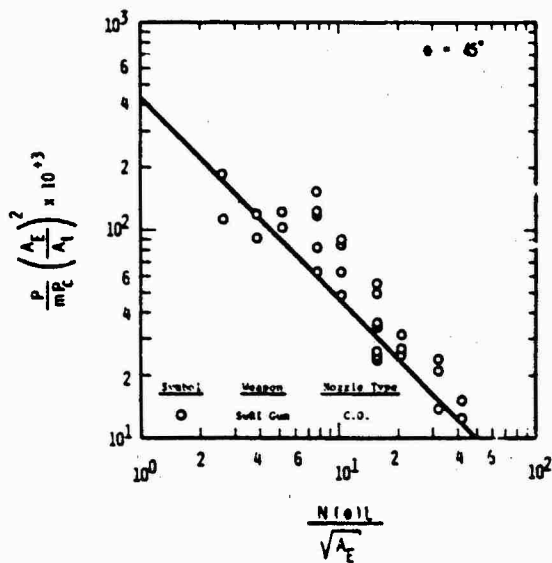


FIGURE 6  
Scaled Pressure vs Scaled  
Standoff for  $\theta = 45^\circ$

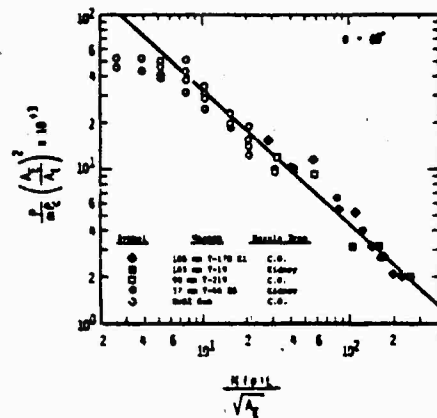


FIGURE 7  
Scaled Pressure vs Scaled  
Standoff for  $\theta = 60^\circ$

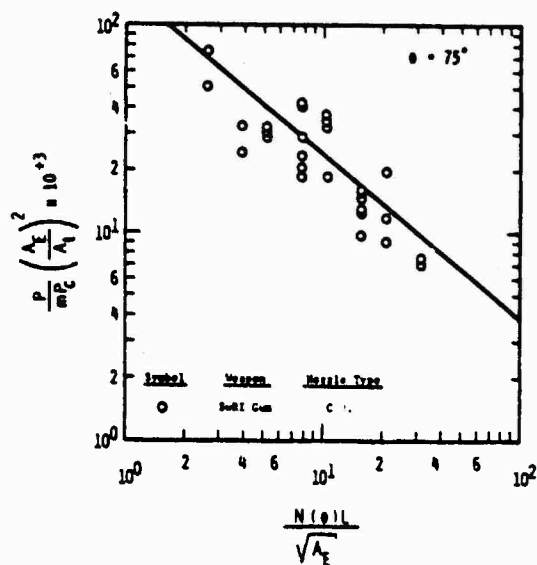


FIGURE 8  
Scaled Pressure vs Scaled  
Standoff for  $\theta = 75^\circ$

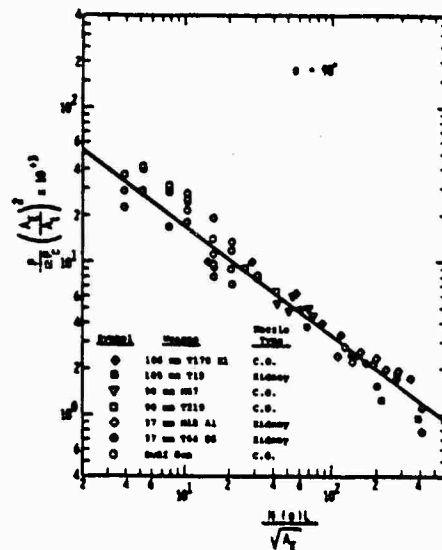


FIGURE 9  
Scaled Pressure vs Scaled  
Standoff for  $\theta = 90^\circ$

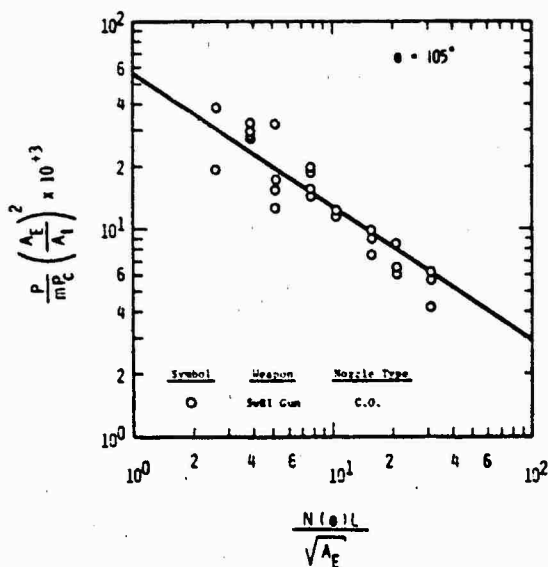


FIGURE 10  
Scaled Pressure vs Scaled  
Standoff for  $\theta = 105^\circ$

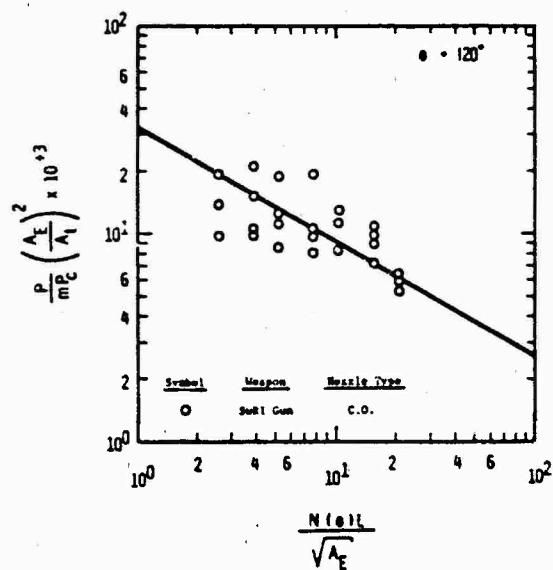


FIGURE 11  
Scaled Pressure vs Scaled  
Standoff for  $\theta = 120^\circ$

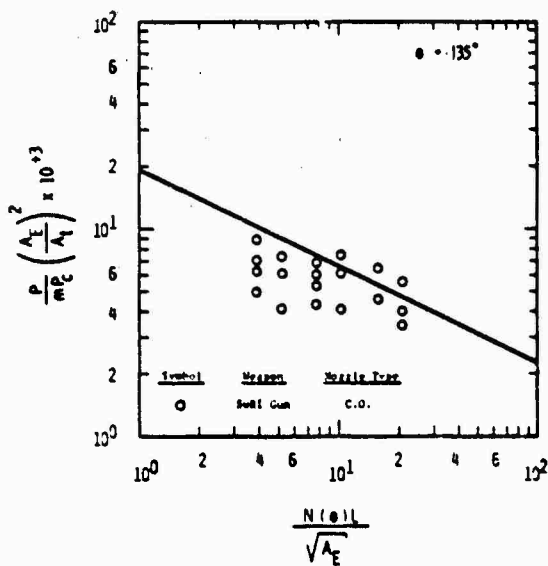


FIGURE 12  
Scaled Pressure vs Scaled  
Standoff for  $\theta = 135^\circ$

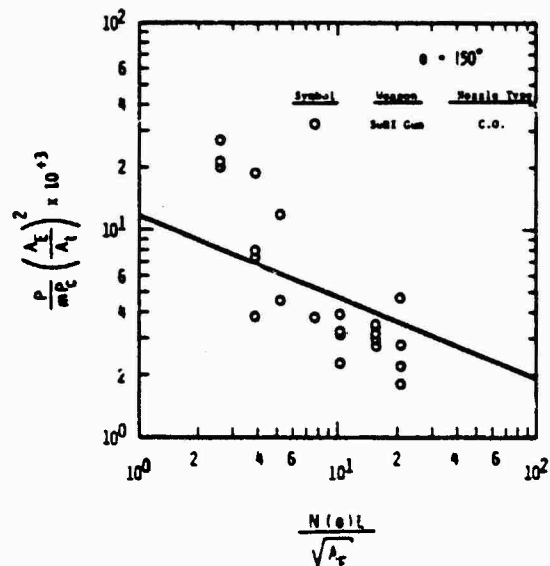


FIGURE 13  
Scaled Pressure vs Scaled  
Standoff for  $\theta = 150^\circ$

105mm T19, 75mm T21, and 57mm M18A1 have kidney nozzles, whereas the other three weapons and the SwRI special test chamber have central orifice nozzles. Table 1 lists the weapon parameters  $P_C$ ,  $A_E$ , and  $A_t$  associated with each of the weapon systems. The SwRI test device is not listed in this table because its properties are variable and are given in Reference 1. The experimentally-measured pressures do scatter about the

line, and accuracy becomes poorer as the location of interest is moved forward of the breech. One standard deviation for measured pressures as a percentage of the predicted pressure is +9.5% between 0 and 90 degrees, +11.3% between 105 and 150 degrees, and +9.8% overall. These breech blast pressure comparisons show that both forward and aft of the breech, a general solution has been developed and is given by Equation (1).

TABLE 1  
Weapon Parameters Used to Scale Results

Weapon	Reference	$P_C$ (psi)	$A_E$ (in. <sup>2</sup> )	$A_t$ (in. <sup>2</sup> )	Nozzle Type
57mm T66E6	2	7,100	7.05	2.95	Kidney
90mm T219	3	3,700	23.87	6.82	C.O.
105mm modified M27	4	Various	35.5	Various	C.O.
105mm T19	5	9,260	17.48	9.30	Kidney
75mm T21	6	10,000	9.67	4.67	Kidney
57mm M18A1	7,8	6,500	7.05	2.95	Kidney
106mm T170E1	9	10,200	17.90	10.00	C.O.

Similarly-scaled impulse plots were made for constant values of  $\theta$  in 15-degree increments from 0 to 150 degrees as seen in Figures 14 through 24. Not as much recoilless rifle impulse data are available in the literature as pressure data, because investigators have just begun to realize the importance of impulse, and reducing records to obtain impulse from transient pressure traces requires additional tedious work. Thus, with the exception of a 57mm gun and two 105mm weapon systems, the majority of the impulse data are from SwRI test firings using the special test chamber. Once again, the solid line is the Equation (2) curve fit to the impulse test data. These breech blast impulse comparisons also show that, within the bounds of the weapons studied, both forward and aft of the breech, a general breech blast impulse solution has been developed and is given by Equation (2).

#### DEVELOPMENT OF IMPULSE MODEL LAWS

Because the preceding paper, Reference 1, presents both the history of previous gun blast modeling studies, and develops the scaling law for recoilless

rifle breech blast overpressure, these details will not be presented in this paper. We will only supplement this previous discussion by developing the model law used in this study to scale impulse from breech blast.

The approach used in developing the impulse model laws is to subdivide the problem into two parts so that one model analysis gives the effective energy release emitted from the breech as variations are made in internal gun and propellant characteristics. The second analysis then relates this effective energy release to the blast pressure wave impulses at any location around the breech of the gun. The results of these two solutions can then be combined using empirical observation to obtain a single solution as was given by Equation (4).

The first model analysis to determine the effective energy release  $W_{eff}$  begins with the assumption that engineers can predict the peak chamber pressure  $P_C$  and the burn duration  $T$  for propellants fired in recoilless rifle gun chambers. In addition, the effective energy release is assumed to depend upon the volume  $V$  of the rifle chamber,

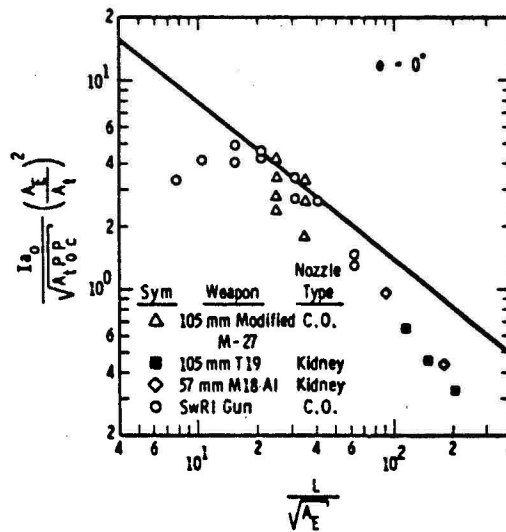


FIGURE 14

Scaled Impulse vs Scaled Standoff for  $\theta = 0^\circ$

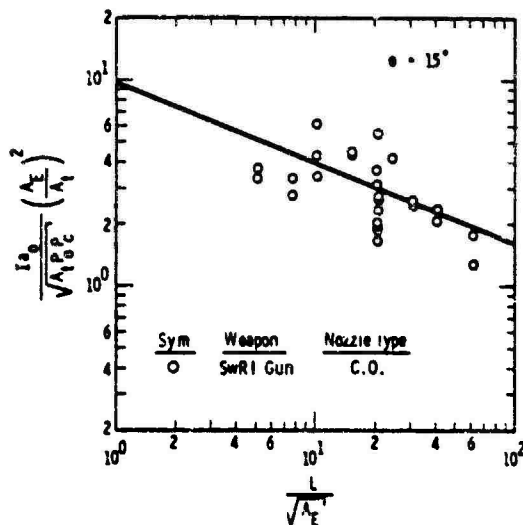


FIGURE 15

Scaled Impulse vs Scaled Standoff for  $\theta = 15^\circ$

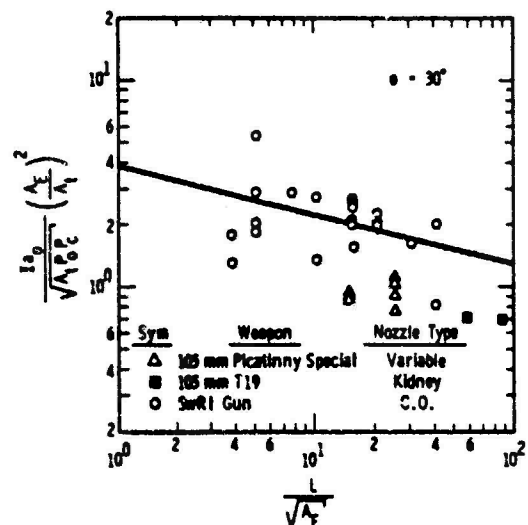


FIGURE 16

Scaled Impulse vs Scaled Standoff for  $\theta = 30^\circ$

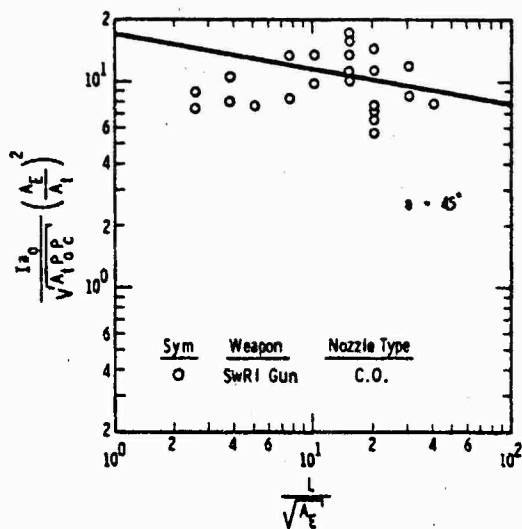


FIGURE 17  
Scaled Impulse vs Scaled  
Standoff for  $\theta = 45^\circ$

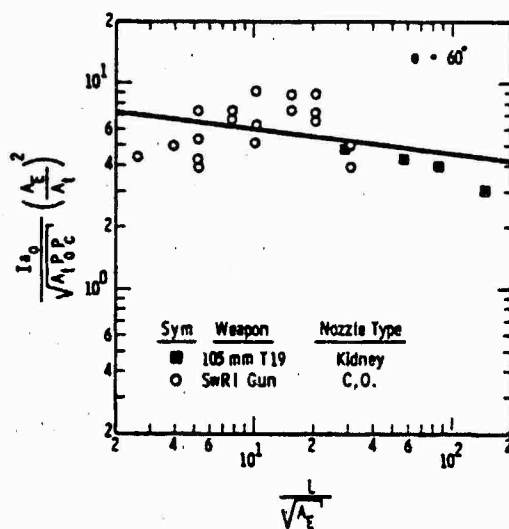


FIGURE 18  
Scaled Impulse vs Scaled  
Standoff for  $\theta = 60^\circ$

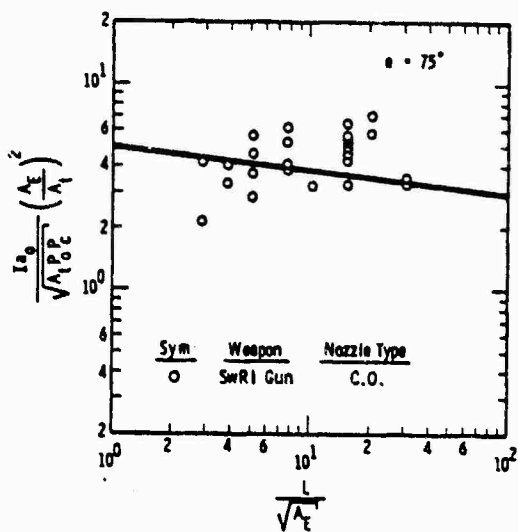


FIGURE 19  
Scaled Impulse vs Scaled  
Standoff for  $\theta = 75^\circ$

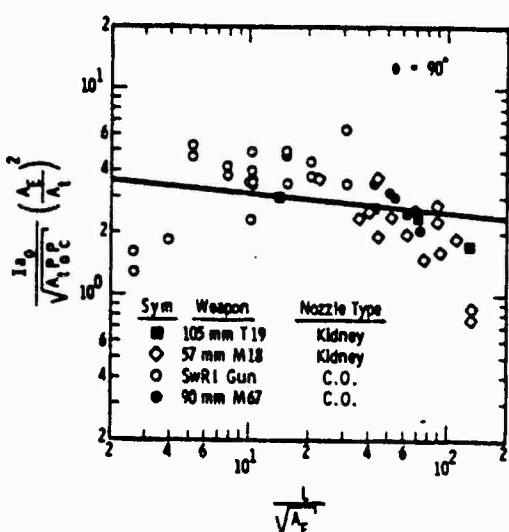


FIGURE 20  
Scaled Impulse vs Scaled  
Standoff for  $\theta = 90^\circ$

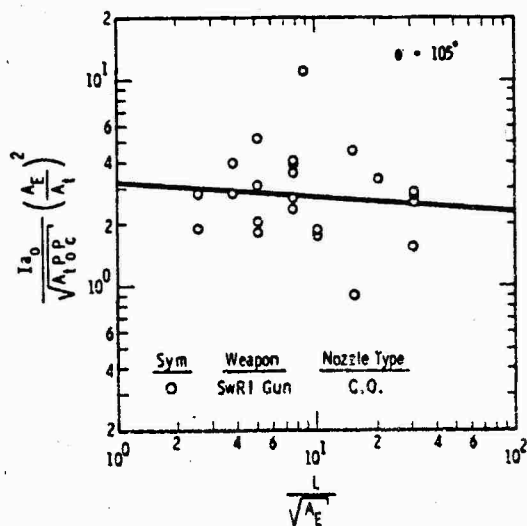


FIGURE 21  
Scaled Impulse vs Scaled  
Standoff for  $\theta = 105^\circ$

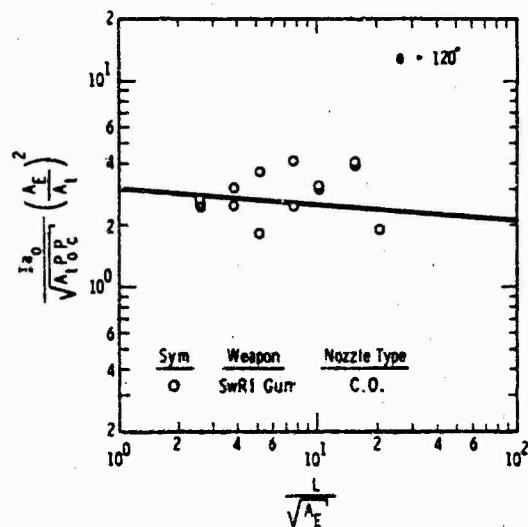


FIGURE 22  
Scaled Impulse vs Scaled  
Standoff for  $\theta = 120^\circ$

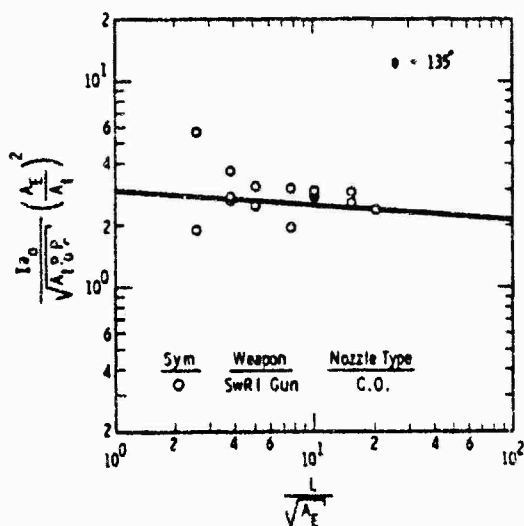


FIGURE 23  
Scaled Impulse vs Scaled  
Standoff for  $\theta = 135^\circ$

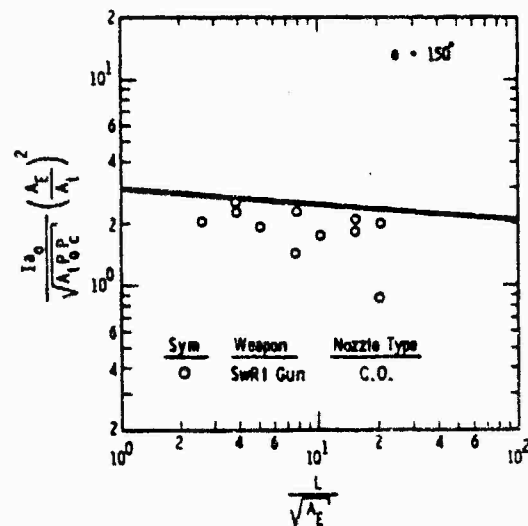


FIGURE 24  
Scaled Impulse vs Scaled  
Standoff for  $\theta = 150^\circ$

the throat area  $A_t$  of the nozzle, the exit area of the nozzle  $A_E$ , the ratio of specific heat  $\gamma$  for the combustion products in the chamber, and the speed of sound  $a$  for the combustion products. This definition of the problem leads to the following dimensional functional relationship for  $W_{eff}$ :

$$W_{eff} = f(V, P_c, T, A_t, A_E, \gamma, a) \quad (5)$$

Equation (5) is an eight-parameter space of dimensional numbers. It can be reduced to a five-parameter space of nondimensional numbers by conducting a model analysis. Although we will omit the algebraic process associated with such an analysis, no new assumptions are made. One acceptable complete set of nondimensional numbers can be given by:

$$\frac{W_{eff}}{P_c A_t^{3/2}} = f\left(\frac{A_E}{A_t}, \gamma, \frac{V}{A_t^{3/2}}, \frac{aT}{A_t^{1/2}}\right) \quad (6)$$

Next the second model analysis is conducted to determine the breech blast impulse  $I$  at some location in space given by distance  $L$  and angle  $\theta$  from a recoilless rifle with an effective energy release  $W_{eff}$  from a nozzle with exit area  $A_E$ . In addition to these parameters, atmospheric conditions must be included in the analysis so any shock waves can be propagated from the recoilless rifle to the point of interest. Although various atmospheric properties could be used, the three we selected were atmospheric pressure  $P_o$ , the ratio of specific heats for air  $\gamma_o$ , and the speed of sound in air  $a_o$ . This definition of the second subproblem leads to the following dimensional functional relationship for impulse:

$$I = \psi(W_{eff}, A_E, L, \theta, P_o, a_o, \gamma_o) \quad (7)$$

A model analysis conducted on the dimensional parameters in Equation (7) reduces the eight-parameter space to a five-parameter space of nondimensional numbers as in Equation (8).

$$\frac{I a_o}{W_{eff}^{1/3} P_o^{2/3}} = \psi\left(\frac{W_{eff}}{P_o A_E}, \gamma_o, \frac{L}{A_E}, \theta\right) \quad (8)$$

Next Equation (6) can be substituted into Equation (8) to eliminate  $W_{eff}$ . If it is recognized that the  $\psi$  function in Equation (8) can actually be several functions, one function relating

$$\frac{W_{eff}}{P_o A_E^{3/2}} \text{ to } \frac{I a_o}{W_{eff}^{1/3} P_o^{2/3}} \text{ and the second}$$

function relating  $\gamma_o, \left(\frac{L}{A_E}, \theta\right)$  to

$$\frac{I a_o}{W_{eff}^{1/3} P_o^{2/3}}, \text{ then substitution of}$$

Equation (6) into Equation (8) gives:

$$\frac{I a_o}{P_c^{1/3} P_o^{2/3} A_t^{1/2}} = \phi_1\left(\frac{P_c A_t^{3/2}}{P_o A_E^{3/2}}, \frac{A_E}{A_t}, \gamma, \frac{V}{A_t^{3/2}}, \frac{aT}{A_t^{1/2}}\right) \phi_2\left(\gamma_o, \frac{L}{A_E}, \theta\right) \quad (9)$$

Equation (9) can only be reduced further through empirical observation. The first observation is that the ratio of specific heats  $\gamma$  for most propellant products is essentially a constant (about 1.2) as is the ratio of specific heats  $\gamma_o$  for air (about 1.4). The other observations, which were also made in Reference 1 for breech blast overpressures, are that the quantities

$V/A_t^{3/2}$  and  $aT/A_t^{1/2}$  are unimportant relative to the importance of the other nondimensional parameters. Figures 14 through 24 which fail to have the chamber volume  $V$  and the duration  $T$  in them present large amounts of data justifying the elimination of  $V/A_t^{3/2}$  and  $aT/A_t^{1/2}$  from the analysis. Using these observations reduces Equation (9) to Equation (10).

$$\frac{I a_o}{P_c^{1/3} P_o^{2/3} A_t^{1/2}} = \phi_1\left(\frac{P_c A_t^{3/2}}{P_o A_E^{3/2}}, \frac{A_E}{A_t}\right) \phi_2\left(\frac{L}{A_E}, \theta\right) \quad (10)$$

The final step is an empirical one. At fixed positions in space, where the  $\phi_2$  function is a constant, the effects of variations in gun chamber properties can be studied by varying either the maximum chamber pressure  $P_c/P_o$  or the

expansion ratio  $A_E/A_t$ . This variation was first performed analytically in a series of finite difference computer runs which eventually lead to the re-

sult that  $\frac{I a_o}{P_c^{1/3} P_o^{2/3} A_t^{1/2}}$  could be divided

by  $\frac{P_c A_t^{3/2}}{P_o A_E^{3/2}}$  to the one-sixth power and



and multiplied by  $A_E/A_t$  to the seven-fourths power to obtain:

$$\frac{I_{a_0}}{\sqrt{P_c P_o A_t}} \left( \frac{A_E}{A_t} \right)^2 = \phi_2 \left( \frac{L}{\sqrt{A_E}} \theta \right) \quad (11)$$

Equation (11) is Equation (4) which was the relationship used to obtain the final functional relationship given in Equation (2).

#### COMPARISON WITH ANALYTICAL COMPUTER RUNS

Early in this program, a one-dimensional, variable cross-section, Lagrangian, shock tube, computer program named GUN-WUNDRY [10] was modified so it could be applied to this breech blast study. GUN-WUNDRY is an artificial viscosity, finite-difference code. Our modifications allowed us to approximate the flow field in the combustion chamber, nozzle, and external environment immediately aft of the breech. A combustion subroutine was added which puts both energy and mass into the combustion chamber flow field from the burning of propellant, and another subroutine was added to automatically rezone the flow field for more efficient running. The burning rate law used in these computations was of the format:

$$r = a + b p^N \quad (12)$$

Table 2 summarizes the results from eight different runs. The side-on specific impulses are all being compared at the exit of the nozzle for different peak chamber pressures and nozzle expansion ratios. The throat area  $A_t$  for all these calculations equals 2.826 in.<sup>2</sup>.

TABLE 2  
Computed Recoilless Rifle Breech Blast Impulses

Run	$\frac{P_c}{P_o}$	$\frac{A_E}{A_t}$	$\frac{I_{a_0}}{o_o A_t^{1/2}}$	$\frac{I_{a_0}}{\sqrt{P_c P_o A_t}} \left( \frac{A_E}{A_t} \right)^2$
1	566	1.8	273	37.1
2	562	1.8	267	36.5
3	593	1.8	270	35.9
4	585	2.1	187	34.1
5	587	2.3	169	37.0
6	1387	4.0	88.1	37.9
7	477	1.8	248	33.8
8	747	1.8	241	28.5
				Avg. 35.1

The quantity  $\frac{I_{a_0}}{\sqrt{P_c P_o A_t}} \left( \frac{A_E}{A_t} \right)^2$  does

vary slightly, but not by much more than 8% from the average 35.1 in the computations. The worst scatter is in run 8 which may be misleading because the expansion angle in the nozzle was only 5 degrees for test 8 alone. The nozzle expansion angle was a more optimum 23 degrees in the other computer runs. The conclusion which we draw from these runs was that the function format given by Equation (11) is adequate. The routine scatter in one's ability to repeat measurements exceeds this error from these much more complex computational efforts.

A similar computational effort was made using this same computer code to determine peak pressures at the exit of various nozzles and to demonstrate the

validity of  $\frac{P}{P_c} \left( \frac{A_E}{A_t} \right)^2$  as a scaling rela-

tionship for pressure. Reference 1 which is the predecessor to this paper contains a table of computed pressures demonstrating the validity of this pressure scaling relationship.

#### CONCLUDING COMMENTS

A solution for recoilless rifle breech blast pressure and impulse both forward and aft of a nozzle has been presented; however, several restricting comments should be made. The first of these comments concerns the actual nozzle exit area as opposed to the effective nozzle exit area. Flow through a divergent nozzle as used on most recoilless rifles can be either under-expanded or over-expanded dependent upon the cone angle. Most nozzle design formulas are based on steady state flow rather than the transient flow conditions which are encountered in the firing of recoilless rifles. This observation means that if the cone angle is too large the flow will be under-expanded and the effective nozzle exit area will be less than the measured nozzle exit area. Conversely, if the cone angle is too small, the flow will be over-expanded and the effective nozzle exit area will be greater than that which would be physically measured. If recoilless rifle pressures and impulses do not agree with this solution, consider the use of another exit area. The same effective exit area should be used with the pressure equations as with the impulse equations as over expansion and under-expansion are physical processes. The SWRI recoilless chamber

impulse and pressure measurements all had an under-expanded nozzle so that  $A_E$  was effectively 1.34 times the actual exit area. Unfortunately, this difference is only a 16% difference in diameter. Because the pressures and impulses scale as the fourth power of diameter, this observation means that large scatter in pressures and impulses can be caused by small changes in nozzle design, atmospheric conditions causing effectively different expansion ratios, and over or under-expanded nozzle design.

Both pressure and impulse contours for recoilless rifles have the expansion ratio  $A_E/A_t$  in the solution. This suggests that the closed breech gun blast solution might be obtained as one limiting case with  $A_E/A_t$  equal to 1.0. Such a manipulation is not acceptable. The closed breech nozzle blast pressure and impulse solutions cannot be generated by using these recoilless solutions with  $A_E/A_t$  equal to 1.0. The solution which has been presented is a curve fit to test results. Outside any limits in  $A_E/A_t$  and  $p_c/p_o$ , the solution is no longer certain. Table 1 should be used for guidance so only interpolations rather than large extrapolations are made when using this solution.

The impulse solution which has been developed results in a series of "fingers" at approximately 15°. These bulges in the contours may be more of a consequence of curve fitting than a representation of reality. Angles such as 0°, 30°, 60°, and 90° have data extending over a large range in scaled distance  $L/\sqrt{A_E}$  than do the intermediate angles such as 15° which have data only over one order-of-magnitude change in scaled distance. The consequences of this observation are that the slopes and ordinates to the log-linear curve fits are not as accurately known at intermediate angles, especially 15°. Although an accurate curve fit is developed close to the nozzle where the data exist, the solution at 15° can become inaccurate at larger standoff distances where the solution is extrapolated to meet the larger standoffs measured at 0°. Any bulges in impulse contours begin when the standoff distances are beyond the standoffs for measured 15° impulse data.

Outside any limits in  $L$  or  $I$ , the pressure and impulse solutions have not been verified and should be used with caution. Note that in Figures 1 and 2 these regions are indicated by broken lines. At extremely large standoff distances our log-linear curve fits cannot possibly apply. All of the solutions

for various angles intersect with one another if one goes far enough away from the breech. This is a consequence of log-linear curve fits to data with scatter. In general, the slope of the curves should decrease with distance until in the far field all of the lines would have the same slope for acoustic or "low pressures". This behavior is not represented in these curve fits, and means that any extrapolation beyond points of intersection have to be incorrect.

For extremely small values of  $L$  or  $I$ , the solutions for both pressure and impulse appear to be conservative. There are several indications in Figures 3 through 24 at some relatively low-scaled standoff,  $L$  or  $I$ , a maximum pressure or impulse occurs; and that the scaled distance at which this occurs is dependent on  $\theta$ . This same effect has been reported for blast fields around vented cubicles [11] and for shock wave patterns in aircraft revetments [12]. In each of these cases the effect was attributed to the development of a highly-turbulent vortex at the free edges which distorts the shock front enough to substantially decrease the peak positive pressure and impulse close to the "wall". Although tests have not yet been conducted to verify this observation for recoilless weapons, it is reasonable to assume that the same mechanism applies.

In closing we would note that an empirical solution has been presented for predicting breech blast pressures and impulses around recoilless rifles. A variety of weapon data at varying angles radiating away from the breech demonstrate that the scaling is valid for a wide variety of recoilless rifles. The major interior ballistic characteristics influencing the breech blast appear to be the peak chamber pressure, the shape of the chamber pressure history, the throat area of the nozzle, and the exit area of the nozzle. Outside the weapon, the spatial distribution of the pressure field and impulse fields depends upon the type of nozzle, the effective exit area of the nozzle, and one's position in space relative to the breech.

Probably this solution is more accurate aft of the breech than forward of the nozzle. Any actual gun system will have a muzzle blast as well as a breech blast which at significant distances forward of the breech will result in an interaction of the blast waves from the two sources. This solution is limited as it does not include the results of recoilless rifle muzzle blast.

# ACKNOWLEDGEMENTS

This program has been a three-year study sponsored by the U.S. Army Research Office in Research Triangle Park, North Carolina under ARO Project No. P-13984-E. Their technical monitor was Mr. James J. Murray whose support is greatly appreciated.

Various Southwest Research Institute personnel assisted in this study. Mr. Randall Ricker made the finite difference computer computations. Mr. Patrick Zabel designed and had fabricated the propellant test chamber which was used to obtain large amounts of data. Mr. Marvin Burgamy, Mr. Richard Hoffman, Mr. Ernest Garcia, and Mr. Richard Cervantes conducted all SWRI experimental gun firing tests. Mr. Victor Hernandez drew all figures in this report, and either Mrs. Newman or Mrs. Carroll typed this paper and all reports. The assistance of these individuals and that of those who are always inadvertently overlooked is greatly appreciated.

# REFERENCES

- [1] Westine, P.S., Ricker, R.E., "Empirical Procedures for Estimating Recoilless Rifle Breech Blast Overpressures," 49th Shock and Vibrations Symposium, Huntsville, AL, October 1978.
- [2] "Ballistic Analysis of Blast Pressure Results for 57mm Recoilless Rifle T66E6," Analytical Laboratory Report 55-B-67, January 10, 1956.
- [3] "Ballistic Analysis of Blast Results for 90mm Recoilless Rifle, T219 (PAT)," Analytical Laboratory Report 56-B-120, October 18, 1956.
- [4] Zimmerman, U.R., Vecchio, R.A., "Back Elast Determination of a 105mm Recoilless Rifle for an Aerial Artillery Weapon System," Picatinny Arsenal Technical Report 3420, August 1966.
- [5] "Firing Record No. M-46345," Project No. 6001 (428-M5-245), Ordnance Research and Development Center, Aberdeen Proving Ground, MD, August 10, 1945.
- [6] "Investigation of the Effect of Blast from Recoilless Rifles," Armor Research Foundation, Contract No. DA-11-022-ORD-1227, for Frankfort Arsenal, June 30, 1954.
- [7] "Engineer Design Test of Sound Pressure Level Measurement of Rockets and Recoilless Rifles," Firing Record No. P-74650, USATECOM Project No. 8-7-2320-02, Aberdeen Proving Ground, MD, August 1967.
- [8] Baker, W.E., Westine, P.S., Bessey, R.L., "Blast Field About Rockets and Recoilless Rifles," Southwest Research Institute, Contract No. DAAD05-70-C-0120 for Ballistic Research Laboratories, May 1971.
- [9] "Peak Pressures for Breech and Muzzle Blast Measurements 106mm Rifle, T170E1 Mount, 106mm, T149E3," Analytical Section, A&A Division, Development and Proof Services, August 14, 1953 (No Report Number).
- [10] Piacesi, R., Gates, D.F., Seigel, A.E., "Computer Analysis of Two-Stage Hypervelocity Model Launchers," Proceedings of Sixth Symposium on Hypervelocity Impact, pages 157-174, August 1963.
- [11] Keenan, W.A., Tancreto, J.E., "Blast Environment from Fully and Partially-Vented Explosions in Cubicles," Civil Engineering Laboratory, Naval Construction Battalion Center, for Picatinny Arsenal, Technical Report 828, November 1975.
- [12] Teel, G., Coulter, G., "A Study of Flow Patterns in Aircraft Revetments," Ballistics Research Laboratory, BRL Memorandum Report No. 1536, Aberdeen, MD, February 1964.

DISCUSSION

Voice: I was interested in your normalized pressure relationship. Was the normalizing coefficient "M" obtained directly from pressure data?

Mr. Westine: Yes, but there are some calculated data that I could supplement that with.

Voice: Is it subject to the rate of pressure build up?

Mr. Westine: I don't think it is as subject to the rate of the build-up as it is to the time history. A conventional pressure-time history in the chamber will give you a peak and it decays. But there have been some fresh weapons. Now if you just put M of 1 you are describing that character pretty well and that's fine. But suppose you want to reduce the breech blast, and one of the ways of doing that is to tailor the shape; that is keep the same impulse imparted to the projectile but try to make it a rectangular pressure pulse. Then you have tailored the burning of the propellant so that you have a pressure time history that is very rectangular. And that was largely an empirical effort but you will find that you can divide the average pressure by the peak pressure and get a pretty good guess for the magnitude of M.

PREDICTING THE MOTION OF FLYER PLATES DRIVEN BY  
LIGHT-INITIATED EXPLOSIVE FOR  
IMPULSE LOADING EXPERIMENTS \*

R. A. Benham  
Explosives Testing Division 1533  
Sandia Laboratories  
Albuquerque, New Mexico 87185

(U) The light-initiated high explosive, Silver Acetylide-Silver Nitrate, has been used to simulate x-ray blowoff impulse loading on recovery vehicles in order to excite structural response. High velocity thin flyer plates have been used in other experimental techniques to deliver impulsive loads through a tailored pressure pulse. These methods excite both structural and material response. This paper explores the possibility of using light-initiated high explosive to accelerate thin flyer plates to high velocities for impulse loading which may produce both material and structural response. A simplified model of the explosive multipoint detonation and expansion process is developed which leads to a calculation of the motion of the flyer plate. Comparisons between calculations and measurements from experiments indicate that the simplified model is sufficient for flyer motion predictions. Impulse experiments using light-initiated explosive to produce both material and structural response can now be designed.

\* This work was supported by the United States Department of Energy (DoE).

## INTRODUCTION

(U) The light-initiated high explosive, Silver Acetylide-Silver Nitrate, has been used to simulate x-ray blowoff impulse loading on reentry vehicles [1-3] in order to excite structural response. In this method, a nearly simultaneous impulse loading is achieved by spraying a contoured coating of explosive directly on the structure's surface and then creating a surface detonation by exposure to an intense flash of light.

(U) Currently, the pressure delivered to the structure's surface is set by the explosive detonation and gas expansion process and there has been little attempt in the past to tailor the pressure loading. In order to study material response, as well as structural response on such an impulse test, the pressure pulse shape must be controlled. A conventional method of pressure pulse shaping for simulated nuclear environments is to accelerate a flyer plate to a high velocity which then impacts the test surface delivering the impulse load. [4,5] The flyer plate material and impact velocity, along with the target material, will determine the impulse and pressure pulse shape delivered to the impacted surface. W. E. Baker [6] conducted a series of tests in 1971 which proved the feasibility of using light-initiated explosive to accelerate flyer plates for impulse testing. In his paper, it was shown that: (1) flyer plates could be accelerated in a condition flat enough to have an impact simultaneity of  $< 2 \mu s$ ; (2) that curved surfaces could be loaded; and (3) that the pressure time data could be recorded.

(U) A flyer plate system which will deliver a contoured, simultaneously applied impulsive load to a curved surface requires that the transit time from the flyer's initial position to impact be the same at every location. It is necessary, therefore, to be able to calculate the local motion of the flyer plate up to the time of impact.

(U) It is the purpose of this paper to summarize the development of a simplified model of the explosive multi-point detonation and expansion process, which will make possible calculation of the force applied to a flyer plate and, therefore, calculation of the motion of the plate. The paper then summarizes an experimental technique of monitoring the flyer plate acceleration up to terminal velocity using a fast-responding fibre optics transducer system. Comparisons between the calculations and measurements of the motion

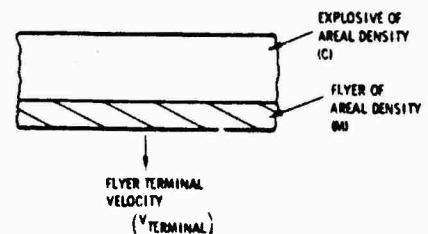
are presented. The agreement seen in the comparisons indicates that the simplified model is sufficient for motion calculations. Impulse experiments using light-initiated explosive to produce both material and structural response may now be designed using this method.

## MODEL DEVELOPMENT

(U) The simplified model of the flyer plate acceleration process evolves in two parts. The first part develops a method of calculating only the terminal velocity of an explosive flyer plate system. The result, verified by experiment, can be used to determine the range of usefulness of this technique for producing the required pressure loading. The second part considers the details of the detonation process and is used to calculate the motion of the flyer plate during the acceleration phase.

### DEVELOPMENT - PART 1

(U) The first part of the study was to verify that thin aluminum flyer plates could be propelled to a precalculated terminal velocity while retaining appropriate planarity and angular orientation. The model of interest is shown in Fig. 1.



LATERAL DIMENSIONS ARE LARGE COMPARED TO THICKNESS DIMENSIONS

Fig 1 - Explosive-Flyer Model

(U) The terminal velocity of this ideal, one-dimensional configuration may be calculated using the Gurney [7] approximation for an open-faced sandwich.

(U) This well-known relation is:

$$V_{\text{terminal}} = V_{\text{TE}} \left[ \frac{\left(1 + 2 \frac{M}{C}\right)^3 + 1}{6 \left(1 + \frac{M}{C}\right)} + \frac{M}{C} \right]^{-1/2} \quad (1)$$

The  $\sqrt{2E}$  is the "Gurney Velocity" and is related to the explosive's ability to propel material.  $M$  and  $C$  are the areal densities of the flyer and the explosive, respectively. The Gurney velocity can be determined from available experimental explosive performance information in the following manner.

(U) If the explosive is placed on a large mass so  $M/C \gg 1$ , then Eq. (1) reduces to:

$$V_{\text{terminal}} = \sqrt{2E} \left[ \sqrt{\frac{4}{3}} \frac{M}{C} \right]^{-1} \quad (2)$$

By recognizing that the specific impulse delivered to the mass  $M$  is the product  $MV_{\text{terminal}}$ , then  $\sqrt{2E}$  can be expressed as a function of the explosive areal density. Equation 3 is the resulting relation for Gurney velocity:

$$\begin{aligned} \sqrt{2E} &= \frac{1}{C} \sqrt{\frac{4}{3}} (MV_{\text{terminal}}) \\ &= \frac{1}{C} \sqrt{\frac{4}{3}} I_{\text{rigid wall}} \end{aligned} \quad (3)$$

$I_{\text{rigid wall}}$  is the specific impulse that would be delivered to a rigid wall and is a measurable quantity for any particular explosive. With the Gurney velocity as a function of areal density, it is possible to utilize Eq. (1) and calculate terminal velocities for various system configurations. This, in turn, can be used to determine if peak ideal impact pressures can be obtained.

(U) Figure 2 is the explosive impulse calibration curve for the light-initiated explosive of interest. The Gurney velocity for this particular explosive is shown in Fig. 3. Figure 4 shows terminal velocities calculated using the Gurney theory and data of Fig. 3 for various flyer plate areal densities. The calculations were made using an explosive areal density of  $.060 \text{ gm/cm}^2$ .

(U) Flyer velocity and areal density combinations under the curve may be selected to give the desired combination of impulse and peak pressure delivered to a particular target material.

\*Most of the calibration data presently available for this technique is for explosive areal densities less than  $.060 \text{ gm/cm}^2$ .

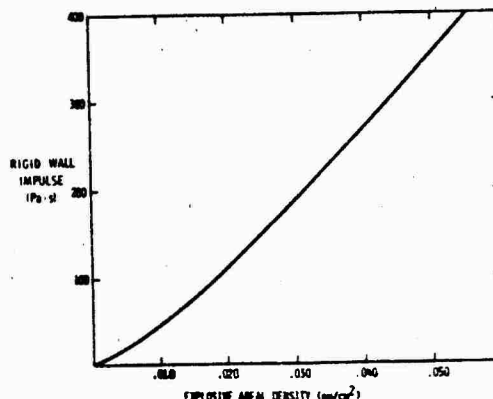


Fig 2 - Light-Initiated Explosive Calibration Curve

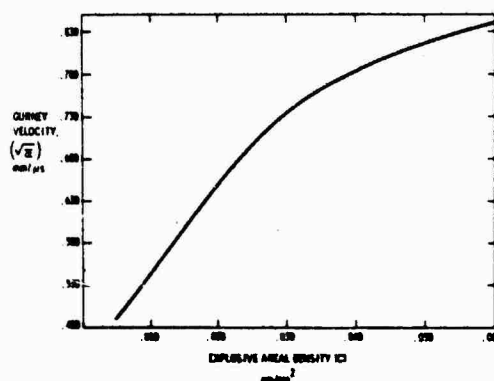


Fig 3 - Gurney Velocity for Light-Initiated Explosive

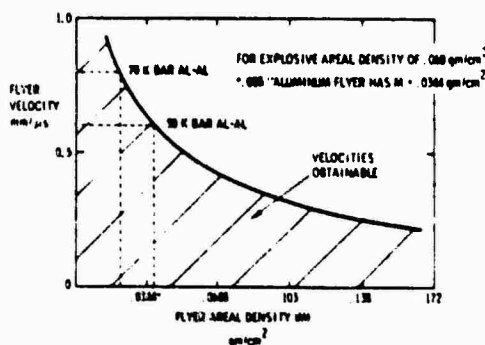


Fig 4 - Calculated Flyer Plate Velocity Versus Flyer Plate Areal Density

Pressures of several tens of Kbar can be obtained in heat shield materials of interest. For reference, the results of an aluminum flyer striking an aluminum target are shown. These pressures are of approximate magnitude for material response experiments.

(U) An experiment was set up in which a uniform layer of explosive was deposited on a thin aluminum flyer plate. The explosive was surface-initiated and three flash x-ray exposures were made as the flyer traveled through a small gap. As can be seen in Fig. 5, the flyer plate remained flat

except for edge effects. The measured terminal velocity was within 10 percent of the calculated value. Figure 6 shows the tabulated results from a series of these tests. The details of these experiments are reported elsewhere[8].

(U) It can be concluded from these experiments that:

1. Thin flyer plates of aluminum could be accelerated to terminal velocity while retaining the required planarity and angular orientation.

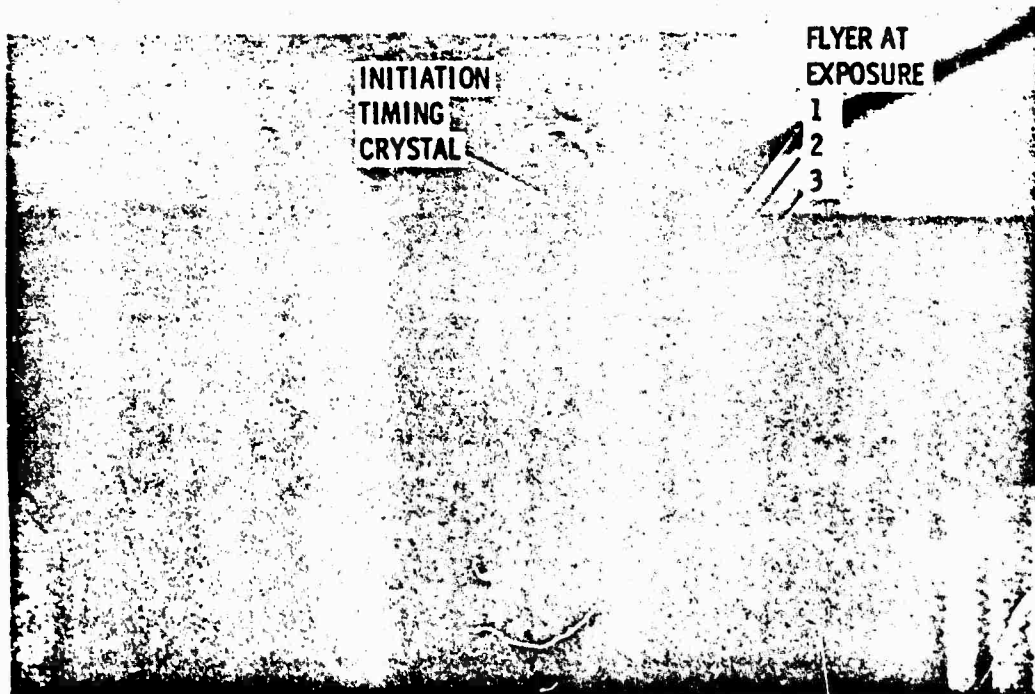


Fig 5 - Flash X-Ray Data from Light-Initiated, Explosively Driven Flyer Plate



Test	Explosive Areal Density gm/cm <sup>2</sup> (C)	Effective Flyer Thickness cm	Flyer Areal Density gm/cm <sup>2</sup> (M)	Gurney Predicted Velocity m/μe	Measured Velocity m/μe		Flatness	V <sub>meas. v.c.</sub> V <sub>predicted</sub>
					Displ. Gage Slope	X-ray Velocity (V <sub>12</sub> )		
1	.0217±.05	.0360	.099	.11140	[1]	.12100	No measurable wrinkle or tilt in first .5 cm	1.086
2	.0225±.05	.0370	.1019	.11372	.11999	.11965	"	1.051
3	.0225±.05	.0373	.1012	.11440	[1]	.11728	"	1.025
[3]	.0226±.05	.0368	.100	.10386	[2]	.11293	"	1.087

[1] Initial slope difficult to measure because the explosive initiated during electrical "blackout" time from light source capacitor discharge

[2] No displacement gages used

[3] Conducted to observe flyer after impact with the surface

Fig 6 - Flyer Plate Experimental Results

- The Gurney method of predicting final velocity is adequate.
- Pressures of interest (calculated) in material response experiments can be obtained.

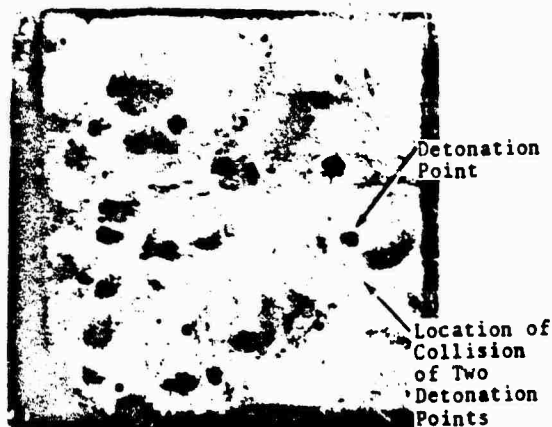
## DEVELOPMENT - PART 2

(U) In designing a simultaneously applied impulse load over a structural surface, it is also necessary to know the total transit time of the flyer plate through a gap. Hence, the nature of the acceleration phase of the flyer plate must be understood.

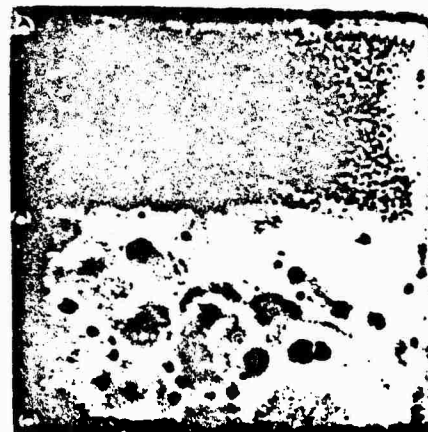
(U) Based on physical measurements and observations of the explosive initiation process, a simple model has been developed. The most important experimental observation was that of the detonation pattern left on the metal surface where the explosive was initiated. The observation of detonation patterns and use for estimating explosive initiation simultaneity was first observed several years ago by W. E. Baker[9]. With low-initiation light level, only a few initiation points occurred, as in Fig. 7A. As the light level increases, the density of initiated points increase, Figs. 7B through 7D. It can also be seen that the initiation starts at a point and then propagates radially outward until

intersecting the wave from an adjacent initiation.

(U) Figure 8 shows a sketch of the important factors involved in the process of the detonation and gas expansion. The details of the calculations are contained in another document[10]. The explosive is assumed to initiate at many points equally spaced over the exposed surface. A spherical detonation wave expands through the explosive and pressure is locally applied as the wave intersects the target surface. The magnitude of pressure is calculated by assuming the explosive products have expanded into the detonated explosive's initial volume plus the volume of a cone above the explosive made by the escaping gases. The velocity of escaping gases is estimated from a Gurney approximation[7]. The pressure is averaged over the surface as the process continues. The average pressure increases until adjacent detonation waves intersect and extinguish. The pressure then decreases until all of the explosive is consumed. (After the explosive has all detonated, the gas expands ideally.) The bottom of Fig. 8 shows the shape of the average pressure pulse on a flyer plate as calculated using this model of explosive behavior. The pressure load applied to the flyer plate can be used to determine the displacement



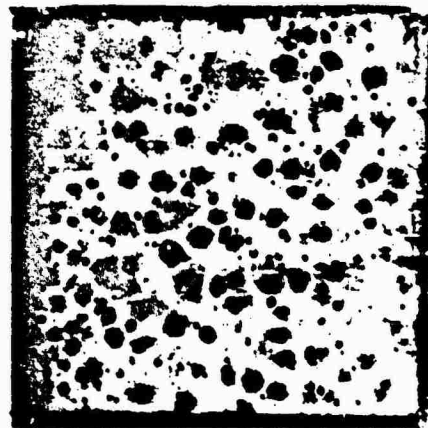
A. LOW INITIATING LIGHT LEVEL



C. TOP SIMILAR TO B  
BOTTOM SIMILAR TO D



B. HIGH INITIATING LIGHT LEVEL



D. INTERMEDIATE INITIATING LIGHT LEVEL

Fig 7 - Explosive Detonation Patterns

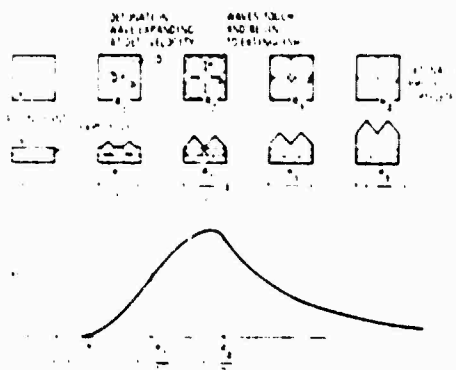


Fig 8 - Detonation and Gas Expansion Model

history of the plate during the acceleration phase.

(U) An experiment was devised to measure the displacement history of a flyer plate using a fibre optic[11,12] system\* to sense motion even in the high noise environment caused by the capacitor bank discharge light source. Figure 9 shows a sketch of the experimental setup. The flyer plate was very

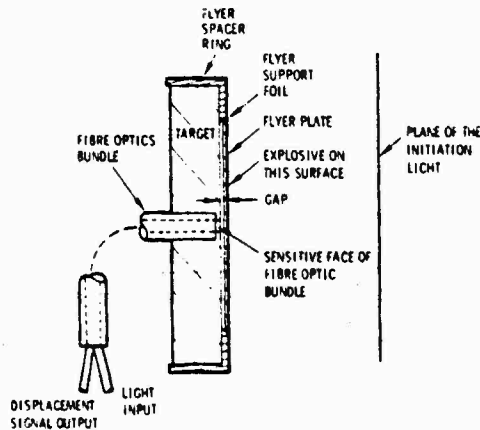


Fig 9 - Flyer Motion Measurement Experiment

precisely positioned away from the target surface. A uniform layer of explosive was sprayed onto the face of the flyer and detonated. The flyer plate moved through the gap with the fibre optics transducer sensing the motion. The details of the system, as well as the data reduction techniques for the fibre optic displacement transducer, are described in another report[10].

(U) Figure 10 shows the calculated motion compared to the measured motion. The calculated terminal velocity using this method was the same as measured and calculated in Part 1 of the development. The agreement is seen to be quite good considering that the approach is very simple and based upon phenomenon that have not yet been verified.

The fibre optic system was designed so that light was transmitted through half of the fibres in the bundle and then was reflected from the flyer surface back to the other half of the fibres. The amount of received light is related to the gap between the flyer reflective surface and the bundle and.

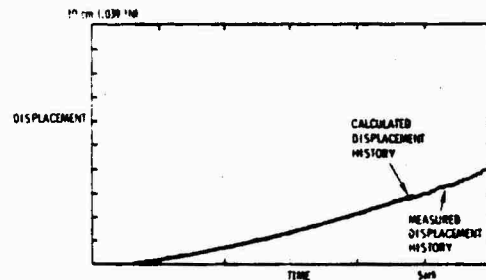


Fig 10 - Comparison of Predicted and Measured Flyer Plate Motion

## CONCLUSIONS

(U) This work is far from complete, but it does provide a foundation on which to build impulse tests where both structural and material response are important. The process of relating a flyer plate of known mass and velocity to a pressure delivered to a target has been much documented and the problems, such as flyer wrinkling and the air cushion[4,5] effect, are recognized but not addressed here.

(U) The basic work required for understanding the process of using light-initiated high explosive for driving flyer plates has been developed and no serious problem areas have been discovered. The analytical tools required to design a simultaneously applied flyer plate impulse load to a structure are now available.

## ACKNOWLEDGEMENTS

(U) The author would like to thank Dave Shirey, Ben Duggins, Phil Higgins, and Louis Parra for producing the experimental data and to Anna Maria Carroll for preparing the report.

## REFERENCES

1. R. A. Benham and F. H. Mathews, "X-Ray Simulation with Light-Initiated Explosive," the Shock and Vibration Bulletin No. 45, Part 4, June 1975.
2. R. A. Benham, "Simulation of X-Ray Blowoff Impulse Loading on a Reentry Vehicle Aft End Using Light-Initiated High Explosive," the Shock and Vibration Bulletin No. 46, Part 3, August 1976.
3. R. A. Benham, F. H. Mathews, and P. B. Higgins, "Application of Light-Initiated Explosive for Simulating X-Ray Blowoff Impulse Effects on a Full-Scale Reentry Vehicle," the Shock and Vibration Bulletin No. 47 Supplement, September 1977.
4. J. Z. Farber, G. W. Seman, and T. Ciolkosz, Magnetic Flyer Combined Response Testing of Composite Specimens, Air Force Weapons Laboratory Technical Report No. AFWL-TR-69-18, December 1969.
5. M. R. Birnbaum, L. M. Murphy, and D. L. Wesenberg, Flyer Target Impact Interaction for Dissimilar Materials, Sandia Laboratories Report No. SCL-DR-72-0032, July 1972.
6. W. E. Baker, W. G. Martin, and E. W. Spacek, Jr., The Use of Light-Initiated Spray Explosive to Accelerate Flyer Plates, Air Force Weapons Laboratory Technical Report No. AFWL-TR-70-114, March 1971.
7. J. E. Kennedy, "Explosive Output for Driving Metal," Proceedings of the 12th Annual Symposium ASME and University of New Mexico, Behavior and Utilization of Explosives in Engineering Design, March 1972.
8. R. A. Benham, Preliminary Experiments Using Light-Initiated High Explosive for Driving Thin Flyer Plates, Sandia Laboratories Report No. SAND79-1847, February 1980.
9. F. O. Hoese, C. G. Langer, and W. E. Baker, "Simultaneous Initiation Over Large Areas of a Spray-Deposited Explosive," Experimental Mechanics Vol. 8, No. 9, pp 392-97, September 1968.
10. R. A. Benham, An Initiation and Gas Expansion Model for the Light-Initiated Explosive Silver Acetylide-Silver Nitrate, Sandia Laboratories Report No. SAND79-1829, February 1980.
11. Vern Barr, Sandia Laboratories/Livermore, private communications.
12. C. Mensdier, C. Kissinger, and H. Adkins, "The Futonic Sensor," Instruments Division, Mechanical Technology, Inc.; Bulletin No. 02-100, 1975.

## Fragments

### SCALING OF INITIATION OF EXPLOSIVES BY FRAGMENT IMPACT

W. E. Baker, M. G. Whitney, V. B. Parr

Southwest Research Institute  
San Antonio, Texas

An important explosives safety problem is the propagation of accidental explosions in manufacturing or storage facilities by high-speed fragment impact on bare or cased explosives from detonation of one fragmenting shell or warhead. Many experiments have been run to determine the severity of this problem, and to determine safe separation distances.

Almost all past testing has been strictly empirical. High-speed simulated fragments are launched by gun or explosive projection to impact on bare or cased explosive "receptors," and violence of reaction is recorded. Although much of this work is carefully done and reported, data fitting and prediction methods have been almost totally empirical, and specific for given fragment and receptor characteristics.

This paper reports a similitude analysis of the title problem, scaling of test results from the literature, and a careful survey of the scaled results. Correlations are made of the scaled results from various investigators, and implications drawn regarding the physics of the initiation processes for fragment impacts on bare and cased explosives. Scaled prediction curves are given, with error bands.

#### INTRODUCTION

Most severe explosions occur in munitions in storage or transport, or in magazines or ready-storage racks in combat, because high-velocity fragments from the detonation of a single warhead impact other munitions and cause a chain reaction or "mass detonation" of most of the energetic materials in their munitions. Rather than dwell on the numerous case histories of such events, we, instead, plan to review here the controlled experiments which have been conducted to quantify the phenomena occurring in initiation of solid explosives by penetrating fragment impact, and to sort out and correlate some of the possible initiating mechanisms via a similitude analysis of this complex problem.

#### BACKGROUND

In attempting to quantify effects

of fragment initiation of the solid explosives and propellants which include the bulk of energetic materials in munitions, all past experiments have had to considerably simplify the problem. They have done the following:

1. Employ fragment simulators which are regular solids, either cylinders or rectangular parallelepipeds, rather than irregular chunks;
2. Launch the fragment simulators with a flat face forward;
3. Impact the explosive "receptor" normal to one of its surfaces;
4. Use gun launch and explosive projection as the two methods to project fragments with controlled velocity in a controlled direction; or
5. Conduct few tests on solid propellants, compared to tests on explosives.

They determine the reaction of the explosive to the impact in various ways, and describe the reaction by such terms as "no reaction," "burn reaction," "violent reaction," "deflagration," or "detonation." For any given fragment simulator and explosive receptor configuration, tests were conducted by varying the impact velocity, and recording the explosive reaction. Fortunately, the increments in impact velocities in these tests to go from "no reaction" to either "violent reaction" or "detonation" are small enough once some threshold velocity is reached, that a critical velocity for initiation by fragment impact can be determined more or less independently of the methods used to determine explosive reaction.

We limit our review of fragment initiation work to those studies which present enough data reported in enough detail to allow scaling and inclusion in our scaled data comparisons, and to those which give good discussions of the physics of possible initiation processes. We also include no discussion of classified work.

One of the first comprehensive studies was that of Slade and Dewey[1]. They conducted an extensive series of gun-launched firings of steel and brass cylindrical, flat-faced projectiles against bare Tetryl and Composition B explosive discs, and Tetryl discs covered with a thin steel cover plate on the impacted side. They determined values for impact velocities having 50% probability of causing detonation ( $V_{50}$ ) using the statistical methods of Golub and Grubbs [2]. They noted that kinetic energy per se had no direct effect on initiation, but that impact velocity and type of explosive were the principal determinants for initiation. Unfortunately, because they decided early in the program that projectile mass, mass per unit area, or kinetic energy were not important parameters, they did not always report these quantities, so we cannot scale all of their data. A number of the projectiles fired by Slade and Dewey[1] were in the shape of stepped cylinders, with sub-caliber méplats\* machined on the impacting surface.

Reeves[3] conducted a series of gun-launched firings using cylindrical steel projectiles, primarily with a length-to-diameter ratio of one, against explosive-loaded artillery projectiles. All of the projectiles in the series

with adequate data for scaling were filled with cast Composition B explosive. Reeves[3] used a modified form of the statistical methods of Golub and Grubbs [2] to determine  $V_{50}$  values for each set of firings. He also fired against inert-loaded projectiles to determine  $V_{50}$  values for perforation of the projectile walls, and noted that these values correlated well with  $V_{50}$  values for initiation of violent reactions in the Composition B explosive. Reeves' data are supplemented by similar tests conducted quite recently at Socorro, New Mexico under contract to BRL[4]. This report gives data only, with no statistical estimates of  $V_{50}$  values. Some of these tests were designed to determine thresholds of reaction, rather than detonation.

Quite recently, Frey, et al[5], reported several series of tests of gun-launched steel cylinders against steel plate covered and lightly confined cylinders of Octol and Composition B. Test data are given in their report, but no  $V_{50}$  values are reported. This excellent report also gives the best physical insight into possible fragment impact initiation processes we have found, and the results of many more tests of spherical projectiles against explosive receptors. We do not include these latter test results in our data analysis because the impact geometry differs too greatly from the flat-face impact common to all the other tests.

Explosive projection, using plastic attenuators between a donor charge and rectangular parallelepiped fragment simulator breakup, has been used in several studies to determine steel fragment impact initiation of bare solid and molten explosives, and lightly-confined explosives with cover plates. The first series of such tests is reported by McLean and Allen[6], and includes impacts on bare and covered Pentolite and Cyclotol. Only the bare explosive tests in this series are complete enough for our use. Petino, et al[7], in the second test series, tested the fragment initiation of solid and molten Composition B with steel cover plates and very light confinement. The third report, by Petino and Leondi[8], gives data for initiation of bare and covered molten and solid Amatex charges. None of these three reports obtain  $V_{50}$  values for initiation by statistical methods, but instead rely on graphical plots and curves which separate data points into detonation and no-detonation regimes. These authors state that momentum-per-unit impact area seems to correlate with initiation for each casing thickness.

\* The term "méplat" is used in ballistics to describe a blunt nose of a projectile.

References 1, 3, 4, 5, 6, 7 and 8 form the data base for our analysis. Only data for flat-faced fragment simulators impacting bare or cased solid explosives are used.

Explosive initiation tests by metal impacts which do not simulate penetrating fragment impacts are also common practice. In the most widely used such test, thin metal flyer plates of the same frontal area as flat-faced specimens of bare explosive are accelerated by plane-wave explosive lenses or light-gas guns and impacted into the explosive slabs, applying high-pressure, short duration square pressure pulses to a surface of the explosive. From these data, the parameter

$$E_c = \frac{P^2(\Delta t)}{\rho_0 V_s}, \quad (1)$$

called critical energy (but really an energy-per-unit area) has been shown to correlate with initiation of detonation. In this equation,  $P$  is impact pressure,  $\Delta t$  is pressure duration,  $\rho_0$  is initial explosive density, and  $V_s$  is shock front velocity in the explosive. Because  $\rho_0$  and  $V_s$  are constants for a given explosive, the reduced quantity  $P^2(\Delta t)$  is often used in place of  $E_c$  (see Howe and Frey[9]).

Howe and Frey[9] use physical reason and scaling to conclude that a good criterion for initiation of well-confined explosives by fragment impact is impulse (momentum) per unit area divided by casing thickness. They use data from References 3 and 4 to support their conclusion.

A number of empirical equations for predicting fragment initiation appear in the literature. Frey, et al[5], give a good description of several and note their limitations. We report none of them here because most will only fit one particular set of data. The physical parameters associated by some authors with initiation have already been mentioned or will be mentioned.

#### MODEL ANALYSIS

A large number of physical and geometric parameters can conceivably be important in initiation of violent reactions of fragment-impacted explosives, solid propellants or munitions containing these energetic materials. These parameters describe the projectile, the impact conditions, and the cased explosive or propellant target.

We first list the pertinent parameters and the physical dimensions of each parameter in a Force-Length-Time (FLT) system. This list is given in Table 1. Then, using methods of dimensional analysis[10], the parameters can be combined in a set of dimensionless groups, or pi terms which must remain invariant if the physics of the problem are to remain unaltered. In this instance, the 18 dimensional parameters yield a set of 18-3 or 15 pi terms, which are given in Table 2.

TABLE 1  
Physical Parameters for Explosive Initiation by Fragments

Parameter	Symbol	Dimension
<u>Projectile</u>		
Mass	$M_p$	$FT^2/L$
Material Density	$\rho_p$	$FT^2/L^4$
Material Sound Velocity	$a_p$	$L/T$
Impacting Cross-Section Area	$A$	$L^2$
Length	$L$	$L$
Geometry	$t_{ip}$	—
Material Strength	$\sigma_p$	$F/L^2$
<u>Impact</u>		
Initiation Velocity	$V_{50}$	$L/T$
Kinetic Energy	$E$	$FL$
Momentum	$I$	$FT$
Obliquity	$\theta$	—
<u>Casing</u>		
Thickness	$h$	$L$
Density	$\rho_c$	$FT^2/L^4$
Strength	$\sigma_c$	$F/L^2$
Geometry	$t_{ic}$	—
<u>Explosive</u>		
Density	$\rho_e$	$FT^2/L^4$
Sound Velocity	$a_e$	$L/T$
Slope of Hugoniot	$S_e$	—

Let us compare these dimensionless groups with the initiation criteria proposed by various investigators, and perhaps some new criteria. This is done in Table 3, which gives some criteria discussed previously, their dimensions, and the pi terms which should or may correlate with each criterion. We concentrate in this table on projectile, impact and cover plate or casing thickness rather than on explosive or propellant properties,

TABLE 2

Pi Terms for Explosive Initiation  
by Fragments

Symbol	Term	Description
$\bar{M}_p$	$(M_p/\rho_p A^{3/2})$	Scaled Projectile Description
$\bar{L}$	$(L/A^{1/2})$	
$t_{ip}$	$t_{ip}$	
$\bar{\sigma}_p$	$(\sigma_p/\rho_p a_p^2)$	
$\bar{V}$	$(V/a_p)$	Scaled Impact Parameters
$\bar{E} = \bar{M}_p \bar{V}^2/2$	$(E/\rho_p a_p^2 A^{3/2})$	
$\bar{I} = \bar{M}_p \bar{V}$	$(I/\rho_p a_p A^{3/2})$	
$\theta$	$\theta$	
$\bar{h}$	$(h/A^{1/2})$	Scaled Casing Parameters
$\bar{\rho}_c$	$(\rho_c/\rho_p)$	
$\bar{\sigma}_c$	$(\sigma_c/\rho_p a_p^2)$	
$t_{it}$	$t_{it}$	
$\bar{\rho}_e$	$(\rho_e/\rho_p)$	Scaled Explosive Properties
$\bar{a}_e$	$(a_e/a_p)$	
$S_e$	$S_e$	

because most testing series have been done for specific explosives, with other parameters varied. What normally is done is to vary impact velocity  $V$  until a range of explosive reactions is obtained, and determine the limit velocity for the particular fragment type and explosive target. Also, by far the most testing has been done with simulated steel fragment: impacting, bare, steel-cased, or steel-covered high explosives, so there have been minimal or no variations in  $\bar{\rho}_p$ ,  $\bar{\sigma}_p$ ,  $\bar{\sigma}_c$ , or  $\bar{\rho}_c$ .

In the next section, we will compare scaled data from the literature with several pi terms or combinations of pi terms from Table 2, and will try to ascertain which initiation criteria apply in various impact situations.

## DATA ANALYSIS

To compare data from various investigators, we must not only scale (make dimensionless) the data, but must also reduce all raw data in the same manner. We can perform these operations in either order; we choose to first apply statistical methods to the raw data to obtain values for  $V_{50}$  on a consistent basis.

The method used to estimate the parameters from the raw data was developed by Golub and Grubbs[2]. This method allows the computation of the ballistic limit velocity,  $V_{50}$ , the standard deviation, and the variance and covariance of the estimate when there is a zone of mixed results. A zone of mixed results exists[11] when the highest velocity, called BIGA at which the projectile is defeated by the target (in our case, no reaction) is greater than the lowest velocity, called SMALL, at which the target is defeated (reaction). When no mixed zone exists, only the  $V_{50}$  and standard deviation parameters can be estimated.

The method is based on the assumption of the Normal Distribution of the critical velocities, where

$P_i = \int_{-\infty}^{t_i} (1/\sqrt{2\pi}) \exp(-t^2/2) dt$  is the probability of a complete penetration (or reaction) at the velocity,  $V_i$ , and  $t_i = \frac{V_i - u}{\sigma}$  is the deviation in velocity from  $V_{50}$  expressed in standard units, and  $u$  and  $\sigma$  are the unknown mean and standard deviation in velocity to be estimated.

The maximum likelihood equations are:

$$\frac{\partial L}{\partial u} = \frac{1}{\sigma} \left[ \sum_{j=1}^m \frac{z_j}{q_j} - \sum_{i=1}^n \frac{z_i}{P_i} \right] = 0 \quad (2)$$

$$\frac{\partial L}{\partial \sigma} = \frac{1}{\sigma} \left[ \sum_{j=1}^m \frac{t_j z_j}{q_j} - \sum_{i=1}^n \frac{t_i z_i}{P_i} \right] = 0 \quad (3)$$

where:  $n$  = number of penetrations (reactions),

$m$  = number of no penetrations (no reactions),

$z_j$  = ordinate of normal distribution at  $t_j$ ,

$$q_j = \int_{t_j}^{\infty} (1/\sqrt{2\pi}) \exp(-t^2/2) dt,$$



TABLE 3  
Possible Criteria for Detonation or Violent Chemical  
Reaction Under Impact

No.	Initiation Criterion	Dimensions	Related Pi Term Or Terms	Remarks
1	$E_c = \frac{p^2 \Delta t}{\rho_0 U_s}$	F/L	$\bar{E}, t_{ip}$	Criteria for flyer plate initiation tests
2	$p^2 \Delta t$	$FT^2/L^4$	$\bar{E}, t_{ip}$	Reduced form relating to flyer plate initiation tests
3	$\frac{I_c = M_p V_{50}}{Ah}$	$FT^2/L^3$	$(\bar{I}/\bar{h}) = (I/\rho_p a_p Ah), \bar{L}, t_{ip}$	Proposed for fragment impact on cased explosives and propellants
4	$I/A = M_p V_{50}/A$	$FT/L^2$	$\bar{I}, \bar{h}, \bar{L}, t_{ip}$	Proposed for fragment impact on cased explosives; different values for different case thickness
5	$V_{50}^2 A^{1/2}$	$L^3/T^2$	$\bar{V}_{50}, t_{ip}$	Physical basis unknown
6	$E/A = M V_{50}^2/2A$	F/L	$\bar{E}$	Scaled Kinetic energy (kinetic energy per unit area)
7	$M_p V_{50}^2/A^{1/2}$	F	$\bar{E}, \bar{L}, t$	British and ARRADCOM empirical fits can be cast in this form
8	$\frac{M_p V_{50}^2}{Ah}$	$F/L^2$	$(\bar{E}/\bar{h}) = (E/\rho_p a_p^2 Ah)$	Scaled energy counterpart of 3
9	$V_{50}$	L/T	$\bar{V}_{50}$	Postulated for fragment impact initiation of bare explosive

$z_1$  = ordinate of normal distribution at  $t_1$ ,

$$p_1 = \int_{-\infty}^{t_1} (1/\sqrt{2\pi}) \exp(-t^2/2) dt.$$

The necessary simultaneous equations for iteration on  $\mu$  and  $\sigma$  to satisfy Equations (2) and (3) are:

$$-\frac{\partial L}{\partial \mu} = \frac{\partial^2 L}{\partial \mu^2} \Delta \mu + \frac{\partial^2 L}{\partial \mu \partial \sigma} \Delta \sigma, \quad (4)$$

$$-\frac{\partial L}{\partial \sigma} = \frac{\partial^2 L}{\partial \mu \partial \sigma} \Delta \mu + \frac{\partial^2 L}{\partial \sigma^2} \Delta \sigma, \quad (5)$$

where,  $\mu_0$  and  $\sigma_0$  are beginning estimates for  $\mu$  and  $\sigma$ ,

$$\Delta \mu = \mu - \mu_0, \text{ and}$$

$\Delta \sigma = \sigma - \sigma_0$  give the approximate errors in  $\mu_0$  and  $\sigma_0$  for the increments to be added to the estimates.

The second partial derivations of  $L$  (the likelihood function) are also needed for the iterations given in Equations (6), (7), and (8).

The approximate variances of  $\mu$  and  $\sigma$  are obtained from the expected values of the second derivatives of the likelihood function, which are given in Equations (9), (10), and (11), where  $N$  is the sum of the number of penetrating ( $n$ ) and non-penetrating ( $m$ ) shots.

$$\frac{\partial^2 L}{\partial L^2} = \frac{1}{\sigma^2} \left[ \sum_{j=1}^m \frac{t_j^2 z_j^2}{q_j} - \sum_{j=1}^m \frac{z_j^2}{q_j} - \sum_{i=1}^n \frac{t_i^2 z_i^2}{p_i} - \sum_{i=1}^n \frac{z_i^2}{p_i} \right] \quad (6)$$

$$\frac{\partial^2 L}{\partial L \partial \sigma} = \frac{1}{\sigma^2} \left[ \sum_{j=1}^m \frac{t_j^2 z_j}{q_j} - \sum_{j=1}^m \frac{t_j z_j^2}{q_j} - \sum_{i=1}^n \frac{t_i^2 z_i}{p_i} - \sum_{i=1}^n \frac{t_i z_i^2}{p_i} \right] \quad (7)$$

$$\frac{\partial^2 L}{\partial \sigma^2} = \frac{1}{\sigma^2} \left[ \sum_{j=1}^m \frac{t_j^3 z_j}{q_j} - \sum_{j=1}^m \frac{t_j z_j^3}{q_j} - \sum_{j=1}^m \frac{t_j^2 z_j^2}{q_j} - \sum_{i=1}^n \frac{t_i^3 z_i}{p_i} + \sum_{i=1}^n \frac{t_i z_i^3}{p_i} - \sum_{i=1}^n \frac{t_i^2 z_i^2}{p_i} \right] \quad (8)$$

$$E \left( \frac{\partial^2 L}{\partial L^2} \right) = \frac{1}{\sigma^2} \sum_{k=1}^N \left[ - \frac{z_k^2}{q_k} - \frac{z_k^2}{p_k} \right] \quad (9)$$

$$E \left( \frac{\partial^2 L}{\partial L \partial \sigma} \right) = \frac{1}{\sigma^2} \sum_{k=1}^N \left[ - \frac{t_k^2 z_k}{q_k} - \frac{t_k z_k^2}{p_k} \right] \quad (10)$$

$$E \left( \frac{\partial^2 L}{\partial \sigma^2} \right) = \frac{1}{\sigma^2} \sum_{k=1}^N \left[ - \frac{t_k^3 z_k}{q_k} - \frac{t_k z_k^3}{p_k} \right] \quad (11)$$

Under the assumption that approximately

$$-E \left( \frac{\partial^2 L}{\partial L^2} \right) = E \left[ \left( \frac{\partial L}{\partial L} \right)^2 \right] = A_{uu}$$

$$-E \left( \frac{\partial^2 L}{\partial L \partial \sigma} \right) = E \left[ \left( \frac{\partial L}{\partial L} \right) \left( \frac{\partial L}{\partial \sigma} \right) \right] = A_{u\sigma}$$

$$-E \left( \frac{\partial^2 L}{\partial \sigma^2} \right) = E \left[ \left( \frac{\partial L}{\partial \sigma} \right)^2 \right] = A_{\sigma\sigma},$$

the variance-covariance matrix of  $\hat{Q}$  and  $\hat{\sigma}$  is:

$$\begin{vmatrix} A_{uu} & A_{u\sigma} \\ A_{u\sigma} & A_{\sigma\sigma} \end{vmatrix}^{-1} = \begin{vmatrix} A^{uu} & A^{u\sigma} \\ A^{u\sigma} & A^{\sigma\sigma} \end{vmatrix}$$

from which,

$$A^{uu} \approx \sigma_Q^2,$$

$$A^{\sigma\sigma} \approx \sigma_\sigma^2, \text{ and}$$

$A^{u\sigma}$  is the approximate covariance of  $\hat{Q}$  and  $\hat{\sigma}$ .

The values for 50% probability of explosive reaction or detonation under simulated fragment impact computed in the manner just described were cast into dimensionless forms shown in Table 2.

Almost all projectiles were steel, which was assumed to have a sound velocity  $a_p = 5000$  m/s and a density  $\rho_p = 7.83 \times 10^3$  kg/m<sup>3</sup>. A few were brass, which was assumed to have a sound velocity  $a_p = 3444$  m/s and a density  $\rho_p = 8.75 \times 10^3$  kg/m<sup>3</sup>. Some potentially important pi terms, including those which are scaled forms of initiation criteria, listed in Table 3, are  $\bar{V}_{50}$ ,  $\bar{M}_p$ ,  $\bar{L}$ ,  $\bar{h}$ ,  $\bar{I}$ ,  $\bar{E}$ ,  $\bar{I}/\bar{h}$ , and  $\bar{E}/\bar{h}$ . From the test reports, it appears that the type of explosive is also important, as is the degree of explosive confinement. We then divide the data into three sets: 1) bare explosive, 2) lightly-confined explosive, and 3) heavily-confined explosive\*. Tables 4, 5 and 6 give these scaled data. Most values for  $\bar{V}_{50}$  also show standard deviations, as do those terms which can be obtained from  $\bar{V}_{50}$  by simple multiplication or division by a known quantity. Type of explosive is shown, as are the references.

A number of plots of various scaled parameters from Tables 4, 5 and 6 are possible. Let us consider each table separately.

\* Lightly-confined explosives include all explosives which have cover plates or are enclosed in weak containers. Heavily-confined explosives were all artillery shells whose casings can only be ruptured by internal pressures of many atmospheres.

TABLE 4  
Scaled Fragment Initiation Data for Heavily-Confined Explosives

$\bar{V}_{50}$	$\bar{M}_p$	$\bar{L}$	$\bar{h}$	$\bar{I}$	$\bar{E}$	$\bar{I}/\bar{h}$	$\bar{E}/\bar{h}$	Explosive	Reference
0.205 +0.043	0.563	0.565	0.559	0.115 +0.024	0.01185	0.205+0.043	0.0212	Comp B	Socorro
0.218 +0.011	1.13	1.13	0.705	0.246 +0.012	0.0134	0.350+0.017	0.0190	"	(1979)
0.311 +0.016	1.13	1.13	0.705	0.351 +0.018	0.0546	0.498+0.026	0.0775	"	"
0.122 +0.007	1.13	1.13	0.520	0.1379+0.0079	0.00840	0.266+0.015	0.0152	"	"
0.136 +0.009	2.25	2.26	0.654	0.306 +0.020	0.0208	0.468+0.030	0.0318	"	"
0.1226+0.0074	1.12	1.12	0.411	0.137 +0.008	0.00842	0.333+0.019	0.0205	"	"
0.0914+0.0144	1.12	1.13	0.327	0.1024+0.0055	0.00468	0.313+0.017	0.0143	"	"
0.1212+0.0144	1.12	1.13	0.327	0.1357+0.0161	0.00823	0.415+0.049	0.0252	"	"
0.2116+0.0050	1.13	1.13	0.259	0.239 +0.006	0.0253	0.923+0.023	0.0977	"	"
0.1454+0.0070	1.13	1.13	0.191	0.1643+0.0079	0.0239	0.860+0.041	0.125	"	"
0.1398+0.0306	1.12	1.12	0.151	0.1566+0.0343	0.01094	1.037+0.227	0.0725	A-3	"
0.105 +0.002	1.12	1.13	0.120	0.1176+0.0022	0.00617	0.980+0.018	0.0514	"	"
0.406 +0.020	0.668	0.700	1.366	0.271 +0.013	0.0550	0.199+0.010	0.0403	Comp B	H. Reeves
0.322 +0.010	0.705	0.714	1.097	0.227 +0.007	0.0366	0.207+0.006	0.0334	"	(1972)
0.254 +0.009	0.818	0.853	0.915	0.208 +0.007	0.0264	0.227+0.008	0.0289	"	"
0.526 +0.135	0.806	0.846	1.52	0.424 +0.109	0.112	0.280+0.072	0.0736	"	"
0.375 +0.018	0.668	0.700	1.14	0.250 +0.012	0.0469	0.220+0.011	0.0412	"	"
0.297 +0.023	0.705	0.714	0.913	0.210 +0.016	0.0311	0.229+0.017	0.0341	"	"
0.236 +0.010	0.818	0.853	0.762	0.193 +0.008	0.0228	0.253+0.010	0.0299	"	"
0.328 +0.017	0.705	0.714	1.27	0.231 +0.012	0.0378	0.182+0.009	0.0298	"	"
0.260 +0.014	0.818	0.853	1.058	0.213 +0.011	0.0280	0.201+0.010	0.0261	"	"
0.358 +0.066	0.705	0.714	1.189	0.252 +0.047	0.0451	0.212+0.040	0.0379	"	"
0.284 +0.018	0.818	0.853	0.992	0.232 +0.015	0.0329	0.234+0.015	0.0332	"	"

TABLE 5  
Scaled Fragment Initiation Data for Lightly-Confined Explosives

$\bar{V}_{50}$	$\bar{M}_p$	$\bar{L}$	$\bar{h}$	$\bar{I}$	$\bar{E}$	$\bar{I}/\bar{h}$	$\bar{E}/\bar{h}$	Explosive	Reference
0.1756+0.0056	4.21	—	0.573	0.739 +0.023	6.49x10 <sup>-2</sup>	1.290+0.040	1.14 x10 <sup>-1</sup>	Tetryl	Slade
0.180 +0.008	1.56	1.58	0.573	0.299 +0.013	2.69x10 <sup>-2</sup>	0.522+0.023	4.7 x10 <sup>-2</sup>	"	&
0.181 +0.013	1.66	1.58	0.573	0.301 +0.021	2.73x10 <sup>-2</sup>	0.525+0.037	4.76 x10 <sup>-2</sup>	"	Dewey
0.1556+0.0052	3.44	—	0.573	0.535 +0.018	4.16x10 <sup>-2</sup>	0.934+0.031	7.26 x10 <sup>-2</sup>	"	(1957)
0.1326+0.0030	2.31	2.23	0.487	0.306 +0.007	2.03x10 <sup>-2</sup>	0.628+0.014	4.16 x10 <sup>-2</sup>	"	"
0.283 +0.035	0.702	0.695	0.232	0.1987+0.0246	2.81x10 <sup>-2</sup>	0.856+0.106	1.211x10 <sup>-1</sup>	Comp B	Petino,
0.335 +0.002	0.137	0.134	0.134	0.0459+0.0002	7.59x10 <sup>-3</sup>	0.342+0.001	5.66 x10 <sup>-2</sup>	"	DeMelia,
0.284 +0.036	0.275	0.269	0.134	0.0781+0.0099	1.11x10 <sup>-2</sup>	0.582+0.074	8.23 x10 <sup>-2</sup>	"	Rindner
0.335 +0.002	0.275	0.269	0.403	0.0921+0.0006	1.54x10 <sup>-2</sup>	0.229+0.001	3.82 x10 <sup>-2</sup>	"	(1976)
0.264 +0.014	0.341	0.344	0.115	0.0900+0.0048	1.19x10 <sup>-2</sup>	0.783+0.042	1.03 x10 <sup>-1</sup>	"	"
0.387 +0.0004	0.136	0.136	0.135	0.0526+0	1.02x10 <sup>-2</sup>	0.390+0	7.56 x10 <sup>-2</sup>	Amatex	Petino &
0.420 +0.0002	0.136	0.136	0.269	0.0571+0	1.20x10 <sup>-2</sup>	0.212+0	4.46 x10 <sup>-2</sup>	"	Leondi
0.336 +0.001	0.272	0.271	0.135	0.0914+0.0003	1.54x10 <sup>-2</sup>	0.677+0.002	1.14 x10 <sup>-1</sup>	"	(1978)
0.253 +0.0002	0.388	0.392	0.133	0.0982+0	1.24x10 <sup>-2</sup>	0.738+0	9.30 x10 <sup>-2</sup>	"	"
0.1998+0.0014	4.51	4.513	1.137	0.901 +0.006	9.00x10 <sup>-2</sup>	0.792+0.005	7.92 x10 <sup>-2</sup>	Octol	Frey,
0.1460+0.0020	2.26	4.513	1.137	0.330 +0.004	2.41x10 <sup>-2</sup>	0.290+0.004	2.12 x10 <sup>-2</sup>	"	et al
0.3988+0.0044	1.000	2.381	2.257	0.3998+0.0044	7.95x10 <sup>-2</sup>	0.177+0.002	3.52 x10 <sup>-2</sup>	Comp B	(1979)

TABLE 6  
Scaled Fragment Initiation Data for Bare Explosives

$\bar{V}_{50}$	$\bar{M}_P$	$\bar{L}$	$\bar{I}$	$\bar{E}$	Explosive	Reference
0.1094	0.695	1.053	0.0761	$4.16 \times 10^{-3}$	Tetryl	Slade
$0.1088 \pm 0.0016$	2.17	2.77	$0.236 \pm 0.003$	$1.286 \times 10^{-2}$	"	&
$0.164 \pm 0.011$	1.94	2.77	$0.318 \pm 0.021$	$2.61 \times 10^{-2}$	"	Dewey
$0.156 \pm 0.013$	2.92	4.15	$0.454 \pm 0.038$	$3.53 \times 10^{-2}$	"	(1957)
0.165	2.917	--	0.481	$3.97 \times 10^{-2}$	"	"
$0.1045 \pm 0.0006$	11.67	--	$1.220 \pm 0.007$	$6.37 \times 10^{-2}$	"	"
$0.157 \pm 0.003$	17.38	--	$2.73 \pm 0.052$	$2.14 \times 10^{-1}$	"	"
$0.231 \pm 0.009$	27.23	--	$6.29 \pm 0.25$	$7.26 \times 10^{-1}$	"	"
$0.1257 \pm 0.0012$	3.86	--	$0.485 \pm 0.005$	$3.04 \times 10^{-2}$	"	"
0.0774	2.31	2.23	0.1787	$6.92 \times 10^{-3}$	"	"
$2.389 \pm 0.016$	22.2	--	$8.63 \pm 0.36$	1.678	Comp B	"
$0.263 \pm 0.014$	26.9	--	$7.07 \pm 0.38$	$9.30 \times 10^{-1}$	"	"
$0.1788 \pm 0.004$	1.502	--	$0.269 \pm 0.006$	$2.40 \times 10^{-2}$	"	"
$0.1792 \pm 0.106$	3.86	--	$0.692 \pm 0.041$	$6.20 \times 10^{-2}$	"	"
$0.1702 \pm 0.0126$	2.31	2.23	$0.393 \pm 0.029$	$3.34 \times 10^{-2}$	"	"
$0.185 \pm 0.012$	0.838	0.834	$0.155 \pm 0.010$	$1.43 \times 10^{-2}$	Pentolite	McLean
$0.128 \pm 0.001$	0.814	0.800	$0.104 \pm 0.008$	$6.66 \times 10^{-3}$	"	&
$0.0728 \pm 0.0006$	0.442	0.444	$0.0322 \pm 0.0002$	$2.34 \times 10^{-3}$	"	Allan
$0.213 \pm 0.002$	0.838	0.834	$0.1784 \pm 0.0002$	$1.90 \times 10^{-2}$	Cyclotol	(1965)
$0.1452 \pm 0.0002$	0.814	0.814	$0.1182 \pm 0.0002$	$8.58 \times 10^{-3}$	"	"
$0.292 \pm 0.0082$	0.136	0.136	$0.0397 \pm 0.011$	$5.80 \times 10^{-3}$	Amatex	Petino &
$0.291 \pm 0$	0.272	0.271	$0.0792 \pm 0$	$1.15 \times 10^{-2}$	"	Leondi
$0.217 \pm 0.001$	0.388	0.392	$0.0842 \pm 0.0004$	$1.83 \times 10^{-2}$	"	(1978)

For the heavy confinement tests in Table 4, almost all of the data are for a single explosive Composition B. But, Reeves[3] and Howe and Frey[9] show other test data giving  $V_{50}$  values for violent reactions in other explosives and also in some solid propellants which are essentially independent of explosive type. So, all data are plotted without explosive identification. The independent variable chosen for plots from Table 4 is  $\bar{h}$ . Figure 1 shows  $\bar{V}_{50}$  plotted versus  $\bar{h}$  with one standard deviation limit shown as well as mean values for  $\bar{V}_{50}$ . In several instances, the Socorro tests[4] gave  $V_{50}$  values for reaction threshold (burning), as well as detonation threshold. These are indicated in Figure 1 by R and D respectively. Also included is a point for  $\bar{h}=0$  for tests by Slade and Dewey[1] on bare Composition B. One can see that a reasonably good correlation between two scaled parameters can be made in this figure, with  $\bar{V}_{50}$  relatively constant for  $0.12 < \bar{h} < 0.40$ , but increasing much more rapidly for  $0.40 < \bar{h} < 1.50$ . Various other plots were made, e.g.,  $\bar{I}, \bar{E}, \bar{I}/\bar{h}$  versus  $\bar{h}$  but the only other one which appeared to give good correlation was  $\bar{I}/\bar{h}$ . This plot is shown in Figure 2. One can see that the third criterion in Table 3, constant  $\bar{I}/\bar{h}$ , applies reasonably well for values of  $\bar{h} > 0.7$ , but that this criterion fails for smaller  $\bar{h}$ .

A statistical fit (solid line) has been made to the data shown in Figure 2. A 90% confidence interval can be established on the 0.87 correlation coefficient  $r$ , using the method developed by Fisher[12]. With 23 data points and  $r = 0.87$ , the 90% confidence interval on  $r$  are from 0.75 to 0.94. That is, based on the data, we are 90% confident that the true value of  $r$  is between 0.75 and 0.94. Thus, the correlation between the two variables is significant, and the prediction equation has some value in predicting the value of the dependent variable for a given value of the independent variable. The equation is:

$$\bar{I}/\bar{h} = 0.2368 \bar{h}^{(-0.6710)} \quad (12)$$

This equation is valid over the range  $0.012 \leq \bar{h} \leq 1.50$ .

We feel that either Figure 1 or Figure 2 can be used as bases for establishing empirical initiation criteria for heavily-confined explosives, as shown by the eye-fitted curves. Degree of confidence in the curves can be estimated from the scaled data. In no case should scaled parameters be predicted beyond the data limits.

The data in Table 5 unfortunately include variations in too many parameters and too little data for any one set

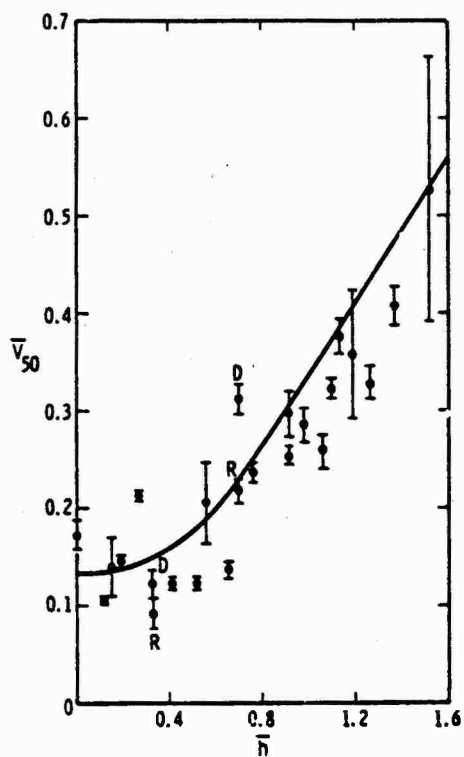


FIGURE 1

$\bar{V}_{50}$  vs  $\bar{h}$ , Heavy Explosive Confinement

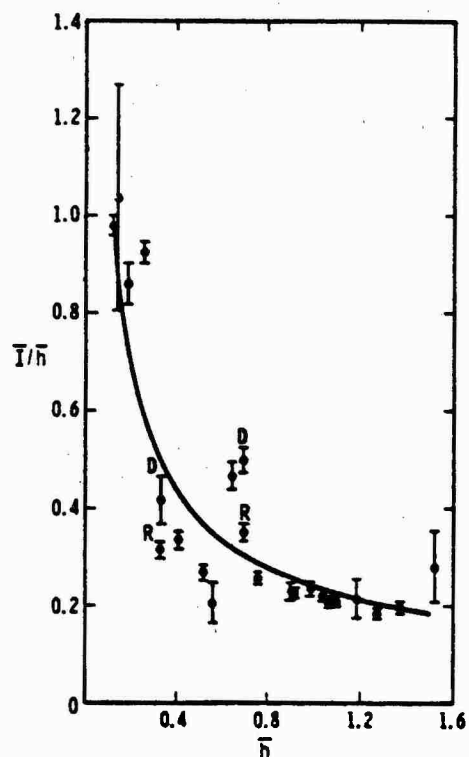


FIGURE 2

$\bar{I}/\bar{h}$  vs  $\bar{h}$ , Heavy Explosive Confinement

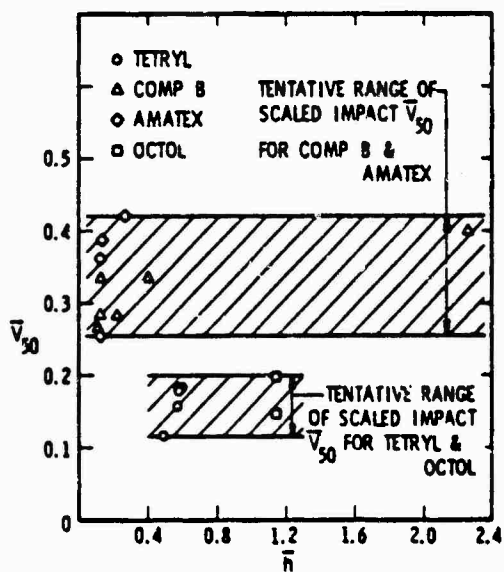


FIGURE 3

$\bar{V}_{50}$  vs  $\bar{h}$ , Light Explosive Confinement

of parameters. The 17-test series in this table include tests on four types of explosive, over a rather large range of both scaled mass  $\bar{M}_p$ , scaled length  $\bar{L}$ , and scaled thickness  $\bar{h}$ . Plots of  $\bar{I}$ ,  $\bar{E}$ ,  $\bar{I}/\bar{h}$ , and  $\bar{E}/\bar{h}$  versus  $\bar{h}$  showed wide scatter and no apparent correlation, even for a single type of explosive. Only the plot of  $\bar{V}_{50}$  versus  $\bar{h}$  seems to group data, primarily by type of explosive, with Amatex and Composition B forming a relatively insensitive group, and Tetryl and Octol another more sensitive group. A very tentative indication from these data is that  $\bar{V}_{50}$  values for a given explosive depend only weakly on  $\bar{h}$ , but additional data at intermediate values of  $\bar{h}$  could drastically change this conclusion.

For the scaled bare explosive test data in Table 6, we chose  $\bar{M}_p$  as the independent variable. By plotting  $\bar{V}_{50}$  versus  $\bar{M}_p$ , Figure 4, we see a rather weak dependence of  $\bar{V}_{50}$  on  $\bar{M}_p$ , but significant differences between certain types of explosives. Other plots were made, and those of  $\bar{I}$  and  $\bar{E}$  versus  $\bar{M}_p$  also gave reasonable correlations, provided one separates the explosives into several groups. These plots are shown in Figure 5 and 6. Possible functional relationships drawn by eye appear in Figure 4, 5 and 6 with Tetryl and Pentolite forming the most sensitive class, Composition B and Cyclotol somewhat less sensitive, and Amatex least sensitive of the explosives tested. Because  $\bar{V}_{50}$  has a very weak dependence on  $\bar{M}_p$ , it should provide the best estimate for initiation of bare explosive, as first suggested by Slade and Dewey[1].

A general feature of the scaled data in Tables 4 through 6 and Figures 1 through 6 is that consistent data are collected by various investigators, using different test methods and different methods of assessing severity of reaction. This fact has not before been apparent because only limited attempts have been made to scale the data.

#### CONCLUSIONS AND DISCUSSION

Some conclusions in this study are:

- (1) A similitude analysis of the problem of fragment impact initiation of bare explosives identifies potential important dimensionless groups in this problem.
- (2) Analysis of test data scaled in accord with the dimensional analysis shows good agreement between results of different investigators, and allows some empirical predictions of critical impact velocities for a number of specific fragment/receptor combinations.

(3) Initiation criteria differ for (a) bare explosives, (b) lightly-confined explosives, and (c) heavily-confined explosives.

(4) For a single type of bare explosive, the principal initiation criterion is a scaled impact velocity for 50% probability of initiation,  $\bar{V}_{50}$ , which is weakly dependent on scaled projectile mass  $\bar{M}_p$ , but is independent of scaled momentum, scaled kinetic energy, or other combinations of scaled parameters. Significant differences in these  $\bar{V}_{50}$  values occur for different types of explosive.

(5) For heavily-encased explosives such as explosive fillers in artillery shells,  $\bar{V}_{50}$  is strongly dependent on scaled casing thickness  $\bar{h}$ . Either a plot of  $\bar{V}_{50}$  versus  $\bar{h}$  can be used as an initiation criterion, or a plot of  $\bar{I}/\bar{h}$  versus  $\bar{h}$ . For values of  $\bar{h} > 0.7$ , the latter criterion gives essentially a constant value.

(6) For lightly-confined explosives, test data are much more sparse and include simultaneous variations of too many scaled parameters for firm conclusions. But, the experimental evidence to date indicates that  $\bar{I}$ ,  $\bar{E}$ ,  $\bar{I}/\bar{h}$ , or  $\bar{E}/\bar{h}$  are not consistent initiation criteria. A possible (but very tentative) criterion is again simply  $\bar{V}_{50}$  for any given type of explosive, with weak dependence of this parameter on  $\bar{h}$ .

(7) Of the criteria given in Table 3, many may be valid for certain confinement conditions or certain ranges of scaled parameters, but none apply universally.

Hopefully, this similitude analysis and subsequent comparison of scaled data on impact initiation of explosives has served to collate past data and to help identify scaled parameters which can be used to predict this phenomenon for some bare and cased explosives. There are obviously large data gaps for initiation of lightly-cased explosives, for tests on new insensitive explosives, and for tests with casings of materials other than steel. The dimensionless parameters given in this paper should help subsequent investigators in test planning, and should also help to minimize the number of such tests which must be conducted.

We believe that the use of the scaled data and approximate prediction curves in Figures 1 through 6 should be preferable to use of past empirical formulas for prediction of explosive initiation by fragment impact. In particular, these plots clearly show the limits of extant test data, and also the level of accuracy one can expect in predictions.

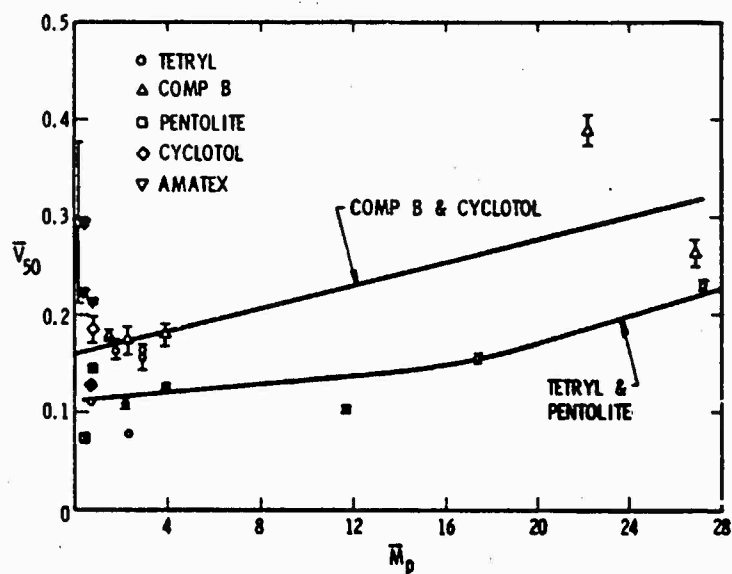


FIGURE 4  
 $V_{50}$  Vs  $\bar{M}_p$ , Bare Explosives

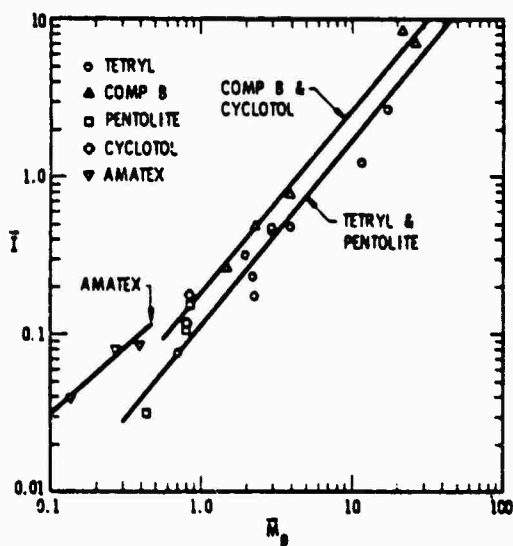


FIGURE 5  
 $\bar{I}$  Vs  $\bar{M}_p$ , Bare Explosives

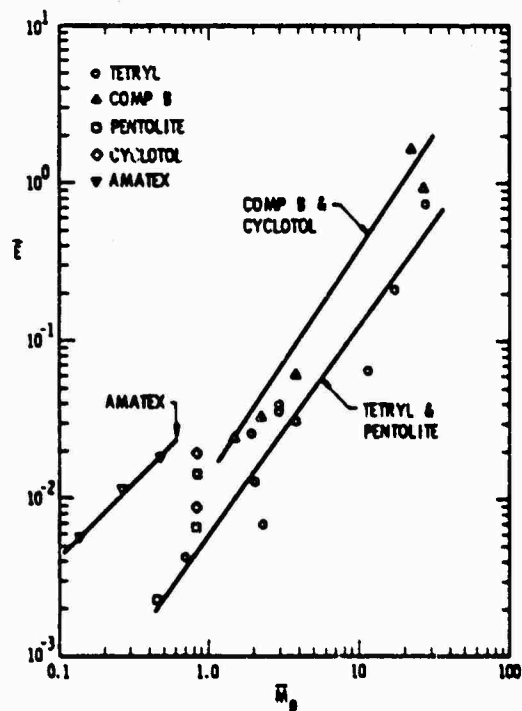


FIGURE 6  
 $\bar{E}$  Vs  $\bar{M}_p$ , Bare Explosive

#### ACKNOWLEDGEMENTS

This work was performed under Contract DACA87-79-C-0091 with Huntsville Division, U.S. Army Corps of Engineers. Grateful acknowledgement is made for their support and for their giving permission to publish this work.

#### REFERENCES

- [1] Slade, D.C., Dewey, J.M., "High Order Initiation of Two Military Explosives by Projectile Impact," Ballistic Research Laboratories Report No. 1021, July 1957, Aberdeen Proving Grounds, MD, (AD 145868).
- [2] Golub, A., Grubbs, F.E., "On Estimating Ballistic Limit and Its Precision," BRL Technical Note 151, March 1950, USA, BRL (AD 51120).
- [3] Reeves, H.J., "An Empirically-Based Analysis on the Response of HE Munitions to Impact by Steel Fragments," Ballistics Research Laboratory Memorandum No. 2031, March 1970, Aberdeen Proving Ground, MD (AD 508607).
- [4] NMT/TERA No. TD-78-1266-U, Vol. 1, "Vulnerability of 105mm HE Projectiles to Fragment Impact," New Mexico Institute of Mining and Technology, TERA Group, Socorro, NM, August 1978.
- [5] Frey, R.B., Howe, P.M., Trimble, J., Melani, G., "Initiation of Explosive Charges by Projectile Impact," Technical Report ARBRL-TR-02176, Aberdeen Proving Ground, MD, June 1979.
- [6] McLean, D.G., Allan, D.S., "An Experimental Program to Determine the Sensitivity of Explosive Materials to Impact by Regular Fragments," Final Report, Contract No. DA-19-020-ORD-5617, December 1965 (AD 477875).
- [7] Petino, G. Jr., DeMella, D., Rindner, R.M., "Sensitivity of Cased Charges of Molten and Solid Composition B to Impact by Primary Steel Fragments," PA-TR-4975, Picatinny Arsenal, Dover, NJ, June 1976.
- [8] Petino, G. Jr., Leondi, M.F., "Sensitivity of Molten and Solid Amatex Charges to Impact by Primary Steel Fragments," ARLCD-CR 78011, ARRADCOM, Dover, NJ, April 1978.
- [9] Howe, P.M., Frey, R.B., "Catastrophic Reaction of Compartmentalized Ammunition - Causes and Preventative Measures," Army Science Proceedings, Vol. 1, pages 145-108, 1978.
- [10] Baker, W.E., Westine, P.S., Dodge, F.T., Similarity Methods in Engineering Dynamics, Hayden Book Co., New Rochelle, NJ, 1978.
- [11] Misey, J., "Analysis of Ballistic Limit," ARBRL-MR-02815, USA, BRL, Aberdeen Proving Ground, MD, March 1978.
- [12] Arkin, H., Colton, R., Tables for Statisticians, Barnes & Noble, NY, 1950.



## DISCUSSION

Mr. Mathews (Sandia Laboratories): Did your duration of pressure loading versus initiation fit into the data scheme ascribed to the initiation work in the "pop" plots?

Mr. Baker: They appear to fit very poorly. There is one initiation criteria that comes from the flyer plate work which is essentially the  $P$  squared delta  $T$ . That is similar but that comes out of the Livermore-Los Alamos work and it works beautifully for flyer plate impacts. That converts in our dimensionless terms to an energy per unit area. That didn't work too well for most of the things that we did. It would work for bare explosives.

Mr. Mathews: What is the equivalence?

Mr. Baker: There is very likely some equivalence when one deals with bare explosives. One of the conclusions is that it is very hard to differentiate between these different initiation criteria as we have seen. We have several alternatives when we can't differentiate between them. "Pop" plots may be all right for bare explosives but they are very poor for heavily confined explosives.

Mr. Salive (David Taylor Naval Ship Research & Development Center): Do you think that these correlations would handle the problem of hypervelocity particles that might come from a shaped charge jet for cased explosives?

Mr. Baker: Something like this would probably work because we have Hugoniot properties for the explosives; but there wasn't a sufficient data bank to fit using the way we have of fitting it. I think the model analysis would be applicable.

Mr. Salive: What about the problem of massive fragments like massive pieces of structure crashing into cased explosives? Do you think that these types of nondimensionalized correlations would handle that problem?

Mr. Baker: Something like it but not with the parameters that we have because we assumed that we would have compact fragments that could penetrate either the bare explosive or the cased explosive. I think you would have to alter the parameters and worry about that. That would be primarily like a crushing type of initiation. That wouldn't be handled in this paper.

Mr. Mathews: Was there any evidence in the data of delays between excitation and violent response?

Mr. Baker: Yes, but not in the bare explosive. You either have a detonation that occurred or something very similar to a detonation that occurred during the early stages of the fragment penetrating the explosive. In the heavily cased explosive apparently the primary mechanism for these violent reactions is something with a lot of delay, and Howe and Frey are very careful to differentiate between a violent reaction and a detonation. When you are at the threshold, the fragment penetrates and sits there and something happens later. By later I may mean seconds later or many seconds later; so it is more like perhaps a cook-off phenomenon, that is a different phenomenon occurs. So you are going from one regime to another when you go from either bare or very lightly cased explosives to the heavily confined things.

Voice: Does time appear in your analysis?

Mr. Baker: Not explicitly but you could have rearranged the  $P$  terms to get a scaled time if you wished.

Mr. Salive: Did the statistical analysis give you any indication whether high order or low order detonation was strictly a time dependent function, or whether there was some statistical probability associated with getting high order or low order detonations a given impact condition?

Mr. Baker: In a few cases, and this comes out of the data taken from the Terra test, they could get two different regimes. They could get one velocity regime where they knew they had a delayed reaction and another higher velocity regime where they knew they were getting something very much like a detonation, if not a real detonation. Sometime they could differentiate but at other times the threshold between nothing happening and the detonation was so sharp that they couldn't differentiate.

Mr. Salive: So there was really no sense of mixed results?

Mr. Baker: Oh yes there was always a sense of mixed results and that is built into the statistics. But the difference between a reaction and a detonation could only be determined in a few instances.

EQUATIONS FOR DETERMINING FRAGMENT PENETRATION  
AND PERFORATION AGAINST METALS

Ingrid M. Gyllenspetz

National Defense Research Institute (FOA)  
Stockholm, Sweden

(Currently studying with Southwest Research Institute,  
San Antonio, Texas)

To use computer models successfully to calculate munitions effects in targets, one must be able to calculate fragment impact. These equations must be functional for fragments of different materials, sizes and velocities, and for plates of various thicknesses and materials. The equations used today in both Sweden and the United States are based on test data and contain constants that represent many parameters. Therefore, to use these equations for new relationships, new test data are needed.

Similitude modeling, which has been used in this paper makes it possible to develop approximate equations covering a wide range of variations in the parameters. The equations presented here can be useful in simplified munitions effects calculations and for estimations when no test data are available. The test data and equations found in the literature are used to validate these equations and show the relationships of the nondimensional terms.

INTRODUCTION

The equations used in both Sweden and the United States to calculate munitions effects in targets are severely limited. The Swedish equations are not valid for striking velocities higher than 1500 m/s and most of the U.S. equations are valid only for steel fragments.

Work performed during the Space Program gives test data that can be used to extend these equations to higher velocities. These data also allow for a variety of materials for both penetrators and fragments.

In Westine, et al [1], a review is made of existing penetration equations. Westine, et al, show that these equations can be modified to contain a group of specific nondimensional factors (pi terms). Table 1 is a list of parameters and pi terms for the equations used in this paper. A parameter not listed in this work is the speed of sound in the

target material. Care must be taken when the equations are used for materials with sound velocities different from steel or aluminum.

Two equations are presented:

(1) An equation to calculate the depth of penetration: This equation works well with materials such as aluminum, various steels, and copper in various combinations, with various shaped fragments such as discs, spheres and rods, and with striking velocities as high as 5-8 km/sec.

(2) An equation to calculate the ballistic limit (the striking velocity needed for a fragment to just perforate a plate): Nondimensional factors are geometric similarity, density and energy similarity. Parameters include length and diameter of the fragment, thickness of target plate, density of fragment and target, strength of target, and striking velocity of fragment.

TABLE 1  
List of Parameters

Symbol	Parameter	Fundamental Units of Measure
P	Depth of Penetration	L
h	Thickness of Target Plate	L
$h_1$	Thickness of First Plate	L
$h_2$	Thickness of Second Plate	L
$S_D$	Distance Between Target Plates	L
l	Length of Fragment	L
d	Diameter of Fragment	L
$m_o$	Mass of Fragment	FT <sup>2</sup> /L
$m_r$	Residual Mass (largest piece)	FT <sup>2</sup> /L
$V_o$	Velocity of Impact	L/T
$V_r$	Residual Velocity	L/T
$V_{BL}$	Ballistic Limit	L/T
$\rho$	Density	FT <sup>2</sup> /L <sup>4</sup>
S	Shear Strength	F/L <sup>2</sup>
t	Index; Target	
p	Index; Penetrator	
$k_1, k_2, \dots$	Constants	
Pi Terms of Interest:		
$P/d, h/d, l/d, S_D/d, m_r/m_o, V_r/V_o, V_{BL}/V_o, \rho_p/\rho_t$ , and $\rho V^2/S$		

Bouma and Burkett[2] present a similar work on depth of penetration. They have achieved better agreement than reported here, but have used more parameters. Sometimes, it is more desirable to have a simple, compact equation that can be used either as an assumption when no test data are available, or in a computer model when the target is not well described. Furthermore, depth of penetration is not as important as the ballistic limit and perforation of multi-layered targets.

An attempt is made to use the same nondimensional factors to obtain the residual mass and the velocity of a fragment after it perforates a target. In some instances, it is possible to calculate the fragment perforating a second plate from these equations.

#### DEPTH OF PENETRATION

Although not as important as other parameters, a large amount of data exist on depth of penetration. According to the assumptions made in Reference 1, the

nondimensional factors used for depth of penetration can be used to determine other parameters. In Reference 1, it is shown that several equations based on test data can be arranged as follows:

$$P/d = k \left( \frac{\rho_p}{\rho_t} \right)^a \left( \frac{l}{d} \right)^b \left( \frac{\rho_p V_o^2}{S_t} \right)^\gamma \quad (1)$$

low striking velocity

$$P/d = k' \left( \frac{\rho_p}{\rho_t} \right)^{a'} \left( \frac{l}{d} \right)^{b'} \quad (2)$$

high striking velocity

The values of  $a, a', b, b'$  and  $\gamma$  vary from report to report. As can be seen from these equations, the power of  $V$  varies from rather strong to very weak as the velocity increases.

One equation where  $l/d$  has a wider range than in other work is by Christman, et al[12]. This is expressed as

$$P/d = \left( \frac{l}{d} - 1 \right) \left( \frac{\rho_p}{\rho_t} \right)^{1/2} + k \left( \frac{\rho_p}{\rho_t} \right)^{1/3} \left( \frac{\rho_p V_o^2}{B} \right)^{1/3} \quad (3)$$

where  $B$  is Brinnell Hardness. However, this equation cannot be used for very low velocities. For example, when  $V_o = 0$ , the equation has a non-zero value for  $P/d$ . Assuming that even the first term in the equation should be dependent on the striking velocity, a plot can be made of the test data where the axes are:

$$Y = \frac{k_1 P/d}{k_2 \left( \frac{l}{d} - 1 \right) \left( \frac{\rho_p}{\rho_t} \right)^{1/2} + \left( \frac{\rho_p}{\rho_t} \right)^{1/3}}$$

$$X = k_3 \left( \frac{\rho_p V_o^2}{S_t} \right)^{1/2}$$

This plot is shown in Figure 1. For  $k_1 = 0.4, k_2 = 0.6$  and  $k_3 = 0.05$ , the test data can be approximated by

$$Y = \tanh X \quad (4)$$

In Figure 1, a line is used between the symbols to show that the test data are curve-fitted. The dispersion seems rather large, but the test data cover a wide variation in fragment size, shape and density and in target density and strength.

Symbol	Penetrator	Target	Shape	Diameter (mm)	Ref.
--------	------------	--------	-------	---------------	------

●	4340	St1-4340	Sphere	0.476	9
●	Cu	HP Cu	"	0.159, 0.318, 0.476	9
●	Al	HP Al	"	0.150, 0.318, 0.476	9
●	Al	Al 6061	"	0.318, 0.476	9
●	Cu	HP Al	"	0.159, 0.318, 0.476	9
●	Al	HP Cu	"	0.159, 0.318, 0.476	9
●	Al	Al 2024-T4	"	0.159, 0.318, 0.476	9
●	Al	St1-1015	"	0.508, 1.016	2
●	1015	St1-1015	"	1.270	2
●	Al	Al 2024-T3	"	0.559	2
●	Al	Al 2024-T3	"	3.2	11
●	St1	Al 2024-T3	Rod	$t/d = 3, d = 3.2$	3
●	1015	St1 1015	"	$t/d = 3, d = 3.2$	3
●	Al	Al 2024-T3	"	$t/d = 3, d = 3.2$	3
●	Al	St1-1015	"	$t/d = 3, d = 3.2$	3
●	1015	St1-1015	"	$t/d = 3-12, d=3.2-2$	12
●	Al	Al-1100	Disc	$t/d = 0.16$	12
●			Sphere	$t/d = 1$	12
●			Rod	$t/d = 2.08$	12

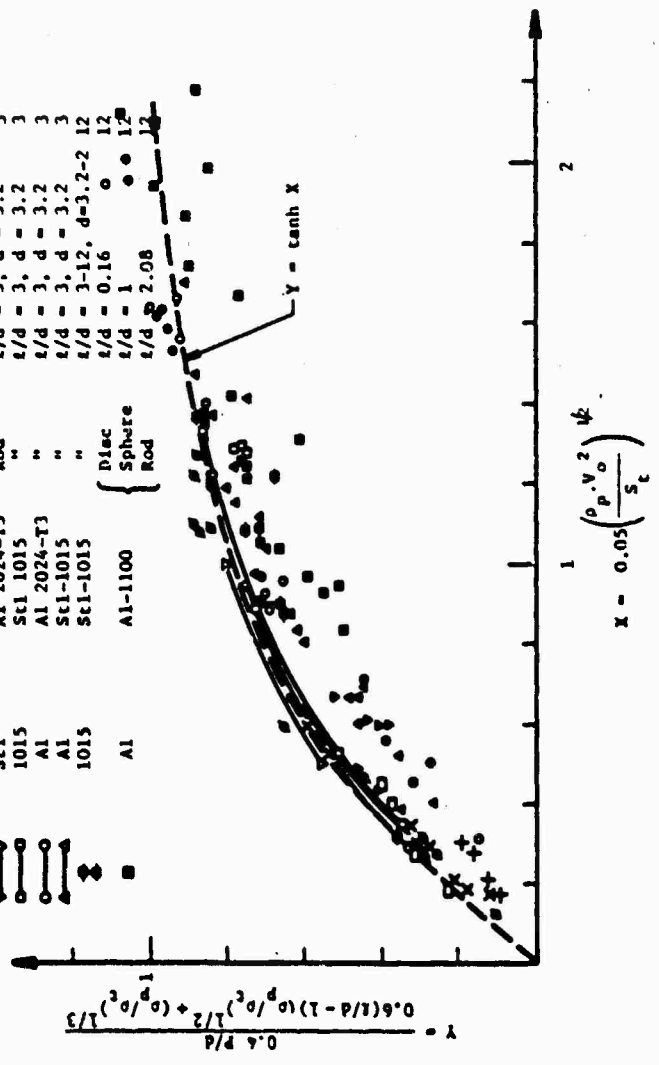


FIGURE 1  
Depth of Penetration

## BALLISTIC LIMIT

Data for the ballistic limit of single sheet, finite thickness targets are difficult to obtain and consequently are rare. Furthermore, the definition of these data can differ. For each velocity, a probability of perforation exists with a given fragment-plate combination, and usually this probability is thought to increase as velocity increases. This is shown in Figure 2. The ballistic limit is defined as  $V_{50}$ .

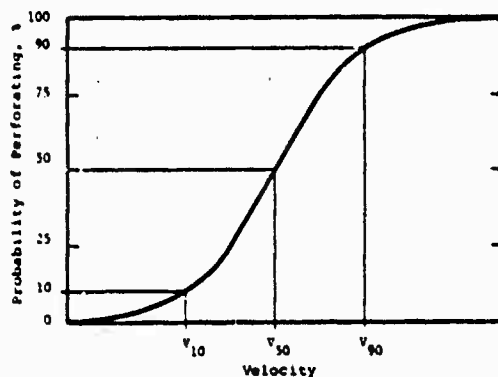


FIGURE 2

Probability of Perforation Curve

The equations used in Sweden to calculate the ballistic limit for different material combinations can be approximated by one equation using the same pi terms as for depth of penetration.

$$Y = \tanh X \quad (5)$$

$$\text{where } Y = \frac{k'_1 h/d}{(\rho_p/\rho_t)^{1/2}}$$

$$X = k'_3 \left( \frac{\rho_p V_{BL}^2}{S_t} \right)^{1/2}$$

Only equations for spherical fragments have been used, thus the term  $l/d$  cannot be evaluated. The agreement between Equation (5) and the Swedish equation is shown in Figure 3, where  $k'_1 = 0.22$  and  $k'_3 = 0.05$  have been used.

The test data for ballistic limit in the literature are also only for spheres. However, in Christman, et al [3], the ratio  $h/P$  is given for different  $l/d$  values for aluminum against aluminum. Equations (4) and (5) give for  $\rho_p = \rho_t$

Symbol	Penetrator	Target	Shape	Ref
—○—	Steel	Steel	Sphere	4
—○—	Steel	Al	"	4
—○—	Al	Al	"	4
—○—	Al	Steel	"	4
—○—	Tungsten	Al	"	4
—○—	Tungsten	Steel	"	4

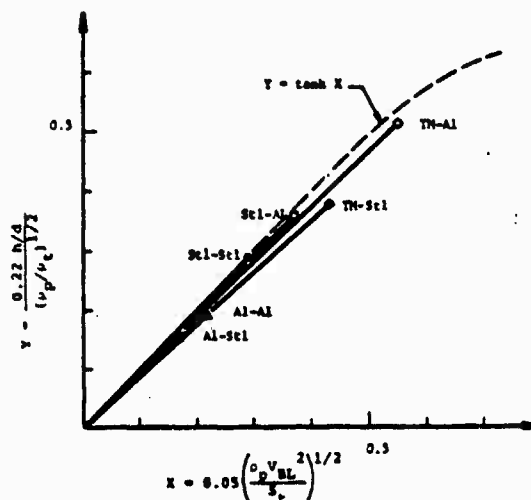


FIGURE 3

Ballistic Limit; Swedish Equations for Spherical Equations

$$A = \frac{h(\text{sphere})}{P} = \frac{k_1}{k'_1 [k'_2 (l/d - 1) + 1]} \quad (6)$$

where  $A$  is the ratio of the thickness of the plate, if the fragment is spherical to the depth of penetration.

The values given in Christman, et al [3], are compared with  $A$  and some assumptions of the  $l/d$  term that can make Equation (5) valid even for rods. This is shown in Table 2. The term  $(l/d)^{2/3}$  is selected as the term that gives the best agreement.

TABLE 2

$l/d$	$h/P$	$A$	$A(l/d)^{1/3}$	$A(l/d)^{2/3}$	$A[0.5(l/d - 1) + 1]$
1	1.8	1.82	1.82	1.82	1.82
3	1.7	0.83	1.20	1.73	1.66
5	1.55	0.53	0.91	1.55	1.59

The Thor equation [4] for ballistic limit is

$$V_{BL} = 10^C (h \text{ Avg})^A m_0^B (\sec \theta)^Y \quad (7)$$

where Avg is the average impact area of the fragment and C, A, B, and Y have different values for different target materials

For perpendicular impact, and if the assumption

$$C = A = -B \quad (8)$$

is made, then the Thor equations can be rearranged as

$$V_{BL} = 10^C \rho_p^{-A} (h/d)^A (\ell/d)^{-A} \quad (9)$$

The Thor equations are based on tests where two types of fragments were used. These fragments had  $\ell/d$  ratios of

Type I  $\ell/d = \{0.99, 0.78, 0.76, 0.94, 0.99\}$

Type II  $\ell/d = \{0.77, 0.63, 0.61, 0.71, 0.77\}$

The Type II fragments are probably more common than Type I.

If  $\ell/d = 0.7$  is chosen as an average, Equation (8) can be compared with the nondimensional form. In Figure 4, all test data, the Swedish equations, and the Thor equations are compared to the equation

$$Y = \tanh X \quad (10)$$

where

$$Y = \frac{k_1' h/d}{(\ell/d)^{2/3} (\rho_p/\rho_t)^{1/2}}$$

$$X = k_3' \left( \frac{\rho_p V_{BL}^2}{S_t} \right)^{1/2}$$

$$k_1' = 0.22 \text{ and } k_3' = 0.05.$$

For spherical fragments ( $\ell/d = 1$ ) some values of the ratio  $h/p$  are found in the literature. Equations (4) and (10) give for  $\ell/d = 1$

$$B = h/P = \frac{k_1' (\rho_p/\rho_t)^{1/2}}{k_1' (\rho_p/\rho_t)^{1/3}} \quad (11)$$

Symbol	Penetrator	Target	Shape	Diameter (mm)	Ref
●	Steel	Al 2024-T3	Sphere	d = 2.38	1
○	Al	Al 2024-T3	"	d = 3.17, 6.76	2
○	Al	Al 2024-T3	"	d = 1.90	10
○	Hoton Stl	Al	"	d = 1.78, 3.52	11
○	Steel	Al and Stl	Rod	d/d = 1.7	8
○	Steel	Steel	Sphere	"	4
○	Steel	Al	"	"	6
○	Al	Al	"	"	6
○	Al	Steel	"	"	6
○	Tungsten	Al	"	"	6
○	Tungsten	Steel	"	"	6

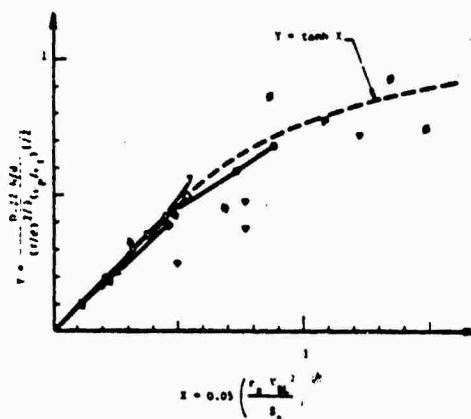


FIGURE 4

Ballistic Limit

Table 3 shows B compared to  $h/P$  values for a variety of targets and penetrators.

TABLE 3

Penetrator	Target	Striking Velocity km/s	h/P From Literature	B	Reference
Aluminum	Lead	3	1.375	1.42	[5]
Aluminum	Copper	3	1.375	1.67	[5]
Steel	Titanium	6.1 - 7.6	1.74 - 2.09	1.98	[6]
Steel	Aluminum	6.1 - 7.6	1.78	2.14	[6]
Steel	Magnesium	6.1 - 7.6	3.33 - 3.42	2.32	[6]
Steel	Beryllium	6.1 - 7.6	>5.36	2.29	[6]
Glass	Steel	?	1.4	1.46	[3]
Glass	Aluminum	?	1.66	1.73	[3]

In Bruce[6], only  $h$  is verified by tests, and  $P$  is calculated from an equation which has not been validated for magnesium and beryllium. Furthermore, these tests were run for very small angles ( $2^\circ - 10^\circ$ ) between the fragment trajectory and the target plate.

#### PENETRATION OF A SECOND PLATE

It is more difficult to describe fragment penetration capability in multi-plate targets than in single-plate targets. Figure 5 illustrates this problem. To simplify the problem, we assume that the materials of the two plates are the same and that the space between the two plates is so large that the results are independent of that parameter. Westine, et al[1], and Humes, et al[7], show that this should occur if  $S_D > 15$ .

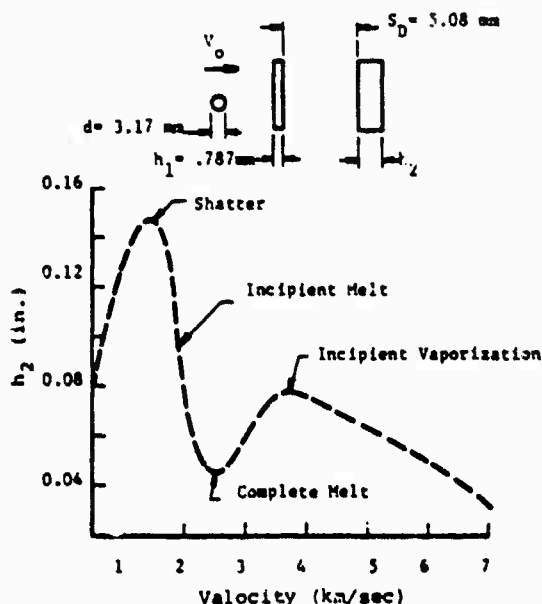


FIGURE 5

Threshold Velocity for Just Penetrating Various Thicknesses of Shielded Targets

One way to solve this problem is to find the residual velocity and mass and then use those values against the next plate. This method is used in the Thor equations. However, it seems that for some penetrator-target combinations, these equations give penetration capability after the maximum is reached that is too low. An example is shown in Figure 6 where the results of the Thor

equations are compared to some test data of steel fragments against aluminum sheets found in Bouma and Burkett[2].

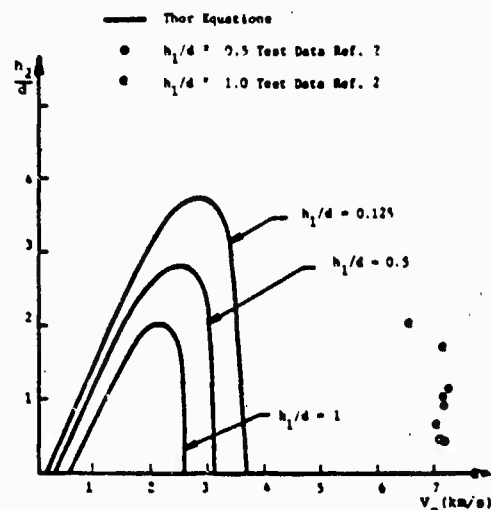


FIGURE 6

Thor Equation Compared to Test Data

The Thor equations give a low penetration capability because the residual mass decreases to zero. It should be possible to use nondimensional terms to find functions for the residual velocity and mass. An example is the Denver Research Institute (DRI) equation. Substituting the symbols used here, and rearranging terms gives

$$\frac{V_r}{V_0} = \frac{\sqrt{1 - (V_{BL}/V_0)^2}}{1 + \frac{h/d}{l/d(\rho_p/\rho_t)}} \quad (12)$$

Although this equation can theoretically be used for any kind of material, data exist only for steel fragments.

It is difficult to find residual mass test data for the many penetrator-target combinations that exist. The data base in Project Thor[8] is limited to compact steel fragments, and the factor  $h/d$  is not systematically varied. Figure 7 shows  $m_r/m_0$  as a function of the striking velocity. However, the shape of the curve in Figure 7 will vary as  $l/d$ ,  $h/d$ ,  $\rho_p/\rho_t$  and the penetrator material varies.

It is important to find the conditions of the penetrator breakup, because the penetrator capability for a second

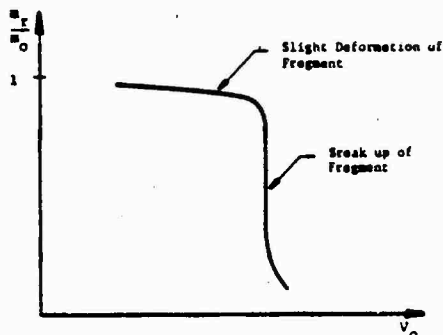


FIGURE 7  
Residual Mass

for a second plate will be decreased drastically. In this paper an attempt is made to find the breakup conditions for steel fragments, using test data from Project Thor[8]. These results are shown in Figure 8 where the breakup limit is given by the dashed line. To use the data in Figure 8 for other penetration materials, an assumption is made that the breakup limit depends on  $\rho_p V_0^2$  rather than  $V_0$ . If this assumption is used, the breakup limits for copper and aluminum spheres for a given  $h/d$  could possibly be determined from Figure 8. These limits have been compared to test data in Maiden, et al[11], and diagrams in Humes, et al[7].

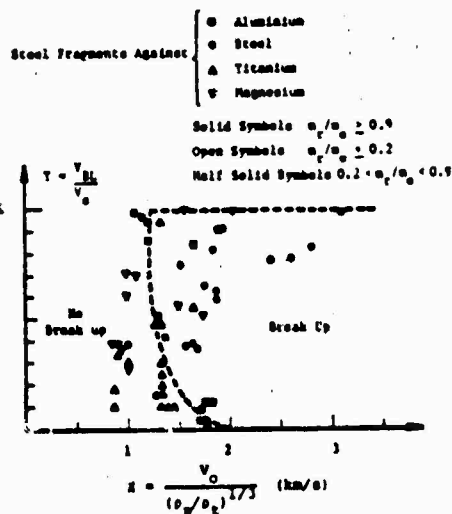


FIGURE 8  
Conditions for Fragment Breakup, Compact Steel Fragments

Figures 9 and 10 show these data transformed to depth of penetration in the second plate. The term  $(V_0 - V_{BL})$  is used for the striking velocity against the second plate and the fragment is assumed to have its original shape. As can be seen in Figures 9 and 10, the breakup limits appear just before the maximum of the curve, but too early for the smallest  $h/d$  values. Equation (4), which is also illustrated in these figures, is of course only valid before the fragment deforms too much.

## CONCLUSIONS

The equations for depth of penetration and ballistic limit seem to give enough agreement with test data to be useful in simplified munitions effects calculations. The equations are valid for very high striking velocities and many different combinations of penetrator and target materials. However, care must be taken when these equations are used for materials with sound velocities different from steel or aluminum.

Fragment penetration capability in multi-layered targets is difficult to predict when conditions are such that the fragment will breakup. More test data are needed to find these conditions as the data reported here are only for compact steel fragments. However, examples cited in this paper show that it should be possible to find some function of nondimensional factors that could be used for predicting fragment breakup of other materials.

## ACKNOWLEDGEMENTS

This program was performed while the author was studying at Southwest Research Institute, San Antonio, Texas. Funds were provided by the National Defense Research Institute, Stockholm, Sweden.

Many of the ideas which were pursued came from Mr. Peter S. Westine of Southwest Research Institute; Dr. Wilfred Baker reviewed the results and Miss Deborah J. Stowitts edited the paper. The help of these individuals and other SWRI staff members is greatly appreciated.

## REFERENCES

- [1] Private discussions with P. Westine and W. Baker, SWRI.
- [2] Bouza, D., Burkett, W., "Multivariable Analysis of Mechanics of Penetration of High-Speed Particles," NASA CR-664, December 1966.



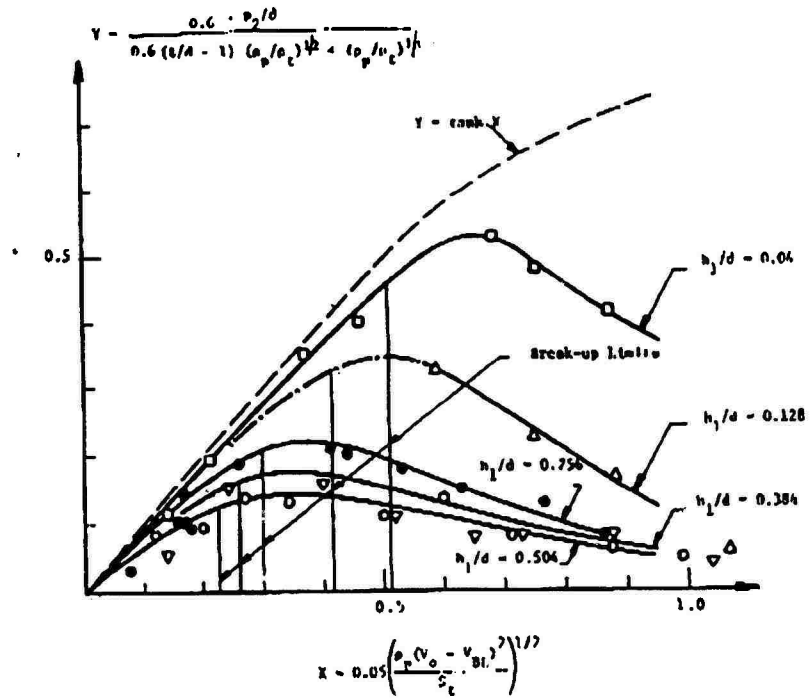


FIGURE 9

Aluminum Spheres Against Aluminum Plates, Depth of Penetration in the Second Plate

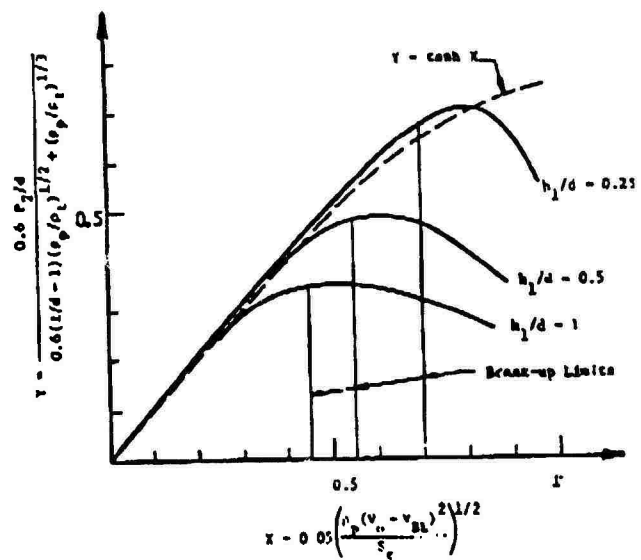


FIGURE 10

Copper Spheres Against Aluminum Plates; Depth of Penetration in the Second Plate

[3] Christman, D., Wenzel, A., Gehring, J., "Penetration Mechanism of High-Velocity Rods," Seventh Hypervelocity Impact Symposium, February 1965.

[4] Rilbe, U., "Splitters Genomslagsför-måga," FOA 2A 2525-44, April 1970 (Swedish).

[5] Smith, F., Clayden, W., Wall, C., Winter, F., "Hypervelocity Impact Experiments at ARDE, Fort Halstead," Fifth Symposium on Hypervelocity Impact, Vol. 1, Part 2, April 1962.

[6] Bruce, E., "Review and Analysis of High Velocity Impact Data," Fifth Symposium on Hypervelocity Impact, April 1962.

[7] Humes, D., Hopfo, R., Kinard, W., "An Experimental Investigation of Single Aluminum Meteor Bumpers," Fifth Symposium on Hypervelocity Impact, Vol. 1, Part 2, April 1962.

[8] Project Thor, Technical Report No. 47, The Resistance of Various Metallic Materials to Perforation by Steel Fragments, Empirical Relationships for Fragment Residual Velocity and Residual Weight, Ballistic Research Laboratory, April 1961.

[9] Sorenson, N., "Systematic Investigation of Crater Formation in Metals," Seventh Hypervelocity Impact Symposium, Vol. VI, February 1965.

[10] Fish, R., Summers, J., "The Effect of Material Properties on Threshold Penetration," Seventh Hypervelocity Impact Symposium, Vol. VI, February 1965.

[11] Maiden, C., Gehring, J., McMillan, A., "Damage to Thin Targets by Hypervelocity Projectiles," General Motors Co., May 1964.

[12] Christman, D., Gehring, J., McMillan, A., "Hypervelocity Impact Studies on Aerospace Materials and Structures," General Motors Co., August 1963.

#### BIBLIOGRAPHY

1. Averbuch, J., Bodner, S., "Analysis of the Mechanics of Perforation of Projectiles in Metallic Plates," Int. J. Solids Structures, Vol. 10, 1974.

2. Averbuch, J., Bodner, S., "An Investigation of Oblique Perforation of Metallic Plates by Projectiles," Exp. Mech., Vol. 17, 1977.

3. Averbuch, J., Bodner, S., "Experimental Investigation of Normal Perforation of Projectiles in Metallic Plates," Int. J. Solids Structures, Vol. 10, 1974.

4. Backman, M., Goldsmith, W., "The Mechanics of Penetration of Projectiles into Targets," International Journal of Engineering Science, Vol. 16, No. 1, 1978.

5. Bouma, D., Burkett, W., "Multivariable Analysis of Mechanics of Penetration of High-Speed Particles," NASA CR-664, December 1966.

6. Bruce, E., "Hypervelocity Impact on Single Thin Sheet Structures--Incipient Perforation Conditions," Seventh Hypervelocity Impact Symposium, Vol. VI, February 1965.

7. Bruce, E., "Review and Analysis of High Velocity Impact Data," Fifth Symposium on Hypervelocity Impact, November 1961.

8. Christman, D., Gehring, J., McMillan, A., "Hypervelocity Impact Studies on Aerospace Materials and Structures," General Motors Co., August 1963.

9. Christman, D., Wenzel, A., Gehring, J., "Penetration Mechanism of High-Velocity Rods," Seventh Hypervelocity Impact Symposium, February 1965.

10. Fish, R., Summers, J., "The Effect of Material Properties on Threshold Penetration," Seventh Hypervelocity Impact Symposium, Vol. VI, February 1965.

11. Greenspon, J., "An Approximate Non-dimensional Representation of the Thor Equations," Technical Report No. 178, October 1976.

12. Herrmann, W., Jones, A., "Correlation of Hypervelocity Impact Data," Fifth Symposium on Hypervelocity Impact, November 1961.

13. Humes, D., Hopfo, R., Kinard, W., "An Experimental Investigation of Single Aluminum 'Meteor Bumpers'," Fifth Symposium on Hypervelocity Impact, Vol. I, Part 2, April 1962.

14. Maiden, C., Gehring, J., McMillan, A., "Damage to Thin Targets by Hypervelocity Projectiles," General Motors Co., May 1964.

15. Marom, I., Bodner, S., "Projectile Perforation of Multi-Layered Beams," Int. J. Mech. Sci., Vol. 21, 1979.

16. Olshaker, A., Hjork, R., "Hydrodynamics Applied to Hypervelocity Impact I: Scaling Laws for Dissimilar Materials, II. The Role of Melting and Vaporization in Hypervelocity Impact," Fifth Symposium on Hypervelocity Impact, November 1961.

17. Project Thor, Technical Report No. 47, April 1961.
18. Rilbe, U., "Splitters Genomslagsförmåga (Fragment Penetration)," FOA 2A 3536-44, April 1970. (In Swedish)
19. Smith, F., Clayden, W., Wall, C., Winter, F., "Hypervelocity Launchers and Hypervelocity Impact Experiments at ARDE, for Halstead," Fifth Symposium on Hypervelocity Impact, Vol. I, Part 2, April 1962.
20. Sorenson, N., "Systematic Investigation of Crater Formation in Metals," Seventh Hypervelocity Impact Symposium, Vol. VI, February 1965.

#### DISCUSSION

Mr. Pearson (Air Force Flight Dynamics Laboratory): I did not understand the significance of the ratio of  $h$  over  $p$  being greater than one. What are the definitions of  $h$  and  $p$ ?

Mrs. Gvilienspetz: The  $h$  is the thickness of a plate that a fragment will just be able to perforate and the  $p$  is the depth of penetration in a semi-infinite target.

Mr. Selive (David Taylor Naval Research and Development Center): These equations are very important not only in selecting materials to defeat fragments but also as algorithms and programs designed to evaluate the penetration of the fragments from fragmenting warheads into different types of structures. This is of vital interest to analysts that are interested in armor and to analysts that are interested in evaluating ship vulnerability, airplane vulnerability or land vehicle vulnerability. These types of equations are always being scrutinized and everybody with the computerized vulnerability programs are very interested in getting the latest and most effective equations to use in their programs.

## BREACHING OF STRUCTURAL STEEL PLATES USING EXPLOSIVE DISKS (U)

D. L. Shirey  
Explosives Testing Division 1533  
Sandia Laboratories  
Albuquerque, New Mexico 87185

(U) Methods for predicting the threshold for explosive breaching of structural steel plates are described in this report. Both empirical and theoretical methods of predicting charge size have been developed for explosive disks. Theory is compared with test results. Experiments are discussed which investigate the residual energy remaining in a sheared plug when the breaching threshold is exceeded.

### INTRODUCTION

(U) Protective structures suitable for storage of hazardous materials are of interest to both civilian and military agencies. Methods are being developed to predict the response of basic elements in these structures to a variety of attacks. The response of mild steel plates subjected to breaching attack by circular disks of explosive is investigated in this paper.

(U) This work resulted from the need for a theory which would predict breaching thresholds of steel plate. Although explosive punching and forming of metals is a fairly well-developed technology [1], the tearing of a hole through structural steel plates without the benefit of a die or form has been studied only in terms of quantities of explosive required for significant "overkill". The breaching threshold, defined as the point at which the explosive energy will just produce a complete hole, was of sufficient interest to substantiate a series of experiments. A second topic of interest was to account for the plug's mass and energy when the explosive attack exceeded the structure's breaching threshold. This information would be useful in assessing internal damage.

(U) It was decided that a series of simple experiments involving explosive disks and common structural steel could be conducted quickly and efficiently. Mathematical formulae would

then be derived and compared with the empirical data until a reasonable fit was obtained.

### TEST SETUP

(U) The tests were planned to establish threshold values of Detasheet explosive thickness required to penetrate various thicknesses of structural steel plate at hole diameters of up to 18 inches.

(U) For all experiments, EL 506 Detasheet was used due to its availability, ease of handling, and its ability to sustain full detonation in relatively thin layers. Several attempts were made to detonate thin (.045 to .090 inch) disks of composition C-4 explosive on 1/4-inch thick steel. In all cases, the composition C-4 failed to sustain detonation beyond a small booster patch of Detasheet.

(U) All Detasheet charges were cut by hand; weighed carefully to determine an accurate average thickness value; and bonded, in layers when necessary, to the steel test plates. For symmetry, all charges were circular disks single-point detonated at the center. See Fig. 1.

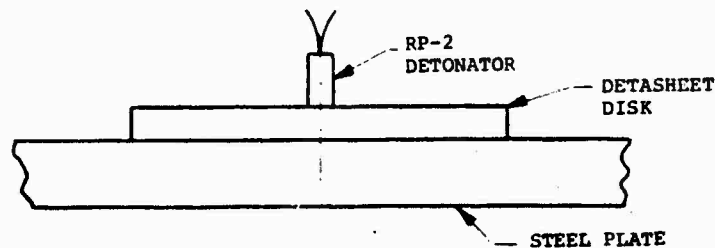


Fig 1 - Test Arrangement

### TEST PROCEDURE

(U) A total of 26 tests was required to establish threshold values for 2-, 3-, 4-, 5-, 6-, 8-, 12-, 16-3/8, and 18-3/8-inch plate. In all cases, the hole diameter produced by threshold or greater charges was approximately 3/8 inch less than the diameter of the charge that produced it. Results are plotted in Fig. 2.

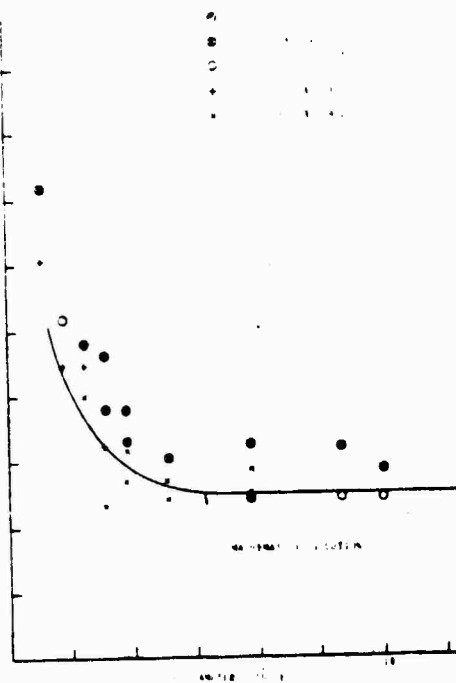


Fig 2 - Test Results for 1/4-Inch Plate

(U) A total of 16 tests was required to establish threshold values for the 1-inch plate using charge diameters of 2, 3, 4, 6, 9, 12, and 19-1/2 inches. Penetration was

impossible at diameters of 2 and 3 inches due to the severe edge relief suffered by the thicker charges. In all cases, the hole diameter produced by threshold or greater charges was approximately 1-1/2 inches less than the diameter of the charge that produced it. Results are plotted in Fig. 3.

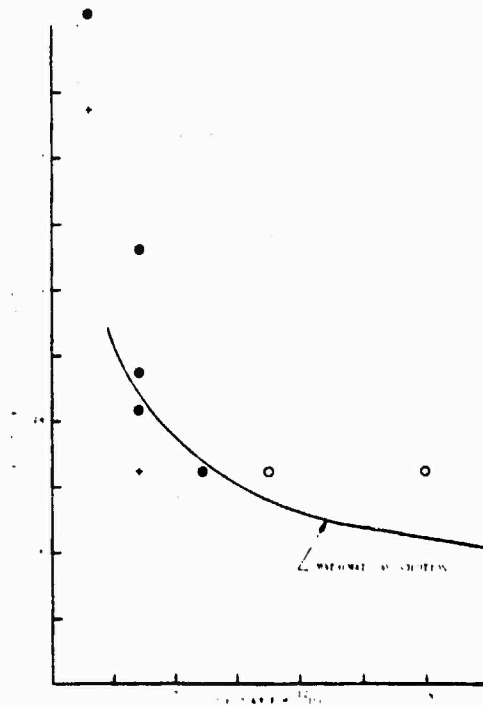


Fig 3 - Test Results for 1-Inch Plate (key same as Fig. 2)

(U) The third phase of testing involved filling the gap between the two extremes of plate thickness. To accomplish this, thresholds were established for 1/2- and 3/4-inch plate thicknesses at a diameter of 12 inches. Since the 12-inch diameter charge falls

on the flat portion of both the 1/4- and 1-inch curves, testing with larger diameter charges was unnecessary.

(U) First-time estimations of charge thickness for both the 1/2- and 3/4-inch plates were made by scaling linearly between threshold values for 1/4- and 1-inch plates. A near threshold value was determined with the first try on a 1/2-inch plate while three tests were required to bracket a threshold value for a 3/4-inch plate. Results are plotted in Fig. 4.

side of the plate began to occur until a completely spalled piece, somewhat larger in diameter than the charge, was produced. A slightly thicker charge produced tearing of the remaining material at a smaller diameter than the charge.

(U) Threshold was considered attained when the tearing exceeded 75 percent of the eventual hole circumference and back spall was complete.

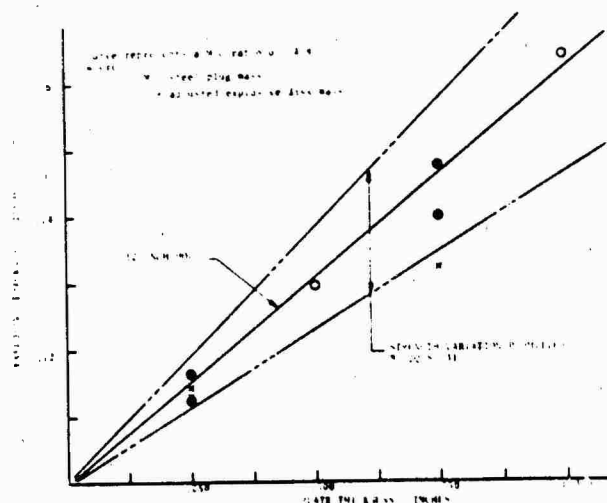


Fig 4 - Test Results for 12-Inch Hole in 1/4-, 1/2-, 3/4-, and 1-Inch Plates (key same as Fig. 2)

(U) It should be noted that, due to the relatively liberal thickness and ultimate tensile stress tolerances permitted by Specification QQ-S-741, significant variations in penetration resistance may exist between plates of the same nominal thickness. Strength variations may range from  $\pm 22$  percent on the 1-inch plate to  $\pm 29$  percent on the 1/4-inch plate.

#### EXPERIMENTAL OBSERVATIONS

(U) In addition to the empirical data gained from the breaching experiments, several observations were made that were worthy of note.

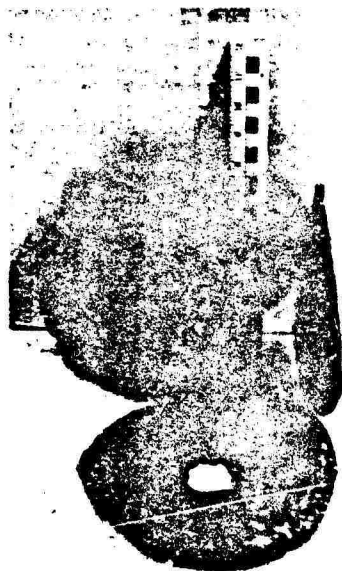
(U) With few exceptions, the failure mode appeared to be the same regardless of plate thickness or charge diameter. As the threshold was approached from the low side, a progressively deeper depression was produced in the steel plate. As charge thickness increased, scabbing of the back

(U) As the charge thickness exceeded threshold values, a complete hole was produced accompanied by complete spallation of the extracted plug. Increasing the charge thickness reduced the spalling effect until, eventually, a complete disk with no observable spall was cut from the test plate. Typical post-test specimens are shown in Figs. 5 through 7.

(U) For all penetrations except those below 6 inches in diameter in the 1-inch plates, the hole diameter was less than the charge diameter by approximately 1-1/2 times the plate thickness. A 19-1/2-inch diameter charge produced an 18-inch hole in a 1-inch plate.

#### MATHEMATICAL SOLUTION

(U) Following the test series, an attempt was made to develop a mathematical means of predicting breaching thresholds in structural steel plates.



◀ Fig 5 - Typical "Plugs" Resulting from Complete Breaching

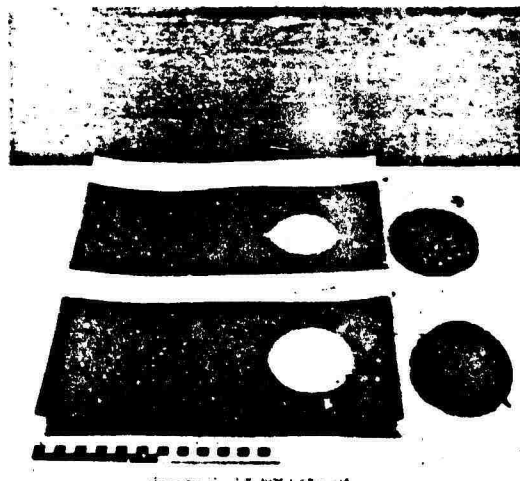
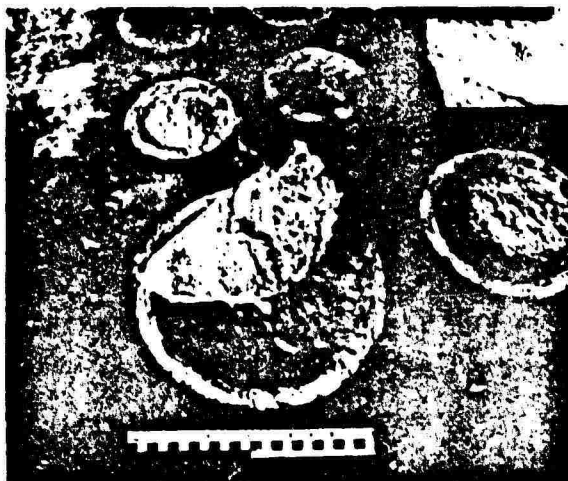


Fig 6 - Five-Inch Diameter Charge-- 1/4-Inch Plate, Required to Establish Threshold ▶



▶ Fig 7 - Threshold Test on 1-Inch Plate - Back Side

(U) Basically, the solution compares the energy required to shear a disk from a steel plate and the kinetic energy contained in a free-standing steel disk propelled by the detonation of an equal diameter explosive disk in contact with it. See Figs. 8 and 9.

and

$$D_{MIN} = D_{AVE} - .75H \quad (3)$$

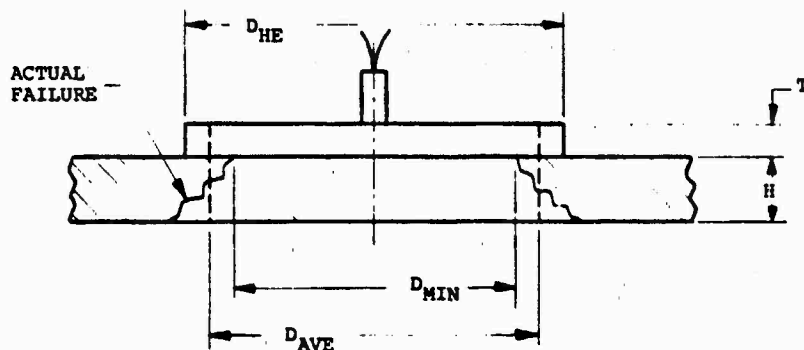


Fig 8 - Dimensions for Shear Energy Calculation

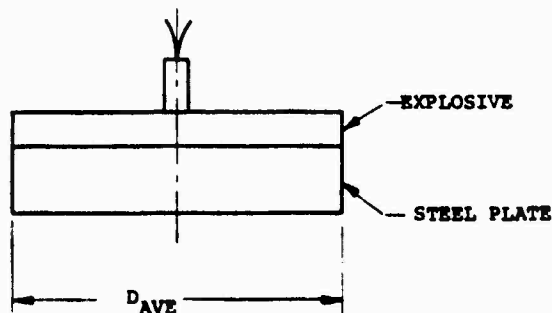


Fig 9 - Free-Standing Disk Configuration for Kinetic Energy Calculation

(U) Using measurements obtained from the test specimens,

$$D_{MIN} = D_{HE} - 1.5H \quad (1)$$

therefore,

$$D_{AVE} = D_{HE} - .75H \quad (2)$$

(U) By simplifying the irregular failure pattern into a simple cylindrical plane, the shear energy required to punch a disk of diameter  $D_{AVE}$  from a steel plate may be expressed as:

$$U = \pi D_{AVE} \int_0^H (H - Y) \tau_u dY \quad (4)$$

$$= \frac{\pi D_{AVE} H^2 \tau_u}{2}$$



where:

- U = shear energy
- H = plate thickness
- Y = displacement in the axial direction
- $\tau_u$  = ultimate static shear stress of material times rate factor (100,000 psi for mild steel)

(U) The kinetic energy in a free-standing disk propelled by an explosive of the same diameter and in contact with it (see Fig. 9) is defined by the Gurney equation [2]:

$$E = \frac{1}{2} \frac{M V^2}{P} \quad (5)$$

$$= \frac{M_P}{2} \frac{(\sqrt{2E})^2}{\left(1 + \frac{2M_P}{C}\right)^3 + 1} + \frac{M_P}{C}$$

where:

- $M_P$  = mass of driven plate
- C = mass of explosive (.052 lb/in<sup>3</sup> for Detasheet)
- $\sqrt{2E}$  = Gurney velocity constant (7480 ft/sec for Detasheet)

(U) If this analysis is applied to the material directly underneath the explosive disk, a shear failure should occur whenever the energy applied by the explosive exceeds the shear energy required to punch a hole in the plate.

$$E \geq U \quad (6)$$

(U) One modification to mathematical solution must be made at this point. According to Figs. 2, 3, and 4, the explosive thickness for threshold becomes constant at hole diameter values of approximately 12 inches. Applying formula (5), a plate energy corresponding to a plate velocity of 420 ft/sec is calculated; therefore:

$$V_{\text{FAILURE}} \geq 420 \text{ ft/sec} \quad (7)$$

(U) Thus, when conditions (6) and (7) are met, the plate should be breached by a hole equal to  $D_{\text{MIN}}$  (see

Fig. 8) using a charge of diameter  $D_{\text{MIN}} + 1.5H$ .

## SCALING TECHNIQUES

(U) These experiments have been restricted to steel plates with thicknesses between 1/4 and 1 inch and diameters of 18 inches and under. Keeping certain phenomena in mind, however, should allow the results to be scaled to other thicknesses and hole diameters.

(U) Using Figs. 2, 3, and 4 for hole sizes greater than 9 inches, the threshold explosive thickness becomes constant and equal to the amount required to drive an unrestrained metal disk of diameter  $D_{\text{AVE}}$  to a velocity of 420 ft/sec. This behavior should hold for explosive thicknesses within practical limits.

(U) For hole diameter to plate thickness ratios of less than 6, the curves become nonlinear and more complicated to scale. A reasonable approximation can be made by applying equations (4), (5), and (6); however, additional explosive energy side losses must be accounted for if explosive thickness to steel thickness ratios exceed .65. Employing Eq. (2) and data from numerous experiments involving explosively-driven "flyer plates", a discount angle of 30° from the cylindrical shear plane ( $D_{\text{AVE}}$ ) must be used as illustrated in Fig. 10. The shaded mass then becomes C in Eq. (5).

## RESIDUAL VELOCITY

(U) In addition to the experiments already discussed, a series of four tests was conducted to study the residual velocity of steel plugs produced by explosive charges which exceeded the breaching threshold. According to the mathematical solutions established, the residual velocity should be predicted by subtracting the required shear energy (4) from the Gurney free-standing plate calculation and (5) solving for velocity.

(U) For verification of the Gurney formula, two tests were performed on precut stainless steel, free-standing plate configurations using different explosive thicknesses (.120 and .235 inch). See Fig. 11. Resultant plate velocity was measured using a pulse x-ray system and the results are compared to prediction in Table I.

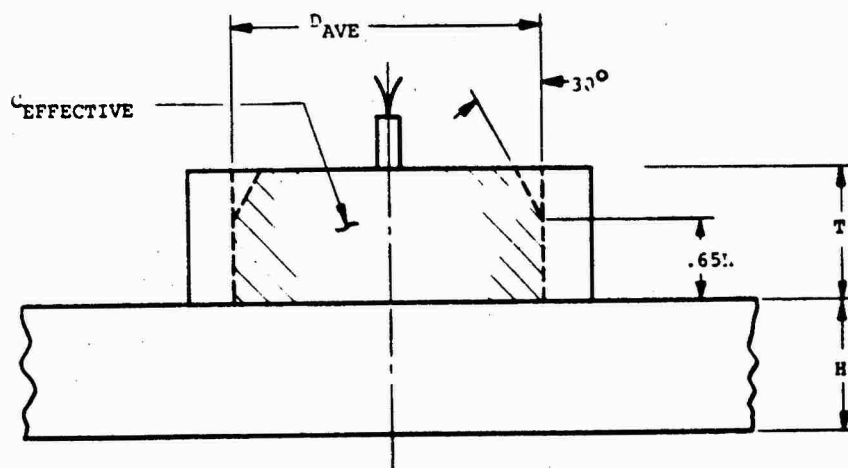


Fig 10 - Explosive Discounting Geometry

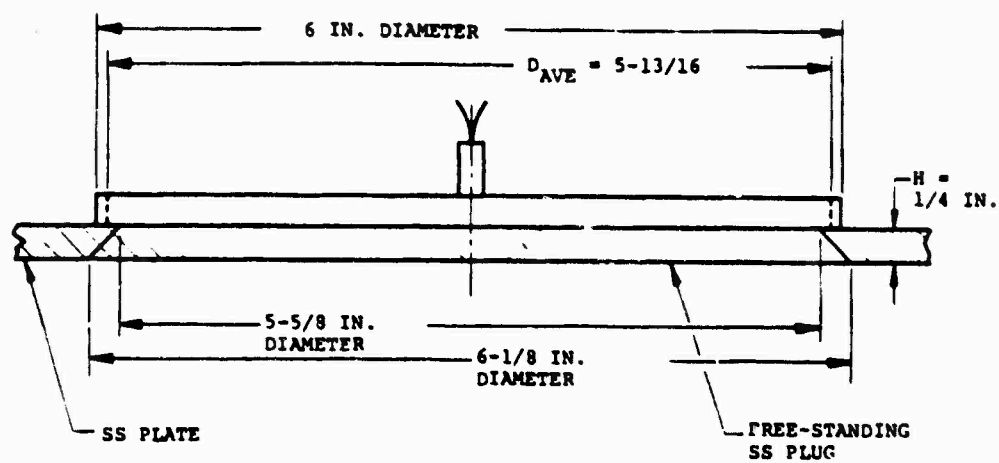


Fig 11 - SS Free-Standing Plate Setup

TABLE 1  
STAINLESS STEEL PLATE VELOCITY  
(NO METAL SHEAR)

HE THICKNESS (in)	MEASURED VELOCITY (ft/sec)	PREDICTED VELOCITY (ft/sec)
0.120	548	538
0.235	988	1005

TABLE II  
STRUCTURAL STEEL PLUG VELOCITY  
(AFTER SHEAR)

HE THICKNESS (in)	MEASURED VELOCITY (ft/sec)	PREDICTED VELOCITY (ft/sec)
0.111	395	300
0.235	930	922

TABLE III  
RESIDUAL ENERGIES

HE THICKNESS (in)	MEASURED ENERGY (ft/lb)	U (PREDICTED)	U (MEASURED)
0.120 - no shear	8859		
0.235 - no shear	28796		
0.111 - sheared	4640	4745	4219
0.235 - sheared	25700	4745	3096

(U) Two similar experiments were then conducted using uncut structural steel plates and 6-inch explosive charges of the same thickness. The resultant velocities of the sheared

plugs were measured and are compared with prediction in Table II. Predicted and measured shear energies are given in Table III.

(U) These comparisons verify that the Gurney equation using an explosive disk with diameter  $D_{AVE}$  correctly describes the kinetic energy imparted to free-standing metal plates. A useful estimate of a sheared plug's residual velocity can then be made by subtracting shear energy.

## CONCLUSIONS

(U) Empirical data and mathematical solutions described herein should be useful tools in predicting breaching thresholds in structural steel plates. Estimations of the residual velocity of a plug which has been sheared from a plate by an explosive charge that exceeds threshold can also be made.

## REFERENCES

1. A. A. Ezra, Principles and Practice of Metal Working, Garden City Press, Ltd.
2. J. E. Kennedy, "Explosive Output for Driving Metal," Behavior and Utilization of Explosives in Engineering Design, 12th Annual Symposium, New Mexico Sections ASME.

## DISCUSSION

Mr. Salive (David Taylor Naval Ship Research and Development Center): Having looked into breaching holes into the bottoms of ships in order to scuttle them that would look like a rather simple solution when you are not trying to push the ocean out of the way too.

Mr. Shirey: It is a simple solution and there is no attempt to say that it is an exact solution but it is a little more than we had when we started. It seems to work quite well.

Mr. Salive: Why did you decide to use explosive disks instead of something like a linear shaped charge?

Mr. Shirey: The original problem arose when we were asked to run some experiments to simulate a terrorist kind of attack such as a ball of C-4 explosive slipped against a steel wall; obviously that is quite complicated in geometry and we felt a disk would most closely approximate that kind of an attack. It is a bulk attack; rather than trying to find the method that would most easily penetrate we were asked to investigate an attack that involved just a mass of explosives so that is why the disk came about.

Mr. Salive: I hope your terrorists haven't heard about those hollow shaped wine bottles that the French used in World War II.